



NASA/ OHIO SPACE GRANT CONSORTIUM

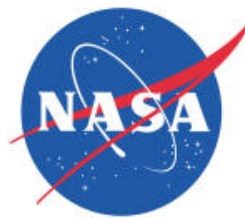
2019-2020 ANNUAL STUDENT RESEARCH SYMPOSIUM PROCEEDINGS XXVIII



NASA Astronauts Robert Behnken, left, and Douglas Hurley are seen inside the SpaceX Crew Dragon Endeavour spacecraft onboard the SpaceX GO Navigator recovery ship shortly after having landed in the Gulf of Mexico off the coast of Pensacola, Florida, August 2, 2020

Photo Courtesy of NASA

April 3, 2020
Symposium was not held at the Ohio Aerospace Institute due to COVID-19
Cleveland, Ohio



Follow OSGC on:



*Just click on any Section or Student Name,
and it will link you to the page immediately!*

TABLE OF CONTENTS

	<u>Page(s)</u>
Table of Contents	2-8
Foreword	9
Member Institutions	10
Pre-Service Educator Workshop Photographs	11-17

<i>Student Name</i>	<i>College/University</i>	<i>Page(s)</i>
Aoward, Mikayla L.	The University of Akron	18-20
Behavior of Sandwich Core Under Extreme Temperature Conditions		
Beardslee, Jacob M.	The Ohio State University.....	21-25
Screech Noise Modes in Supersonic Rectangular Twin Jets		
Bendele, Shaun A.	Columbus State Community College	26-27
Password Security and Brute Force Hacking		
Birchfield, Karlee D.	University of Cincinnati.....	28-32
Thermal Analysis of Laser Powder Bed Fusion Using Finite Element Modeling		
Brown, Owen C.	Miami University.....	33-39
Chemical Signature of Cured Epoxy Fracture Surfaces		
Buchman, Zachary J.	The University of Toledo.....	40-43
An Investigation of Maximum Power-Point Tracking for Space Applications		
Burk, Jennifer A.	Columbus State Community College	44-45
A Leachate and Strength Analysis of Fly Ash Encapsulated by Cement		
Butts, Marie C.	Cedarville University.....	46-50
Effects of Netrin-3 on THP-1 Monocytes		
Byrne, Liam J.	Columbus State Community College	51-52
Healthier Road Construction		
Chamberlain, Timothy J.	Youngstown State University	53-55
Design of Ranque-Hilsch Vortex Tube for Temperature Sensitive Paint Testing		

<i>Student Name</i>	<i>College/University</i>	<i>Page(s)</i>
Ciminillo Delamotte, Grace	Columbus State Community College	56-57
Comparative Study of Glulam-Members and Steel-Members Used In the Construction Field		
Clarchick, Victoria L.	Marietta College	58-59
BelleFlex Dehydrator and the Efficiency of Phase Separation		
Coleman, Katrina A.	University of Dayton.....	60-61
Industry 4.0 in the Retail Sector: Sustainability of Food Retail with a Focus on Food Insecurity in Dayton, OH		
Cox, Austin C.	The University of Toledo.....	62-63
The Importance of Video Games in Education		
Cresanto, Alexis C.	Youngstown State University	64-66
Detection of Hazardous Substances		
Commons, Lauren M.	The University of Akron	67-68
Choosing a PEG for a Hybrid Cardiac Hydrogel		
Deisler, William A.	Ohio Northern University	69-70
Modeling Liquid Propellant Rocket Nozzle using MATLAB and SolidWorks		
Dunson, Brandon L.	Sinclair Community College	71-72
Small Business Promotion through Web Development		
Eden, Brennan S.	Cincinnati State Technical and Community College	73
Graphene Future Technologies		
Evans, Rachel E.	Wright State University.....	74-81
Thermal Modeling of Coordinated Multi-Beam Additive Manufacturing		
Everswick, Rachelle E.	Cedarville University.....	82-83
Relationships within Ecosystems		
Fertig, Adam J.	Kent State University	84-90
Thermal Investigation of sUAS Motors Under Varying Power Conditions		

<i>Student Name</i>	<i>College/University</i>	<i>Page(s)</i>
Fitter, Ethan J.	Cincinnati State Technical and Community College	91-92
HAAS Stimulator		
Francis, Kirshaun D.	Central State University	93-96
Solar Shadow		
Gamertsfelder, Jacob O.	University of Cincinnati.....	97-101
Study of Atomization Behaviors of Liquid Monopropellants in Pintle Injectors		
Gartner, Bradley T.	Lakeland Community College	102-103
Removing and Preventing Ocean Microplastics		
Goetz, Dustin T.	The Ohio State University.....	104-107
3D-Printed Electrochemical Cell for <i>In Situ</i> Analysis		
Gomez Carrillo, Andrea.	Wright State University.....	108-112
Combined fNIRS and EEG Probe for Improved TBI Monitoring		
Graves, Jordan A.	Central State University	113-114
Health and Wellness Testing Assessment		
Ha, Matthew J.	University of Cincinnati.....	115-117
Optimized Supercritical CO₂ Compressor Design		
Hardnock, Emily A.	Kent State	118
Remote Sensing of the US Virgin Islands Spring 2020		
Hartnagel, Christopher L.	University of Dayton.....	119-122
Polymerized Liquid Metal Network Characterization for Stretchable RF Devices		
Hartswick, Delenn R.	Baldwin Wallace University	123-124
The Neuroscience of Gender – Exploring the Link between Prenatal Hormone Exposure and Sex-Specific Neuroanatomy in a Rat Model		
Hauerwas, Joel A.	Case Western Reserve University.....	125-129
Development of Flapping Winged Micro Air Vehicle Control Systems		
Henninger, Brevin F.	Cedarville University.....	130-133
3D-Printed Poly (lactic acid) Scaffolds for Regenerative Medicine: Does PLA Degrade, Support Osteoblastic Cellular Growth?		

<i>Student Name</i>	<i>College/University</i>	<i>Page(s)</i>
Huncik, Elainie C.	Youngstown State University	134-135
Understanding and Comparing Stars		
Issa, Marola W.	Cleveland State University	136-140
The Influence of Interfacial Properties on the Propulsion of Active Janus Particles Near an Air-Water Interface		
Jackam, Laura R.	Ohio University	141-145
The Effect of Diabetes Mellitus on Bone Fracture		
Jackson, Mystal E.	Lorain County Community College	146
Uncovering the Recipe for Synthetic Mineral Water		
Jewell, Madison M.	Wright State University.....	147-151
Effect of DNA Methyltransferase Inhibition in Hypoxic and Normoxic Conditions on Cellular Proliferation and Potential Growth Regulators in Human Diffuse Intrinsic Pontine Gliomas		
Kahn, Jason W.	The University of Toledo.....	152-153
Robust, Solvent-Free Anion Exchange Membranes for Fuel Cells		
Kaminski, Margaret M.	Kent State University	154-155
We Are Going on a Road Trip, Exploring Exoplanets and Life in Space		
Kosir, Shane T.	University of Dayton.....	156-163
A Machine Learning Framework for Drop-in Volume Swell Characteristics of Sustainable Aviation Fuel		
Kungle, Johnathan L.	Marietta College	164-167
Alternatives to Decommissioning Offshore Infrastructure: Artificial Reefing		
Lemonis, Niccolo D.	The University of Akron	168-172
High-Temperature, Flexible, Piezoelectric Transducers Based on Nylon-11 Nanowires		
Lin, Nathan E.	Youngstown State University	173-174
A Numerical Study of a Cyclone Separator at Reduced Operating Pressures		
Lorenz, Margaret A.	University of Cincinnati.....	175-177
Our Solar System		
Loughnane, Faith A.	University of Dayton.....	178-187
Effect of Airfoil-Preserved Undulations on Wing Performance		

<i>Student Name</i>	<i>College/University</i>	<i>Page(s)</i>
Malkus, Mikala J.	The Ohio State University.....	188-192
An Application of Modal Decomposition to Supersonic Flow Over a Wall-Mounted Turret		
Martin, Sara A.	Lorain County Community College	193
Determining the Influence of a Novel Mutation located in the C-terminal Cytoplasmic Domain of the CCR5 Gene on Infectivity of Primate Lentiviruses		
Mason, Taylor M.	Miami University.....	194-197
Evaluating the Effect of Electrode Configuration in Electrostatic Actuators for Increasing the Intensity of Vibrotactile Feedback		
Mastorovich, Clayton R.	Lorain County Community College	198
GC-MS Analysis of Spirits		
Matousek, Spencer T.	The University of Akron	199-202
Millimeter-Wave Polarimetry for Non-Contact Investigations of Aluminum Alloy Microstructure		
Matz, Stephen M.	Cleveland State University	203-206
Channel Detection and Synchronization in Ultra-Wideband Communication Systems		
McBryer, Madison M.	Kent State University	207-208
Classifying Clouds through Inquiry		
McCaskey, Cameron D.	The University of Toledo.....	209-210
Wireless Mesh Networking for Swarm Robotics		
McCullough, Molly M.	Columbus State Community College	211-212
Future Advancements in the Field of Programmable Logic Controllers		
Mileski, Joseph W.	Ohio Northern University	213-216
Direct Numerical Simulation of Cavity Flow		
Mitchell, Sara A.	Cedarville University.....	217-220
Investigations of Radiohalos from the Galway Batholith in Ireland		
Myers, Zane R.	Ohio Northern University	221-222
Drone Equipped Temperature Probing Hardware (DEPTH)		
Nixson, Roneishah S.	Cincinnati State Technical and Community College	223-224
Determination of Menthol in Peppermint Oil		

<i>Student Name</i>	<i>College/University</i>	<i>Page(s)</i>
O'Neill, Collin J.	The Ohio State University	225-230
Active Flow Control in an Aggressively Offset High-Speed Inlet/Diffuser Model		
Ogorodnikas, Rokas	University of Cincinnati.....	231-233
Optimized Compressor Stator Design with Supercritical CO₂		
Opacich, Katherine C.	University of Dayton.....	234-242
An Investigation on Kernel Growth Variations between Conventional Spark Discharges and Nanosecond-Pulsed High-Frequency Discharges		
Pickering, Lynn K.	University of Cincinnati.....	242-246
Genetic Fuzzy Based Tetris Player		
Roman, Sara J.	Kent State University	247
AR Overlay System Abstract		
Rosul, Alex J.	Kent State University	248-254
Using VPCA Spectral Decomposition to Analyze Optical Components Off the USVI with Sentinel – 3A/B OLCI		
Shapley, Sarah M.	Baldwin Wallace University	255-260
Effects of A PADI2 Inhibitor During Zebrafish CNS Myelination		
Shasteen, Hayley D.	Kent State University	261-265
The Role of Sunlight Exposure in Tasks of Inhibition in Patients with Systemic Lupus Erythematosus		
Shumway, Dylan Z.	Miami University.....	266-267
Reproducing Radial Pulse Waveforms Using a Hybrid Pulsatile System		
Slater, Michael K.	University of Cincinnati.....	268-270
Life-Size Scale of Our Solar System		
Smith, Ethan A.	Ohio Northern University	271-272
Gravitropism: Growing Plants in Space		
Tesny, Erin M.	Cleveland State University	273-279
Design of Heat Exchanger for Intense Cooling of Inlet Bleed Air at High Mach Numbers		
Wagner, Grant A.	Youngstown State University	280-281
Calibration of Optical Paints for Aerodynamic Testing		

<i>Student Name</i>	<i>College/University</i>	<i>Page(s)</i>
Walsh, Sara L.	Wright State University.....	282-285
Why Software Projects Fail: A Case Study in Implementing a GUI for a Satellite Imaging AI Training System		
Warkentien, Paul A.	Lorain County Community College	286-287
3D Printed Multi Materials for Aerospace Applications		
Watkins, Reese J.	Cedarville University.....	288-291
Characterization of the Effects of Aging on the THP-1 Human Monocyte Cell Line		
Watts, Ryan	Ohio Northern University	292
Selection of Appropriate Airfoil and Wing Parameters		
Willoughby, Michelle M.	Cincinnati State Community College	293-297
The Effectiveness of a Small Portable Solar Panel Set-Up		
Woller, Patrick G.	Baldwin Wallace University	298-304
Aquaporin-4 Distribution Correlates to Increase In Tau Accumulation In Sprague Dawley Rats Fed a High Fructose Diet		
Zandier, Reis L.	Youngstown State University	303-307
Detection of Cocaine via Physically Functionalized Carbon Nanotubes-Sensors		
Zirkle, Andrea L.	Lorain County Community College	308
Flavor Profile of Moonshine Homemade from Apples and Double Distilled		

FOREWORD

The Ohio Space Grant Consortium (OSGC), a member of the NASA National Space Grant College and Fellowship Program, awards graduate fellowships and undergraduate scholarships to students working toward degrees in Science, Technology, Engineering and Mathematics (STEM) disciplines at OSGC-member universities. The awards are made to United States citizens, and the students are competitively selected. Since the inception of the program in 1989, over 1,320 undergraduate scholarships and 181 graduate fellowships have been awarded.

Matching funds are provided by the 24 member universities/community colleges, the Ohio Aerospace Institute (OAI), and the Ohio Department of Higher Education (State of Ohio). Note that this year ~ \$500,000 will be directed to scholarships and fellowships representing contributions from NASA, the Ohio Aerospace Institute, State of Ohio, member universities, foundations, and industry.

By helping more students to graduate with STEM-related degrees, OSGC provides more qualified technical employees to industry. The research conducted for the Master's fellowship must be of interest to NASA. A prime aspect of the scholarship program is the undergraduate research project that the student performs under the mentorship of a faculty member. This research experience is effective in encouraging U. S. undergraduate students to attend graduate school in STEM. The Education scholarship recipients are required to attend a workshop conducted by NASA personnel where they are exposed to NASA educational materials and create a lesson plan for use in their future classrooms.

Due to COVID-19, the Annual Student Research Symposium scheduled for Friday, April 3, 2020, at the Ohio Aerospace Institute was cancelled. All student presentations are posted on the OSGC website at:
<http://www.osgc.org/symposium.html>

Research reports of students from the following schools are contained in this publication:

Affiliate Members

- The University of Akron
- Baldwin Wallace University
- Case Western Reserve University
- Cedarville University
- Central State University
- Cleveland State University
- University of Dayton
- Kent State University
- Marietta College
- Miami University
- Ohio Northern University
- The Ohio State University
- Ohio University
- University of Cincinnati
- The University of Toledo
- Wright State University
- Youngstown State University

Community Colleges

- Cincinnati State Technical and Community College
- Columbus State Community College
- Lakeland Community College
- Lorain County Community College
- Sinclair Community College

MEMBER INSTITUTIONS

Affiliate Members

- Baldwin Wallace University..... James W. McCargar, Ph.D.
- Case Western Reserve University Roger D. Quinn, Ph. D.
- Cedarville University Robert Chasnov, Ph.D., P.E.
- Central State University Augustus Morris, Jr., Ph.D., P.E.
- Cleveland State University Wei Zhang, Ph.D.
- Kent State University Joseph D. Ortiz, Ph.D.
- Marietta College..... Prof. Craig Rabatin, P.E.
- Miami University James Moller, Ph.D., P.E.
- Ohio Northern University..... Jed E. Marquart, Ph.D., P.E.*
- The Ohio State University Dr. Mo Samimy
- Ohio University..... Dr. Shawn Ostermann
- The University of Akron..... Dr. Craig C. Menzemer
- University of Cincinnati Dr. Kelly Cohen
- University of Dayton..... Dr. Robert J. Wilkens
- The University of Toledo Dr. Lesley M. Berhan
- Wilberforce University Jennifer N. Williams, Ph.D.
- Wright State University Mitch Wolff, Ph.D.
- Youngstown State University Kevin J. Disotell, Ph.D.

Community Colleges

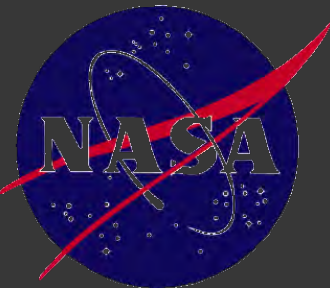
- Cincinnati State Technical and Community College Professor Abigail Yee
- Columbus State Community College..... Professor Jeffery M. Woodson, M.S., I.E.
- Cuyahoga Community College Prof. Michelle S. Davis
- Lakeland Community College..... Professor Tom Ciferno
- Lorain County Community College..... Regan L. Silvestri, Ph.D.
- Sinclair Community College Eric C. Dunn

NASA Glenn Research Center - Representatives

- Dr. M. David Kankam
- Ms. Susan M. Kohler
- Mr. Robert F. LaSalvia



*Dr. Marquart also serves as Director of the Ohio Space Grant Consortium



PRE-SERVICE EDUCATOR WORKSHOP

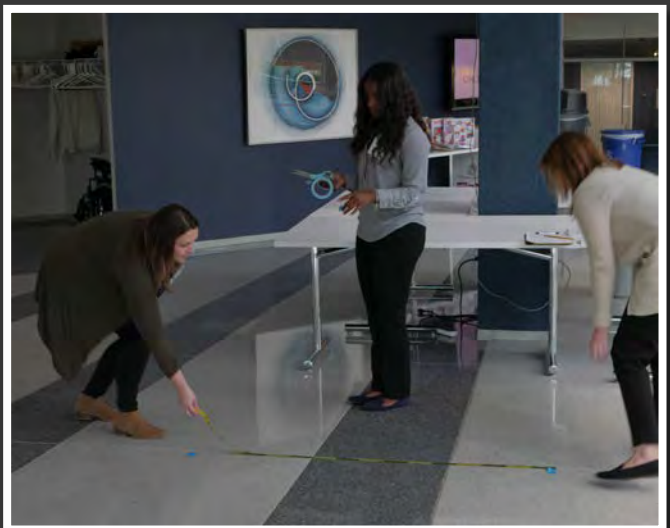
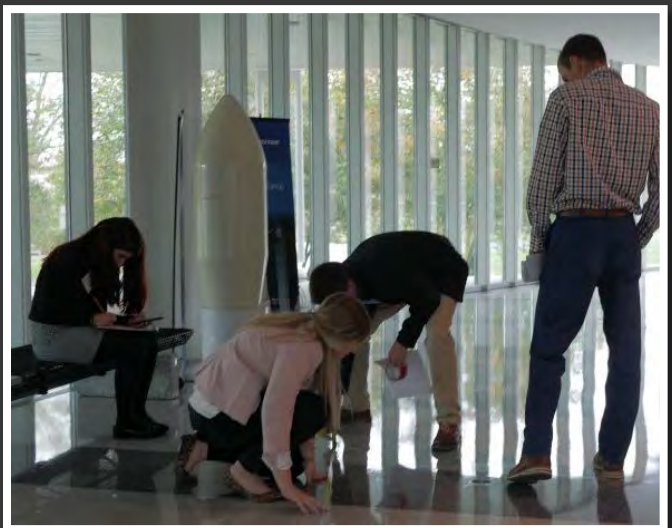


Held at the Ohio Aerospace Institute
October 25, 2019

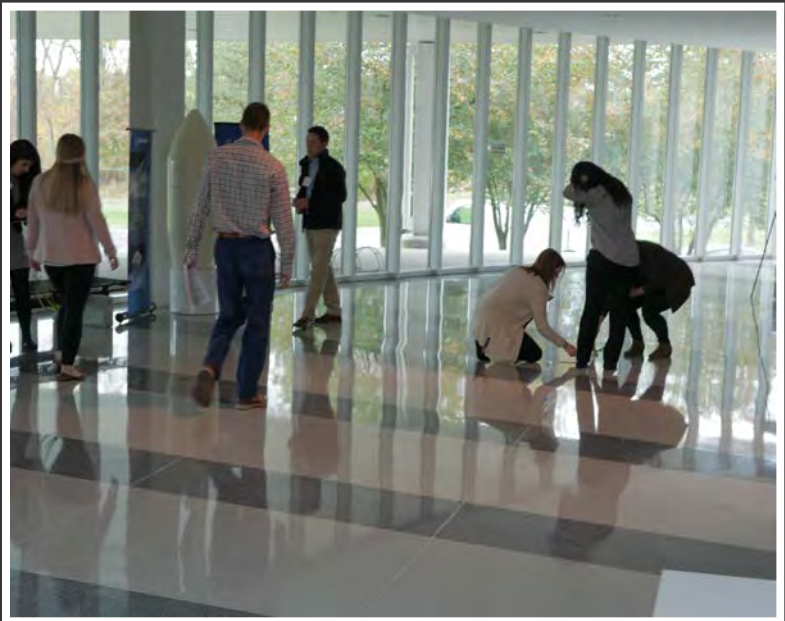
Due to the COVID-19 pandemic, the 2020 Student Research Symposium was cancelled. The student reports may be viewed at: <http://osgc.org/publications.html>

Please enjoy the following pictures from our last in-person gathering: the 2019 Pre-Service Educator Workshop.

STUDENTS UTILIZE MOBILE APPS TO MEASURE AND TRACK SPACE: LAND COVER (FIND YOUR PACE)



PREPARATION





LAND COVER WALK



Ethan Smith (Ohio Northern University) sends his team's Crew Exploration Vehicle (CEV) into the Ohio Aerospace Institute's airspace to see how it fares in landing.



GROUP PHOTO

Behavior of Sandwich Core Under Extreme Temperature Conditions

Student Researcher: Mikayla L. Aowad

Advisor: Dr. K. T. Tan

The University of Akron
Mechanical Engineering

Abstract

Composite materials are being utilized in many industries including aerospace, marine and wind energy because of the high stiffness, low weight and high strength properties of the material. The type of composite material studied here is a sandwich structure. This means the material is designed with three layers and adhesive. There are two lightweight, but strong face sheets and a thick shear-resistant core. This research focuses on the microstructures of the core material and how temperature affects the overall mechanical behavior. Three types of foam core are being studied: H, PN and F. They are made of cross-linked polyurea and PVC, polyethylene terephthalate and thermoplastic polyether sulfone, respectively [1]. There are multiple densities of each type of foam. The density is given as the number after the type of foam in kg/m³. The specific specimens used in this study are H60, H100, F50, F90, PN115, PN200 and PN250. This study evaluates arctic effects on mechanical properties in varying types of foam core at varying densities along with general analysis on how microstructure affects mechanical properties of the foam.

Project Objectives

Foam core tensile, compressive and shear stress have been thoroughly studied, but this study investigates the bending stress of the foam core. Having data on how their mechanical properties will change with temperature is important so that considerations can be made when designing structures and choosing materials during their operating conditions.

Methodology Used

To test the bending strength of the foam cores, a three-point bend test is performed [2]. The specimen is placed so that it is resting on its two end points. The third bending point is applied by an anvil attached to the crosshead of Instron 5582 universal testing machine. The crosshead of the machine is displaced at 5 mm per minute. Some of the foams are expected to be flexible and resist permanent deformation, while some foam types are expected to be brittle and split into two or three pieces. For the specimens being tested at low temperature, they are to be cooled at -22°C overnight and conditioned in the environmental test chamber for 2 minutes before the test is started. The test will be run at -70°C. Liquid nitrogen is attached to the Instron 5582 test machine via cooling chamber. Once testing is complete, the data will be analyzed to determine any correlation between variables and strength or variables and temperature. The variables include density, cell size, cell shape, cell wall thickness.

Significance and Interpretation of Results

Based on Figure 1, as the density of the material increases, the strength does as well. It is also seen that low temperature specimens have a higher strength when compared to room temperature specimens. The only specimen that did not follow this trend was PN250. The reason for this is unknown, but may be caused by having only a small sample size of specimens. Similar densities between the F and H groups have similar strengths, but when comparing F and H to PN, the strength of PN115, is less than H100 and

F90. This is caused by the different types of polymers that make up the foams. The micro-computed tomography images (Figure 2) show that as the density of the foam increases, so do the number of cells in view, which is expected. The PN group has a rounder cell shape compared to the F and H groups. The cell shape and pattern of F and H groups is similar, and this reinforces the results of Figure 1 that F and H group foams have similar strengths at similar densities. Due to the extremely low density of F50, the scanner picked up multiple layers of the foam at once, which is why the image appears to be very dense. The dense lines shown in PN115 and PN250 are due to the manufacturing process and do not influence results. In conclusion, the density of the foam and the strength of the foam have a positive correlation. The density and temperature have a negative correlation. This is due to the brittleness of the foam as the temperature decreases. The foam can take on more strength, but it becomes more brittle and more likely to break at the lower temperatures as well. Further analysis of μ CT images will assist in calculating cell wall thickness in each foam. Cell wall thickness models are being developed to estimate cell wall thickness and compare with measurements from the μ CT images. Microscope images will also be utilized for further understanding of how cell shape affects foam mechanical properties as well.

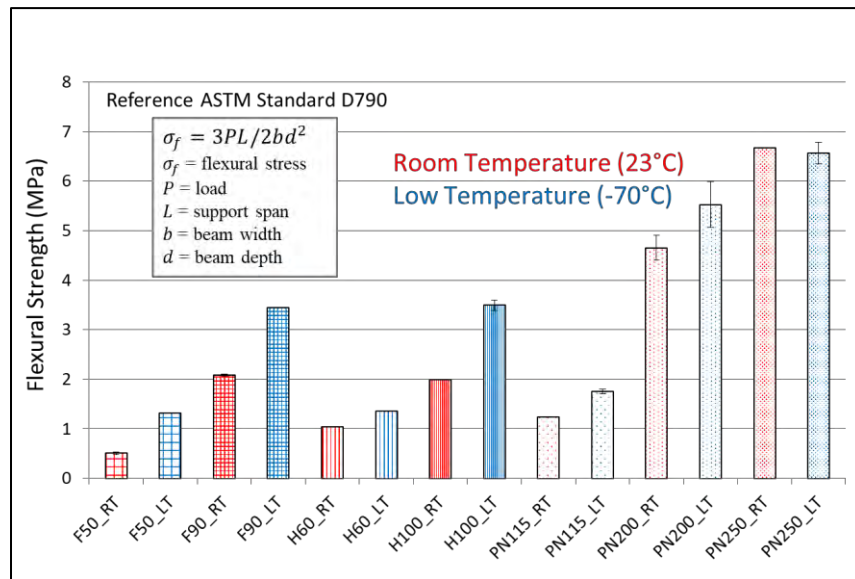


Figure 1. Maximum Flexural Strength [2].

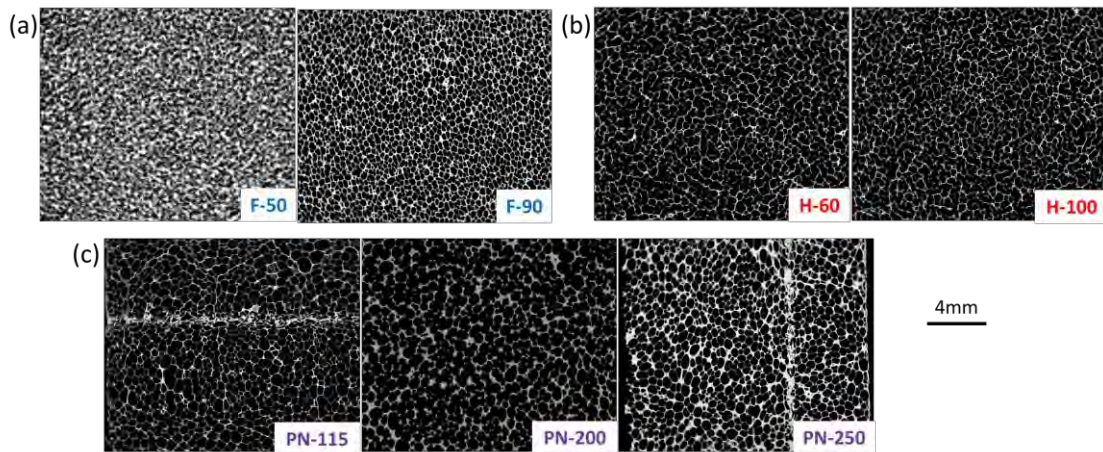


Figure 2. Micro computed tomography (μ CT) images for (a) F type; (b) H type; (c) PN type foam.

Acknowledgements

I would like to thank Dr. K. T. Tan for offering me the opportunity to join his research group early in my college career and grow my passion and interest for research. Thank you to OSGC for awarding me with this amazing scholarship opportunity. I would also like to thank my family and friends for supporting me in my research.

References

1. "Guideline to Core and Sandwich." *Diabgroup*, www.diabgroup.com. PDF
2. ASTM Standard D790, 2003 (2007), "Standard Test Methods for Flexural Properties of Unreinforced and Reinforced Plastics and Electrical Insulating Materials," ASTM International, West Conshohocken, PA, 2007, www.astm.org

Screech Noise Modes in Supersonic Rectangular Twin Jets

Student Researcher: Jacob M. Beardslee

Advisor: Dr. Mo Samimy

The Ohio State University
Mechanical and Aerospace Engineering Department

Abstract

Jet noise has been an issue for commercial and military aircraft since the advent of jet-powered flight. Circular jets have been the dominant configuration for military jets throughout history with a significant amount of research focused on their noise characteristics. The next generation of tactical aircraft are expected to have more integrated aerodynamic and propulsion systems for stealth, superior performance, and agility. For such an integration, rectangular jets are preferred over circular jets. The rectangular shape will produce different flow structures compared to circular jets therefore presenting many new aspects to investigate regarding their noise characteristics. The dominant noise sources for supersonic jets include mixing noise from large-scale turbulent structures, broadband shock associated noise, and screech.

Screech, which has an upstream and sideline directivity, can be detrimental to the structural integrity of the engine nozzle if the noise frequency is close to the natural frequency of the structural component. In addition, screech and shock associated noise could inflict significant pain and damage to hearing of the crew on aircraft carriers helping with the takeoff and landing of the aircraft. Screech is a discrete tonal noise produced in imperfectly expanded supersonic jets. The interaction between shock waves, formed from a nozzle operating at off-design conditions, and large-scale turbulent structures in the shear layer form acoustic waves traveling in the upstream direction outside the jet. These acoustic waves interact with the receptive region of the jet-plume, located in the vicinity of the nozzle exit, reinforcing the formation of large-scale turbulent structures and creating a closed feedback loop [1]. A large amount of the initial research conducted on screech were for circular jets. Axisymmetric, helical, and flapping modes were found for screech tones depending on the Mach number and operating regime of the jet [2]. For twinjets, coupling of the twinjet's flow and acoustic fields can occur which causes significant noise amplification. Screech modes for rectangular twin jets are notably different. The acoustic waves travel in the twinjet plane for circular twinjets but for rectangular twinjets, acoustic waves travel primarily in the plane normal to the twinjet plane [1]. This changes the coupling effect by altering the noise directivity for rectangular twinjets, causing different screech modes to occur [1].

Project Objectives

The ultimate goal of this project is to explore the flow physics of closely spaced, low aspect ratio rectangular nozzles for a range of operating regimes and to control the jets using Localized Arc Filament Plasma Actuators (LAFPAs). LAFPAs control the flow by producing thermal perturbations that excite the large-scale turbulent structures in the jet shear layer [3]. The growth of these structures can be controlled by changing the frequency and timing of the LAFPAs [3]. Coupling between turbulent structures in twin jets may then be reduced, thus reducing the overall noise amplification between the jets. The specific objective of this work is to identify the screech modes for flow regimes ranging from highly overexpanded to highly underexpanded cases.

Methodology

Experiments were conducted in the jet anechoic facility at Gas Dynamics and Turbulence Laboratory within The Ohio State University's Aerospace Research Center. The facility is an anechoic chamber with dimensions of $6.5\text{ m} \times 5.6\text{ m} \times 3.4\text{ m}$ covered with fiberglass wedges. Three five-stage compressors, that store air in two 43 m^3 cylindrical tanks at a maximum pressure of 16 MPa, are used to supply high-pressure air. The air is dried, filtered, and passed through a series of screens in the jet's settling chamber before entering the jet plenum that is attached to the nozzle assembly with a circular mounting plate.

The apparatus used for experimental testing was a pair of two-dimensional bi-conical converging-diverging nozzles with an aspect ratio of 2 and a design Mach number of 1.5 which can be seen below in Figure 1a [4]. The spacing of the nozzles, from center to center, is 1.708 in. which corresponds to 2.35 equivalent exit diameters. The nozzle width and height are 0.95 in. and 0.475 in. respectively. Flight conditions are simulated using a high-pressure air pipe at the center of a co-flow duct that is attached to the nozzle assembly using a circular mounting plate. To ensure a tight seal, an O-ring was designed for the interface between the nozzle assembly and circular mounting plate. A series of tests were conducted at various flight speeds to ensure that there were no major leaks in the assembly. Sealant was applied to interfaces where leaks were detected. The ideally expanded Mach number of the assembly was determined with a Mach Number sweep of $M_j = 1.4$ to $M_j = 1.6$ where far-field microphone data for polar angles of 30° , 90° , and 120° were collected while the nozzle assembly was placed at an azimuthal angle of 90° . The pressure spectra were then analyzed to determine the ideally expanded flow Mach number. There should be no shock system for the ideally expanded flow case from a nozzle designed using method of characteristics therefore noise peaks due to screech and broadband shock associated noise would be absent. This was difficult for the present setup, as the nozzles used were bi-conical nozzles with sharp throat (military style nozzles) as a shock system created at the nozzle throat caused there to be no case where screech and broadband shock associated noise was not present. The case where the noise peaks were lowest was determined to be the ideally expanded case which was close the design Mach number of 1.5.

A near-field microphone array was used to determine screech modes for the assembly. Five Brüel and Kjær 4939 $\frac{1}{4}$ in. microphones were held using a 15 in. \times 15 in. rectangular frame as seen in Figure 1b. The microphones were positioned at an axial location of $x/D = 0$ and a radial location of $r/D = 5$ as it is far enough away from the jet shear layer to record screech's acoustic signature. The microphone array, along with the rectangular mount, were wrapped in acoustic foam to prevent sound reflections.

The near-field acoustic signals acquired by the near-field microphones were amplified and band-pass filtered with Nexus 2690 signal conditioners. Test runs were conducted before acquiring data in order to set each microphone's gain levels so that the entire dynamic range was used without saturating the channels. Once the gain levels were set, the microphones were calibrated using a Brüel and Kjær model 4231 acoustic calibrator. The calibrator converted the measured voltage data to equivalent sound pressure level (SPL). For each data point, 400 blocks of 8192 samples were acquired for a sampling frequency of 200 kHz resulting in 24.4 Hz frequency resolution. A Fast Fourier Transform code in MATLAB was used to calculate the Power Spectral Density (PSD) for each block of data then the average over the 400 blocks was calculated. The PSD was then converted to SPL in decibels.

A MATLAB code that calculates the wavelet coherence between two microphone signals was used to obtain the relative phase and coherence between the two jets for the microphone data. The code calculates the phase angle and magnitude of the wavelet coherence as a function of time and frequency.

Regions of coherence greater than 0.7 are obtained and temporal averages of the phase and coherence are calculated for these regions. Examining regions of high coherence only allows for reliable determination of the phase of the signals.

Experimental Results

Phase and coherence values were obtained for the Mach range $M_j = 1.25$ to $M_j = 1.85$ at intervals of 0.05. For $M_j = 1.25 - 1.55$, high coherence values between the two jets were registered around the screech fundamental frequency in the vertical plane with a phase difference of 180° . For $M_j = 1.60 - 1.65$, high coherence values between the two jets were registered around the screech fundamental frequency in the vertical plane with a phase difference of 0° . At $M_j = 1.70$, high coherence values between the nozzles around the screech fundamental frequency were registered in both the vertical and horizontal planes with a phase difference of 0° . For $M_j = 1.75 - 1.85$, the fundamental screech peaks were registered for microphones 2 and 3 only while the first harmonic peaks were registered in microphones 1 and 4 as was the case for $M_j = 1.25 - 1.55$. High coherence between the two jets around the screech fundamental peaks were registered in the vertical plane with a phase difference of 0° . A summary of these results for the 3 coupling modes identified can be seen in Table 1 below. Phase and coherence plots along with the near-field pressure spectra for $M_j = 1.25$ can be seen below in Figure 2. These plots were used to identify the phase, coherence, and screech peaks for each Mach range.

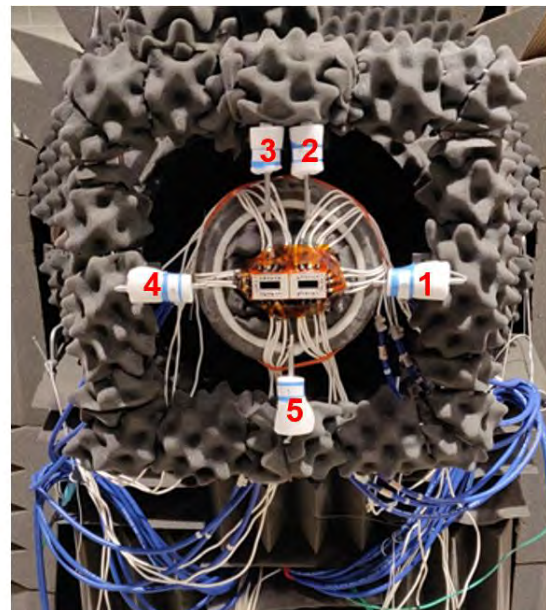
Significance and Interpretation of Results

3 different coupling modes were identified for the Mach range tested. Mode I ($M_j = 1.25 - 1.55$) experiences out-of-phase flapping in the vertical plane. Mode II ($M_j = 1.60 - 1.65$ and $1.75 - 1.85$) experiences in-phase flapping in the vertical plane. Mode III ($M_j = 1.70$) experiences in-phase coherence in both the vertical and horizontal planes, characteristic of an axisymmetric mode.

Figures and Tables



a)



b)

Figure 1. a) Twin Jet Assembly b) Near-field Microphone Array.

Table 1. Coupling Modes for Rectangular Twin Jet

Range of Mach numbers	Coupling Mode	Mode Characteristics
$M_j = 1.25 - 1.55$	Mode I	Out-of-phase flapping in vertical plane
$M_j = 1.60 - 1.65$	Mode II	In-phase flapping in vertical plane
$M_j = 1.70$	Mode III	In-phase coherence in vertical and horizontal planes
$M_j = 1.75 - 1.85$	Mode II	In-phase flapping in vertical plane

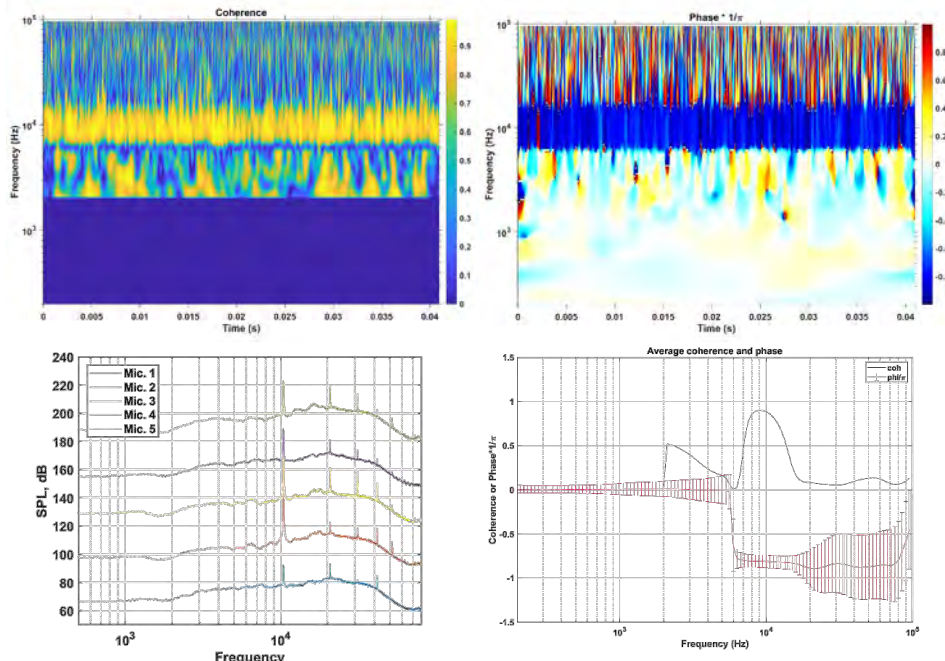


Figure 2. Near-Field Coherence/Phase/Spectra for $M_j = 1.25$

Acknowledgments

The author would like to thank Ata Esfahani, Dr. Nathan Webb, and Dr. Mo Samimy for their guidance and support. The author would also like to thank The Ohio State University and the Office of Naval Research for providing funding and Ohio Space Grant Consortium for providing me scholarship in my senior year.

References

1. Kuo, C., Cluts, J., and Samimy, M. "Exploring Physics and Control of Twin Supersonic Circular Jets." *AIAA Journal*, vol. 55, no. 1, 2017, pp. 68–85., doi:10.2514/1.j054977.
2. Powell, A., Umeda, Y., Ishii, R. "Observations of the Oscillation Modes of Choked Circular Jets." *The Journal of the Acoustical Society of America*, vol. 92, no. 5, 1992, pp. 2823–2836., doi:10.1121/1.404398.
3. Samimy, M., Webb, N., and Crawley, M., (Invited Paper) "Excitation of Free Shear-Layer Instability in High-Speed Flows," *AIAA Journal*, Vol. 56, No. 5, 2018, pp. 1770-1991.

4. Esfahani, A., Webb, N., and Samimy, M., "Exploring Physics and Control of Twin Rectangular Supersonic Jets." Will be presented at the AIAA Aviation Conference, June 2020, Reno, Nevada.

Password Security and Brute Force Hacking

Student Researcher: Shaun Bendele

Advisor: Kent King

Columbus State Community College
Cyber Security

Passwords are used for almost everything from email to zip files to online games. This form of authentication is risky and can usually be broken easily. Code for brute force password breakers can be found easily on sites such as Stack Overflow, a site used to exchange lines of code. There are ways to secure a login page and these are steps in the right direction for password security.

It is easy to break passwords that have little to no protection on the login site. When researching this, me and my advisor wrote a code that gathered passwords from a master list and tried it against a zip file. The Python code was fairly easy to write and took about thirty minutes to get it working correctly. The code was run from a command prompt on my computer and anyone with about three minutes of downloads can run it as well. The passwords were drawn from a file that can be found with an easy Google search.

Password dictionaries are large files that contain millions of passwords and is accessible by anyone with internet access. A fairly popular dictionary comes from a site called Crackstation. This site has a zip file with 1,493,677,782 words in it that have come from many different places. “The list contains every wordlist, dictionary, and password database leak that I could find on the internet. It also contains every word in the Wikipedia databases as well as lots of books from Project Gutenberg. It also includes the passwords from some low-profile database breaches that were being sold in the underground years ago.” (CrackStation’s Password Cracking Dictionary). The file that was easy to download had been measured to break thirty percent of the passwords tried on their sites and 49.98% of passwords during a test of 373,000 human passwords.

These password files are loaded into a script and tested against a login screen until one works. A zip file is easy to experiment on because it has no login page security. You can attempt the password as many times as needed and it does not lock you out. This is a flaw of having a secure zip file with your passwords in it or having a master list anywhere on your computer. Other websites and login screens have some security against brute force hacking, but nothing is one hundred percent secure yet.

One way to secure a login screen is adding a limit to the number of guesses possible before it locks the page and you cannot attempt any more times. This is slightly effective against brute force hacking because the hacker cannot run the code after three attempts, so it takes them much more time to back out of the page every time they are locked out. Another way to secure the website more is to make the user reset their password after a certain number of failed attempts, locking the account for a certain period of time, or in some phones, wiping all data from the device and returning it to a factory reset state.

These kinds of securities are sometimes unnecessary because the information on the site is not sensitive enough to warrant these measures. They can waste time and stop productivity. A good median for people that is widely available is two-factor authentication. This sends a code to a trusted phone number and the website requests that code after typing in your password. There are ways around this but they are expensive and unreliable. Experts recommend enabling this for every site that allows it. This is a step in the right direction but is not perfect yet.

Reference

1. *CrackStation's Password Cracking Dictionary*. 26 May 2019. 15 March 2020.

Thermal Analysis of Laser Powder Bed Fusion Using Finite Element Modeling

Student Researcher: Karlee Birchfield and Balachander Gnanasekaran

Advisor: Dr. Yao Fu

University of Cincinnati

Department of Aerospace Engineering and Engineering Mechanics

Abstract

Additive manufacturing has quickly found widespread applications in various industries, because it allows for manufacturing of complex geometries, weight reduction, material waste minimization, and improved component quality. This has especially gained attention in the aerospace industry due to its ability to repair complex and expensive parts instead of replacing them.^[1] While there are many benefits that come with using additive manufacturing, there are also many challenges. One of the challenges is understanding the thermal residual stress generated during the formation of the part.^[2] The aim of this work is to model the laser powder bed fusion process to provide an effective way to understand the relationship between process parameters and temperature history. This process was modeled in Abaqus with a user defined Fortran subroutine to simulate the laser with a moving heat flux. It is found that there is an increase in max temperature and melt pool size with increasing laser power or decreasing scan speed.

Project Objectives

The scope of this project is to develop a finite element model to gain a deeper understanding of the relationship between process parameters, temperature history, and thermally induced residual stresses in the laser powder bed fusion (LPBF) process. In LPBF, metallic powders are uniformly spread on the building platform by a rake instead of being blown out from nozzles as in directed energy deposition (DED) method. A focused laser beam scans the surface according to the prescribed path and selectively melts the powders in this layer, after which a new layer of powders is spread after lowering the building platform to the distance of the layer thickness. The layer height of LPBF is in the scale of tens of microns, which is much thinner than that of DED and electron beam melting (EBM) products.^[2] High residual stress created when using this technique can lead to cracking, fatigue-failure, distortion and the need for support structures. This modeling strategy can predict temperature distribution and melting pool size which serves as a beginning step towards a full residual stress analysis.^[3]

Methodology Used

The LPBF process was modeled using Abaqus with a user defined Fortran subroutine to simulate the laser with a moving heat flux. The thermal analysis was done with stainless steel 316L. The thermo-physical material properties required are specific heat (0.5 kJ/kg/K), density (7.99 g/cm²) and thermal conductivity (0.201 W/m·K).^[4]

A rectangular domain of 34mm x 7.3mm x 150mm was used with 8 node hexahedral elements with an initial temperature of 20°C. A laser path was defined across the top surface of the rectangular domain with the laser parameters listed in Table 1. The heat flux was defined by the following equation.

$$q(x,y) = \frac{\alpha_R P}{\pi r_0^2} \exp \left\{ -\frac{r^2}{r_0^2} \right\}$$

Table 1. The Process parameters used to define heat source

Laser Power (W)	2000	Radius of Laser Beam (mm)	2
Scan Speed (mm/s)	10.4	Absorption Efficiency (%)	40

Results and Discussion

The figure below shows the temperature distribution as the laser moves across the rectangular domain. The laser increased the temperature of the powder to exceed its melting point, turning the powder into liquid and creating a melt pool. The size and shape of the melt pool can also be seen in the figure below. The melt pool dimensions are 10.2mm x 9.7mm x 4.38mm compared to the laser diameter of 4mm. Once the laser passes, the temperature returns below its melting point where it then cools and hardens to form a segment of the first layer. Figure 2 shows the temperature of node 231 throughout the simulation. This node reaches a max temperature of 2516K when the simulation is at 4 seconds.

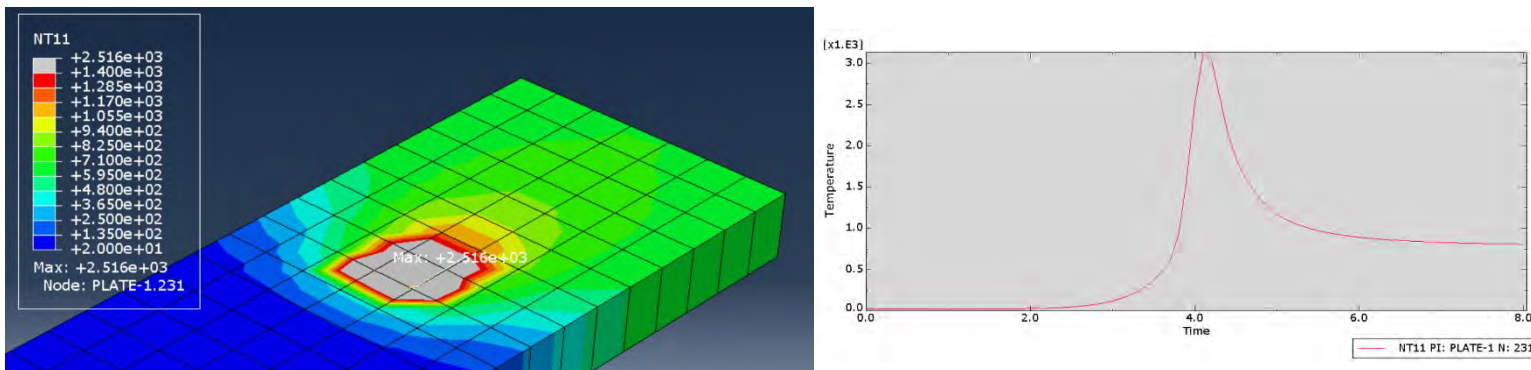


Figure 1a). Thermal distribution and geometry of melt pool, b) Temperature evolution at a node

To understand the effects laser power and scan speed on melt pool size and the max temperature, 7 additional cases were simulated. These cases are listed in Table 2.

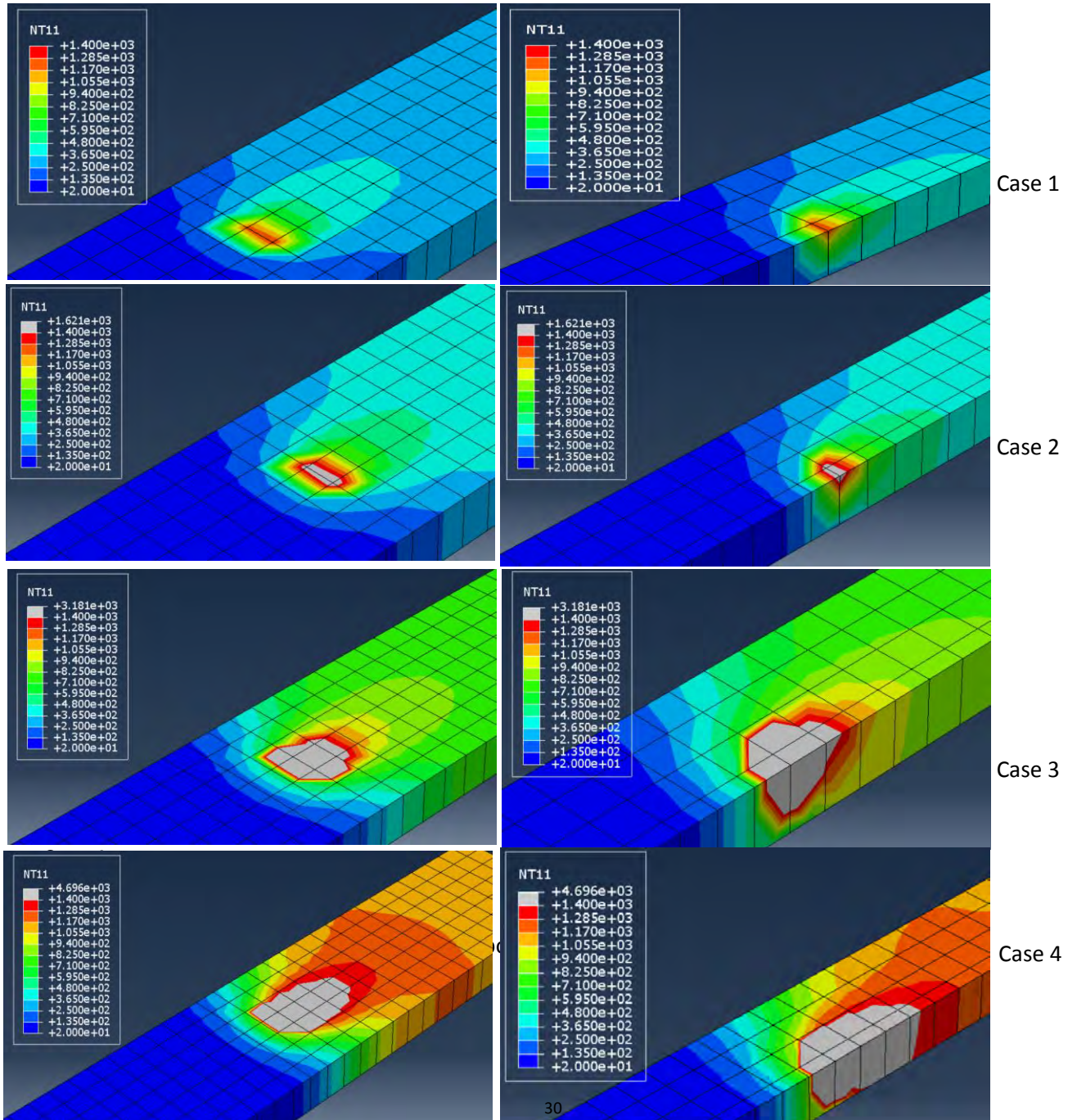
Table 2. Test cases varying in laser power and scan speeds

Case	Laser Power (W)	Scan Speed (mm/s)	Melt Pool Size (mm)	Max Temperature (K)
1	800	10.4	N/A	1305
2	1000	10.4	2.5 x 6.3 x 1.1	1624
3	2000	10.4	10.2 x 9.5 x 4.3	3181
4	3000	10.4	20.4 x 14.5 x 7.3	4696
5	2000	15.0	9.9 x 9.8 x 3.3	2461
6	2000	7.5	12.5 x 11.2 x 4.7	2795
7	2000	5.0	22.5 x 16.9 x 7.3	4527

The first four cases depict changes in melt pool properties as laser power increases at a constant scan speed. The final three cases show the changes in melt pool properties as the scan speed was changed at a constant laser power, melt pool does not form when the laser power is 800 W as the maximum temperature does not go beyond the melting temperature of the material. It can be seen from the above test cases that both laser power and scan speed have a direct effect on the melt pool size and the max temperature. Table 2 shows that an increase in laser power causes an increase in both melt pool size and max temperature. This is shown in Figure 3. Additionally, at a lower power of 800W, the melt pool is rather narrow and does not have a trailing edge as seen in other studies.^[3] This is largely

attributed to the lower energy density of the laser which does not cause the melting of the powder. As the laser power increases there is a clear evolution of melt pool shape. The melt pool starts to resemble a teardrop with lengthening trailing edge that grows in a direction opposite to that of the direction of the laser.

Furthermore, a decrease in scan speeds creates a larger melt pool and leads to a higher max temperature. Figure 4 shows the change in melt pool shape and thermal characteristics as the scan speed decrease with a constant laser power. At the lowest scan speed, the maximum temperature recorded is 4527 K which is higher than the melting temperature of the material. The leads to a larger melt pool as more powder particles tend to have a temperature larger than the melting point of the powder as heat diffusion is not very fast. Lower scan speed would also mean that the laser spends more time at each point of the substrate leading to a local increase in energy which increases the temperature of the powder at that point. As the scan speed increases, the melt pool decreases in size and so does the maximum temperature that is recorded.



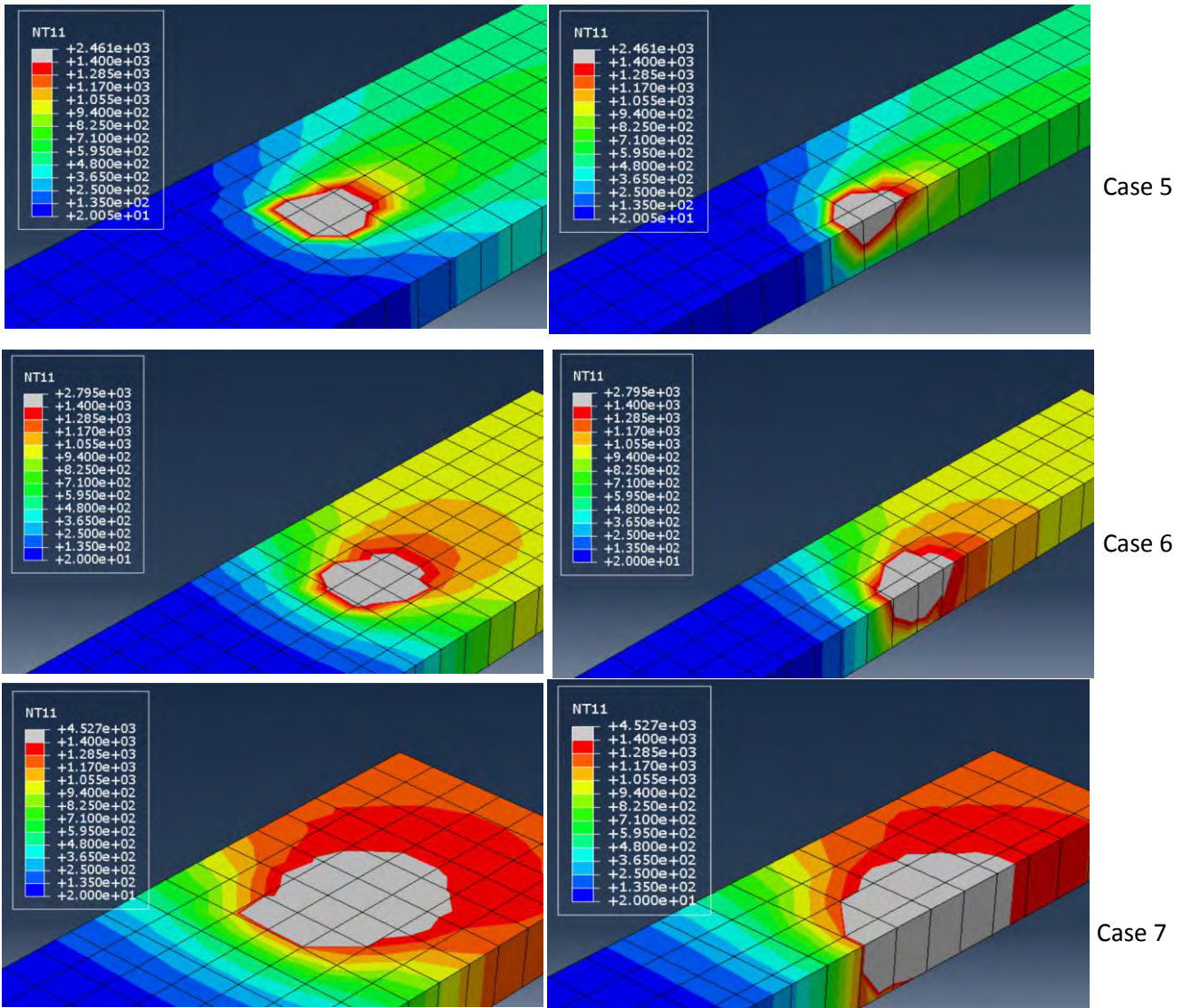


Figure 4. Variation in temperature and melt pool shape with decreasing scanning speed.

Conclusion and Future Work

Using finite element modeling it was found that as the laser power increased, there is an increase in the maximum temperature recorded in the system. Additionally, the size of the melt pool increased as the laser power increased. Furthermore, an increase in scan speed caused a decrease in maximum temperature and a decrease in the size of the melt pool. This has been attributed to the quick movement of the laser that causes a decrease in the exposure of powder reducing its energy absorption. To further investigate the LPBF process, a full thermal residual stress analysis should be completed. This would include simulating the building of layers within a sequentially coupled thermo-mechanical microstructural finite element model and multiphase field model.^[5]

References

1. Direct Metal Deposition Fabrication Process for Metal 3D Prints. (n.d.). Retrieved March 31, 2020, from <https://www.sculpteo.com/en/glossary/dmd-definition/>
2. Gouge, M., Michaleris, P., (2018) "An Introduction to Additive Manufacturing Process and Their Modeling Challenges: Laser Powder Bed Fusion Systems" in Thermo-Mechanical Modeling of Additive Manufacturing.
3. Parry L., Ashcroft I., Bracket D., Wildman R. D., Kolacinski R. (2014) "Investigation of Residual Stresses in Selective Laser Melting", In Key Engineering Materials Vol. 627, pp. 129-132.
4. Türkyılmaz, M. "A Designers' Handbook Series No 9004: High-Temperature Characteristics of Stainless Steels".
5. Li, Q., Ghanasekaran B., Fu Y., Liu G.R., "Prediction of Thermal Residual Stress and Microstructure of Additive Manufacturing Processes of Direct Laser Metal Deposition via a Coupled Finite Element and Multiphase Field Framework".

Chemical Signature of Cured Epoxy Fracture Surfaces

Student Researcher: Owen C. Brown

Advisor: Dr. James C. Moller

Miami University

Mechanical and Manufacturing Engineering Department

Abstract

Epoxy resins are versatile polymers that are utilized in a wide range of composite materials relying on the integrity of the epoxy's matrical molecular structure to prevent mechanical failure within their application. The mechanisms of chemical bond failure in resin epoxies are largely unknown and influence the mechanical behavior in epoxy resin applications that could result in catastrophic system failure if left undiscovered. This article reports the investigation of the chemical cross-links that are apparent on the fractured surface of a widely available epoxy cured at known temperatures and fractured in a controlled atmosphere. This was done via a repeatable procedure that isolates independent variables from affecting the results of the experiment contrary to existing procedures. Continued progress towards finalizing this procedure will provide definitive evidence of the fundamental influence of chemical bond links on the epoxy's deformation and failure behavior resulting in higher factors of safety and overall confidence in epoxy applications.

Introduction/Project Objectives

As a result of their diverse mechanical properties, high thermal and chemical resistance, and low thermal coefficients, epoxy resin thermosets' multifunctionality and utilization in engineering applications have consistent growth. Resin epoxies belong to an individual chemical group and are classified as polyepoxides, a class of reactive prepolymers and polymers which contain epoxide groups. Epoxy resins react i.e., cross-link, with either themselves through catalytic homopolymerization, or with a wide range of co-reactants referred to as polyfunctional hardeners. The extensive range of stoichiometric possibilities results in an ever-expanding list of epoxy applications, from advanced adhesives to composite matrices. According to market research carried out by TMR, "the thermoset resin market is projected to reach more than US\$ 15 billion by the end of 2022 at a compounded interest growth rate of over 5% [8]." With the increasing use of epoxies in industry, the consequences of defects and failure of epoxy can vary from inconvenient to catastrophic, just as with any other material in engineering applications.

Developing a repeatable procedure to discover the fundamental influence of chemical bond links on the epoxy's deformation and failure behavior is clearly necessary to determine the strength and safety of epoxy in applied context. This research focuses on the chemical reactions associated with the fracture behavior of cross-linked resins.

There have been other similar research studies in the past. To our knowledge, the actual curing histories in these were not well-controlled. Because epoxy curing is exothermic, the curing rate is temperature-dependent, and resins are poor diffusers of heat, the temperature inside the curing sample likely exceeds the control temperature by a significant amount [1,9]. It is critical to control the temperature to preserve the integrity of the study and reduce the results' uncertainty. If the epoxy is in fact not cured at the intended temperature history, unknown variations in cross-link density and type occur in the cured sample. Good control of curing chemistry is particularly important for this experiment in that fracture

involves mechanochemical reactions. To make proper inferences from the observable data, it is important to have an accurate idea of the original cured structure.

The overall aim of this research is to expose and identify the vital chemical bond chains that lead to mechanical failure in a “widely available” and frequently studied epoxy resin with maximum accuracy. The vital chemical bonds will be shown by observing the differences of chemical bond chains that appear in epoxy fracture with changes in stoichiometry and curing temperatures. The significance of those bonds will be related to resin’s mechanical failure behavior by observations of the apparent broken chemical bond chains and known mechanical property values to infer structure-property relationships. It is essential to the study that a well-controlled curing and fracture environment is provided to reduce variability and ambiguity regarding the cross-linked structure of epoxy resins. The study will also increase the accuracy of the results by reducing the effects of blending variability by curing multiple epoxy samples at one time. The final objective of this research is to generate an experiment methodology that is repeatable and can be recreated by other researchers.

Research Methodology

A specific procedure must be created and outlined to meet the goals of this research. The first step of the procedure is to produce multiple cured epoxy samples in a controlled environment to reduce experiment error during curing. A vacuum oven will be heated to 150°C. A calculated amount of resin will be placed into a mixing beaker and melted in the oven as the vacuum removes most of the residual air from the melting resin. While the resin is melting, more than enough hardener will be measured and pulverized by mortar and pestle. A 0.364 ratio of the curing agent will be blended into the resin until no granules of the hardener can be seen. The blend will then be placed back into the vacuum oven for degassing as needed. Following these procedures, the blend will be poured into four aluminum molds that are designed and manufactured to cure 6 samples (0.375d x1in) at once and will be evenly heated by an element controlled by a temperature controller programmed with a set curing schedule. The molds will be sprayed with a dry PTFE releasing agent before pouring and the hardened samples removed from the mold by ejector pins.

A set of temperature controllers and their respective aluminum molds will be used to cure epoxy of the same stoichiometry but according to different curing schedules. From this technique, multiple epoxy samples can be cross-linked in the molds while each controller cures its set of epoxy samples at a different temperature schedule. Not only will this expedite the process of obtaining samples cured in different ways, but the aluminum molds will also keep the epoxy samples close to a target temperature throughout the curing process, as the controller heats and soaks the molds accordingly. The challenges of this technique could be the loss of heat from the aluminum molds, but this could be mitigated with insulation. The technique is more accurate than the common approach of using an oven in which the air temperature around the samples (not the actual temperature of the epoxy) is controlled. A proposed curing schedule designed from similar research projects can be seen in Table 1.

Table 1. Proposed curing schedule

Proposed Curing Schedule

2hr	150C
3hr	200C
10hr post cure	200C

The following steps will expose and identify the key chemical bonds that are associated with resin fracture. After the samples of epoxy have been attained from the previous steps of the procedure, the cured samples will be fractured in a controlled atmosphere to represent general mechanical failure. This is done in this experiment with a custom-made vacuum chamber containing a coffee grinder to pulverize the sample. The sample will be placed in the grinder inside the chamber, the chamber will then be purged of atmosphere, and then filled with an inert gas that can bond with free radicals of broken bonds such as Nitrogen [1]. Following the pulverization of the sample, the pressure in the chamber will be returned to atmospheric pressure and the pulverized sample will be collected and filtered using a 10µm filter paper to obtain fine particles for reflective infrared spectroscopy. FTIR spectroscopy is an analytical technique widely used in chemistry to identify and study the chemical signature of molecule side groups, the chemical bonds that influence epoxy fracture behavior can be identified.

The final step will involve analysis of the infrared spectroscopy data to identify the dependence of vital bond types on stoichiometry and curing temperature. From this relationship, never-before-seen evidence about the influence of each chemical bond in epoxy fracture behavior can be formulated. This procedure can then be re-applied to other epoxies, expanding the knowledge of the influence of different chemical bonds on epoxy failure behavior.

Preliminary Results

Meticulous planning, organization, and confidence has been required during each step of this study and the work since the project's start in January of 2019 has not gone on without breakthroughs and promising preliminary results. Networking and tuning temperature controllers, fabricating mechanical experiment apparatuses, and providing a strong foundation for infrared (FTIR) spectroscopy results were all essential achievements towards meeting the objectives of the research.

To achieve the most accurate curing temperature history across multiple samples at one time, 4 Omega temperature controllers with heating elements and thermocouples were networked and tuned to provide monitorable and consistent heating of the samples in their respective aluminum molds. Tuning the PID gains proved to be somewhat enigmatic however by trial and error the proper gains were selected for a reasonable settling time with little overshoot. The curing schedule that would be carefully created later can be easily programmed and subsequently monitored simultaneously across the controllers with the proper USB and Omega driver software.

A new vacuum oven was provided by the provost of Miami University to the mechanical and manufacturing engineering labs which provide the ability to degas the resin and blended epoxy while it's heating in the oven. This will support the blending process greatly and reduce interference from most of the atmospheric air bubbles that could form in the blend otherwise.

Another valuable achievement towards the results of this research was the design and fabrication of a custom vacuum chamber enabling the hardened samples to be pulverized in a controlled and known atmosphere. Designing a pressure vessel and the ensuing fabrication of the assembly required numerous hours of brainstorming, analysis, part sourcing, machining, and assembly testing to fulfill the requirements of the design's function. In addition to the ability to hold a vacuum, the assembly was also required to show the internal pressure of the chamber via a high-pressure gauge, provide sealed feedthrough electricity to the coffee grinder, and provide integration with a system of piping and valves that would allow filling and purging of the chamber with different gasses. An electric coffee grinder is placed inside the chamber containing a cured epoxy sample and activated from the outside of the chamber after the chamber has been purged of air and then filled with a known gas, such as nitrogen.

This is done to cap free radicals that are created when bond-links are broken on the surface as the sample is fractured [1].

The most recent and challenging feat of the project thus far was obtaining preliminary test results by Diffused Reflectance FTIR spectroscopy. The machine that was used is a Thermo-Nicolet NEXUS 670 FTIR manufactured by Thermo Scientific. Using the Diffused Reflectance spectroscopy (DRIFTS) method (opposed to Attenuated Total Reflection (ATR) method) many tests were performed on previously cured epoxy samples to calibrate the machine and provide stable and accurate results. These results would be compared to multiple resources that provide correct examples of DGEBA (bisphenol A) based epoxy resin spectra. The epoxy sample used to hone and troubleshoot the results of the NEXUS 670 was a blend of EPON 828 resin and the DGEBA (bisphenol A/DER 332) curing agent. The initial challenge was learning the fundamentals of FTIR spectroscopy and the workings of the machine from zero experience. The second was changing out parts of the machine and troubleshooting inaccurate results. The beam splitter was a major component that required replacement for a different beam splitter to allow for mid-IR scans which are between the wavenumbers of 4000 and 7000 cm⁻¹. Before replacing the original KBR beam splitter with an XT-KBR beam splitter, only near-IR scans between the wavenumbers of 400 and 4000 cm⁻¹ could be performed on the sample which did not provide as many desired peaks for cross-referencing the spectra's accuracy. After installing the new beam splitter, the machine's scans produced noisy and unusable spectra. The machine's IR source gains were calibrated through software diagnostics and the number of scans was increased. As Figure 1 shows, the signal-to-noise ratio increases with the number of scans.

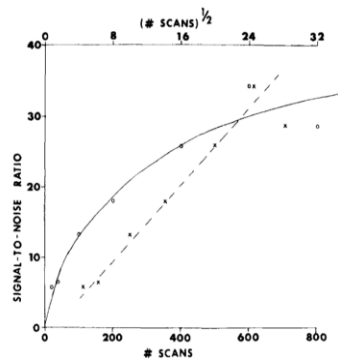


Figure 1. Change in signal-to-noise ratio with number of scans [6].

A comparison of spectra between moderately pulverized and finely pulverized samples of epoxy powdered with pestle and mortar showed that a finely pulverized sample will greatly reduce noise in the spectra. This led to the conclusion that fine particles must be sorted from the moderately pulverized samples by some means. Noise in the following test spectra was sufficiently reduced by those measures although more fine-tuning and noise-reduction is recommended to clearly define the final results of the study.

After using the FTIR machine and gaining experience over many hours of testing, reading, and troubleshooting, the preliminary results of the near-IR and mid-IR spectra for a pulverized sample can be seen in Figure 2 and 4.

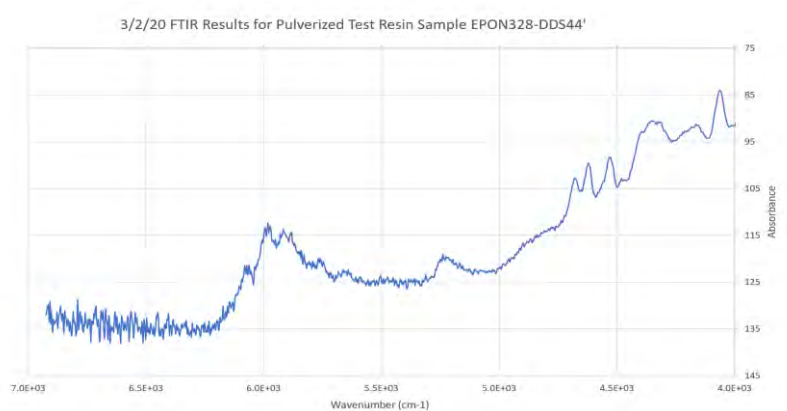


Figure 2. Mid-FTIR spectrum results for a finely pulverized DGEBA epoxy system test sample. Note that noise is still very prevalent as the wave number increases beyond 5500cm⁻¹

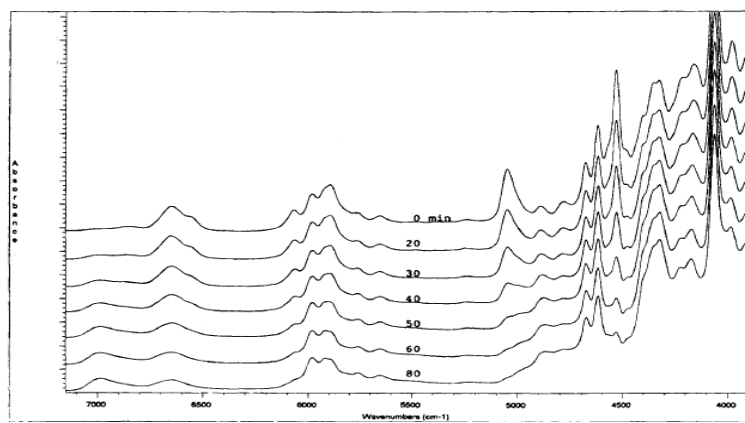


Figure 3. Near-IR spectra of DGEBA system during reaction at 90°C with reaction time as parameter [7]

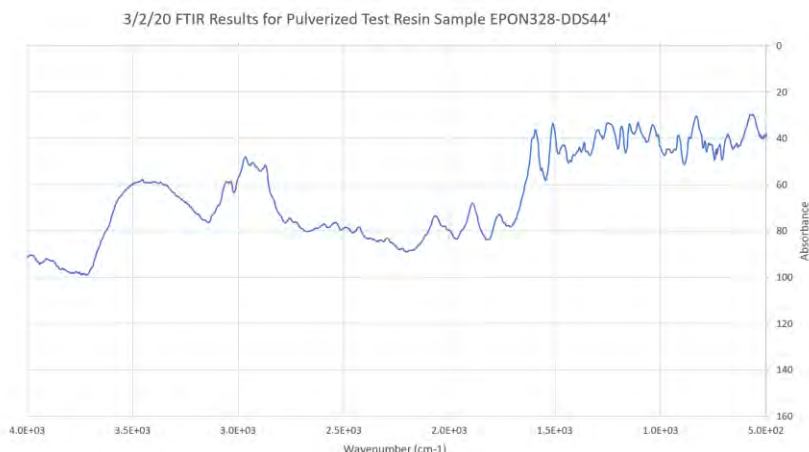


Figure 4. Near-FTIR spectrum results for a finely pulverized DGEBA epoxy system test sample

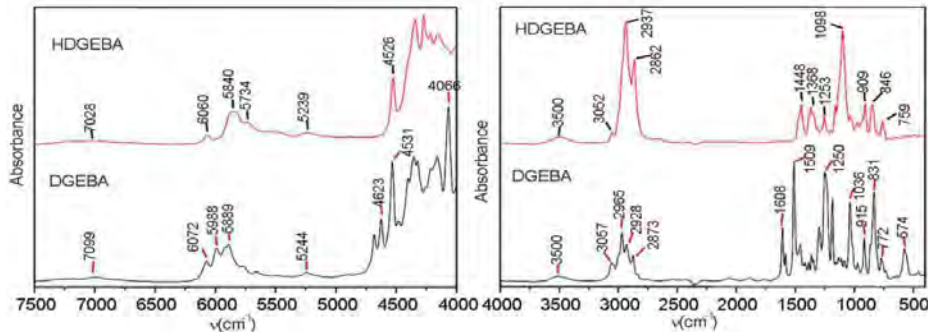


Figure 5. Near and mid-FTIR spectra of DGEBA and HDGEBA epoxy systems [3]

When the spectra produced from this study's test sample is compared with spectra from other resources, such as those in Figures 3 and 4, it becomes evident that there are similarities and differences concerning the peaks between the test spectra and resource spectra. Many peaks exist in both the test spectra however the peaks that exist in the test spectrums that do not exist in the resource spectrum and vise versa have yet to be explained. Confirming the accuracy and causes of those peaks or the lack thereof needs to be studied further to ensure that future results are not compromised by bad data.

Future Work

The final results of this study will be obtained after future work on this project has been completed. Despite the work previously mentioned, there is still much to do in many areas of this project to achieve the desired quality of the results and research objectives. In short, the next steps of the project would be to execute the following tasks: finalizing the pulverization apparatus (pipe-gas system assembly), curing new epoxy test samples for FTIR analyzation, investigating any unknown spectra data, fine-tuning the FTIR machine/settings to reduce all noise, investigating the peaks from properly cured and fractured samples, and finally, characterizing the vital peaks of proper samples to molecular bond-chains to associate them with fracture behavior and known mechanical properties of the epoxy. In addition to these tasks, computer modeling results could solidify and reiterate the conclusion of the study, although that is beyond the specific objectives of this research. The outcome of this research will change how the industry utilizes epoxies and expand the knowledge and applications of epoxy resins. Providing comparable results and a reproducible procedure that discovers the fundamental evidence needed to understand the basic chemical origins of epoxy failure, industries utilizing thermosets and other researchers can create new epoxy applications with the certainty of their epoxy's mechanical behavior.

Acknowledgments

The author would like to thank the Ohio Space Grant Consortium and Miami University for their support of this work.

Additionally, the author would like to thank Dr. Moller for his advisement, support, and expertise throughout the course and continuation of this research.

References

1. Fanconi, B.m., et al. "Free Radicals and New End Groups Resulting from Chain Scission: 2. Mechanical Degradation of Polyethylene." *Polymer*, vol. 23, no. 7, 1982, pp. 1027–1033., doi:10.1016/0032-3861(82)90403-7.
2. Feuerhahn, M. (1986) *Kunststoffe* 76,872-873.
3. González, María González, et al. "Applications of FTIR on Epoxy Resins - Identification, Monitoring the Curing Process, Phase Separation and Water Uptake." *Infrared Spectroscopy - Materials Science, Engineering and Technology*, 2012, pp. 261–280., doi:10.5772/36323.
4. J. Cantwell, W & Kausch, H. (1993). Fracture behaviour of epoxy resins. 10.1007/978-94-011-2932-9_5
5. Stoeckel, T. M., et al. "Chain Rupture and Tensile Deformation of Polymers." *Journal of Polymer Science: Polymer Physics Edition*, vol. 16, no. 3, 1978, pp. 485–500., doi:10.1002/pol.1978.180160311.
6. Koenig, Jack L. "Application of Fourier Transform Infrared Spectroscopy to Chemical Systems." *Applied Spectroscopy*, vol. 29, no. 4, 1975, pp. 293–308., doi:10.1366/000370275774455888.
7. Mijovic, Jovan, and Jony Wijaya. "Etherification Reaction in Epoxy-Amine Systems at High Temperature." *Polymer*, vol. 35, no. 12, 1994, pp. 2683–2686., doi:10.1016/0032-3861(94)90400-6.
8. TMR. "Thermoset Resin Market - Global Industry Analysis, Size, Share, Growth, Trends, and Forecast 2016 - 2024." Transparency Market Research, TMR, Jan. 2020, www.transparencymarketresearch.com/thermoset-resins-market.html.
9. Zhurkov, S. N., et al. "Mechanism of Submicrocrack Generation in Stressed Polymers." *Journal of Polymer Science Part A-2: Polymer Physics*, vol. 10, no. 8, 1972, pp. 1509–1520., doi:10.1002/pol.1972.160100808.

An Investigation of Maximum Power-Point Tracking for Space Applications

Student Researcher: Zachary J. Buchman

Advisor: Dr. Raghav Khanna

The University of Toledo
Electrical Engineering and Computer Science

Abstract

Maximum power-point tracking (MPPT) is investigated in this paper for its use in space-based photovoltaic (PV) arrays. PV arrays are critical, fundamental pieces in space power systems such as the International Space Station, the upcoming Lunar Gateway, and numerous spacecrafts utilizing electric propulsion. When an I-V (current vs. voltage) curve is graphed for a photovoltaic system, the “knee” of the curve represents the maximum power-point (MPP), which is shown in Figure 1. Since power is the product of voltage and current, this point is where the system’s power output is at a maximum. Photovoltaic systems have a fluctuating output due to variations in the amount of solar irradiance it receives as well as its environmental temperature. This inherent fluctuation necessitates a tracking mechanism that will adjust the load (typically a boost converter) in order to achieve ideal power transfer at the MPP, referred to as MPPT. MPPT is not a novel concept, but its application to space systems presents unique challenges not considered for earth-based systems which must be considered when selecting an MPPT approach.

Project Objectives

The space environment creates unique operating conditions that are not seen on earth. For example, the International Space Station experiences 16 solar-cycles each day. The amount of irradiance and the temperature of the cells of its PV array are subjected to frequent, extreme fluctuations. These fluctuations have a drastic effect on the PV array’s output voltage, and the MPPT algorithm chosen for such an application must be able to handle these changing conditions. There are many MPPT approaches used today and there are hundreds of papers exploring different MPPT techniques. The main objective of this project is to identify a suitable MPPT algorithm for the space environment.

Methodology Used

Generally, PV arrays are connected to a DC-DC converter to be better utilized in an electric power system. In this paper, a simple boost converter architecture is considered. For this architecture, the output voltage of the array is converted from a lower DC voltage to a higher DC voltage. An example of an MPPT controller attached to a PV array and boost converter is provided in Figure 2. The main investigation conducted in this work compares the attributes of several methods of MPPT for the given system architecture. The effectiveness of each MPPT approach in conditions of high variance will be evidence for their suitability in the space environment. Additionally, the complexity of the implementation of each method is critical in order to reduce cost and weight while maintaining high reliability.

Results Obtained

There are many MPPT methods to select from, but only three will be considered for sake of brevity. One of the simplest and most general approaches is the perturb and observe method. This method evaluates the derivative of the power output with respect to the output voltage (dP/dV) to determine where the system’s voltage is with respect to the MPP. If dP/dV is a positive value, the introduced voltage

perturbation moves the system's operating point closer to the MPP. The opposite is true if dP/dV is a negative value [1]. One of the main drawbacks with this method is that the MPP is rarely achieved; rather, the operating point oscillates around the MPP which is inherently inefficient. Perturb and observe is referred to as a hill climbing method as the operating point is constantly moving back and forth on the graph from Figure 1. Additionally, this approach requires a perturbation from external circuitry which is undesirable. Finally, the perturb and observe method can be confused by variations in atmospheric conditions, resulting in the system operating undesirably [2].

Incremental conductance is another hill-climbing method that operates similarly to perturb and observe. Rather than using the output power of the system, incremental conductance uses both the instantaneous and incremental conductance (I/V and dI/dV , respectively.) A flowchart for one implementation of this method is shown in Figure 3. Although it has been claimed that this method is an improvement over the perturb and observe method, it has been shown that these methods are nearly identical [1]. In some cases, incremental conductance performs worse than perturb and observe in rapidly changing weather conditions. At high variations of irradiance, the system is subject to confusion much like the perturb and observe method in variable atmospheric conditions [3].

Ripple correlation control (RCC) is similar to the hill-climbing methods, but has a subtle, significant difference. Rather than introducing a perturbation to the system, the ripple effect caused by the switching of the controller. This can be seen clearly in Figure 5. Because RCC is able to utilize this inherent perturbation, the design of a controller will be simpler as it does not require external perturbation accommodations [4]. The foundation of RCC relies on the fact that the product of the derivatives of the array power and voltage are positive when array voltage is below the MPP voltage, negative when array voltage is greater than the MPP voltage, and zero when array voltage is equal to the MPP voltage [5]. This approach has shown to be an improvement over both hill-climbing methods [6]. RCC can also be incorporated into a PV system in both analog and digital fashions. Figure 6 provides an example of an analog circuit, while Figure 2 can be considered with a microcontroller as the main control unit. RCC has proven to have better tracking effectiveness, transient performance, and dynamic range compare to the hill climbing methods [4].

Significance and Interpretation of Results

While both hill-climbing methods have acceptable performance, it is believed that RCC is a superior choice for a space-based system containing a PV array. RCC additionally has the flexibility to be incorporated in both analog and digital fashions. An analog approach has the benefit of being more reliable as it is not as susceptible to as many single event failures as a digital system in the space environment. Alternatively, if rad-hardened digital electronics are available a digital system could be chosen for the sake of a simpler implementation and increased flexibility.

Figures/Charts

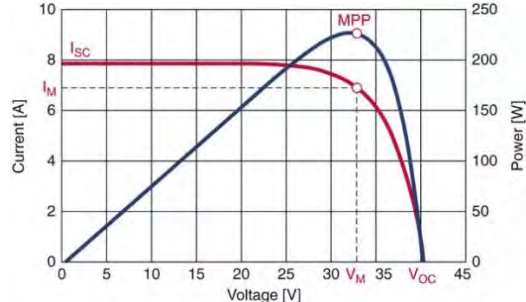


Figure 1. Graph of Current/Power versus Voltage [7].

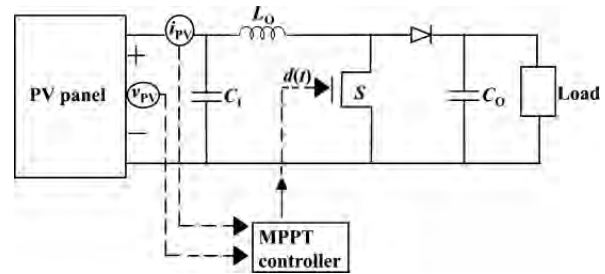


Figure 2. Example of MPPT controller in a photovoltaic boost converter system [5].

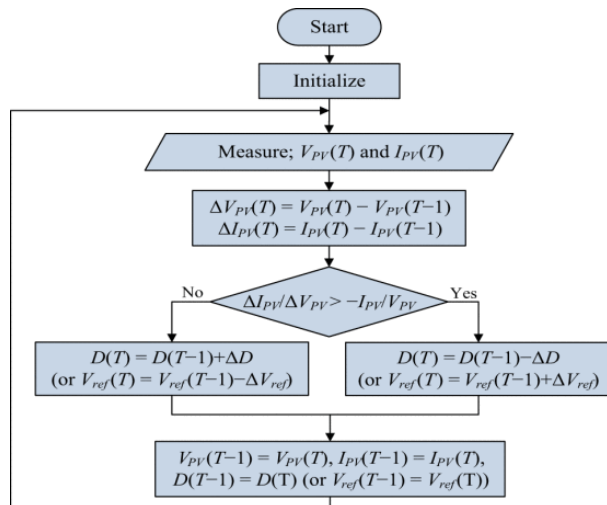


Figure 3. Flowchart for Incremental conductance algorithm [3].

	Constant Voltage	P&O	INC
Measured parameters	V_{PV}, I_{PV}	V_{PV}, I_{PV}	V_{PV}, I_{PV}
Decision based on change in	one parameter (V_{PV})	one parameter (P_{PV})	two parameters (V_{PV} and I_{PV})
Perturbation parameter	N/A	V_{ref} or D	V_{ref} or D
PV array dependent	yes	no	no
Implementation	analog or digital	analog or digital	digital
Implementation cost	very low	low	slightly higher
Steady-state fluctuations in array voltage	no	yes	yes
Convergence speed	very fast	parameter dependent	parameter dependent
Dependence of tracking efficiency on cell temperature & irradiance level	highly dependent	less dependent	less dependent
Lower tracking efficiency at rapidly changing irradiance	no	yes	yes
Confusion due to noise	no	yes	less confusion than P&O
Confusion due to system dynamics	no	yes	less confusion than P&O
Confusion due to irradiance increase	no	yes	more confusion than P&O
Confusion due to irradiance decrease	no	yes	yes
Tracking efficiency; reference voltage control	91%	95% - 98%	95% - 98%
Tracking efficiency; duty ratio control	N/A	96% - 99%	96% - 99%

Figure 4. Further comparison between perturb and observe and incremental conductance [3].

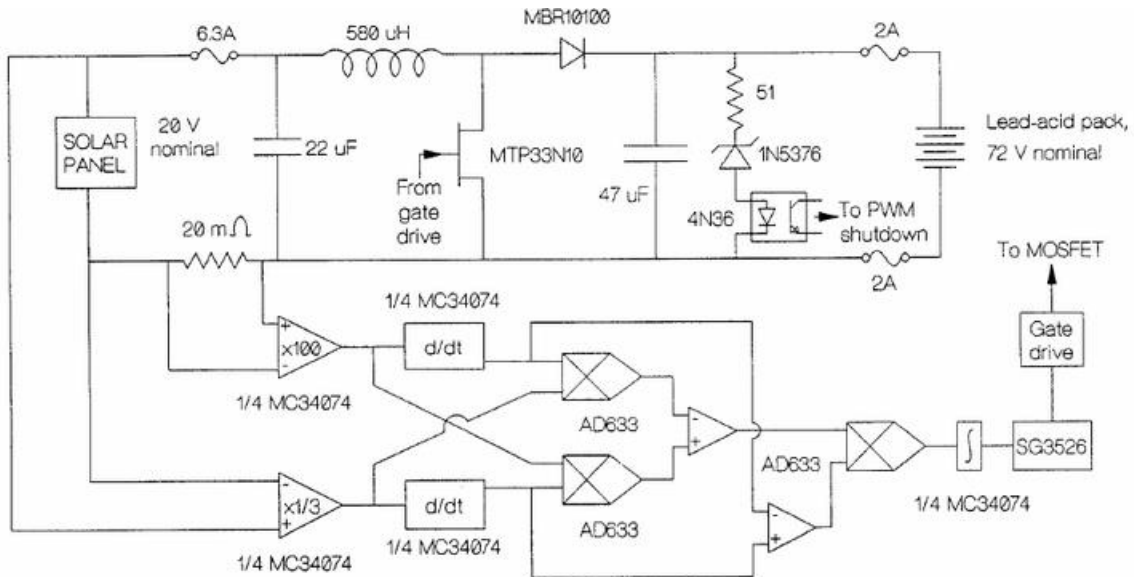


Figure 6. An example of an analog circuit implementing RCC [6].

Acknowledgments

The author would like to thank his advisor, Dr. Raghav Khanna, as well as the members of the Power Electronics lab at the University of Toledo. Additionally, the author would like to thank the Ohio Space Grant Consortium for the opportunity to conduct this research.

References

1. D. Sera, L. Mathe, T. Kerekes, S. V. Spataru and R. Teodorescu, "On the Perturb-and-Observe and Incremental Conductance MPPT Methods for PV Systems," in *IEEE Journal of Photovoltaics*, vol. 3, no. 3, pp. 1070-1078, July 2013.
2. N. Femia, G. Petrone, G. Spagnuolo and M. Vitelli, "Optimization of perturb and observe maximum power point tracking method," in *IEEE Transactions on Power Electronics*, vol. 20, no. 4, pp. 963-973, July 2005.
3. M. A. Elgendi, B. Zahawi and D. J. Atkinson, "Assessment of the Incremental Conductance Maximum Power Point Tracking Algorithm," in *IEEE Transactions on Sustainable Energy*, vol. 4, no. 1, pp. 108-117, Jan. 2013.
4. T. Esram, J. W. Kimball, P. T. Krein, P. L. Chapman and P. Midya, "Dynamic maximum power point tracking of photovoltaic arrays using ripple correlation control," in *IEEE Transactions on Power Electronics*, vol. 21, no. 5, pp. 1282-1291, Sept. 2006.
5. R. Khanna, Q. Zhang, W. E. Stanchina, G. F. Reed and Z. Mao, "Maximum Power Point Tracking Using Model Reference Adaptive Control," in *IEEE Transactions on Power Electronics*, vol. 29, no. 3, pp. 1490-1499, March 2014.
6. Midya, Pallab & Krein, P. T. & Turnbull, R. J. & Reppa, R. & Kimball, J. W. (1996). Dynamic maximum power point tracker for photovoltaic applications. 2. 1710 - 1716 vol.2. 10.1109/PESC.1996.548811.
7. <https://bluesat.com.au/maximum-power-point-tracking/>

A Leachate and Strength Analysis of Fly Ash Encapsulated by Cement

Student Researcher: Jennifer A. Burk

Advisor: Jeffrey Bates, Ph.D., CHMM, Professor, Program Director

Columbus State Community College

Environmental Science, Safety, and Health Program

Abstract

While the production of coal combustion residuals (CCR) may be tapering off due to the recent downturn in coal usage for the generation of electricity, the need to manage approximately 110 million tons of fly ash and coal combustion by-products each year remains. CCRs are reused in a wide variety of building materials, such as brick, concrete block, cement mixtures, asphalt, and wallboard. When CCRs are properly reused it reduces the use of virgin resources, lowers greenhouse gas emissions, reduces the cost of coal ash disposal, and aids in improving the strength and durability of building materials. When properly encapsulated in certain products, the materials have proven to be an effective method of either halting or slowing the leachability of various elements, but some concerns for the release of certain hazardous elements in the environment remains.

Approximately one-third of CCRs are in the form of fly ash, which for many years has been mixed with Portland cement to improve the properties of concrete. This research evaluates the properties of several ratios of Portland Cement to fly ash. The goal is to evaluate the leachability of certain components for various solidified mixtures, as well as testing the strength of the solids under force. Monolithic mixtures of Portland cement and fly ash were exposed to a mild acid for two days, with the resulting leachate being tested for various elements using a handheld X-ray fluorescence (XRF) analyzer and the Oakton multi-Parameter Meter. The strength of these mixtures was tested using a concrete compression machine, the Forney ST-900-VFD-MP Universal Testing Machine.

Project Objective

The goal of the project is to evaluate the leachability of certain components for various solidified mixtures, as well as testing the strength of the solids under force.

Methodology Used

Various proportions of Portland cement and coal fly ash were mixed; the different proportions varied from 100 percent cement/0 percent fly ash to 20 percent cement/80 percent fly ash. The mixtures were combined with tap water that was measured at 50 percent by volume to the solids. Concrete test cylinders with a diameter of 4 inch (102 mm) and a height of 8 inches (203mm) were filled with the mixtures. The cylinders of the mixtures were cured for a period of five days. The five monoliths of Portland cement and fly ash mixtures were then partially submerged for 48 hours in a 1000 ml leaching solution consisting of deionized water and nitric acid, with the solution having a pH of 5.0. The resulting leachate solution was evaluated using the Oakton Multi-Parameter Meter, and measured for pH, TDS, and conductivity. A sample of fly ash and the five samples of the leachate were analyzed for various elements using a handheld X-ray fluorescence analyzer, the Delta Family XRF Handheld Analyzer (XRF). The five monoliths were then tested for compressive strength using a Forney ST-900-VFD-MP Universal Testing Machine (FSTM).

Results Obtained

Results of this project, associated with the various testing methods, show the best ratio of Portland cement to fly ash is Sample #2 at 80:20; not only was the Pb content lowest, the conductivity was the lowest proving Sample #2 to be the greatest encapsulation of CCR's and the sample leached the fewest hazardous elements. Sample #2 proved the strongest of the Fly ash samples in the strength testing and failed at a Max Load of 30,974 lbf: the encapsulation of 20% fly ash decreased the strength of Sample #2 by a little more than 20% of Sample #1.

Significance and Interpretation of Results

The significance of the results proves the encapsulation of fly ash is an effective method for reuse and can potentially help eliminate massive amounts of fly ash waste.

Overall, the results and data were limited as only one trial was sampled and tested; had there been several trials of each test, the results would have been more accurate and precise. The data from the Oakton Multi-Parameter Meter test for pH jumped up and down and formed a zigzag pattern from Sample #1 to Sample #5; the inconsistency in the pH test may be a result of not having measured the concrete and fly ash more precisely, when first mixing the materials, or the testing device alone was the cause of the bad data. Again, had more trials been run, more data could prove wherein the issue lies. Another consideration of the data collected during the Oakton Multi-Parameter Meter test is that Sample #5 tested low for conductivity with a 4.00 umhos/cm and 0 ppt TDS potentially proving error in preparing the sample or error in the meter.

The tests in this study demonstrate the validity of encapsulation, and generally show that the leaching of fly ash contaminants and the strength of Portland cement is not compromised until ratios of greater than 40% fly ash is mixed with Portland cement.

References

1. Coil, David, Higgman, Bretwood "Hig", and McKittrick, Erin. "Coal Combustion Wastes." www.groundtruthtrekking.org/Issues/AlaskaCoal/Coal-Ash-Combustion-Wastes.html. Accessed January 26, 2020.
2. Daniels, John L., Das, Gautham P. "Influence of Flow Rate on Leachability." www.coalcpjournal.org/papers/2018/1946-0198-10-3-34.pdf. Accessed January 26, 2020.
3. Eastern Research Group, Inc. (ERG) for EPA under EPA Contracts EP-D-11-006 and EP-W-10-055. "LEAF Guide to Testing Leachate." https://www.epa.gov/sites/production/files/2019-05/documents/final_leaching_environmental_assessment_framework_leaf_how-to_guide.pdf. Accessed February 16, 2020.
4. Ritter, Stephen, K. "A New Life for Coal Ash." Chemical & Engineering News, February 15, 2016. <https://cen.acs.org/articles/94/i7/New-Life-Coal-Ash.html>. Accessed February 26, 2020.

Effects of Netrin-3 on THP-1 Monocytes

Student Researcher: Marie C. Butts

Advisors: Dr. Heather Kuruvilla, Dr. Kaleb Pauley

Cedarville University
Department of Science and Mathematics

Abstract

The netrin protein family has been found to have a strong importance in developmental signaling throughout many different kingdoms. Though netrin-1 has been well classified, little is known of the signaling effects of netrin-3. Netrin-3 has been shown to have an inhibitory effect on mitotic activity in *Tetrahymena thermophila*. Due to the decreased mitotic activity, netrin peptides were then administered to THP-1 human monocytes and HeLa cells in order to compare the effects. Netrin does not seem to have an effect on mitotic activity in THP-1 cells but may play a role in metabolic rates due to a pH change in the media. No pH changes were noted in the HeLa cells, leading to the conclusion that the pH change may be due to cell type rather than species of origin. Studies are being conducted to determine the metabolic signaling pathway of both cell lines.

Project Objectives

The objective was to see if netrin-3 peptides have a similar effect on human cells when compared to *Tetrahymena thermophila*. Two different netrin-3 peptides, N3C and N3N, were used to compare the effects of both peptides on human cell lines. Netrin-3 has been shown to decrease mitosis in *Tetrahymena*, and yet it is unknown if similar effects will be seen in human cells (Khol, 2018). Multiple human cell lines were used during testing to determine if the effects of netrin have different effects on different cell types or if the response is seen in various human cell lines.

Methodology Used

THP-1 human monocytes were concentrated at 1.0×10^6 cells/mL. Semester 1 focused on comparing the effects of netrin-3 to *Tetrahymena thermophila*. Different concentrations of netrin-3 were used as well as two different netrin peptides, N₃C and N₃N. Both peptides were administered to THP-1 cells on the day of plating and allowed to incubate for at least 48 hours. The starting netrin concentrations of each were 0.5ug, 1ug, and 2ug. No significant effects were seen at such low concentrations, so concentrations were increased to 1ug, 2ug, and 3ug. Again, no significant effects were noted, and concentrations were increased to the final concentrations of 2ug, 3ug, and 4ug for each peptide. All experiments contained a control of PBS. Each experiment contained 3 tests for the control and 3 different concentrations. After 48 hours, the cell count was recorded for each test. Immunofluorescence was then performed due to a noted color change in the media of treated cells.

Semester 2 used HeLa cells as well as THP-1 human monocytes were used. Due to a noted color change in the media from Semester 1, HeLa cells were used for comparison. HeLa cells were concentrated to 8.5×10^4 cells/well. Netrin peptides were then added 24 hours after plating, and the cell count was measured 48 hours after plating. THP-1 human monocytes were concentrated at 1.0×10^6 cells/mL. A peptide concentration of 4ug was placed in each well for both cell types. Cell count and cell media pH was recorded after 48 hours of initial plating for both cell types. Cell media records for HeLa cells in the third experiment were not able to be taken due to human error.

Results Obtained

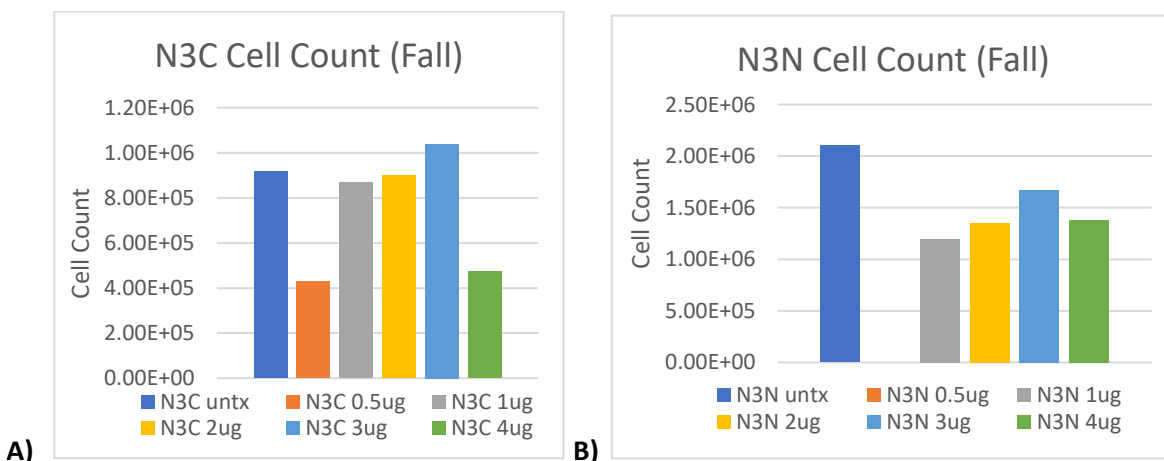
Experiments in Semester 1 showed that neither peptides had any significant effect on mitosis regardless of concentration. After each experiment, the tests treated with netrin appeared to have a yellow media color indicating a drop in pH. An increase in metabolism was a proposed reason for the drop in pH. Immunofluorescence targeting phosphotyrosine was performed because netrin often signals through tyrosine kinases in vertebrates, and the increased metabolic rate associated with signaling could result in the decreased pH seen in the cell media. Concentrations of 0.5ug and 4ug of N3C peptide showed to have a significant cell count reduction. All concentrations of N3N showed to have a significant cell count reduction except 0.5ug, which was not tested due to miscommunication between students, and 1ug. Significant changes were seen between those treated with the peptides and the PBS control at concentrations of 4ug for both peptides.

Both HeLa cells and THP-1 human monocytes were used in order to see if the pH decrease was due to cell type or a function of all human cells. A netrin concentration of 4ug was used for each test for both cell types with PBS as the control. No significant change was noted between netrin-treated cells and PBS control cells for either cell type. Measurements of pH showed no significant change between netrin-treated HeLa cells and PBS control. However, a significant difference was noted between netrin-treated THP-1 human monocytes and PBS control. T-Tests were performed to give a p-value of 0.03 for N3C peptide to PBS while a p-value of 0.005 was calculated for N3C to PBS for both THP-1 human monocytes and HeLa cells.

Significance and Interpretation of Results

The results show that Semester 1 contradicts Semester 2. Both netrin-3 peptides decreased mitosis in human cells at a concentration of 4ug, though did not have any significant effects in Semester 2. Netrin-3 does have an effect on THP-1 human monocytes by causing a decrease in pH though the exact reason for the decrease is still unknown. This change appears to be cell type specific since no such results were noted in HeLa cells.

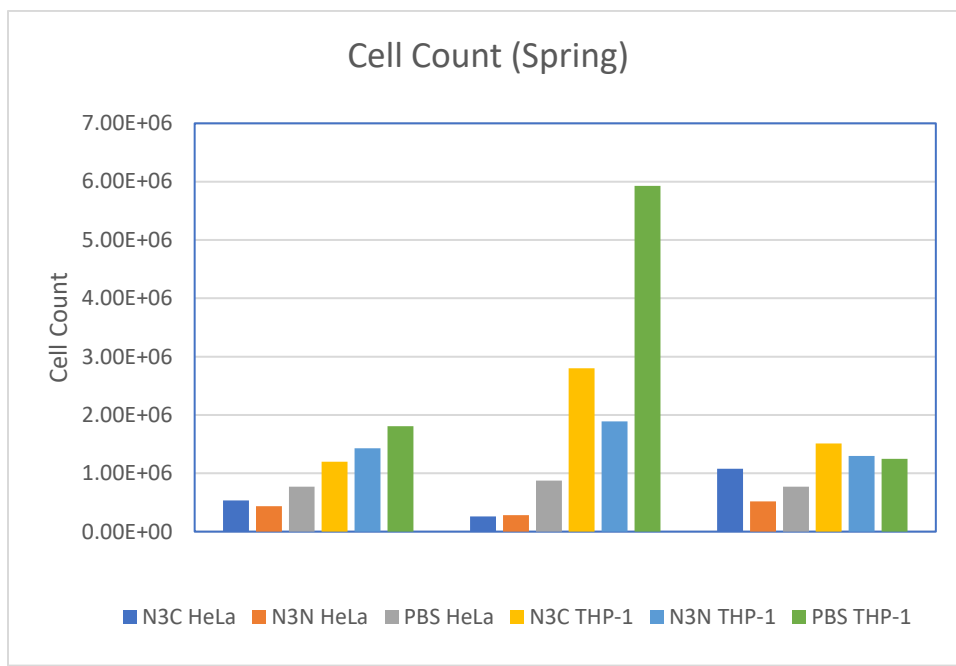
Figures and Tables



Graph 1. Cell Counts from Semester 1 comparing concentration of netrin-3 amounts for both peptides.
A) Cell Count for N3C peptide B) Cell Count for N3N peptide

Table 1. p-values for Cell Count from Semester 1 in Graph 1

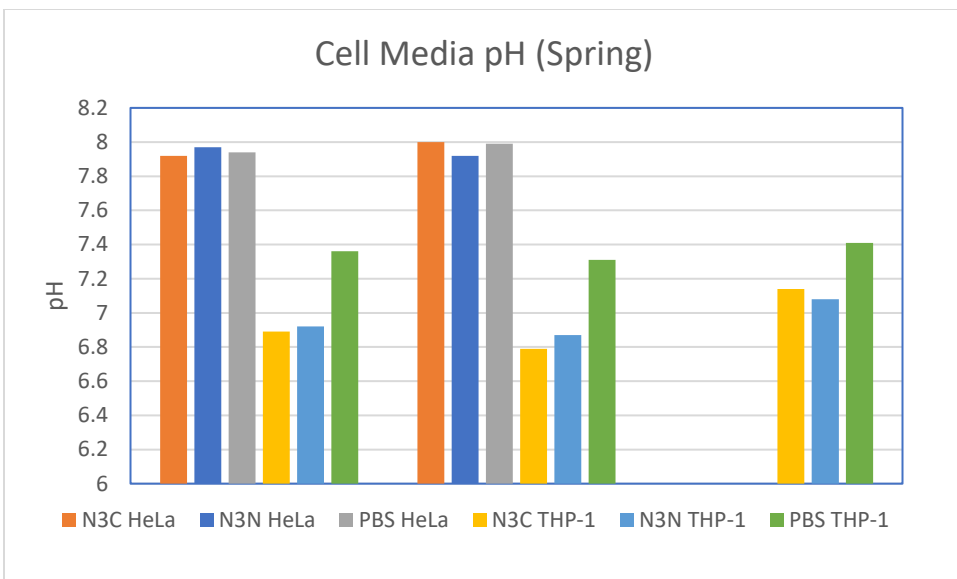
N3C p-values		N3N p-values	
untx-0.5	0.005031	untx-0.5	NA
untx-1	0.337393	untx-1	0.056129
untx-2	0.096663	untx-2	0.007655
untx-3	NA	untx-3	0.040872
untx-4	0.021098	untx-4	0.021447



Graph 2. Cell Count for HeLa and THP-1 treated with both netrin-3 peptides

Table 3. p-values for Figure 3.

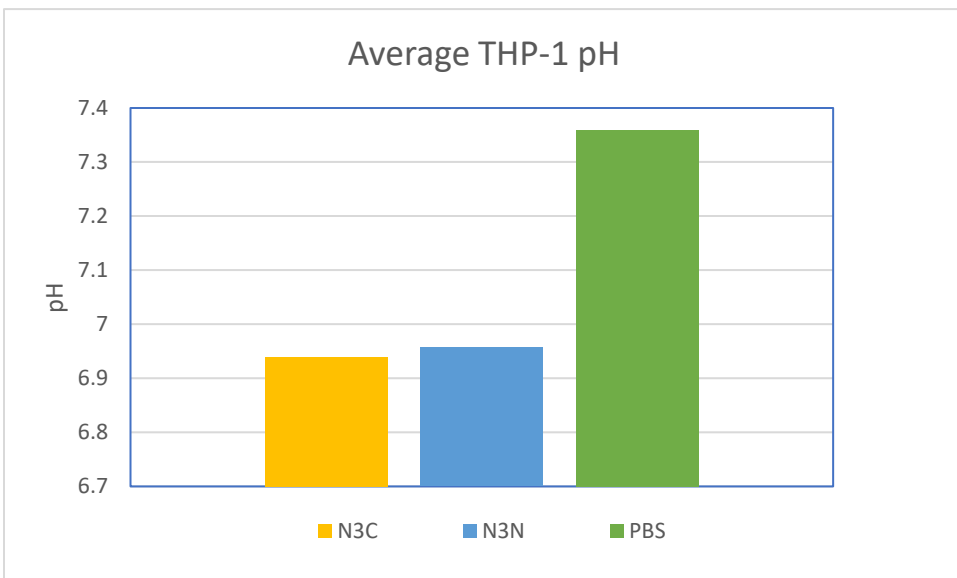
P-Values	
N3C HELA-PBS	0.386423
N3N HELA-PBS	0.093668
N3C THP-PBS	0.330047
N3N THP-PBS	0.276518



Graph 3. pH measurements for both cell types. Cell media was not measured in 3 due to human error.

Table 3. p-values for Figure 3.

N3C to PBS p-value	N3N to PBS p-value
0.030112362	0.005112224



Graph 4. Average pH from THP-1 human monocytes

Acknowledgments

The author of this paper would like to thank Dr. Heather Kuruvilla, Dr. Kaleb Pauley, and Dr. Sharon Cooper for their continued guidance and input in the project as well as Claire Burton, Katie Flint, David Gibbs, and Reese Watkins for their assistance in research. The author would also like to thank the Ohio Space Grant Consortium for their support.

References

1. Keedy, M. D., Yorgey, N. K., Hilty, J. S., Price, A. R., Hassenzahl, D. L., & Kuruvilla, H. G. (2003). Pharmacological evidence suggests that the lysozyme/PACAP receptor of *Tetrahymena thermophila* is a polycation receptor. *Acta Protozoologica*, 42(1), 11.
2. Khol, Bethany & Malik, Katelyn & Ward, Kenneth & Merical, Matthew & Parks, Lois & Hermann, Stephanie & Paulding, David & Kuruvilla, Heather. (2018). Netrin-3-peptides are chemorepellents and mitotic inhibitors in *Tetrahymena thermophila*. *Current Topics in Peptide and Protein Research*. 19. 63-73.
3. Mace, S. R., Dean, J. G., Murphy, J. R., Rhodes, J. L., & Kuruvilla, H. G. (2000). PACAP-38 is a chemorepellent and an agonist for the lysozyme receptor in *Tetrahymena thermophila*. *Journal of Comparative Physiology A: Neuroethology, Sensory, Neural, and Behavioral Physiology*, 186(1), 39-43.

Healthier Road Construction

Student Researcher: Liam J. Byrne

Advisor: Dean Bortz

Columbus State Community College
Construction Management

Abstract

The research project I conducted will be comparing and contrasting the different materials that are commonly and uncommonly used for the roadways. I will be considering the cost of each material, the environmental impact that each one has, the strength and toughness of the different materials, and the drainage abilities of each material. I plan to investigate all these things and potentially find out what the cheapest and most environmentally friendly and strongest option is.

I then want to develop a plan on how a city could implement the best option for their roadways and be able to see the overall benefits from it. My greatest concern is for the environment and I am going to place the highest priority on that because I feel that if we are willing to spend more now for a greener world it will pay off for the next generations.

Project Objective

To find out what the strongest, cheapest and most environmentally friendly alternative to asphalt for road construction is.

Methodology Used

I used a search engine on the internet to look up scholarly articles on different country's attempts to use different road construction materials. I found lots of different ideas that did not work out to well but then I found one from the Netherlands that seemed very promising.

Results Obtained

The plastic road was invented by the companies KWS, Wavin and Total. They made a bike path in Zwolle, Netherlands. The bike path is made of almost entirely recycled plastic. According to the inventors it should last 2 to 3 times as long as a normal road.

Significance and Interpretation of Results

The biggest impact is that they can prefabricate all the sections of the road. This might not sound like that big of a deal, but imagine if majority of "road construction" wasn't done on the road, but in a factory and then when all the pieces were made all they had to do was install them. This could change road construction jobs that take years and only take a few months. The other major positive of plastic roads is that they are made of almost entirely recycled plastic. This means that we would not be wasting all the plastic that we use but using it for our roads. So, it is very environmentally friendly. The other reason of why it being made of plastic is very important is that it is cost effective most of the material needed to make it is something that we would just throw away anyway.

References

1. "The Disadvantages of Asphalt." *Hunker*, www.hunker.com/12546353/the-disadvantages-of-asphalt.
2. Marinelli, Janet, et al. "World's First Recycled Plastic Bike Path Opens in The Netherlands." *Yale E360*, 17 Sept. 2018, e360.yale.edu/digest/worlds-first-recycled-plastic-bike-path-opens-in-the-netherlands.
3. Peters, Adele. "This Bike Path Is Made from Recycled Plastic." *Fast Company*, Fast Company, 14 Sept. 2018, www.fastcompany.com/90236069/this-bike-path-is-made-from-recycled-plastic.
4. Williams, Len. "Is It the End of the Road for Asphalt and Concrete?" *RSS*, 14 Sept. 2018, eandt.theiet.org/content/articles/2018/09/is-it-the-end-of-the-road-for-asphalt-and-concrete/.

Design of Ranque-Hilsch Vortex Tube for Temperature Sensitive Paint Testing

Student Researcher: Timothy J. Chamberlain

Advisor: Dr. Kevin Disotell

Youngstown State University

Department of Mechanical, Industrial, and Manufacturing Engineering

Abstract

The Ranque-Hilsch vortex tube employs the use of high velocity, compressed gas injected through a tangential inlet to a swirling chamber where the flow separates into a hot and cold stream. This effect allows a separate hot and cold stream to be created from only one gas supply. The generation of the cold stream of flow for cooling applications cannot be understated since the device requires no moving parts and just a compressed supply of gas. However, though the tube is generally recognized for generating this effect, the underlying physical laws that govern the effect have not been agreed upon in a single complete hypothesis [1]. The purpose of the research conducted during a State of Ohio STEM Scholarship during Spring Semester 2020 was to design a vortex tube that allows for temperature sensitive paint (TSP) to be applied on the surface of the tube, allowing for measurements of the temperature field in follow-on work.

Project Objectives

The objective for this project was to create a vortex tube that incorporated a tangential inlet, swirl chamber, and acrylic outlet sections for compatibility with intended measurement techniques. The tangential inlet was designed to gradually channel the flow from the mass flow meter to the entrance of the swirl chamber, without any rapid contractions, so as to minimize disturbing the flow and incurring any pressure loss. The swirl chamber was to feature one single tangential inlet with a smooth interior that transitioned seamlessly to one outlet. With one outlet, a uniflow tube was to be created. However, so that a counterflow setup could be made in the future, the other side of the swirl chamber was designed so as to receive another outlet tube, if desired. The design was to incorporate smooth transitions between parts so as not to disturb the flow. Finally, maximal viewing opportunity was prioritized to be able to collect as much data from the TSP as possible.

Methodology

To accomplish the stated objectives, the first design was developed based on prior models and functional tubes created by other researchers. Going forward, design meetings were held weekly, and updates were made to reflect the goals. Finally, the manufacturability of the assembly was discussed with the partnering machine shop so as to not unnecessarily overcomplicate the design. After all of these tasks were undertaken during spring semester, the design was manufactured and received in April 2020.

Results Obtained

To simplify manufacturing, the tangential inlet for the swirl chamber was separated from the swirl chamber as a separate component (Figure 1). The inlet of this part was designed to thread onto a half inch NPT thread and match the internal diameter of the adjacent pipe. Over a span of around three-quarters an inch, the diameter of the inlet went from less than 20 millimeters to three millimeters. The swirl generator was designed with a clean transition from the tangential inlet to the three-millimeter hole on the side of the swirl chamber. The diameter of the swirl chamber, a 1 inch bore, was designed to transition smoothly from the aluminum swirl chamber to the acrylic outlet tube. Additionally, the acrylic tube was designed to be a removable part for painting and general accessibility. As such, the tube was press fit into a collar that threaded into the swirl chamber. This allowed a seamless transition from the swirl chamber to the acrylic outlet. The back of the swirl chamber was also accessible and filled with an acrylic plug for viewing. This was attached by a bolted flange and sealed with an O-ring. The size of the plug was enlarged so the O-ring would not obstruct the view through the plug (Figure 2). The acrylic plug can be removed, and a cold end outlet can be added utilizing the threaded holes for the fasteners with a new design. The final assembly is shown in Figure 3.

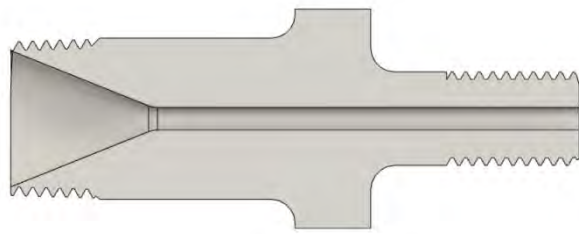


Figure 1. Tangential inlet fitting.



Figure 2. Section view of vortex tube.

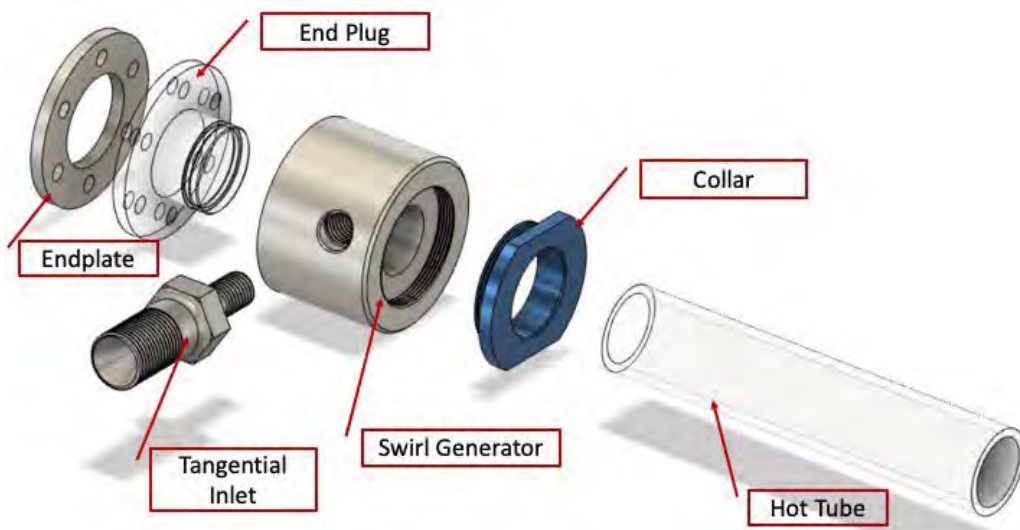


Figure 3. Assembly of the vortex tube.

Significance

A new test apparatus was designed and fabricated. The vortex tube can be used in future work to characterize the temperature profile inside the tube, using the TSP, and better understand the Ranque-Hilsch effect.

Reference

1. Xue, Y., Arjomandi, M., & Kelso, R., 2010, "A critical review of temperature separation in a vortex tube," *Experimental Thermal and Fluid Science*, Vol. 34, 1367-1374.

Comparative Study of Glulam-Members and Steel-Members Used In the Construction Field

Student Researcher: Grace Ciminillo Delamotte

Advisor: Dean M. Bortz, M.A., CSI, CDT, CCPR

Columbus State Community College
Design, Construction and Trades Department
Construction Management

Abstract

Conduct a comparative study through a literature review examining the features of strengths, sustainability, and environmental impacts between Glulam-members (*glue-laminated timber*) and steel-members used within the construction field.

Introduction of Key Terms

Glulam-members

According to The Engineered Wood Association, (APA) “glued laminated timber, or glulam, is a highly innovative construction material. Glulam is a stress-rated engineered wood beam composed of wood laminations, or "lams", that are bonded together with durable, moisture-resistant adhesives. The grain of the laminations runs parallel with the length of the member. Glulam is versatile, ranging from simple, straight beams to complex, curved members. Glulam is available in both custom and stock sizes and one of four appearance classifications: premium, architectural, industrial, or framing.”

Steel-members

Steel is a ferrous metal. Its high strength in relation to its weight makes it the material of choice for skyscrapers, and long-span structures such as bridges. Its malleability and weldability allow it to be shaped, bent, and made into different types of components.

Project Objective

The purpose of this study is to research the different qualities of Glulam-members (*glue-laminated timber*) and steel-members and consider their impact within the construction field.

Methodology Used

The foundation used to conduct this study were my college courses and various resources that included research articles, trade publications, construction textbooks, and specifications related to different products.

Results Obtained

The results of this research has led to a deeper understanding of different products used within the construction field and the different qualities for consideration that include strength, sustainability, and environmental impact.

Conclusion

Glulam should be considered within the construction field as a viable alternative to steel. Increased design values, improved product performance, and environmental impact make glulam the superior choice for projects from simple beams and headers in residential construction to soaring arches for domed roofs spanning more than 500 feet.

References

1. "American Institute of Timber Construction Superior Fire Resistance." American Institute of Timber Construction.
2. "Buildings Can Become a Global CO₂ Sink If Made out of Wood Instead of Cement and Steel." *ScienceDaily*, ScienceDaily, 27 Jan. 2020, www.sciencedaily.com/releases/2020/01/200127134828.htm.
3. Dennehy, Kevin. "Using More Wood for Construction Can Slash Global Reliance on Fossil Fuels." *YaleNews*, Yale, 2 Apr. 2014, news.yale.edu/2014/03/31/using-more-wood-construction-can-slash-global-reliance-fossil-fuels.
4. Green, Michael, director. *Why We Should Build More Wooden Skyscrapers*. TED, 2013, www.ted.com/talks/michael_green_why_we_should_build_wooden_skyscrapers/transcript
5. Ike. "Recycling Timber: Wasting Away." *Building*, 28 Oct. 2015, www.building.co.uk/focus/recycling-timber-wasting-away/5078393.article.
6. India Block | 19 March 2019 Leave a comment. "Mjøstårnet in Norway Becomes World's Tallest Timber Tower." *Dezeen*, 2 Aug. 2019, www.dezeen.com/2019/03/19/mjostarne-worlds-tallest-timber-tower-voll-arkitekter-norway/
7. Mehta, Madan, et al. Building Construction: Principles, Materials, and Systems. Pearson, 2018.
8. Oliver, Chadwick Dearing. "Carbon, Fossil Fuel, and Biodiversity Mitigation With Wood and Forests." *Taylor & Francis*, 28 Mar. 2014, www.tandfonline.com/doi/full/10.1080/10549811.2013.839386.
9. Petersen, K A, and B Solberg. "Greenhouse Gas Emissions, Life-Cycle Inventory and Cost-Efficiency of Using Laminated Wood Instead of Steel Construction." *Ohiolink*, 2002, rave.ohiolink.edu/ejournals/article/322357757.
10. "Steel." *Recycling / Steel*, www.recycle-more.co.uk/recycling/steel
11. "Why Glued Laminated Timber Beams Are So Popular in the Construction Industry?" *Epic Home Ideas*, 18 Apr. 2019, www.epichomeideas.com/glued-laminated-timber-beams-in-the-construction-industry/

BelleFlex Dehydrator and the Efficiency of Phase Separation

Student Researcher: Victoria L. Clarchick

Advisor: Professor Ben Ebenhack

Marietta College
Petroleum Engineering

Abstract

The separation of oil, gas, and water in the Oil and Gas Industry is continuously changing. The creation of new processes occur practically every day, yet there is still always a small percentage of water and smaller hydrocarbons still left in the hydrocarbon mixture at the end of the separation process on locations. The purpose of this experiment is to determine if there is a device that can separate the three phases on site locations. The current problem is that there is not a device that is small enough to fit onto locations that can perform the required separation procedure at the rates of the flowing wells. The BelleFlex dehydrator is a device that has the potential to separate the three phases, oil, gas and water, on a smaller scale. This will be important to environmental protection as well as efficient operations. Therefore, outlined in this experiment is the process for how the BelleFlex Dehydrator separates oil, gas, and water.

Project Objective

The scope of this project focuses on the separation of hydrocarbons from water. At this point in time there is not a complete separation between the two liquids. The BelleFlex Dehydrator will be a unit located on each production location. As of current the hydrocarbon mixture runs through a three-phase separator in attempts to divide the mixture into three components.

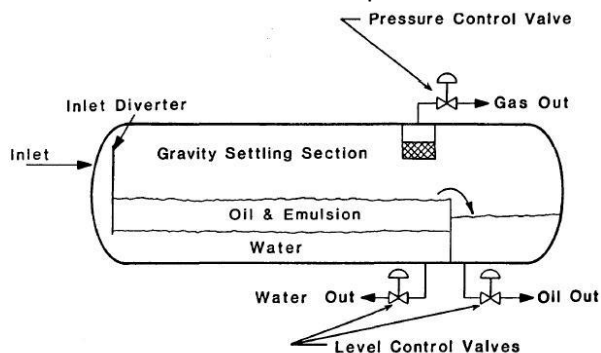
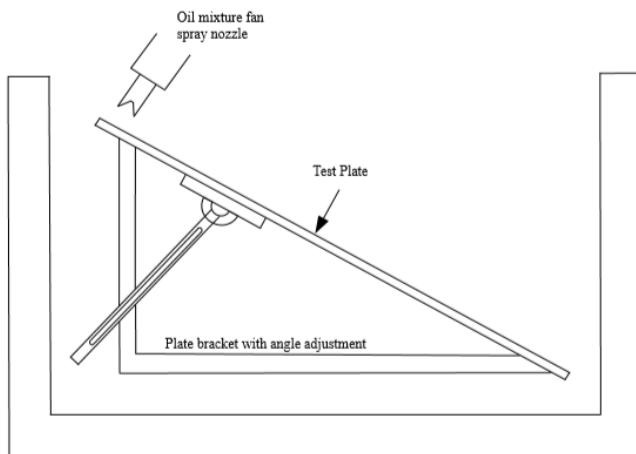


Figure 5-2. Horizontal three-phase separator schematic.

The hydrocarbon mixture is either trucked to a disposal site or stored in an above ground storage tank in attempts to reuse the produced mixture. Some companies like Range Resources have reused about 96% of the produced water in fracturing operations, but this produced water is not a viable option for all fracturing operations. When the water is injected into the well friction reducers, bacteria inhibitors, etc are mixed into the fracturing fluid. Although these additives make up less than 1% of the fracturing fluid some mixtures cannot be used in other wells due to possible reactions within the wellbore. Therefore the water has to be disposed and cannot be reused. If the hydrocarbon can be separated from the water then there is no loss in profits of hydrocarbons.

Methodology Used

To investigate the BelleFlex and the possible range of separation that it can achieve there are many mixtures of water and hydrocarbons created. Using an array of different ratios between hydrocarbons and water the BelleFlex is sent though many tests. The test also include moving toward additive separation. This includes mixing different types of additives with first water alone and then within a hydrocarbon/ water mixture. These different mixtures are then tested and run through the BelleFlex.



BelleFlex Test Apparatus

Results Obtained

The preliminary testing was able to be completed and the results were that separation was possible. From the initial test runs there was evidence of separation and possible places for improvement but due to the COVID-19 shutdown, further testing has been halted. As of now this experiment is still within the testing stages. From the initial results application beyond hydrocarbon/water separation seems possible. If tests continue there are possible results that could lead to the release of purified water back into fresh water systems. This application is far off into the distance but is the ideal end result.

References

1. Chris Jacobs. BelleFlex Test Apparatus. January 20.
2. "From Flowback to Fracturing: Water Recycling Grows in the Marcellus Shale", *Journal of Petroleum Technology*, March 1.
3. "Horizontal Three Phase Separator Schematic", *Oil and Gas Separator*, March 1.
4. "Science and Medical Photos, Illustrations & Video", *Sciencesourceimages*, March 1.
5. "Water Use in Marcellus Deep Shale Gas Exploration", *Chesapeake Energy*, March 1.

Industry 4.0 in the Retail Sector: Sustainability of Food Retail with a Focus on Food Insecurity in Dayton, OH

Student Researcher: Katrina A. Coleman

Advisor: Sean Falkowski

University of Dayton

Department of Engineering Management, Systems, and Technology

Abstract

In recent years, large scale agricultural and food processing industries have experienced a great worldwide digital transformation. The advent of Industry 4.0, which has become popular in Europe, has helped many industries optimize their operations. Relatively new is the idea that food processing industries and other stakeholders in the food distribution supply chain cannot only optimize their processes but also, track and provide timely customer service. This has technical and managerial challenges that might limit the potential benefits of industry 4.0 in the efficient distribution of fresh food produce. For example, food retailers have to meet the increasing customer desire for fresh and high-quality food produce on demand. This has led to overstocking and understocking of some food items, as well as waste in transportation and labor, which adds to the total cost of food. Dayton, Ohio and other cities designated as food deserts have limited access to affordable and healthy high-quality fresh food. Preliminary data from this study suggest that lower-income communities in Dayton do not have immediate access to affordable, healthy and high-quality food. However, the other communities in the Dayton area usually see an oversupply of fresh, affordable and high-quality food in retail shops. Therefore, this study aims to utilize Industry 4.0 concepts to propose a more equitable and efficient way to minimize food insecurity in food deserts and apartheids and create a more sustainable environment.

Methodology

I volunteered at a co-op called Gem City Market 10 hours a week to try to get more of an insight on the city of Dayton and how to combat food insecurity. This led me to find three potential solutions to help solve the issue of food insecurity.

Results Obtained

While participating in a volunteer-internship with the Gem City Market (GCM), I learned about different ways to combat food insecurity using methods of Industry 4.0. Since GCM is run by Co-op Dayton, this introduced me to the idea of a co-op. Defined by the International Co-operative Alliance, “A cooperative is an autonomous association of persons united voluntarily to meet their common economic, social, and cultural needs and aspirations through a jointly-owned and democratically-controlled enterprise.” [2] This means that people gather together and become members (or shareholders) of a company built by the community. This concept is great way to engage the community and bind them together, and also helps the economy. Instead of shopping at Kroger or Wal-Mart or Meijer and giving money to an external source, when you shop at a local grocer, such as GCM, you are putting money back into your own community. Members of the GCM also have a vote in community meetings, and organize events such as the Healthy Eating Children’s Cook-off, where children can participate and be educated on how to cook more nutritious food that they may not normally be exposed to every day. The GCM will also be hiring workers at a livable wage, they have been collecting receipts to see what people normally purchase at the grocery so that they can ensure their shelves will also be stocked with those items, and if the market is successful, shares will be given to members. The concept of GCM was created in 2015

and will be built by the end of 2020 where people will finally be able to shop at their own community market. [3]

Significance and Interpretation of Results

While looking at potential solutions to eliminate the food apartheid in Dayton, I have three ideas that I think have the potential to be very successful. The first being co-ops, that I stated earlier. Co-ops boost the economy, engage the community, and educate shoppers on sustainability and the concept of having a share and a vote within their community [6]. Another idea is a mobile market. There is a successful mobile market in Kansas City, MO and it is essentially a food truck of produce. Their mobile market accepts all forms of payment, including EBT, and they have paid employees as well as volunteers [5]. My last solution is having grocery store chains, or even co-ops like GCM, partner with Community Supported Agriculture (CSA) groups. CSA “allows city residents to have direct access to high quality, fresh produce grown locally by regional farmers” [7]. One farm which participates in CSA is Mission of Mary Farm (MOMF) which was founded by lay Marianists from the Dayton area [4]. MOMF is a nonprofit and strives to help the food desert issue in the Dayton area by providing those of lower incomes with fresh produce at a more affordable price, while also being sustainable [4]. Another organization which grocery stores can partner with is Homefull, which is similar to MOMF, but Homefull also has other services such as housing those living in homelessness [1]. I believe that if grocery stores partner with organizations such as these, it will help resolve the food desert issue, as well as improve the economy, similar to GCM, because those with lower incomes who do not normally purchase produce would start to. It would also be beneficial to the nonprofits, because the larger chain grocery stores could donate their compostable items to these organizations, which would be more sustainable as well as give groups like MOMF and Homefull compost to use.

References

1. “COMMUNITY SUPPORTED AGRICULTURE PROGRAM.” *Homefull*, www.homefull.org/homefull-solutions/urban-agriculture-2/csa/.
2. “Cooperative Identity, Values & Principles.” ICA, www.ica.coop/en/cooperatives/cooperative-identity.
3. Jetpack. “Dayton, Ohio Grocery Store Co-Op.” Dayton, Ohio Grocery Store Co-Op | Gem City Market, gemcitymarket.com/.
4. “Our Programs.” *Mission of Mary Cooperative*, www.missionofmary.org/our-programs/.
5. Sauer, Mary. “This Mobile Grocery Store Wants to Eliminate Food Deserts in Kansas City.” Vice, 3 May 2016, www.vice.com/en_us/article/gvkk9m/this-mobile-grocery-store-wants-to-eliminate-food-deserts-in-kansas-city.
6. “What Is a Co-Op? - Definition of a Cooperative Business.” NCBA CLUSA, ncbaclusa.coop/resources/what-is-a-co-op/.
7. “WHAT IS CSA?” *Just Food*, www.justfood.org/csa.

The Importance of Video Games in Education

Student Researcher: Austin C. Cox

Advisor: Kathy Shan

The University of Toledo
Computer Science Engineering

Abstract

There has been no small amount of discussion and opinions offered about video games and education over the last few decades. Dr. Merrilea J. Mayo (2007) queries, “Video games can teach science and engineering better than lectures. Are they a cure for a numbing 200-person class?” In order for video games to be a viable resource in the educational process, they must not only entice the student to learn but also motivate him or her to solve problems (Sethi, 2012). Using video games is a way to both entertain and educate at the same time as well as motivate students to repeat play and, therefore, further enhance learning of even difficult concepts.

Project Objectives

This case study deals with the use of video games as an educational tool. The specific subject that was introduced through the medium of video games in this project was kinematics. Students with no background in the subject matter were specifically chosen to participate in the study. They were asked to play a certain video game, *Kerbal Space Program*, as an introduction to kinematics. The first part of the study was to determine their specific level of knowledge of kinematics. The second part was to discover whether they had increased their knowledge base as a result of playing an entertaining video game.

Methodology Used

The participants involved with this case study were from various backgrounds and age groups who had never been exposed to the formal study of basic physics concepts many STEM workers and students take for granted. This was done to show that anyone, no matter what background, can utilize the method of video games as a way to learn a new subject. First the students took a pretest consisting of 10 questions, all of which were basic kinematics questions as a control to find the participants’ base knowledge of kinematics. These questions were designed to show if the test-taker had any misconceptions about the laws of motion. An example of the questions on the pre- and post-test is that acceleration due to gravity is independent of mass. Then, participants played *Kerbal Space Program* tutorials uninterrupted for a maximum of eighty minutes. Immediately afterwards each participant took the post-test to measure any increase they may have developed.

Results Obtained

The figure below illustrates the results of the pre- and post-test used in this study. The average score on the pretest was 20% with a maximum of 30%. On the post-test administered after playing the video game, all participants improved their scores. The test results indicate a general improvement in all cases with an average increase of 20% over their original score, and a maximum increase of 40%. These results suggest further study in the use of video games as a viable learning tool is merited.

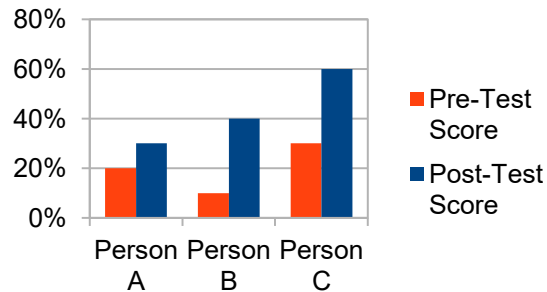


Figure 1. Results of the pre-test and post-test.

References

1. Mayo, Merrilea J. (2007, July). *Games for science and engineering education*. Researchgate. https://www.researchgate.net/publication/220423820_Games_for_science_and_engineering_education
2. Sethi, Chitra. (2012, September 4). *Can Video Games Reshape STEM Education?* ASME.
3. <https://www.asme.org/topics-resources/content/can-video-games-reshape-stem-education>

Detection of Hazardous Substances

Student Researcher: Alexis C. Cresanto

Advisor: Dr. Pedro Cortes

Co-Advisors: Dr. Eric MacDonald & Dr. Byung-Wook Park

Youngstown State University

Chemical Engineering

Abstract

Society is threatened daily by potentially harmful chemical substances that may not be detectable by human sensing. It is essential that these chemicals can be detected accurately and immediately before lives are threatened. To accomplish this, carbon nanotubes are being used as the main detection material in sensor creation because of their electrochemical properties. These properties allow them to detect changes in conductivity in the presence of a foreign substance. The carbon nanotubes must be functionalized specifically for the chemical in testing so that the sensors will not detect incorrectly to similar substances. The production of small and integrated sensors is a beneficial feature for commodity on wearable structures. The answer to this requirement is the incorporation of additive manufacturing on the production of bio-chemical sensing platforms.

Project Objectives

This research investigates the use of carbon nanotubes on 3-D printed electrodes to detect hazardous substances. The electrodes will eventually be used to create flexible sensors as shown in figure 1. When there is a detection made by the sensor, it will be shown by a flashing LED light. These wearable sensors will be used by the department of defense.



Figure 1. Stereolithography printed substrate for creating wearable sensors.

Methodology Used

In the present work, carboxylated single-wall carbon nanotubes (COOH-SWCNTs) have been used as the sensing core for the detection of hazardous materials. The preliminary studies have been performed on the detection of cocaine. Here, epinephrine has been incorporated as the functional group on the carbon nanotubes. This initial work has been carried out in conjunction with a fellow classmate, Reis Zandier. Additional work is being carried out on the detection of cocaine in the solid state. Here, an enclosed chamber with a small fan was constructed so that the solid cocaine could circulate and find its way onto the electrode. Gold-plated electrodes with the functionalized CNTs have been incorporated into the chamber and the testing methodology relies on an electrochemical impedance spectroscopy (EIS).

Results Obtained

The preliminary detection of cocaine in water is shown in figure 2. From the figure, it is observed that the presence of cocaine induces a normalized resistance change of about 5%, since the testing of the control (pure water) resulted in 2% of resistance change. This suggests that a functionalization of epinephrine could be used as the selectivity chemical group for the detection of cocaine.

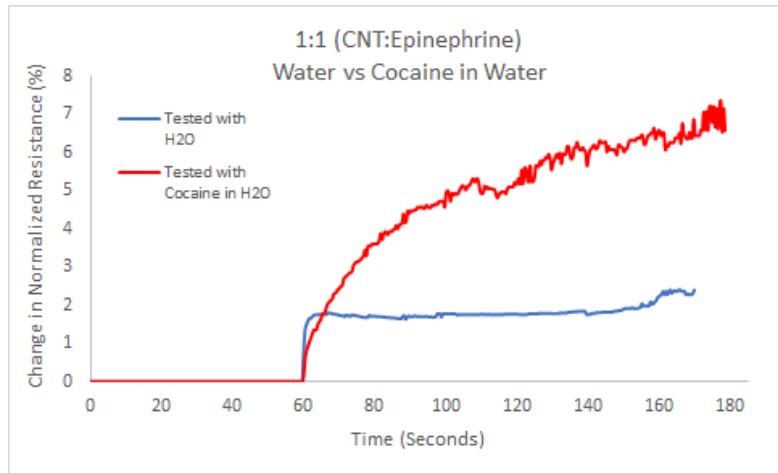


Figure 2. Detection of cocaine in water using epinephrine functionalized SWCNTs.

Additional testing was also performed on the epinephrine functionalized CNTs using a 2:1 volume ratio CNTs vs epinephrine (see figure 3). It was shown that the decrease of the amount of the functional group on the nanotubes resulted in a decrease of the level of cocaine detection. Indeed, the functionalized CNT electrode detecting the cocaine in water seemed to yield an electrical response similar to that displayed by the electrode tested against the pure water (control). These results indicate that a further analysis of the ratio of epinephrine to nanotubes needs to be further investigated.

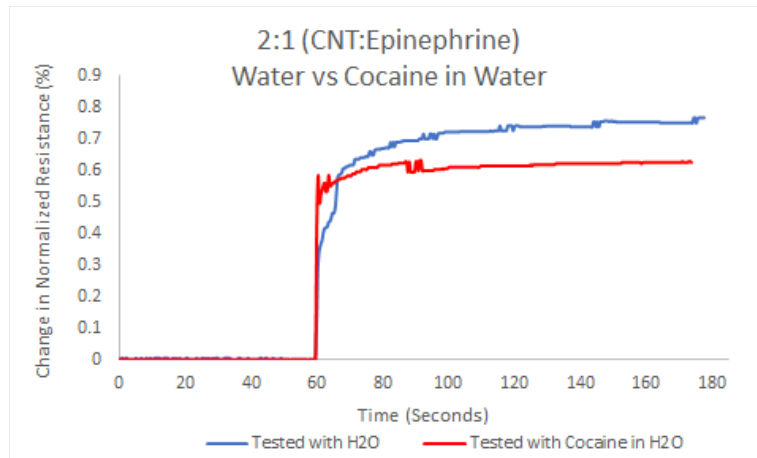


Figure 3. Electrical response of cocaine in water using a high CNT: epinephrine ratio (2:1).

The detection of cocaine in solid state was performed using an EIS platform. Figure 4 shows the gold-plated electrode used for placing the functionalized CNTs. Included in figure 4, is the experimental set-up used for the detection of cocaine on solid state. This work is still in progress, and several modifications are being incorporated into the testing set-up for the detection of cocaine. Variables that

are being considered are the increase of the fan speed and the amount of cocaine used. It is important that fan speed be adequate to ensure the cocaine is circulated onto the electrode. Also, the amount of cocaine added in the chamber needs to be investigated to guarantee its interaction with the CNTs. Indeed, in future testing higher fan speeds and larger masses of cocaine will be used to ensure the particles are reaching the electrode with each trial. Going forward with this research, more testing will be done in different conditions to further examine the detection found. There will also be testing done on additional hazardous gases and explosives.

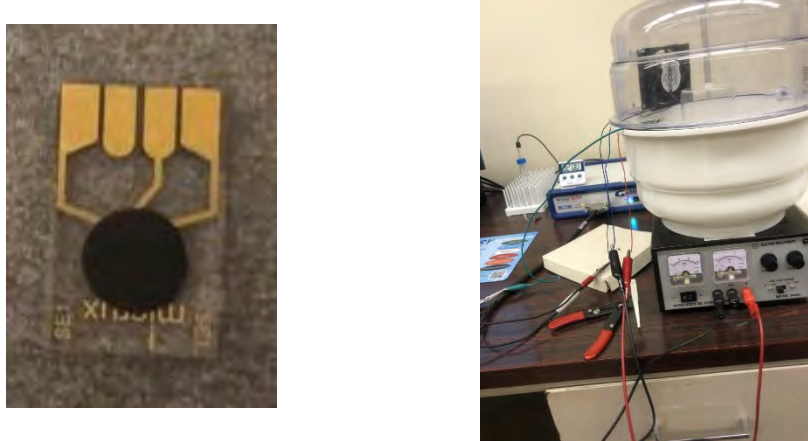


Figure 4. Solid state set-up. Gold-plated electrode with functionalized CNTs (left). Enclosed chamber for detecting the cocaine (right).

Choosing a PEG for a Hybrid Cardiac Hydrogel

Student Researcher: Lauren M. Cummons

Advisor: Dr. Ge Zhang

The University of Akron
Biomedical Engineering

Abstract

A heart attack, or myocardial infarction (MI), is one of the leading causes of cardiovascular related deaths. There are very few long-term effective options for restoring cardiac function after an MI, and new developments must be made for an alternative treatment. Stem cell research has come very far in offering potential therapies for repairing cardiac tissue and improving the function of the heart after a myocardial infarction. One popular experimented solution is a hybrid cardiac hydrogel consisting of a synthetic polymer and the cardiac extra cellular matrix.

Objectives

My objective during this research is to understand the different components that can create a hydrogel, and choosing a synthetic polymer, such as a type of polyethylene glycol (PEG), that will give me the desired results.

Based on the results acquired from the chosen PEG, my objective is to analyze the data and determine if that PEG has any potential for clinical applications or if a new PEG should be chosen to research.

Underlying Theory

Cardiac tissue does not regenerate after a heart attack, and the damage is replaced with scar tissue. This is the reason why finding a therapy to regenerate healthy cardiac cells is necessary for patients who have suffered a myocardial infarction. The hydrogel is a basic gel composed of decellularized extra cellular matrix and a few buffers to keep the conditions appropriate for growing cells. The addition of a polymer allows for adjustments of properties such as gelation and biological activity without being overtly toxic to the cells and cause complications with the host. Using a synthetic polymer to create hydrogels will ease the modification process depending on the desired results.

Methodology

The base for the hydrogels used in this research will be made from decellularized porcine right ventricle cardiac extracellular matrix. The cardiac tissue is decellularized to provide information to the cells that promote growth and healthy physical properties. Once a PEG is chosen, it will be used to create the hydrogel that will be tested. Hydrogels with PEGs are commonly used in 3D cell culture, due to their ability to be reabsorbed by the body without eliciting an immune response. To make sure the PEG will work in a practical application, the hydrogel must be tested for gelation, degradation, swelling, cell toxicity, and rheological properties. These results will determine the ability of the hydrogel with the synthetic polymer to promote cell growth. Modifications can be made to the synthetic polymer as well if further research and testing is necessary.

Conclusion

This research, and others like it, is crucial to finding a solution to healing cardiac tissue after a myocardial infarction. Due to the complex and sensitive nature of cardiac tissue, hydrogels used in clinical settings must have the appropriate characteristics for promoting the growth of healthy cells. These characteristics can be measured and studied by applying cell cultures to the hydrogel and determining the result. Although the process of choosing and testing a synthetic polymer for a hydrogel can be tedious and demanding, finding a hydrogel that can be used in a clinical setting will help save lives.

References

1. "The Beginner's Guide to ECM Gels." *Mimetas*. 6 September 2019.
<https://mimetas.com/article/beginner%E2%80%99s-guide-ecm-gels>. 24 April 2020.
2. Jeffords, Megan E., et al. "Tailoring Material Properties of Cardiac Matrix Hydrogels to Induce Endothelial Differentiation of Human Mesenchymal Stem Cells." *ACS Publications*. 6 May 2015.
<https://pubs.acs.org/doi/full/10.1021/acsami.5b03195>. 24 April 2020.

Modeling Liquid Propellant Rocket Nozzle using MATLAB and SolidWorks

Student Researcher: William A. Deisler

Advisor: Dr. Jed E. Marquart

Ohio Northern University
Mechanical Engineering

Abstract

In today's society, the use of rockets has become almost routine. Companies like NASA and SpaceX regularly send cargo to the International Space Station with minimal failures. As companies continue to perfect their rocket technologies, it is reasonable to imagine a time in the near future where the use of rockets will be an everyday occurrence. In many highly technical projects, such as rocket development, the early development stages are crucial to mission success. In rocket development, having methods to quickly get a baseline understanding of what will be required of the system could help allow engineers more time in the later stages of development such as testing and troubleshooting.

Project Objectives

The objective of this project is to show one potential method to expedite the early stages of rocket development by producing a 3D model of a rocket nozzle using the desired engine performance parameters. According to an article describing NASA's rocket design process, the total design time from concept generation to implementation can be anywhere between a year and five years or more [1]. In most projects, time is money. For this reason, it could be extremely beneficial in rocket development to quickly develop an early prototype engine to narrow down the acceptable design choices.

Methodology Used

One popular method to design nozzles is the Method of Characteristics. This method uses the theory of shock and expansion wave reflection and the idea that flow must be parallel on each side of a slip line to determine the shape of a nozzle [2]. Using the intersections of the left and right running characteristic lines of the flow, the complete set of flow parameters can be defined at various points. The interaction of the left and right running characteristic lines and the flow parameters defined by these lines will define the nozzle shape. An example of a nozzle defined by these characteristic lines is shown in Figure 1 on the following page.

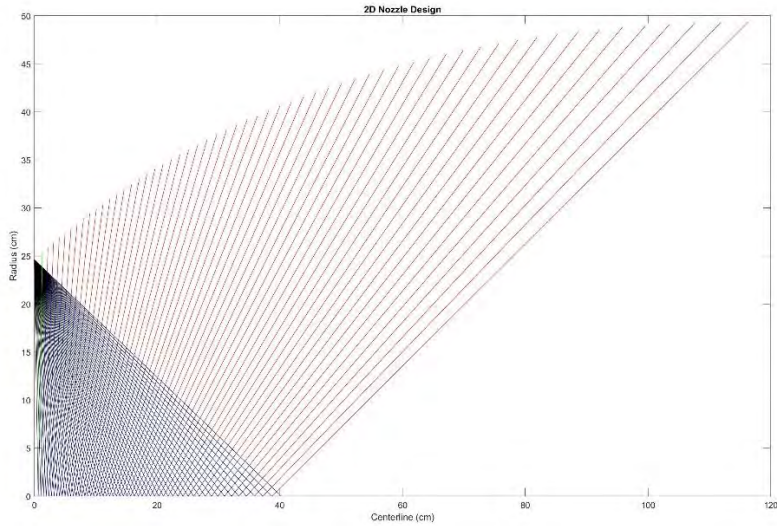


Figure 1. Nozzle created using Method of Characteristics.

Results Obtained

This method is used in a program developed by VDEngineering [3]. Using this code the user can quickly generate a nozzle based on: combustion chamber pressure and temperature, thrust or mass flow rate, optimized altitude, and the coefficient of heats and gas constant for the propellant used. After running the code, the user can then import the calculated points into a CAD program such as SolidWorks to generate a 3D version of the designed nozzle. Two different nozzles with different flight parameters can be seen in Figures 2 and 3 below.

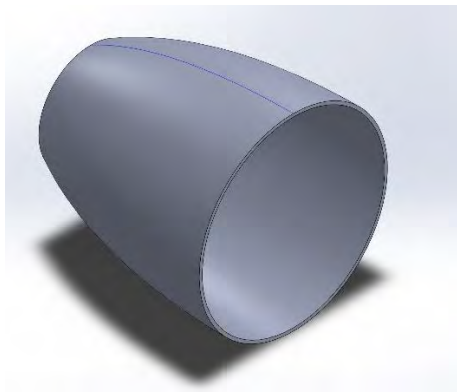


Figure 2. Full scale (space-quality) nozzle.

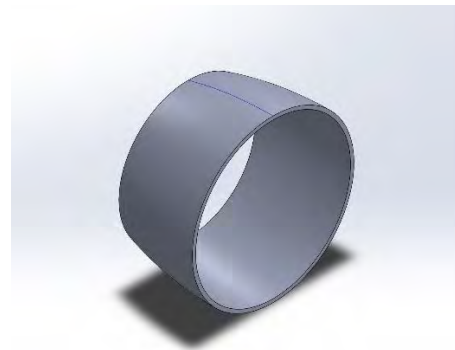


Figure 3. Model rocket scale nozzle.

In the future, the nozzles generated using this program could be tested using CFD analysis and model wind tunnel testing to either verify the design or indicate a necessary redesign.

References

1. (2011, June 20). *J-2X Extra: The Rocket Engine Development Life Cycle* [online]. Available: https://blogs.nasa.gov/J2X/2011/06/20/post_1308600465941/
2. G. Dimitriadi. *Aerothermodynamics of High Speed Flows: Rocket Design* [online]. Available: <http://www.itas-aea.ulg.ac.be/cms/uploads/Aerothermodynamics05.pdf>
3. VDEngineering, *Rocket Engine Design with MATLAB and Solidworks – Method of Characteristics Nozzle Tutorial!* 2018 [Streaming Video]. Available: https://www.youtube.com/watch?v=iRuG_Zbz2Ig

Small Business Promotion through Web Development

Student Researcher: Brandon L. Dunson

Advisor: Dr. Derek Petrey

Sinclair Community College

Departments of Computer & Electronic Engineering, and Computer Informational Science

Abstract

I am currently enrolled in a CIS 1350 (Web Development – HTML & CSS) and I would like to develop a website that would work in a way similar to GasBuddy, but instead refer people to locally-owned businesses and non-profits. The City of Dayton uses CityBOTS to update their information daily. CityBOTS™ is a software service which tracks minority utilization, contract compliance, and vendor certifications for entities maintaining DBE, MBE/WBE, SBE, or other business enterprise programs in Excel format. I started to develop a website and learned how to portray the data in digital map form.

Project Objectives

My objective in this research was to connect data from reliable resources into a website for the promotion of locally-owned businesses and non-profits in the City of Dayton. The City uses the Procurement Enhancement Program to promote diverse businesses: "The City establishes aspirational and annual diversity goals that are placed on construction and goods and services bids. Minority-owned, women-owned and small disadvantaged businesses can certify with the City's PEP program to assist the City with accomplishing [those] goals. When the City seeks diversity in the procurement process, PEP certified companies are contacted by the city or contractors interested in bidding." (Dayton HRC).

Methodology Used

First, I looked at a way to best access the database, CityBOTs, that updates information daily on Dayton's locally-owned businesses. Then I found a platform interface that I thought would be a good model for the website, the Richmond, Virginia Minority Business Directory Search Interface. (Fig 2) It was a JavaScript Google Analytics module inside an HTML page.

Results Obtained

I obtained the CityBOTS data for Dayton-local/minority-/women-owned/small-business enterprises in Excel (Figure 1). I also learned how to integrate an address database into Google Maps (Figure 3).

Significance and Interpretation of Results

Integrating digital media for locally-owned businesses/non-profits will improve their prospects.

Figures/Charts

Figure 1. Current City of Dayton Database for PEP Program.

RVA RICHMOND VIRGINIA OFFICE OF MINORITY BUSINESS DEVELOPMENT

MBD Business Directory Listing

Please select search criteria to list for the directory's businesses

Company:

Work Category: then

If you are a Minority Business Enterprise or an Emerging Small Business, and not listed in our Business Directory, we encourage you to register.

Obtain the [MBD registration form](#) or the [ESB certification form](#).

Note the definition of each is in the upper right corner of the respective form. If you meet the definition, complete the form and either mail or fax your information to our office. Our mailing address and fax number are in the upper left corner of each form.

Figure 2. Richmond, Virginia, Minority Business Directory Search Interface.

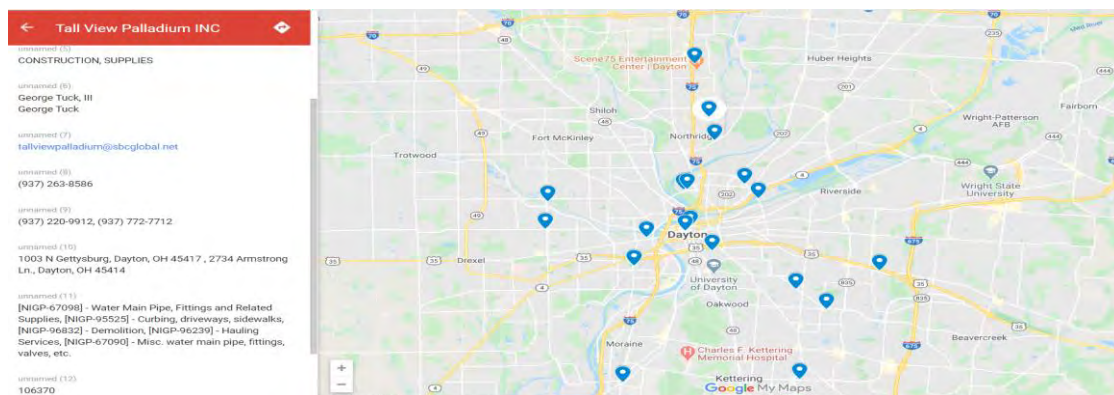


Figure 3. Screenshot of proposed output using Google Maps.

Conclusion

I need to continue to learn CSS, HTML and JavaScript in order to further develop the website. I hope to keep the website up to date with the most recent information on the locally-owned businesses and non-profits in Dayton, Ohio.

References:

1. <https://citybots.com/Home/Links> - database from the City of Dayton for SBE / MBE / LBE
2. <http://daytonhrc.org/business-technical-assistance/certification/> - The City of Dayton HRC (Human Relations Council), Certification
3. <https://apps.richmondgov.com/applications/mbebusinessdirectory/Index.aspx> - The Richmond, Virginia Office of Minority Business Development, Minority Owned Business Directory
4. <https://www.networkworld.com/article/3303581/how-to-pin-a-pile-of-addresses-onto-a-google-map.html> - Sandra Henry-Stocker, Network World, How to Pin a Pile of Addresses onto a Google Map.

Graphene Future Technologies

Student Researcher: Brennan S. Eden

Advisor: Lawrence Feist

Cincinnati State Technical & Community College
Electro-Mechanical Engineering Technology

Abstract

An emerging material with sought after physical properties could change the foundations of many current disciplines; including that of energy storage, transportation, medicine, electronics, and defense industries.

Objective

To determine which (if any) industries will be benefiting when graphene materials becomes more available with mass production.

Methodology

Compare benefit-cost ratio for each industry that can possibly take advantage of the addition of graphene construction or components.

Conclusion

Within the next decade, the price of this material will drop due to increased supply and make the utilization of graphene in major industries a viable asset.

References

1. <https://www.graphene.manchester.ac.uk/>. The University of Manchester.
2. "Military Applications of Graphene." <https://nanografi.com/blog/military-applications-of-graphene/>. © 2020 Nanografi Nano Technology.
3. Peleg, Roni. "Graphene-Info: the graphene experts." <https://www.graphene-info.com/>. ©2004-2020 Metalgrass LTD.
4. "Graphene: The Carbon-Based 'Wonder Material'." <https://www.compoundchem.com/2015/06/23/graphene/>. © 2020 Compound Interest. June 23, 2015.
5. Wang, Brian. "Super aluminum-graphene battery has a 5-second charging time." <https://www.nextbigfuture.com/2017/12/super-aluminum-graphene-battery-has-a-5-second-charging-time.html>. © 2009, 2010, 2011, 2012, 2013, 2014, 2015, 2016, 2017 New big future Inc. December 28, 2017.

Thermal Modeling of Coordinated Multi-Beam Additive Manufacturing

Student Researcher: Rachel E. Evans

Advisor: Dr. Joy Gockel

Wright State University

Mechanical and Materials Engineering Department

Abstract

In additive manufacturing (AM), it is necessary to know the influence of processing parameters in order to have better control over the microstructure and mechanical performance of the part. Laser powder bed fusion (LPBF) is a metal AM process in which thin layers of powdered material are selectively melted to create a three-dimensional structure. This manufacturing process is beneficial for many reasons; however, it is limited by the thermal solidification conditions achievable in the available processing parameter ranges for single-beam processing methods. Therefore, this work investigates the effect of multiple, coordinated heat sources, which are used to strategically modify the melting and solidifying in the AM process. The addition of multiple heat sources has the potential to provide better control of the thermal conditions, thus providing better control of the microstructure of the additively manufactured parts. To model this, existing thermal models of the LPBF process have been modified to predict the thermal effects of multiple coordinated laser beams. These computational models are used to calculate melt pool dimensions and thermal conditions throughout the LPBF process. Furthermore, the results of the simulations are used to determine the influence of the distance between the coordinated laser beams. The predictive method used in this research provides insight into the effects of using multiple coordinated beams in LPBF, which is a necessary step in increasing the capabilities of the AM process.

Project Objectives

The LPBF process is utilized to manufacture small, customized parts with high resolution and fine details. However, the products that result from this process are prone to defects and microstructural variations that can adversely affect the mechanical performance of the part. Utilizing a coordinated multi-beam scanning strategy provides potential avenues for improvements, although not much research has been done for this type of scanning strategy because the experimental capability is not available. As a result, more research needs to be conducted to increase the understanding of the multi-beam LPBF process. The purpose of this research project is to accurately model the thermal behavior of multi-beam LPBF through the use of computer simulations. Moreover, this project aims to utilize these computer simulations to predict the influences of a second heat source on both melt pool geometry and microstructure to guide future equipment development strategies.

Methodology Used

Rosenthal Solution

The Rosenthal solution [1] is a 3-D linear solution to the heat equation for a point heat source traveling at a constant speed, as shown in Figure 1. In this configuration, two laser heat sources travel in the positive x-direction at speed V with absorbed laser power αQ . The system is modeled on the $y_0 = 0$ plane to obtain the solution that corresponds to the maximum melt pool depth.

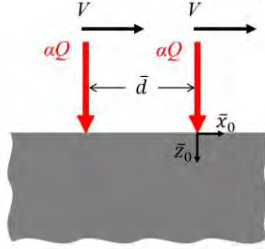


Figure 1. The coordinated multi-beam LPBF configuration that is modeled by the Rosenthal solution.

The Rosenthal solution assumes steady state conditions, a semi-infinite domain, and constant and uniform material properties. The dimensionless form of the equation, given by Vasinota et al. [2], computes the non-dimensional temperature due to the heat source. This dimensionless form can be modified to include the effects of a second heat source to obtain Equation (1), which calculates the dimensionless temperature, \bar{T} , due to two heat sources:

$$\bar{T} = \frac{e^{-\left(\bar{x}_0 + \sqrt{\bar{x}_0^2 + \bar{z}_0^2}\right)}}{2\sqrt{\bar{x}_0^2 + \bar{z}_0^2}} + \frac{e^{-\left(\bar{x}_0 + \bar{d}\right) + \sqrt{(\bar{x}_0 + \bar{d})^2 + \bar{z}_0^2}}}{2\sqrt{(\bar{x}_0 + \bar{d})^2 + \bar{z}_0^2}} \quad (1)$$

The dimensionless distance between heat sources, \bar{d} , and the dimensionless coordinates \bar{x}_0 , \bar{y}_0 , and \bar{z}_0 are defined as:

$$\bar{d} = \frac{d}{2k/\rho cV}, \quad \bar{x}_0 = \frac{x_0}{2k/\rho cV}, \quad \bar{y}_0 = \frac{y_0}{2k/\rho cV}, \quad \text{and} \quad \bar{z}_0 = \frac{z_0}{2k/\rho cV} \quad (2)$$

The boundary of the melt pool is calculated by setting Equation (1) equal to the dimensionless melting temperature, \bar{T}_m , which can be found with Equation (3):

$$\bar{T}_m = \frac{T_m - T_0}{\left(\alpha Q / \pi k\right) \left(\rho c V / 2k\right)} \quad (3)$$

where T_m is the melting temperature, T_0 is the preheating temperature, α is the absorptivity of the laser heat source, Q is the laser power, k is the thermal conductivity, ρ is the material density, c is the specific heat, and V is the laser speed.

As discussed by Bontha et al. [3, 4], the solidification cooling rate and thermal gradient are found through differentiation of Equation (1). The dimensionless cooling rate $\partial \bar{T} / \partial \bar{t}$ can be calculated by taking the partial derivative of Equation (1) with respect to time. The dimensionless thermal gradient $|\nabla \bar{T}|$ is found by taking the magnitude of the x , y , and z components; however, the quantity $\partial \bar{T} / \partial \bar{y}_0$ is equal to zero on the $y_0 = 0$ plane. Therefore, the dimensionless thermal gradient on the maximum melt pool plane becomes:

$$|\nabla T| = \sqrt{\left(\frac{\partial T}{\partial \bar{x}_0}\right)^2 + \left(\frac{\partial T}{\partial \bar{z}_0}\right)^2} \quad (4)$$

where $\partial T / \partial \bar{x}_0$ and $\partial T / \partial \bar{z}_0$ are found by taking the appropriate partial derivatives of Equation (1).

It is important to note that the cooling rate and thermal gradient solutions approach the single-beam Rosenthal solution as d approaches infinity. Therefore, the simulations for multi-beam LPBF with $d = \infty$ can be modeled with the single-beam Rosenthal solution.

Semi-Analytical Approach

In order to include time-dependent heat transfer effects, the LPBF process can be modeled with the semi-analytical approach, which utilizes a transient heat conduction solution to compute temperature data as a result of a circular ring heat source [5-9]. This model assumes a semi-infinite domain and neglects the effects of latent heat and heat loss due to vaporization and convection, while also assuming constant and uniform material properties.

The coordinated multi-beam LPBF scan strategy that is modeled with the semi-analytical solution is represented in Figure 2. In this configuration, two laser beams at a specified offset distance apart travel in the positive x -direction a constant speed. This configuration is very similar to the one modeled by the Rosenthal solution; however, the coordinate system is located differently.

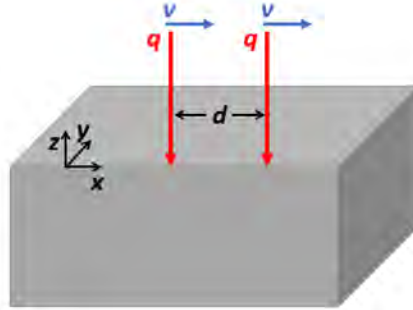


Figure 2. The scanning strategy that is modeled by the semi-analytical model.

The multi-beam semi-analytical solution, which uses the variables given in Table 1, is given by:

$$T(x, y, z) = T_0 + \frac{q}{c_p \rho (4\pi a)^{3/2}} \cdot \int_{\tau_i=0}^{\tau_i=t} \left[\frac{1}{\tau^{3/2}} \exp\left(-\frac{r_0^2 + x^2 + y^2 + z^2}{4a\tau}\right) \cdot I_0\left(\frac{r_0}{2a\tau} \sqrt{x^2 + y^2}\right) \right. \\ \left. + \frac{1}{\tau^{3/2}} \exp\left(-\frac{r_0^2 + (x+d)^2 + y^2 + z^2}{4a\tau}\right) \cdot I_0\left(\frac{r_0}{2a\tau} \sqrt{(x+d)^2 + y^2}\right) \right] d\tau_i \quad (5)$$

where the applied laser power, q , is defined as the product between the absorption coefficient α and the applied laser power P :

$$q = \alpha P \quad (6)$$

Table 1. Variables used in the semi-analytical approach.

Variable	Description	Units
$T(x, y, z)$	Temperature at point (x, y, z)	K
T_0	Initial temperature	K
q	Absorbed power	J/s
c_p	Specific heat	J/K
ρ	Material density	g/cm ³
a	Thermal diffusivity	m ² /s
τ_i	Integration time step	s
t	Time	s
τ	Time available for conduction	s
r_0	Radius of heat source	m
I_0	Bessel function of the first kind, zero order	none
d	Distance between laser beams	m

Similar to the Rosenthal solution, the semi-analytical solution can be differentiated to obtain the cooling rates and thermal gradients. The cooling rate is found through partial differentiation of Equation (5) with respect to t . The thermal gradient is found through the following equation:

$$|\nabla T| = \sqrt{\left(\frac{\partial T}{\partial x}\right)^2 + \left(\frac{\partial T}{\partial y}\right)^2 + \left(\frac{\partial T}{\partial z}\right)^2} \quad (7)$$

where $\partial T / \partial x$, $\partial T / \partial y$, and $\partial T / \partial z$ are the partial derivatives of Equation (5) with respect to x , y , and z .

Just like the Rosenthal solution, the semi-analytical model approaches the single-beam solution as d approaches infinity. Therefore, the simulations for multi-beam LPBF with $d = \infty$ can be modeled with the single-beam semi-analytical solution.

Material Properties and Processing Parameters

In order to maintain consistency, all material properties and processing parameters were kept constant for each simulation, with the exception of the distance between heat sources. The material constants represent the properties of Ti-6Al-4V, and the processing parameters were chosen to resemble realistic parameter sets for LPBF of this material. These values are outlined in Table 2.

Table 2. The material properties of Ti-6Al-4V and the processing parameters chosen for the simulations.

Property	Value
Density	4002.23 kg/m ³
Specific heat	857.68 J/(kg·K)
Thermal conductivity	30.45 W/(m·K)
Melting temperature	1654 K
Absorption coefficient	0.35
Applied laser power	300 W
Laser speed	750 mm/s
Preheat temperature	100 K

Results Obtained

The results in Figure 3 show the melt pool geometries on the x - z plane for six different scan strategies as predicted by the Rosenthal solution. These simulations represent multi-beam scan strategies with offset distances of 0 mm, 0.25 mm, 0.5 mm, 1 mm, 2 mm, and ∞ .

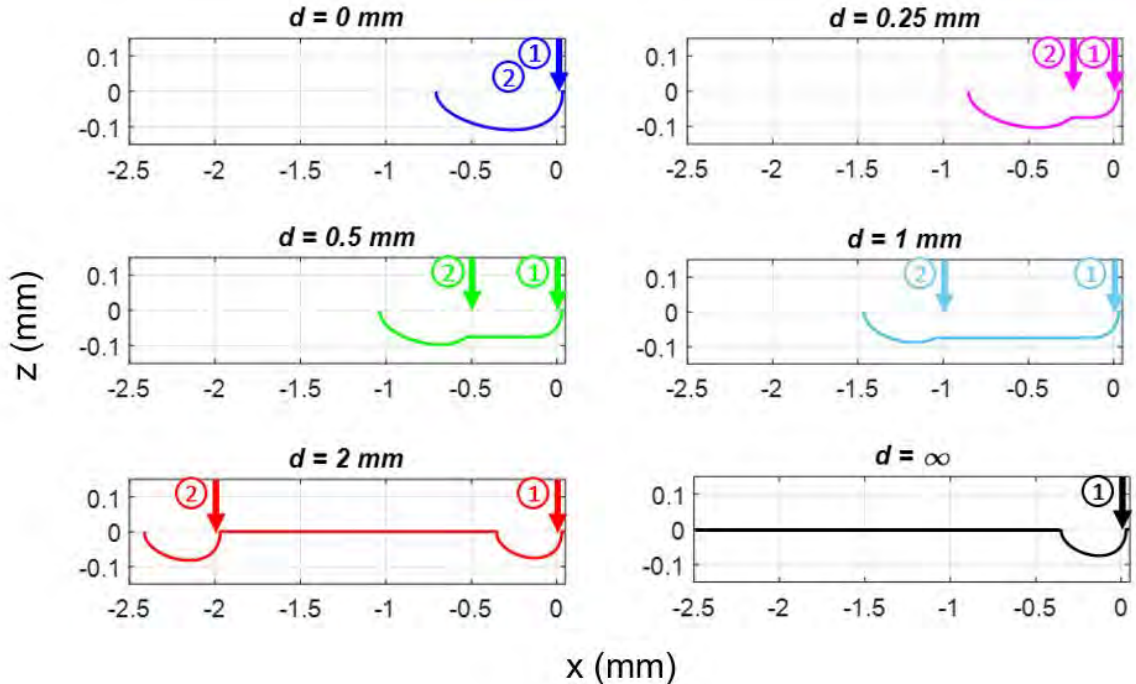


Figure 3. Melt pool geometries of multi-beam LPBF, as predicted by the Rosenthal solution.

The results in Figure 4 show the melt pool geometries on the x - z plane for the same six scan strategies; however, these were calculated with the semi-analytical model.

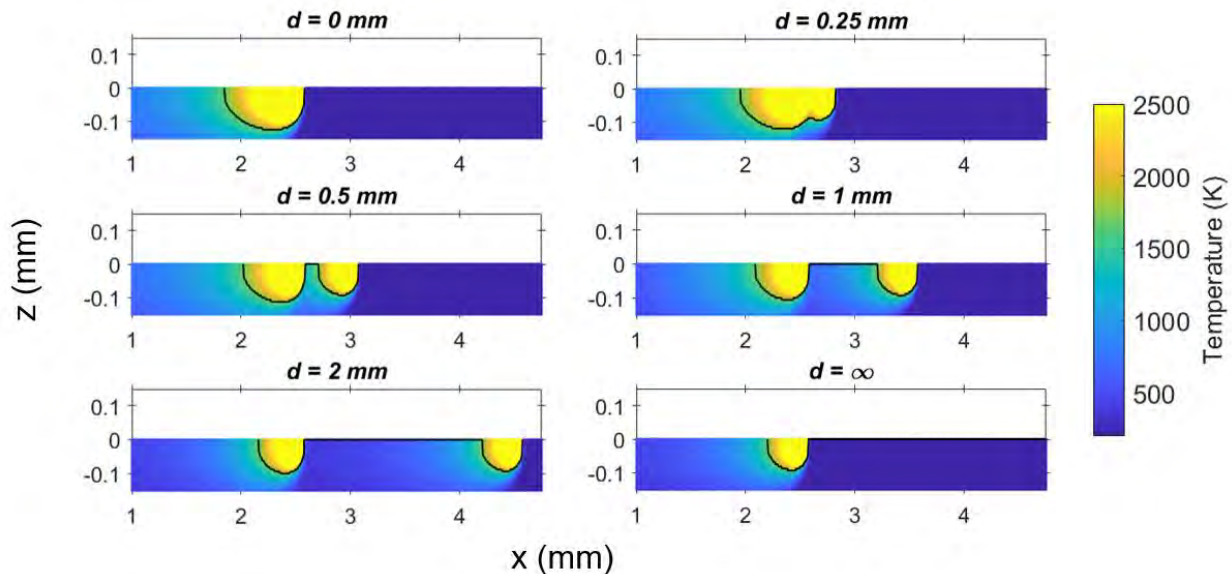


Figure 4. Melt pool geometries of multi-beam LPBF, as predicted by the semi-analytical model.

The maximum melt pool depths and lengths for the above simulations are summarized in Table 3. Here, the melt pool lengths are measured from the front of the leading melt pool to the end of the trailing melt pool. As expected, an increase in the distance between lasers generally causes a decrease in melt pool depth and an increase in melt pool length. This is because spreading out the lasers results in a longer melt pool that does not melt as far into the material.

Table 3. The expected melt pool depths and lengths for multi-beam LPBF, as predicted by both the Rosenthal solution and the semi-analytical model.

	<i>Rosenthal</i>	<i>Semi-Analytical</i>		
	Maximum Melt Pool Depth (μm)	Melt Pool Length (μm)	Maximum Melt Pool Depth (μm)	Melt Pool Length (μm)
$d = 0 \text{ mm}$	108.5	741.6	128.1	731.2
$d = 0.25 \text{ mm}$	103.9	882.1	121.9	878.1
$d = 0.5 \text{ mm}$	96.8	1065.4	115.6	1062.5
$d = 1 \text{ mm}$	88.3	1494.4	106.3	1490.6
$d = 2 \text{ mm}$	81.5	2443.4	100.0	2434.4
$d = \infty$	75.3	383.1	93.8	378.1

The following images show the resulting thermal conditions for six distances between laser beams: 0, 0.25 mm, 0.5 mm, 1 mm, 2 mm, and ∞ . For these results, both the cooling rate and thermal gradient were calculated at the boundary of the melt pool's trailing edge because this is the location at which the material starts to solidify. Figure 5 shows the cooling rates versus the normalized melt pool depth. As shown on the plot, an increase in distance results in an increase in the cooling rate, which also suggests a decrease in grain size. These results make sense; spreading out the laser beams causes the inputted heat to become less localized, thus increasing the rate at which the material cools down.

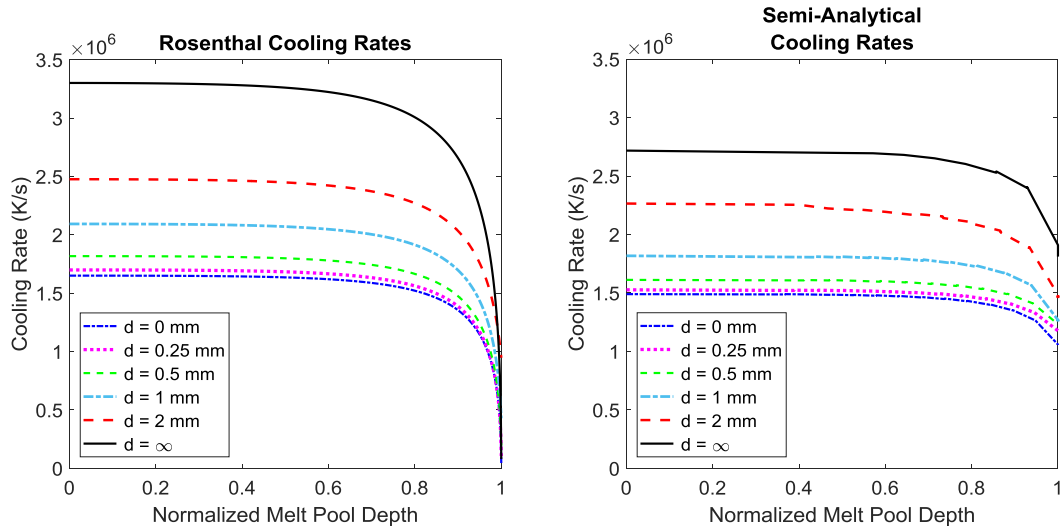


Figure 5. Cooling rate vs. normalized melt pool depth in multi-beam LPBF.

The cooling rates and thermal gradients were then used to create solidification maps in order to predict grain morphology. Columnar grains are elongated and anisotropic, while equiaxed grains are nearly equal in all directions. The solidification map plots the thermal gradient, G , versus the solidification rate, R , which is defined as:

$$R = \frac{1}{G} \frac{\partial T}{\partial t} \quad (8)$$

The solidification maps, shown in Figure 6, use the morphology regions determined by Kobryn et al. [10] for Ti-6Al-4V in AM processes. It can be observed that all the distances modeled here result in mixed grains that transition to columnar grains with increasing melt pool depth. This is true for both the Rosenthal solution and the semi-analytical model. This indicates that the distance between lasers has a negligible influence on the grain morphology. The plots show that an increase in d causes the points to shift slightly above and to the right. This suggests that the distance between lasers has an effect on the G -vs- R results; however, the points remain in the same morphology regions regardless of the distance.

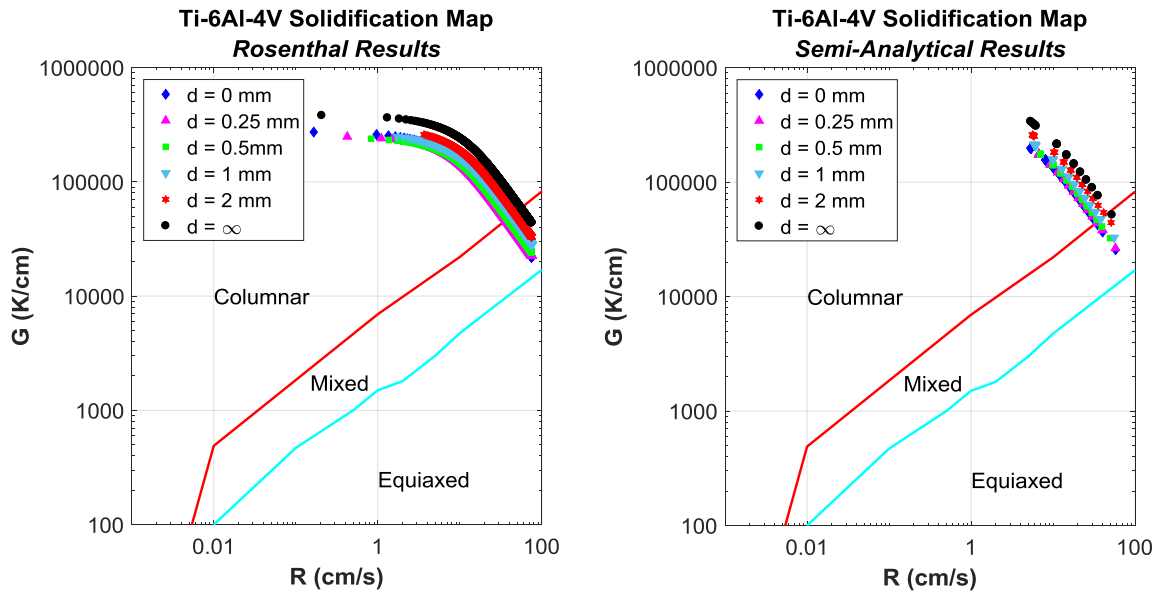


Figure 6. Solidification maps for multi-beam LPBF, using the Rosenthal and semi-analytical approaches.

Significance and Interpretation of Results

Due to the processing parameter ranges of single-beam LPBF, the solidification thermal conditions and microstructures that can be achieved are limited. This can be potentially improved by introducing multiple heat sources to the process. As a result, this work investigates the effect of a second heat source, which travels at the same speed and is located at an offset distance away from the first heat source. The predictive method used here provides insight to the effects of using multiple coordinated beams in LPBF, which is a necessary step in increasing the capabilities of the AM process.

The coordinated multi-beam scanning strategy was modeled with two separate modeling approaches. First, the Rosenthal solution provided steady-state solutions, which is advantageous due to its ability to provide quick results. The semi-analytical approach, however, provided more accurate results due to its inclusion of transient effects. While the results from these methods did differ slightly, they both produced the same conclusions. The addition of a second, identical laser beam results in variations in both melt pool shape and size. Additionally, a second laser beam results in slower cooling rates, or a

larger grain size, which decreases as the offset distance increases. However, the grain morphology is not affected by this, as the results fall in the same morphology regions regardless of the distance between lasers. These results do not provide adequate evidence to conclude that multi-beam LPBF can fix the problems seen in single-beam LPBF. However, there are still many avenues to explore in multi-beam LPBF. For example, the scan strategy can be altered to change the power and speed of each laser independently, or the offset distance could be applied to the y-direction instead of the x-direction.

References

1. D. Rosenthal, "The Theory of Moving Sources of Heat and Its Application to Metal Treatments," *Transactions of the A.S.M.E.*, Vol. 68, pp. 849-866, 1946.
2. A. Vasinota, J. L. Beuth and R. Ong, "Melt Pool Size Control in Thin-Walled and Bulky Parts via Process Maps," in *Solid Freeform Fabrication Proceedings*, Austin, 2001.
3. S. Bontha and N. W. Klingbeil, "Thermal Process Maps for Controlling Microstructure in Laser-Based Solid Freeform Fabrication," in *Solid Freeform Fabrication Proceedings*, Austin, 2003.
4. S. Bontha, N. W. Klingbeil, P. A. Kobry and H. L. Fraser, "Effects of Process Variables and Size-Scale on Solidification Microstructure in Beam-Based Fabrication of Bulky 3-D Structures," *Materials Science and Engineering A*, Vols. 513-514, pp. 311-318, 2009.
5. A. Plotkowski, M. Kirka and S. Babu, "Verification and validation of a rapid heat transfer calculation methodology for transient melt pool solidification conditions in powder bed metal additive manufacturing," *Additive Manufacturing*, Vol. 18, pp. 256-268, 2017.
6. H. Carslaw and J. Jaeger, "The Use of Sources and Sinks in Cases of Variable Temperature," in *Conduction of Heat in Solids*, 2nd ed., Oxford, Oxford University Press, 1959, pp. 255-260.
7. Z. Hou and R. Komanduri, "Magnetic field assisted finishing of ceramics-part 1: thermal model," *Journal of Tribology*, Vol. 120, pp. 645-651, 1998.
8. R. Komanduri and Z. Hou, "Thermal analysis of the arc welding process-part 1. general solutions," *Metallurgical and Materials Transactions*, Vol. 31B, pp. 1353-1370, 2000.
9. R. Komanduri and Z. Hou, "Thermal analysis of the laser surface transformation hardening process," *International Journal of Heat and Mass Transfer*, Vol. 44, pp. 2845-2862, 2001.
10. P. Kobry and S. Semiatin, "Microstructure and texture evolution during solidification processing of Ti-6Al-4V," *Journal of Materials Processing Technology*, Vol. 135, No. 2-3, pp. 330-339, 2003.

Relationships within Ecosystems

Student Researcher: Rachelle E. Everswick

Advisor: Dr. William Jones

Cedarville University
Department of Science and Mathematics

Abstract

This lesson is geared towards high school students in a Biology or Environmental Science class. While learning about ecosystems, the NASA Earth Observatory will be utilized to provide students the opportunity to explore real data from earth. Students will learn about both biotic and abiotic factors within ecosystems. Using the Earth Observatory, students will use the data depicted on global maps to examine net productivity and then compare it with other factors such as rainfall, fire, and surface temperature. They will draw on this data to speculate the relationships between factors and their influence on the net productivity of a given area.

Objectives

By the end of the lesson, students will be able to:

- Analyze real technical data from NASA's Earth Observatory about various factors influencing Earth's physical environment.
- Identify and explain the impact of abiotic factors on vegetation productivity.

Alignment

B.DI.2: Ecosystems

ENV.ES.1: Biosphere
Ecosystems

RST.9-10.7 Translate quantitative or technical information expressed in words in a text into visual form (e.g., a table or chart) and translate information expressed visually or mathematically (e.g., in an equation) into words.

WHST.9-10.4 Produce clear and coherent writing in which the development, organization, and style are appropriate to task, purpose, and audience.

Methodology

Initially, the concept of connections between biotic and abiotic factors will be introduced to connect previous discussion of ecosystems to the current lesson.

To begin the activity, students will survey NASA's Earth Observatory and will look at the global vegetation map. Next, they will familiarize themselves with the global map of net productivity of vegetation, watching the animation move through the years and reading the supplemental information provided. The net primary productivity will represent our biotic feature that we are using to draw relationships to with multiple non-living factors. As they continue the activity, students will complete a worksheet, noting and explaining the trends they notice and the data supporting their observation.

Using the compare feature, students will first compare net primary productivity to land surface temperature. They will identify the relationship between temperature and productivity, filling out their worksheet with a brief explanation of how they reached this conclusion. Next, this comparison process will be repeated with net productivity and total rainfall, again recording the trend they noticed. Students

will then choose from natural abiotic factors which include snow cover, cloud fraction, and water vapor. With the chosen feature, students will continue to compare and describe the relationship between it and the primary productivity. Finally, students will explore the relationship of an anthropogenic factor, such as aerosol density, to the net productivity, to determine how they correlate.

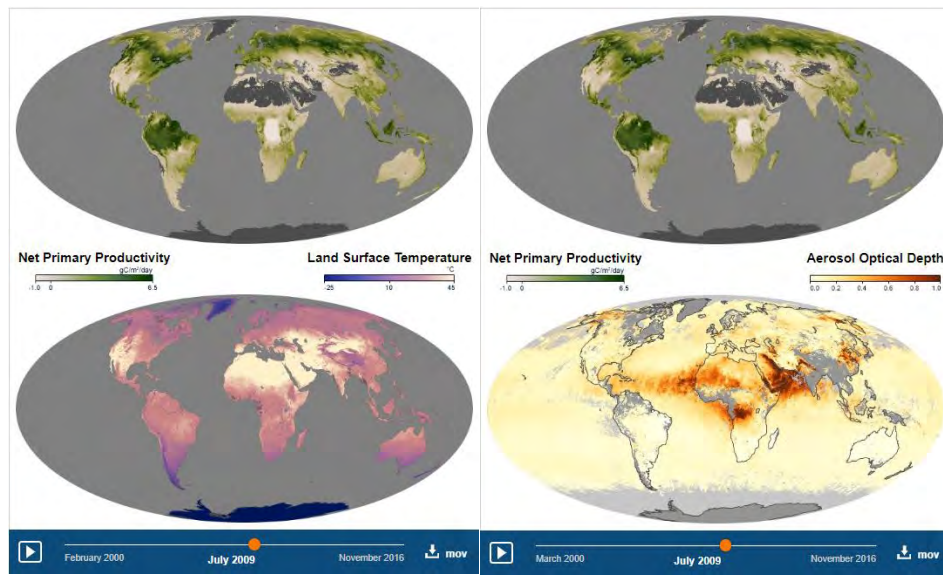


Figure 1. Net Primary Productivity compared to Surface Temperature and Aerosol Density.

This lesson activity takes more of a student-centered constructivist approach in which the students actively build their knowledge. The teacher takes on the role of a facilitator, providing only the framework for the activity and additional help as needed to guide the students through the learning process. Meanwhile, the students take an active role in learning process as they make connections between the various factors through the analysis of the maps.

Assessment and Results

Throughout the class period, the teacher will carry out an informal formative assessment by having conversations with the students and checking on how their work is going. The worksheet completed during the activity will be graded to assess if the student correctly identified the relationship trends and supported the conclusion. If students correctly identify relationships between the productivity and abiotic factors, the teacher will move on with the ecosystem unit. If not, the topic can be presented and taught in a different format.

Conclusion

This lesson activity allows students to use actual data from earth to draw conclusions from. This activity will help reinforce the correlation between abiotic and biotic factors. Using this activity will lead to further ecosystem studies, such as identifying biomes and latitudinal impacts on vegetation. Population studies would be an interesting extension of this lesson.

Thermal Investigation of sUAS Motors Under Varying Power Conditions

Student Researcher: Adam J. Fertig

Advisor: Dr. Blake Stringer

Kent State University
College of Aeronautics and Engineering

Abstract

This research consisted of measuring the thermal properties of various small UAS motors. While an unmanned aerial vehicle (UAV) motor is running the airflow created by the motor-propeller combination is generally able to cool the motor, keeping the motor temperature under control. Once the motor is shut off the airflow created by the motor-propeller is removed, and the temperature of the motor spikes to high and sometimes unsafe temperatures. Landing a UAV is a high power condition, and common practice is to shut the motors down upon landing to prevent rollover. As UAV are continuing to increase in size this means the size of the motor-propeller configurations will continue to increase along with power consumption.

Introduction

Small unmanned aerial systems (sUAS) are a rapidly growing part of the aeronautics field. sUAS are commonly known as drones, and they are 0.55 lbs to 55 lbs in weight, generally with a multi-propeller propulsion system. The applications of these small aircraft fulfill mainly needs, and new uses are being found as the technology continues to advance. They can be used to film movie scenes, analyze crops, inspect rooftops, deliver packages, conduct search and rescue missions, and many more applications.

The drone market is expected to grow from \$14.1 billion in 2018 to \$43 billion by 2024, along with drone sales tripling in the same time frame¹. The hobby market will continue to grow, but the commercial market will lead the advancements in the field. The size of these systems are being pushed to the limits, with strides being made towards air taxis, growing the field of urban air mobility (UAM).

As drones continue to increase in popularity and size, the efficiency of the motors have to be analyzed. One aspect is their thermal properties. Being able to keep a motor cool is very important to the safety of the flight, ensuring the motor does not overheat in mid-air. The objective of the research was to determine the relationship between power and temperature, along with heating and cooling time equations.

Background

During the research, tests were completed on various sized motor-propeller combinations measuring their temperatures while running at high power conditions then immediately shutting down the motor. All of the tests were conducted on Kent State's electric Vertical Take-Off and Landing (eVTOL) Propulsion Test Stand. It investigated the relationships between the size of the motor, temperature, and cooling time; along with finding a function to predict the cooling time from peak temperature. Additionally, ways of cooling the motor were investigated to reduce thermal spikes upon shut down. One option investigated was to return the motor to 20% throttle to self-cool the motor before shutting down, while another cooling method involved developing a new motor housing to test if static pressure was a contributing factor.

Methodology

The research of this project was done using KSU's eVTOL Propulsion Test Stand. Various motors and propeller combinations were tested using several different test scripts. The test scripts were written in JavaScript code to control the experiments and hold variables constant throughout the tests. The test parameters varied in order to test thermal conditions of different operating conditions.

The Propulsion Test Stand is a commercial-off-the-shelf system manufactured by RC Benchmark, it is the Series 1780 Thrust Stand and Dynamometer V1, and can be seen in Image 1. The stand is contained in a plywood constructed frame, with steel plates surrounding the area in the propeller path to protect the operator. The power is supplied using between one and five 12.0 V automotive batteries connected in series, providing over 60.0 V. The sensors can measure multiple variables including: electronic speed controller (ESC) setting, thrust, torque, rotational speed, electric power in, mechanical power out, temperature of probes. The specifications for the Propulsion Test Stand can be found in Table 1.

During the tests several different motors and a couple different propellers were used. One type of ESC was used to run all of the experiments to keep consistency between tests. This ESC was the KDE-Direct UAS125UVC-HE, which has a maximum voltage of 60.9 V, maximum current of 125.0 A, resulting in a maximum power of 6485.0 W. Some trials were ran using a motor without a propeller to gauge a baseline operating condition for the motors. Table 2 shows the motors that were available throughout the research. Table 3 showing the propellers that were available.

Results

There were three main aspects this research investigated, "thermal runaway", "self-cooling", and heating and cooling slope equations. "Thermal runaway" occurs at high power settings when a motor's temperature increases rapidly. This is unsafe, because if a motor was in flight while this occurred the motor could potentially shut down causing a crash. The 7215XF motor displayed this condition repeatedly. "Self-cooling" was another idea investigated. Since the motors get hot after shut down, the idea was to put the motor on a low power setting before shutting down. This theory proved to work and reduce the temperature that a motor would heat to. Lastly the heating and cooling slope equations were investigated. Results showed that the slopes are constant for each motor.

Images, Tables, and Charts

All graphs were created in JupyterLab using Bokeh software.



Image 1: Set up of Kent State University's eVTOL Propulsion Test Stand.



Image 2: Comparison of motor sizes (left to right: RotoMax, 10218XF, P80, 7215XF, U7).



Image 3: Overexposed photograph showing charred coils (top) verses normal coils (bottom) of the 7215XF motor.

Table 1. KSU eVTOL Propulsion Test Stand limits.

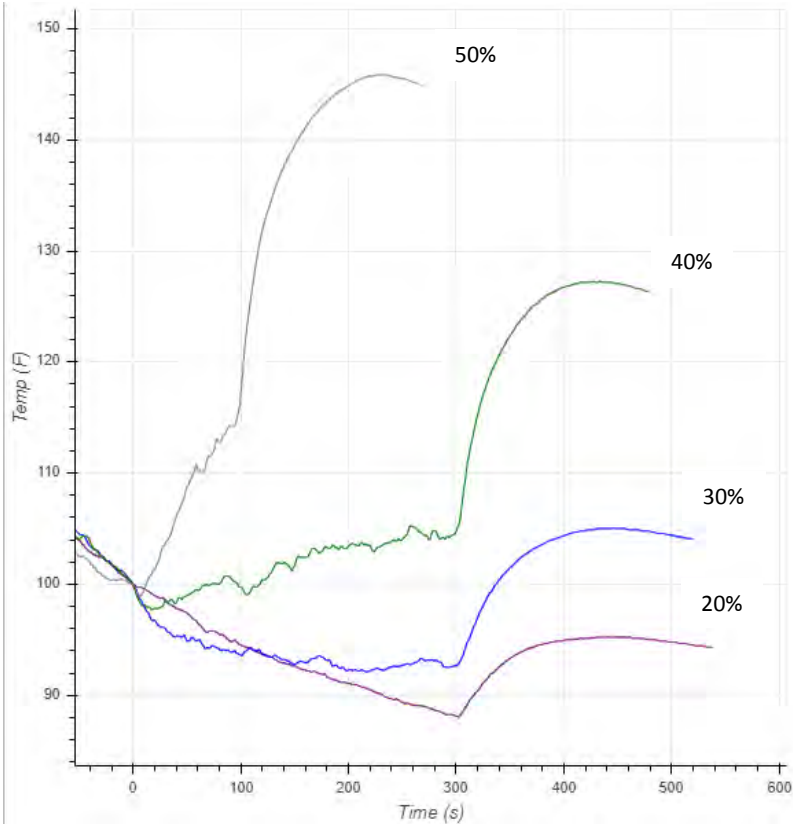
Variable	Maximum
Voltage	60 V
Current	100 A
Speed	190,000 rpm
Thrust	± 44 lbf
Torque	± 7.39 ft-lbf
Power	6.0 kW

Table 2. Shows available motor specifications.

Brand	Motor	Kv Rating	Max V	Max A	Max W
KDE Direct	4215XF	465	26.1	62	1375
KDE Direct	5215XF	220	34.8	72	1595
KDE Direct	7215XF	135	60.9	85	4405
KDE Direct	10218XF	105	60.9	142	7355
T-Motor	U7	490	26.1	62	1375
T-Motor	U13	100	44.4	65	3120
T-Motor	P80	120	44.4	60	2800
T-Motor	F1000	510	29.6	125	4000
Turnigy	RotoMax	150	52.0	190	9800

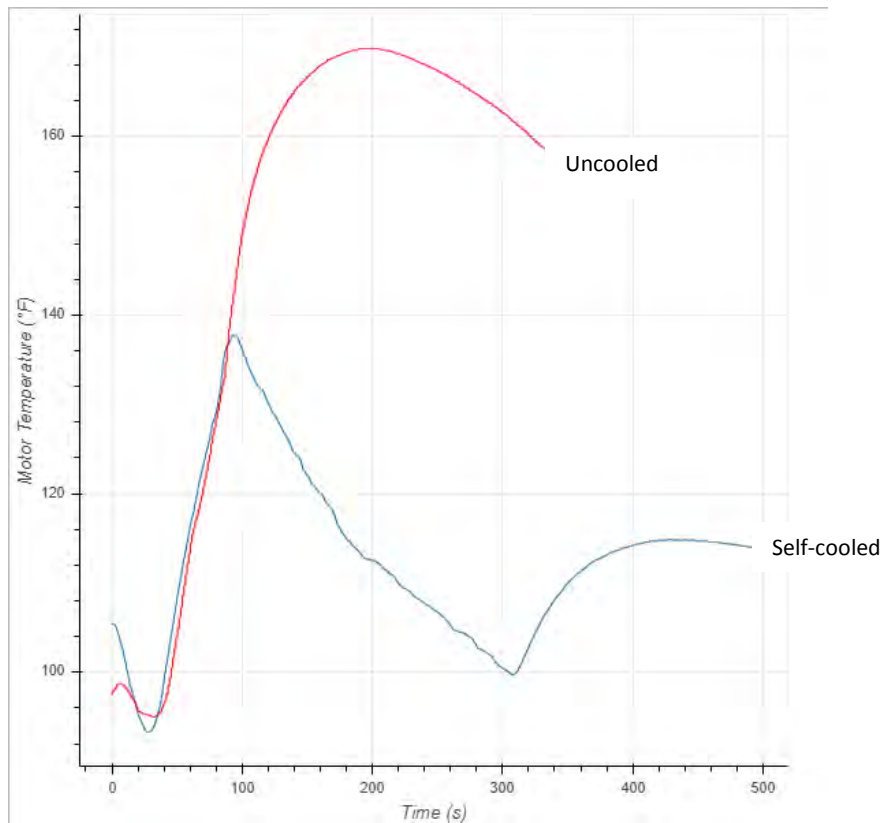
Table 3. Shows available propeller specifications.

Brand	Propeller	Blades	Diameter	Pitch	Solidity
Falcon	27x8.8	2	27	8.8	0.0844
KDE Direct	30.5x9.7	3	30.5	9.7	0.1190
T-Motor	15x5	2	15	5	0.0857



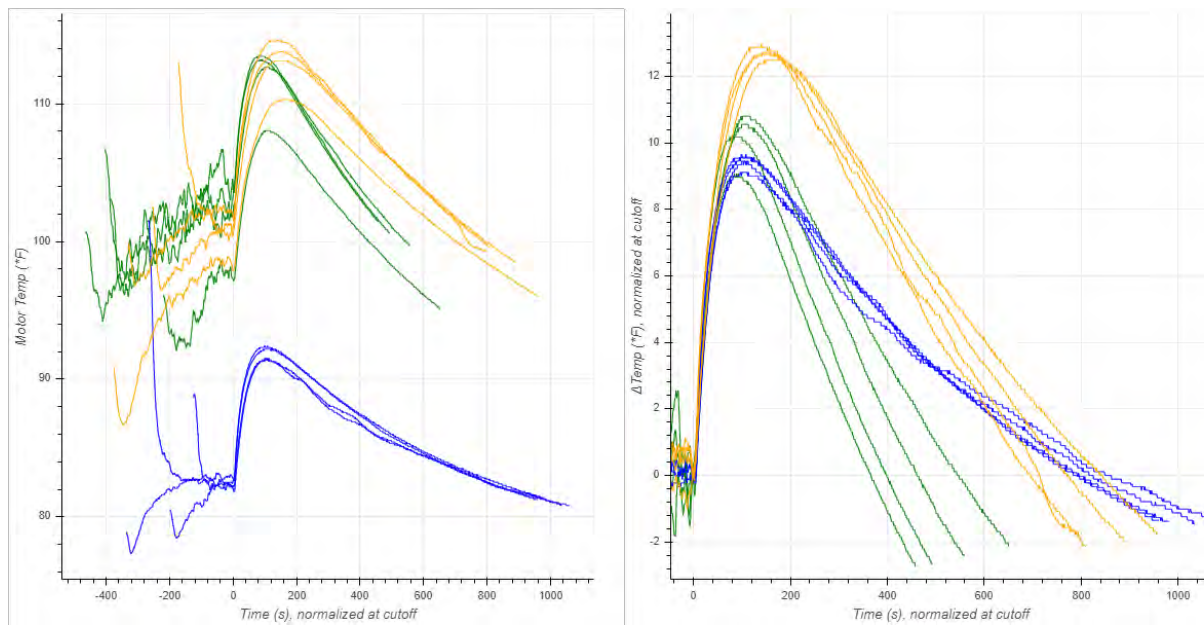
Graph 1: Shows temperature verse time of the 7215XF motor displaying “thermal runaway”.

After the 7215XF displayed “thermal runaway”, the motor was replaced and further testing was conducted. The testing showed the relationship between power and temperature. As power setting increased, the temperature increase post shut-down increased. As seen in Graph 1, the temperature spiked to higher levels. The test was stopped at 50% due to the predicted possibility of “thermal runaway” at higher throttle settings.



Graph 2: Shows the difference of the 7215XF motor being “self-cool” vs uncooled.

After seeing the effects of immediate shut-down of the motor, which is conventional practice after landing, cooling methods were investigated. One idea that was to apply 20% throttle to provide cooling over the motor at a low power setting. The test proved that the motor followed the same heating slope then the 20% throttle was applied, the cooling began immediately. Once it was cooled to 100°F the motor was shut off. This proved that the thermal heating of the motor could be mitigated using a “self-cooling” method.



Graphs 3 & 4: Shows two different views of the cooling slope of three motors (blue- P80, green- 7215XF, orange- 10218XF).

Three motors underwent the same test where they were ran until equilibrium condition then were powered off. The motor then heated up and eventually cooled on its own. Each test on the motors was repeated 4 times. All of the slopes recorded were very similar for each motor, which leads to the theory that the heating and cooling slopes of the motors are consistent amongst the same motor.

Unexpected Results

There was one motor in particular that provided results different than expected, and the research changed after this find to investigate more. The KDE Direct 7215XF motor showed extreme signs of what was considered “thermal runaway”, which is when the motor heats up very quickly to a high temperature. When this motor was ran, sometimes not even close to the maximum specifications, and shut down the temperature spiked to an unsafe level and continued to rise. In some instances it would smoke and char the coils. This can be seen in Image 3. The coils on the 7215XF motor became charred after displaying signs on “thermal runaway”. During a test, the motor heated up to temperatures exceeding 180°F and the motor began to smoke. The motor was cooled using a fan.

Another unexpected result was when the ESC caught fire. During a test, where a motor was being ran with 85-90 amps, under the limit of the ESC, the ESC caught fire. It was immediately put out using a fire extinguisher. After investigating, it is predicted that the solder in the ESC melted causing a short.

Conclusion

SUAS are advancing in many ways. As these systems continue to push the limits and grow in size, one thing to consider are the thermal properties of the motors. This research project has yielded many results and a deeper look into the relationship between power, time and temperature.

Moving forward with the research, the slope equations of the heating and cooling of the motors should be investigated more to figure out if there is a relationship between motor size, power and the

equation. The data shows that there is constant results for each motor. The actually equation should be found and then tested if it can predict temperatures based on motor size and power. Also design work and initial testing was started on a custom motor head for the 7215XF that would provide additional cooling compared to the factory head was started before the global pandemic caused by coronavirus halted test. This design work and manufacturing of the custom head should be completed when possible, and the thermal testing of the custom head should be compared to the results with the factory head.

Acknowledgments

There are several people that I owe my thanks to. First, I would like to thank my research advisor, Dr. Blake Stringer, for being a guide to me for the past five semesters on not only this project but also my work on a project entitled: "Improving Vertical Axis Wind Turbine Feasibility". Secondly, I would like to express my thanks to Professor Trent True for always being willing to help with any manufacturing needs of this project, and allowing me to use his machine shop and tools in order to remove a motor head and begin designing a new head. Thirdly, I owe a great deal of thanks to my research partner and graduate assistant, Alex Gajowski, for further developing the software and hardware of this project, and also conducting countless tests for this project. Without Gajowski this project would not be what it is, especially in terms of numerical analysis and graphical representations. And lastly, I owe a thank you to the College of Aeronautics and Engineering at Kent State University for housing and funding this cutting edge research project that has been going on in numerous different stages for the last four years.

In addition, I owe a very large deal of appreciation to OSGC for granting me the Undergraduate STEM Scholarship.

References

1. L. Schroth, H. Bodecker, and M. Radovic, "The Drone Market Report 2019: The Commercial Drone Market Size and Forecast 2019-2024," DRONEII, Mar. 2019.

HAAS Stimulator

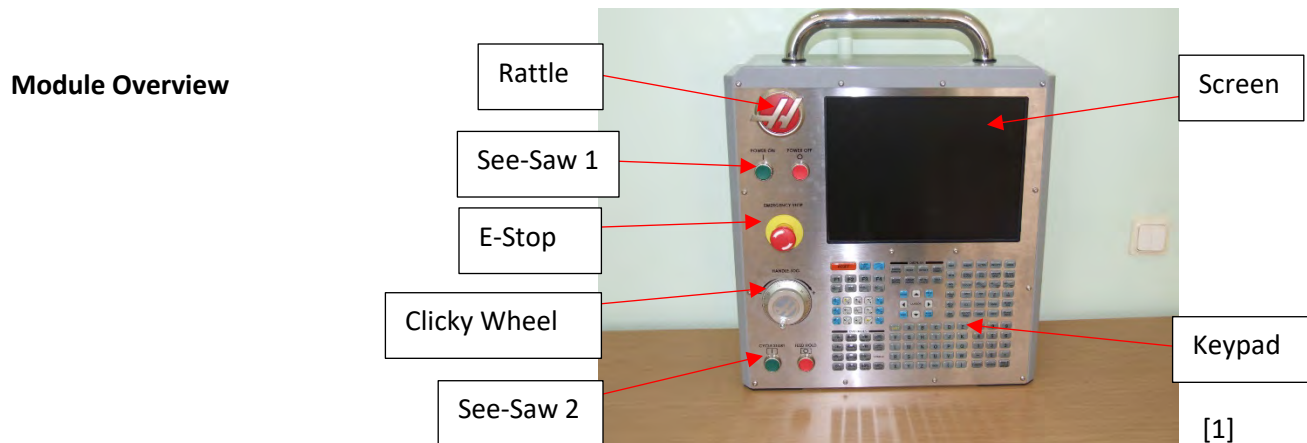
Student Researcher: Ethan Fitter

Advisor: Professor Abigail Yee

Cincinnati State Technical and Community College
Mechanical Engineering Technology

Abstract

Toys are everywhere! Buy Buy Baby, Target, Pottery Barn Kids, (formerly) Toys "R" Us. These are all designed to help children learn and grow physically and mentally, but very few of them are realistic. HAAS is one of the big names in CNC, but their toy department is lacking. In order to help them grow a STEM following from a young age, they need a toy fashioned to look like one of their simulators. There could be colorful pictures accompanied by G-Code that accurately represents the picture, and all of the controls can be converted into entertaining fidget toys. Parents could use it as a fun, educational way to teach, and their children would come to appreciate it later in life as they learn.



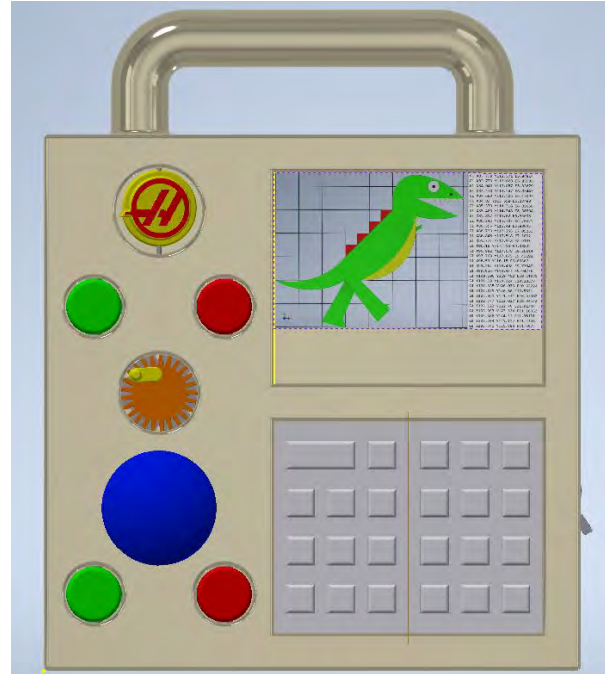
There are several components on the HAAS Simulator that needed to be recreated as toys in order to make it toyetic, including some that need little translation. The clicky wheel, wheel used to move the axes and make selections, can be spun endlessly in either direction and makes many crisp click sounds throughout one rotation. It is built with function in mind but is a perfect fidget toy nonetheless. The only change needed is to make it harder to turn to help build muscles while still being fun. Similarly, the emergency stop (E-Stop) button also needs little change. The concept of a button that, once depressed, needs to be turned for release is already one that sparks curiosity and discovery.

The cycle stop/ cycle start and on/ off buttons needed a little bit more creativity. They are both sets of states that cannot both be true at the same time, so it makes the most sense for them to be represented as see-saws. For the logo, which has no use on the machine other than branding, a spinning rattle was selected.

The focal point of the device is the keyboard and screen. The planned keyboard redesign will portray the numbers and a majority of the letters needed for coding: F, G, I, J, M, S, T, X, Y, and Z. The screen will be a scrolling image of a dinosaur with an accurate depiction of the G-Code used next to it, and it would be activated by pressing anywhere on the keyboard.

Prototyping

All prototypes were printed using a Prusa i3 MK3S printer and modeled in Inventor 2020. They were primarily made of PLA; the most notable deviation was for parts that needed flexibility, which were made using Nylon.



Conclusion

The HAAS simulator can be created into something toyetic, especially if it gets a redesigned exterior by a graphic designer. Moving forward, there need to be many redesigns specifically to meet ASTM F963-17 Standard Consumer Safety Specification on Toy Safety [2]. Paling in comparison to that would be the necessity to make a licensing deal with HAAS and having it tested by actual children.

References

1. "HAAS Simulator." *Use Science*, 8 Feb. 2018, <https://scienceservices.eu/id/item/5129/haas-simulator.html>. Picture.
2. "ASTM F963-17 Standard Consumer Safety Specification on Toy Safety." *ASTM International*, <https://www.astm.org/Standards/F963.htm?A>

Solar Shadow

Student Researcher: Kirshaun D Francis

Advisor: Dr. Saleh Almestiri

Central State University
Manufacturing Engineering Department

Abstract

This project aims to track the sun using a single-axis system which consists of rotation about the z-axis. The overall objective of this project is to optimize the performance of solar panels by collecting as much incident light as possible. By designing a solar tracking device that rotates on one axis, eastward to westward, solar panels will be able collect more incident light and thus collecting more energy. The principle idea of the project is to place a solar panel on a rotational base. This base is moved by gear driven by a worm shaft located beneath the device. The direction of rotation is determined by photocell receptors that are mounted on top of the solar panel. The motor is able to communicate with the photocells through the Arduino board and the motor's direction of rotation can successfully be determined based on which side the light is coming from. The operation was tested, but the device was not fully assembled. Due to the pandemic Covid-19, the campus had to be evacuated.

Statement of Purpose

The purpose of this project is to maximize the energy captured from the sun using a solar panel, by designing a device that will allow the panel to be constantly hit by direct sunlight. In the event that this device makes a difference as little as 20 percent, this device will be noted to have fulfilled its first purpose. Finally, a visibility study can be done to compare the results of this tracker with a stationary tracker under identical conditions. Stationary panels have a longer blind spot duration, meaning when the sun is out of the panel's sight, the amount of energy captured decreases. The proposed device will be able to eliminate these blind spots and ensure a direct incident light on the solar panel for maximum output. This in return minimizes the required surface area of solar panels to meet a specified demand.

Design Approach

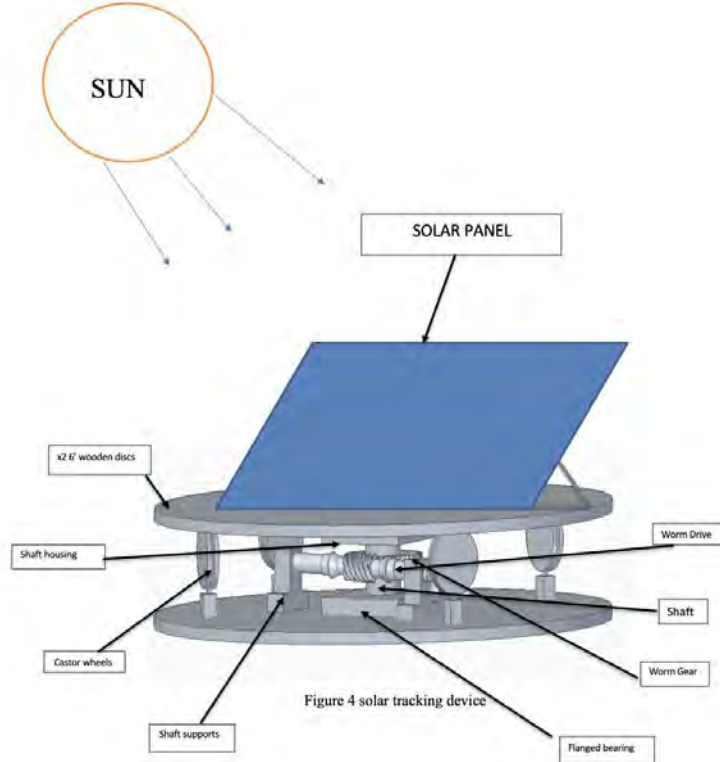
Because this platform is intended to rotate in both directions, I needed to learn about platforms that are able to rotate in both directions. From there, I discovered the rack and pinion method. The rack and pinion method is a method of turning about an axis or in other words, *torque*. I also realized that I needed to move the rack and keep the pinion fixed to the central axis instead of vice versa to produce a multi-direction rotational effect. I did further research until I stumbled across linear actuators. Linear actuators were actually a good idea because they are bipolar and they are compatible with photosensors, since these are the primary sensors for my device. I spoke to my advisor, and he suggested that I try worm shafts and gears. With these gears, you can create a rotation that is high in torque created by the slow-moving stepper motor. The platform is engineered to respond to photocell receptors which will then communicate with an Arduino development board. For instance, when the photocells are shaded and do not detect sunlight, it will then tell the Arduino board to start the stepper motor that drives a worm shaft into a gear connected to the shaft. The easy rotation comes from 1 of 2 in-hub bearings located on the lower half of the wooden platform.

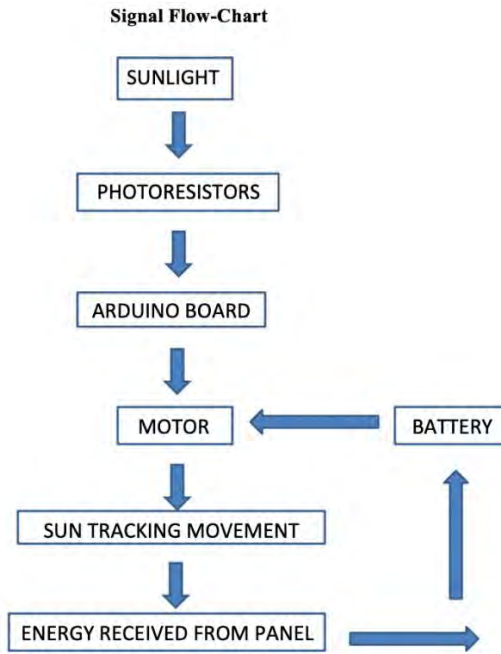
The second design concept was a pulley system that would utilize a pulley belt instead. The pulley would have been easier to build, since it would have required fewer mechanical applications. The setup would

have the motor alongside the machine, instead of underneath the machine. This design concept, however would have some issues along with its ease of built. Firstly, there would have been a lot of “free-play” with the motor, meaning that it would be easy to move the motor or machine with slight disturbances; these disturbances would include natural forces like wind, or unintentional forces like touch the machine. The worm gear design is ideal for this problem, for it is impossible for the motor to be moved by the device because of the structural design. The second issue with the pulley design is the fast deterioration of the belt. Because this device is intended to be used in places with hot climates, it is highly likely that the deterioration rate will increase because of the constant heat attacking it. Eventually, it will become dry and brittle, resulting in the need of a new belt. This would then become a constant problem as well.

A decision was made on the design concept. The worm gear design, in my opinion, is more ergonomic, for the motor has a built-in platform for which it can sit on. The design is neat and compact and all components are centralized in one area. This makes it easier for transportation. Now, numerous calculations must be made. A *weight* limit has to be determined to tell us how much weight and force it can withstand. To determine the withstanding weight, a MatLab code was written to help me with this. This is far easier than obtaining multiple size weights and testing each of them experimentally. Calculations were also needed for the *reaction* on both the wheels and the bearings, the *torque* acting on the worm gear and the worm drive, the *power* needed to drive the maximum weight being withheld by this platform, the *size* motor needed to produce this power to drive this weight and the *coefficient of friction* on the wheels. To determine the reactions of the wheels, I must know the force acting upon the board from the wheel, and the force acting down on the wheel from the board. Calculating the reactions include free body diagrams of the wheel by itself and the board by itself. To compute bearing loads, the forces which act on the shaft being supported by the bearing must be determined.

Figures/Charts





Unfortunately, I was unable to experiment and test the device due to the Covid-19 Pandemic. But it is in my intentions to continue doing so as soon as possible. The pandemic drove me away from my project and forced me back to my home country, The Bahamas.

Acknowledgments

First and foremost, I would like to thank God for giving me the strength and patience to get through this. This has not been an easy journey thus far with the included intervening circumstances and temporal constraints. My mother who has been keeping both me and herself strong despite the devastation which occurred to our home. My father for keeping me financially afloat at times when they were most detrimental.

I also express great gratitude towards my Engineering Professors, for they have been guiding and helping me into a smooth transition into the world after school. I would also like to thank Central State University for the educational-filled four-year experience, for I have learnt far more than I would have had I not attend the school. The entire staff and faculty of Central State University have shown nothing but love and motivation towards me during my entire duration of attending this wonderful university. I would finally like to thank NASA and the Ohio space grant opportunity for allowing me to get hands-on experience with a purpose.

References

1. Bashar Hammad, A.-S. M.-A.-G. (2017). Performance and economic comparison of fixed and tracking photovoltaic systems in Jordan. *Science Direct*, 827-839.
2. Christian Breyer, D. B. (2017, March). Retrieved from Wiley Online Library: <https://onlinelibrary.wiley.com/doi/full/10.1002/pip.2885>
3. Dub, J., & Gang Yang, S. G. (2014). A multipurpose dual-axis solar tracker with two tracking strategies. *Science Direct*, 88-98.
4. Fathabadi, H. (2016). Comparative study between two novel sensorless and sensor-based dual-axis solar trackers. *Science Direct*, 67-76.

5. M. H. M.Sidek, N. W. (2017). Automated positioning dual-axis solar tracking system with precision elevation and azimuth angle control. *Science Direct*, 160-170.
6. Masoumeh Abdollahpour, M. R. (2018). Development of a machine vision dual-axis solar tracking system. *Science Direct*, 136-143.
7. Vijayan Sumathi, R. A. (2017). Solar tracking methods to maximize PV system output – A review of the methods adopted in the recent decade. *Science Direct*, 130-138.
8. Yasser M.Safan, S. M.-S. (2018). Performance evaluation of a multi-degree of freedom hybrid controlled dual-axis solar tracking system. *Science Direct*, 576-585.

Study of Atomization Behaviors of Liquid Monopropellants in Pintle Injectors

Student Researcher: Jacob O. Gamertsfelder

Advisor: Dr. Prashant Khare

University of Cincinnati
Department of Aerospace Engineering

Introduction

The ability to accurately predict multi-phase, multi-scale, multi-physics processes in combustion systems, including gas-turbine, diesel, torpedo and rocket engines is critical to the development of future propulsion systems. Spray atomization characteristics are especially important for combustors using monopropellant fuels because the system performance is conditioned by the propellant droplet size distributions, and is the rate-controlling process [1, 2]. Evaporation of monopropellant and the ensuing combustion are accelerated if the droplet size is smaller, so any atomization process leading to a reduction in drop size is of prime importance in combustor design. Many injectors, such as swirling, pintle, jet impingement, and air-blast atomization are used for this purpose in contemporary liquid-fueled combustion devices. Among these, pintle injectors, also known as variable area injectors have been widely used in diesel, rocket and torpedo engines, most famous among which is the Apollo Lunar Module Descent Engine [3], because of enhanced throttling ability that these injectors provide and their design simplicity [4].

Figure 1 shows a schematic diagram of a centrally located single element pintle injector for monopropellant engines. It consists of an annulus through which the fuel is injected radially into the chamber. In bi-propellant pintle injectors, the oxidizer is often injected through the annulus and the fuel is injected coaxially such that it impinges on the radially emanating oxidizer stream [3, 4]. By moving the pintle thrust can be modulated; the maximum thrust being achieved when the injection orifice is fully open (as shown in Figure 1). As the pintle moves away from the chamber (towards left in Figure 1), injection area reduces leading to lower thrust. Reduction in injection area leads to higher injection velocities, leading to good atomization and ensuing combustion characteristics even at lower thrust conditions.

Although tremendous progress has been made in the last decade to model multiphase flows relevant to pintle injector based configurations [5-7], especially for bi-propellant pintle injectors, prediction and control of spray statistics in realistic chemically reacting configurations (e.g., relevant pressures, Weber and Reynolds numbers) remains an outstanding challenge, not only in industrial/military applications, but even in fundamental scientific endeavors. With respect to monopropellant spray and atomization processes using pintle-injectors, to the best of our knowledge, no comprehensive theories or computational models have been established to analyze and optimize the spray behaviors at relevant design and off-design operating conditions. This situation is further exasperated when the monopropellant fuel is highly viscous; for such fuels, no study in the past has addressed the detailed multiphase flowfield and the associated atomization characteristics at chamber operating conditions, especially for low thrust injection conditions. One of the major challenges arises from the widely disparate length and time scales, and the associated difficulties in resolving local interfacial phenomena (e.g., instabilities, and pinch-off) that dictate the global behaviors. Much of the existing understanding and many of the design tools for liquid fuel injection, atomization and spray for pintle injector based monopropellants engines are, thus, empirically based and established through time-consuming and

costly processes of trial and error. There is, therefore, an urgent need to enhance the fundamental understanding of liquid atomization process and subsequent spray behaviors, and develop predictive models that can be used for efficient design and control of characteristics, such as droplet sizes for monopropellant propulsion engines. Fortunately, recent advances in hardware technologies and numerical methodologies capable of accurately resolving liquid/gas interfaces [8-13] have made it possible to investigate the detailed spray and flow dynamic phenomena, such as, those exhibited in monopropellant pintle injectors, with realistic turnaround times. Therefore, in this research effort, we address the atomization characteristics of a viscous (4.63 times that of water) monopropellant, Otto Fuel II [14, 15] at engine relevant pressures to establish the fundamental physics underlying the atomization and spray behaviors when the orifice is fully open using a volume of fluid based direct numerical simulation methodology developed by P  pinet [13].

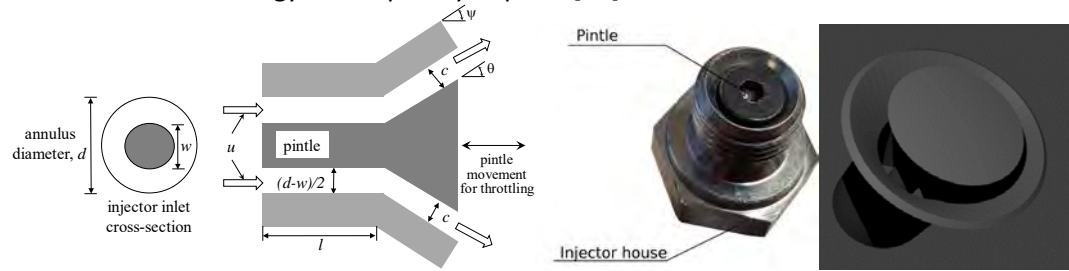


Figure 1. Schematic of the geometry for a monopropellant pintle injector with annulus diameter d , pintle width w , clearance c , and nozzle length l . Monopropellant fuel enters the annulus with a velocity, u . on the middle right is the pintle used in the experimental validation is shown. On the far right there is a 3D rendering of the solid model used in the simulations for comparison.

Technical Approach

The current research poses two stringent challenges that need to be addressed to quantitatively identify the underlying physical processes present when a monopropellant fuel is injected through a pintle valve in the combustion chamber. The major processes are: (1) the presence of multiple phases and frequent interfacial topology changes, and (2) the existence of widely disparate length and time scales that need to be resolved in an accurate and computationally efficient manner. To accurately address the first issue, the most appropriate approach to investigate the flow physics of interest with high-fidelity, is based on Eulerian-Eulerian framework, that is, all relevant phases (liquid and gaseous) being treated as continuous, and the interface between them is captured. This approach is also called the one-fluid approach in the literature [13]. To appropriately resolve the wide range of spatial and temporal scales, an adaptive mesh refinement is adopted such that high-resolution is achieved in a reasonable turnaround time. In addition, to isolate the hydrodynamic mechanisms, all numerical simulations will be conducted at non-vaporizing temperature conditions.

Physical Processes Underlying Otto Fuel II Atomization and Spray Formation

Otto Fuel II is a mixture of 75% 1,2-propylene glycol dinitrate (PGDN), 23% dibutyl sebacate (DBS) and 2% 2-nitrodiphenylamine. The operating conditions consists of a chamber pressure, $p = 106.2$ bar, temperature, $T = 300$ K, and inlet velocity $u = 3.34$ m/s, corresponding to a density ratio of 10, dynamic viscosity ratio of 212, liquid based Reynolds number of 78 and Weber number of 20 (based on gas density). The geometry that is used to investigate the spray and atomization characteristics of this monopropellant is the same as was used for the validation case. It should be noted that Otto Fuel II is 4.6 times as viscous as water.

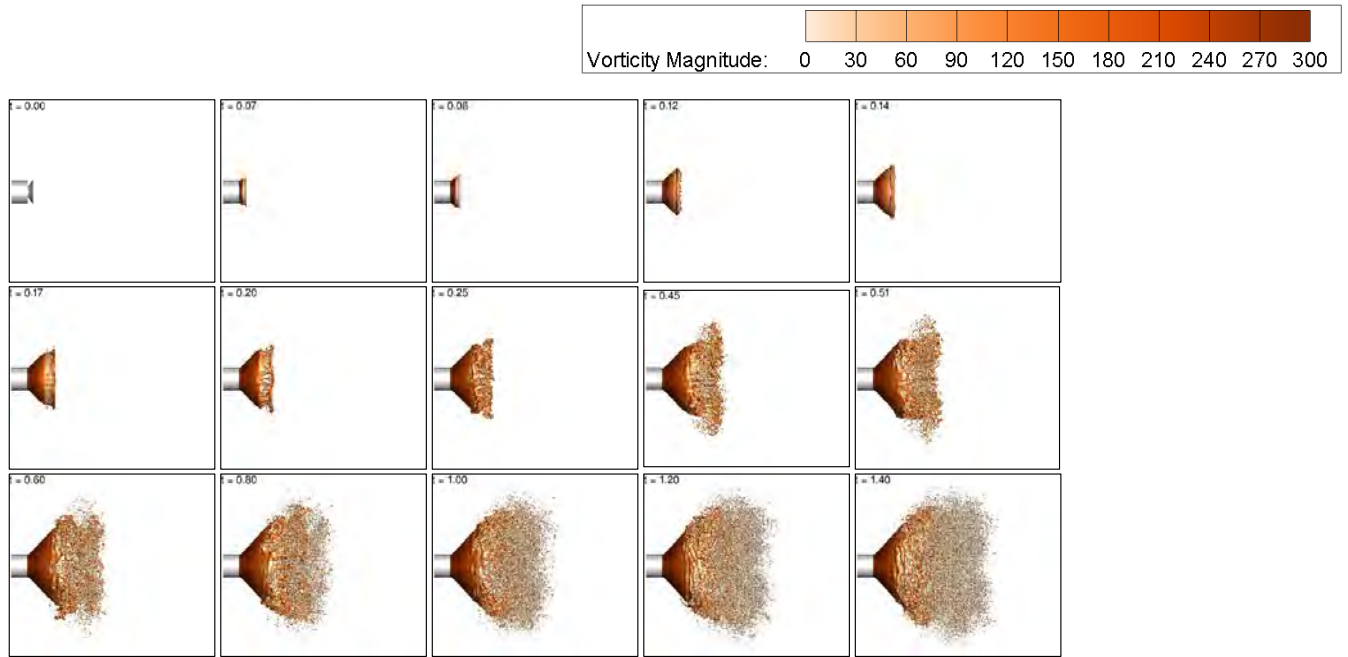


Figure 6. Time evolution of Otto Fuel II spray as it is injected from a pintle injector.
The figures show iso-contours of the Void.

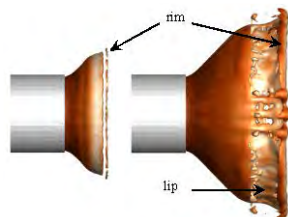


Figure 8. Zoomed in picture showing the formation of the lip, its extension and the rim.

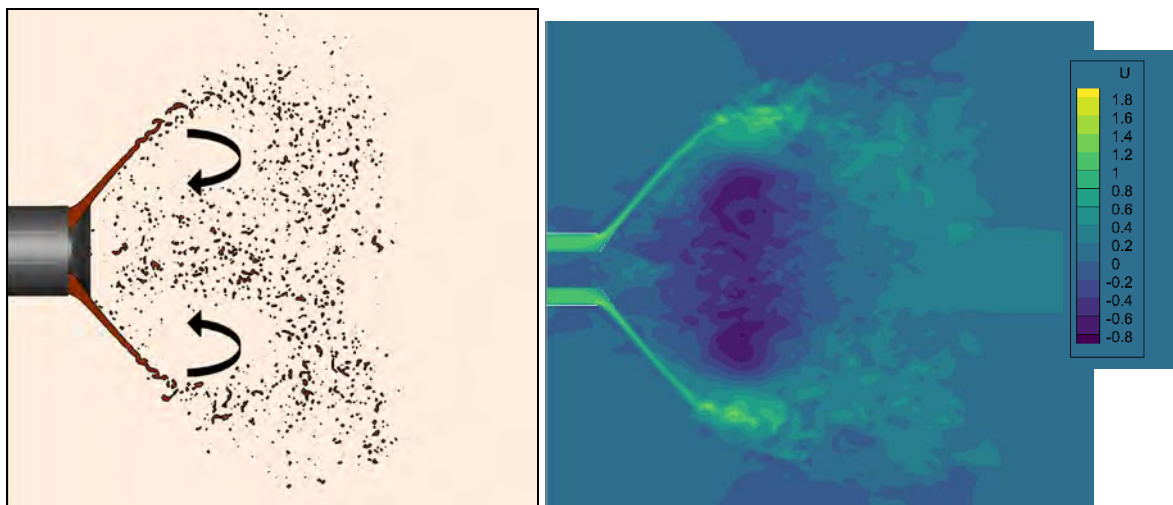


Figure 9: Center plane of the spray showing the hollow cone and the symmetric recirculation zones at $t = 1.2$. Center plane of the spray showing the recirculation zones via reverse velocity plot at $t = 1.6$.

Conclusions and Future Work

In this research, the fundamental processes that lead to the breakup and spray formation when a viscous fuel, Otto Fuel II, injected through a pintle injector were investigated. It was found that the atomization physics proceeds in three steps – (1) the initial detachment of the rim; (2) the formation, stretching, detachment and atomization of the lip and a thicker rim; and (3) the interaction of the ligaments and droplets produced from rim breakup with the hollow cone that further amplifies the instabilities that cause the rim formation and breakup. This process recursively takes place and leads to the formation of a dense spray. A strong low-pressure recirculation zone is formed in the hollow cone that consumes products of rim atomization and prevents further expansion of the cone, both in radial and axial directions. Droplet size distribution, both based on number-based probabilities and mass-based, Sauter mean diameters are also analyzed in the current effort. Because of the formation of a strong recirculation zone, the growth rate of the number of droplets reduces due to droplet collision and coalescence. These simulations provide unique insights of the underlying breakup mechanism in the dense region where experiments remain limited, and therefore the results are vital for spray model development. Future work will be focused on identifying the mechanisms underlying the atomization process during throttling. This will be followed by detailed investigations of vaporizing and reacting Otto Fuel II as it is injected in the chamber through the pintle injector.

Acknowledgments

This research was supported by the Ohio Space Grant Consortium (OSGC). The authors would like to acknowledge the Advanced Research Computing (ARC) center at the University of Cincinnati for the computational infrastructure. The authors also thank Dr. Stephane Pópinet for allowing them to use his VOF and AMR algorithms.

References

1. Faeth, G. M., "Dynamics of secondary drop breakup—A rate controlling process in dense sprays," Proc. ILASS-Europe.
2. Berthoumieu, P., Carentz, H., Villedieu, P., and Lavergne, G., 1999, "Contribution to droplet breakup analysis," International Journal of Heat and Fluid Flow, 20, pp. 492-498.
3. Dressler, G., and Bauer, J., 2000, "TRW pintle engine heritage and performance characteristics," 36th AIAA/ASME/SAE/ASEE Joint Propulsion Conference and Exhibit, American Institute of Aeronautics and Astronautics.
4. Casiano, M. J., Hulka, J. R., and Yang, V., 2010, "Liquid-Propellant Rocket Engine Throttling: A Comprehensive Review," Journal of Propulsion and Power, 26(5), pp. 897-923.
5. Sakaki, K., Kakudo, H., Nakaya, S., Tsue, M., Kanai, R., Suzuki, K., Inagawa, T., and Hiraiwa, T., 2016, "Performance Evaluation of Rocket Engine Combustors using Ethanol/Liquid Oxygen Pintle Injector," 52nd AIAA/SAE/ASEE Joint Propulsion Conference.
6. Son, M., Yu, K., Radhakrishnan, K., Shin, B., and Koo, J., 2016, "Verification on spray simulation of a pintle injector for liquid rocket engine," Journal of Thermal Science, 25(1), pp. 90-96.
7. Nardi, R., Perez, V., and Pimenta, A., 2015, "Experiments with Pintle Injector Design and Development," 51st AIAA/SAE/ASEE Joint Propulsion Conference.
8. Bravo, L., Kim, D., Ham, F., Powell, C., and Kastengren, A., 2019, "Effects of fuel viscosity on the primary breakup dynamics of a high-speed liquid jet with comparison to X-ray radiography," Proceedings of the Combustion Institute, 37(3), pp. 3245-3253.
9. [9] Bravo, L., Kim, D., Ham, F., and Su, S., 2018, "COMPUTATIONAL STUDY OF ATOMIZATION AND FUEL DROP SIZE DISTRIBUTIONS IN HIGH-SPEED PRIMARY BREAKUP," 28(4), pp. 321-344.

10. Owkes, M., and Desjardins, O., 2014, "A computational framework for conservative, three-dimensional, unsplit, geometric transport with application to the volume-of-fluid (VOF) method," *Journal of Computational Physics*, 270, pp. 587-612.
11. Wang, S., and Desjardins, O., 2018, "3D numerical study of large-scale two-phase flows with contact lines and application to drop detachment from a horizontal fiber," *International Journal of Multiphase Flow*, 101, pp. 35-46.
12. Gorokhovski, M. a. H. M., 2008, "Modeling Primary Atomization," *Annual Review of Fluid Mechanics*, 40(1), pp. 343--366.
13. Pópinet, S., 2009, "An accurate adaptive solver for surface-tension-driven interfacial flows," *Journal of Computational Physics*, 228, pp. 5838-5866.
14. Gaworski, C., Leahy, H., Bashe, W., Macewen, J., Vernot, E., and Haun, C., 1985, "A One-Year Inhalation Toxicity Study of Otto Fuel 2," University of California, AAMRL-TR-85-071
15. Abadin, H., and Llados, F., 1995, "Toxicological profile for Otto Fuel II and its components," Department of Health and Human Services, Agency for Toxic Substances and Disease Registry, Atlanta, GA.

Removing and Preventing Ocean Microplastics

Student Researcher: Bradley T. Gartner

Advisor: David Stumpf

Lakeland Community College
Mathematics Department

Abstract

As plastic waste grows more abundant, it continues to migrate to the ocean creating microplastics over time. From collected data, it's predicted that approximately "8 million metric tons of plastic enter ocean from land every year" (Ocean Portal). As all this plastic accumulates in the ocean, it begins to degrade into smaller pieces over time from the sun and saltwater. In return, this plastic turns into microplastics which are pieces smaller than 5 mm. These microplastics have become a major problem because of their difficulty to remove and their effect on the marine ecosystem.

Project Objective

This project will focus on using robotics and humans to remove microplastics from the ocean in the most efficient and environmentally friendly way. Another focus this project will emphasize is finding various and creative ways to prevent more plastic waste from reaching the ocean so that new microplastics can never form.

Methodology

In order to combat the increasing amount of microplastics in the ocean, the use both human and robotic solutions will be necessary to clean the ocean. This mission will focus on cleaning up plastics in the garbage patches that formed from ocean currents driven by wind since that is where most plastic accumulates. Using NASA data from hundreds of buoys placed around the world, scientists can determine where the garbage patches are moving to show where people need to go to clean up the affected areas. Using two specialized robots, these machines will use GPS to navigate to the affected areas and begin extracting microplastics from the ocean. The submarine robots contain an underwater vacuum to collect the surrounding microplastics. Once collected, microplastics will be moved to a storage container with a magnetic filter to trap the microplastics while allowing the saltwater to pass through freely. The magnetic filter will be able to collect more microplastics because while in the ocean, they absorb heavy metals. When the container is filled, it can return to the surface to dispose the waste to a larger robot that stores the plastic waste.

As microplastics are being removed from the ocean, there are many other steps that must be taken in order to prevent the creation of new microplastics. While the machines focus on the task of disposing microplastics, humans must work together to remove larger pieces of plastic from the ocean so they cannot be broken down even further. This can be achieved by using teams of sailboats and divers to sweep sections of the ocean to remove any waste too large for the robots to extract. Using sailboats and robots results in a no-emission solution to extract plastic waste.

While removing plastic from the ocean is important, people must also clean up plastic from land to prevent it from ever reaching the ocean. While recycling, beach cleanups, and educating society on cleaning up plastic waste is important, two solutions that will also reduce the amount of plastic waste reaching the ocean significantly are the use of specialized dams and microorganisms.

Using specialized dams to collect plastic from rivers can be a great step in to preventing ocean microplastics. Scientists discovered that, "over a quarter of the plastic waste that goes into the ocean every year likely comes from just ten rivers" (Ocean Portal). Yangtze, for example, is the river that releases the largest amount of plastic waste. Using specialized dams on these rivers that collect floating plastics while allowing marine life to pass through can help stop the creation of microplastics.

Another solution is using a bacteria called *Ideonella sakaiensis*, which contains a specialized enzyme called α/β -hydrolases that is capable of degrading PET plastic. According to Plastics Insight, "More than half of world' synthetic fiber and bottles demand is fulfilled by PET plastics." If this type of bacteria was to be used in a large scale, factory-type setting, humans could biodegrade large amounts of PET plastic in a matter of weeks versus thousands of years.

Interpetation of Results

The use of these machines and sailboats to remove ocean plastic creates an enviromentally friendly solution that uses no greenhouse gasses. This plan can also be very effective since these robots can continually work most of the day to remove large quantites of microplastics. In addition, focusing on cleaning plastic waste that has not reached the ocean yet is just as important which is why the use of dams on polluted rivers can greatly reduce the creation of future microplastics.

References

1. Jambeck, Jenna. "Marine Plastics." *Smithsonian Ocean*, Apr. 2018, ocean.si.edu/conservation/pollution/marine-plastics.
2. Palm, Gottfried J, et al. "Structure of the Plastic-Degrading *Ideonella Sakaiensis* Mhetase Bound to a Substrate." *Nature Communications*, Nature Publishing Group UK, 12 Apr. 2019, www.ncbi.nlm.nih.gov/pmc/articles/PMC6461665/.
3. Patel, Prachi. "Stemming the Plastic Tide: 10 Rivers Contribute Most of the Plastic in the Oceans." *Scientific American*, 1 Feb. 2018, www.scientificamerican.com/article/stemming-the-plastic-tide-10-rivers-contribute-most-of-the-plastic-in-the-oceans/
4. "Polyethylene Terephthalate Production, Price and Market." *Plastics Insight*, www.plasticsinsight.com/resin-intelligence/resin-prices/polyethylene-terephthalate/
5. Weber, Kristianna. "Micro-Plastics Are a Mega Problem for Marine Animals – Here's What We Can Do!" *One Green Planet*, 25 Oct. 2016, www.onegreenplanet.org/environment/microplastics-problem-for-marine-animals/

3D-Printed Electrochemical Cell for *In Situ* Analysis

Student Researcher: Dustin T. Goetz

Advisor: Dr. Vicky Doan-Nguyen

The Ohio State University

Department of Mechanical and Aerospace Engineering

Abstract

Electrochemical storage systems, such as batteries, are essential for mobile systems and for matching the time-varying energy demands of consumers on renewable energy grids. *In situ* analysis allows researchers to observe the electrochemical mechanisms of the components of batteries in real time which can inform the development of next-generation battery materials. Unfortunately, there is no standard cell for holding battery components during *in situ* analyses, which can lead to non-standardized results across labs. Although there are commercial *in situ* cells and individual labs have designed their own *in situ* cells, factors such as cost, experimental conditions, equipment specifications, and lack of quality control have prevented the adaptation of a single *in situ* design. In this study, we leverage advancements in additive manufacturing to create a cell entirely from 3D-printed components and common commercial parts. This "3D-printed *in situ* cell" is inexpensive, can be easily modified to fit various experimental conditions and types of equipment, and can be manufactured in a decentralized fashion with better quality control than cells with machined parts. This novel cell design allows configuration for *ex situ* analysis or *in situ* x-ray diffraction (XRD) spectroscopy. The cell, in its *ex situ* configuration, is capable of holding a nominal open circuit voltage for twenty-four hours with a loss of 8.53%. Via electrical impedance spectroscopy (EIS), it was determined that the cell has an interfacial resistance of \sim 1800 ohms. The cell, in its *in situ* configuration, is capable of holding a nominal open circuit voltage for seven hours with a loss of only 0.86%. This study aims to spawn the development of a series of "3D-printed *in situ* cells" that can be used as standards in labs globally. Further, this set of standard cells will enable a rapid development of next-generation battery materials.

Objective

Over the past decade research into electrical energy storage has grown rapidly¹. Many of these studies seek to explore novel materials and leverage their unique properties. Thus, it is critical to establish structure-property relationships to develop and evaluate the next generation of higher-performing materials. For battery technology, one way to improve the performance evaluation of the electrode and electrolyte materials is through *in situ* analyses which elucidate the materials' structure-property-performance relationships. For example, there is still limited knowledge about ionic diffusion within the electrolyte and at electrode-electrolyte interfaces of solid-state electrolytes². *In situ* x-ray diffraction (XRD) could be used to analyze these electrolytes to garner a further understanding of ionic diffusion at the interfaces.

To conduct *in situ* XRD tests on battery components, the battery stack must be contained in a cell with a window that x-rays can penetrate. Unfortunately, these cells are relatively expensive, with commercial single-use cells costing around \$25 and commercial reusable cells costing up to \$2,000³. These costs have led individual labs to develop their own *in situ* XRD cells^{4,5} or modify, inexpensive coin cells⁶. Because various cells have been developed by different groups, often for unique applications, the electrochemical landscape has been fragmented, with different studies being conducted with different cells⁷. Furthermore, these cells are not commercially available, meaning that groups wanting to use

these cells must individually manufacture them, often involving machining of custom parts. Decentralized manufacturing of cells and modification of commercial cells could lead to low quality control. The lack of a standard cell makes the comparison of results between labs difficult and could inhibit the development of novel electrochemical materials.

Creating a singular cell for XRD *in situ* analysis is a daunting task due to different experimental setups in each lab (different microscopes, sample holders, and X-ray collection modes as well as different reactivity of the battery components being analyzed)⁷. Thus, if a standardized cell design is to be created it should take inspiration from Borkiewicz, et al.'s AMPIX cell and prioritize versatility⁵.

In an effort to standardize *in situ* cells across labs, we designed an *in situ* cell that is constructed entirely from 3D-printed and commercial components. Whereas other *in situ* cell designs have machined parts, recent developments in 3D-printing technologies allows an alternative route of cell design. By downloading CAD files for 3D-printing and ordering common components from vendors, individual labs can assemble and use *in situ* cells that are identical to those in other labs without machining custom parts or paying the high costs for commercial cells. Furthermore, individual labs can make modifications to the CAD files depending on their experimental conditions. These modified CAD files can then be re-uploaded to share with the research community. It is envisioned that there will be an online repository with cell designs uploaded by researchers, each optimized for different experimental conditions. Each cell design will include CAD files, assembly instructions, and links to commercial components. To demonstrate the feasibility of this approach, we created and tested an *in situ* XRD cell that is constructed entirely from 3D-printed and common commercial components.

Methodology

Data was collected from various prototypes developed over the last year and a half. Figure 1 shows the cell architecture and a bill of materials of the current prototype. The cell is for use with XRD in reflection modes (up to 100° reflection angle) and a Li-based battery stack. The cell is designed for observation of the cathode material during cycling. The cell has stainless steel washers (McMaster-Carr 90107A029) on top of the battery stack and a spacer (MTI CR20SPA02) beneath the stack for electrical conductivity. A stainless-steel wave spring (MTI CR20WS-SPR) is beneath the bottom spacer of the stack. The spring is used to maintain pressure in the cell and maintain conductivity between the spacer in the stack and another spacer beneath the spring. These components are housed inside of the 3D-printed cell top and bottom with an O-ring (Grainger 1CRW4) as a seal. There is a hole in the cell top to allow for the X-rays to reach the stack. Stainless-steel shims (McMaster-Carr 8836A11) protrude from slots in the sides of the cell top and bottom. These shims are in contact with the top and bottom washers and act as current collectors that can be used to cycle the cell. A cell window, in our case Kapton (Grainger 15C543), is placed over the hole in the cell top. A 3D-printed cell cover, also with a hole, is positioned on to the window to hold it in place and a gasket (McMaster-Carr 91367A925) is used as a seal. The whole assembly is held together by three bolts (Grainger 2EB77) that run through the 3D-printed components and wingnuts (McMaster-Carr 90866A009) are used to tighten the cell, compressing the spring.

The 3D-printed components were created using stereolithography (SLA) printing. This method is preferable to fusion deposition modeling for our application because parts created through SLA printing generally have higher precision and are impervious to the electrolyte fluid and air. An Anycubic Photon 3D-printer and 405 nm UV resin was used to print the components.

The cell can also be configured solely for *ex situ* use by removing the window, cover, and gasket, using a modified cell top, and replacing the washer with a spacer. Tests were conducted on the cell in both the

ex situ configuration and *in situ* configurations (both configurations shown in Figure 2). A lithium chip was used as the anode and LiCoO₂ was used as the cathode. 60 µL of 1.0 M LiPF₆ in EC/DMC was used as the electrolyte and a polypropylene Celguard was used as the separator. Initially, open circuit voltage (OCV) tests were conducted on both cell configurations. During these tests, the cell was assembled in the glovebox and the open circuit voltage between the two current collectors (shims) was measured over twenty-four hours. Electrochemical Impedance Spectroscopy (EIS) tests were also conducted on the *ex situ* cell configuration to obtain information regarding the interfacial resistance in the cell.

Results

The test results are shown in Figure 3. The cell, in its *ex situ* configuration, was able to hold an open circuit voltage for twenty-four hours with 8.53% loss. The cell, in its *in situ* configuration, was able to hold an open circuit voltage for seven hours with a loss of 0.86%. Furthermore, the cell, in its *ex situ* configuration, was initially shown to have an interfacial resistance of ~2100 ohms through an EIS test. When the bolts were further tightened, the interfacial resistance dropped to ~1800 ohms.

The overall cost to manufacture the cell is \$13.82 which is significantly less than even the single-use commercial XRD cells. 3.0% of the cost was from 3D-printed components (only material cost was considered), 1.6% of the cost was from the window and 95.4% percent of the cost was from standard commercial components. Figure 1 shows a more in-depth break-down of the component costs.

Significance

The ability to hold an open circuit for extended periods of time is a promising preliminary result for the cell. The 8.53% loss in the *ex situ* configuration mostly occurred during the first hours, likely before the cell had stabilized. The interfacial resistance is much higher than other battery cells. As demonstrated by the results from tightening the screws, increasing the pressure applied to the stack would likely further reduce the interfacial resistance, bringing it closer to the values of other battery cells.

The results from this study showed the potential of this design to become the first of a standardized set of “3-D printed *in situ* cells”. Furthermore, the low cost of the cell makes it potentially a viable alternative to commercial *in situ* cells.

Figures



Parts	Quantity	Cost Per Unit	Vendor
Springs	1	\$ 0.60	MTI
Spacers	2	\$ 0.49	MTI
Washers	1	\$ 0.08	McMaster
Bolts	3	\$ 0.03	Grainger
Wing Nuts	3	\$ 0.09	McMaster
Shims	2	\$ 4.49	McMaster
O-rings	1	\$ 0.06	Grainger
Gasket	1	\$ 2.13	McMaster
Bottom	1	\$ 0.18	3D-Printed
Cover	1	\$ 0.10	3D-Printed
Top	1	\$ 0.13	3D-Printed
Window	1	\$ 0.22	Grainger
Total:		\$ 13.82	

Figure 1. (Left) Exploded Diagram of *In Situ* Cell. (Right) Bill of Materials and Cost Analysis



Figure 2. (Left) *In Situ* Configuration of Cell. (Right) *Ex Situ* Configuration of Cell.

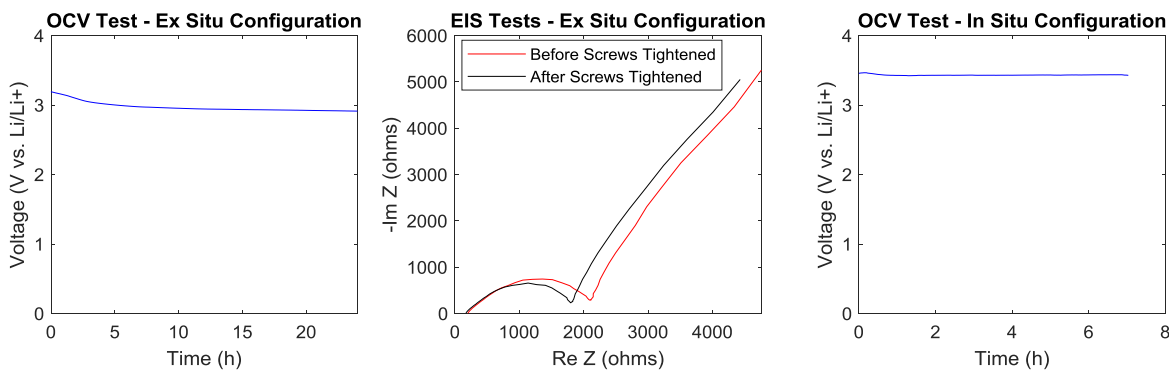


Figure 3. Open Circuit Voltage and Electrochemical Impedance Spectroscopy Tests.

Acknowledgments

The author would like to thank NASA and The Ohio State College of Engineering for scholarship funding for the project. The author would also like to thank Catrina Wilson and Dr. Jerry Gourdin for their advice during the project. Lastly, the author would like to thank Dr. Vicky Doan-Nguyen for her guidance and support throughout the project and throughout his undergraduate career.

References

1. Luo, M. Dooner, and J. Clarke, "Overview of current development in electrical energy storage technologies and the application potential in power system operation," *Applied Energy* (2014)
2. K. Kerman, A. Luntz, V. Viswanathan, Y.-M. Chiang, and Z. Chen, "Review - Practical Challenges Hindering the Development of Solid State Li Ion Batteries," 164, A1731–A1744 (2017).
3. MTI Corporation, "Battery R&D Equipment," (2020).
4. J. Sottmann, V. Pralong, N. Barrier, and C. Martin, "An electrochemical cell for operando bench-top X-ray diffraction," *Journal of Applied Crystallography* 52, 485–490 (2019).
5. O. J. Borkiewicz, B. Shyam, K. M. Wiaderek, C. Kurtz, P. J. Chupas, and K. W. Chapman, "The AMPIX electrochemical cell: a versatile apparatus for in situ X-ray scattering and spectroscopic measurements," *Journal of Applied Crystallography* 45, 1261–1269 (2012).
6. M. N. Richard, "A cell for in situ x-ray diffraction based on coin cell hardware and bellcore plastic electrode technology," *Journal of The Electrochemical Society* 144, 554 (1997).
7. M. Morcrette, Y. Chabre, G. Vaughan, G. Amatucci, J. B. Leriche, S. Patoux, C. Masquelier, and J. M. Tarascon, "In situ x-ray diffraction techniques as a powerful tool to study battery electrode materials," *Electrochimica Acta* 47, 3137 – 3149 (2002).

Combined fNIRS and EEG Probe for Improved TBI Monitoring

Student Researcher: Andrea Gomez Carrillo

Advisor: Dr. Ulas Sunar

Wright State University

Biomedical, Industrial, and Human Factors Engineering

Abstract

There is a need to improve monitoring tools for traumatic brain injury (TBI) patients. Current TBI monitoring techniques are mainly invasive, which put the patient at a higher risk for a second brain injury. These invasive probes are used to measure cerebral blood flow and oxygenation in the brain, imperative to understanding brain activity. Hospitals require a method for real time monitoring of patients without putting them at risk. Continuous-scalp electroencephalography (EEG) and functional near-infrared spectroscopy (fNIRS) offer non-invasive solutions for this real-time brain monitoring. EEG detects electrical activity while fNIRS measures changes in oxygenated and deoxygenated blood, providing crucial neurovascular coupling information needed to assess cerebral activity. This project's goal is to combine EEG electrodes and fNIRS optodes into one wearable device. The device will display the signal of each technique on separate graphs for convenience. The benefit of using two techniques is reliable continuous data. If one technique does not pick up a medical problem, then the other one provides an additional warning. This is essential due to sensitivity issues with EEG and poor signal to noise ratio due to probe-skin contact.

Project Objectives

This project's main objective is to develop a noninvasive and continuous bed-side monitoring system for traumatic brain injured patients. This will be accomplished by combining two modalities (fNIRS and EEG) into a single, compact, wearable device. Successfully engineering this device shows promise in replacing current monitoring methods that are crucial for indicating complications associated with trauma in the brain. These current techniques such as CT scan, MRI, SPECT, PET, and ICP monitoring are limited by either their invasive-nature, cost, single-measurement capacity versus continuous monitoring, machine size, and non-functional measuring capabilities.

An additional objective is to begin characterizing the brain's autoregulation in healthy and traumatic brain injured patients. With trauma being the third leading cause of death worldwide, and at least 1.7 million occurring in the United States yearly [1], understanding the physiology and brain-response to injury is important. However, there is limited knowledge and published literature on TBI patients. This project will also study the hemodynamic responses of subjects undergoing a change of elevation in an attempt to 1) characterize healthy and injured brain hemodynamic autoregulation and 2) validate fNIRS as a method for studying traumatic brain injury.

Methodology Used

Functional near-infrared spectroscopy (fNIRS): To measure hemodynamic changes in the brain the method chosen was fNIRS and a probe was built and shown in Figure 1 below. The probe uses one dual-wavelength LED, two OPT101 detectors, LN3170 current regulators, capacitors, resistors, transistors, and an ArduinoUno.

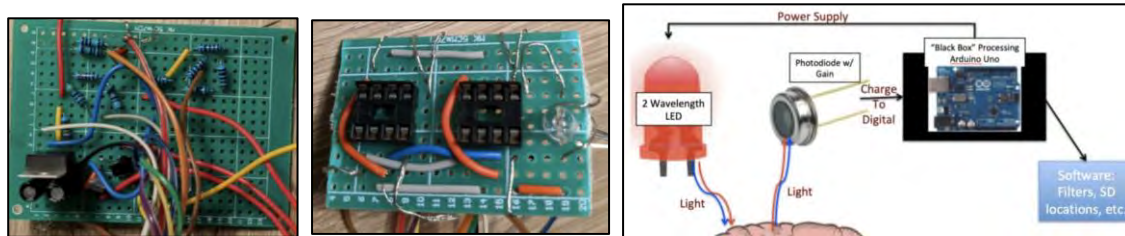


Figure 1. Left & Middle- custom built fNIRS circuit with detectors and LED shown in middle.
Right- diagram depicting the path light takes into the cortex back to detectors and processed as meaningful voltage data from the ArduinoUno to software.

An optical imaging modality, fNIRS detects changes in the concentration of oxygenated (HbO) and deoxygenated (Hb) blood to assess cerebral activity. It uses two different wavelengths in an optical window range of 700 to 900 nanometers, shown in Figure 2a below, where there is good contrast in absorption between the two chromophores [2] and a source detector. As seen in Figure 2b, the source detector receives photons after they have diffused through the skull, cerebral tissue, and blood.

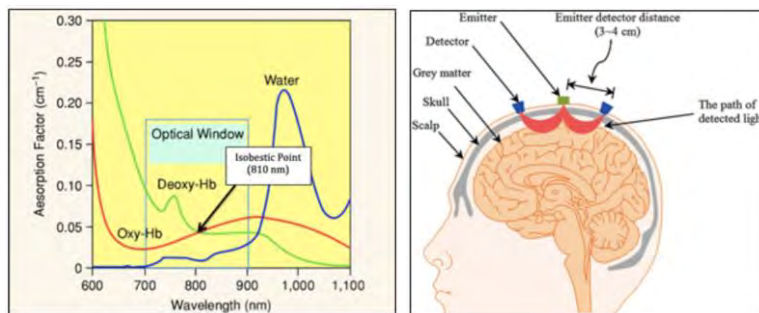


Figure 2. a) Absorption spectrum in near-infrared region with the optical window (700-900nm) highlighted where the contrast between oxygenated and deoxygenated blood is greatest and the absorption of water is not relevant. The isobestic point (810nm) should be avoided since there is no differentiation between deoxy-Hb and oxy-Hb at that wavelength. Adapted from <https://www.researchgate.net/figure/>

Absorption-spectrum-in-near-infrared-NIR-window_fig1_6167556 b) Visual depiction of source to detector configuration in fNIRS showing the light emitter in green, detectors in blue, and banana-shaped light path in red. Source: Naseer and Hong, 2015, Front Hum Neurosci (25)

Since photons received by the detector represent both scattered and absorbed light, the modified Beer-Lambert law, Equation 1 below, accounts for the dispersion. Two wavelengths are used to differentiate between changes of oxygenated and Hb and provide enough variables.

Equation 1: The Modified Beer-Lambert Law

$$I = GI_o e^{-(\alpha_{HB}C_{HB} + \alpha_{HBO_2}C_{HBO_2})L}$$

Where I is attenuated light intensity, G is a constant accounting for measurement geometry, I_o is input light intensity, α_{HB} is the molar extinction coefficient of Hb, α_{HBO_2} is the molar extinction coefficient of HbO_2 , C_{HB} is the concentration of the Hb chromophore, C_{HBO_2} is the concentration of the HbO_2 chromophore, and L is photon path (a function of absorption and scattering coefficients μ_a and μ_s).

Eventually, fNIRS can calculate blood volume and estimate local changes in oxygen metabolism as shown in Equations 2 and 3 below.

Equation 2: Change in Optical Density

$$\Delta OD = \log(I_b/I) = \alpha_{HB}\Delta C_{HB} + \alpha_{HBO_2}\Delta C_{HBO_2}$$

Where I_b is intensity at baseline, I is intensity at another time, ΔC_{HB} is the change in concentration of the Hb chromophore, and ΔC_{HBO_2} is the change in concentration of the HbO chromophore.

Equation 3: Blood Volume

$$Hb_{TOTAL} = THC = \Delta C_{HBO_2} + \Delta C_{HB}$$

Where Hb_{TOTAL} is the blood volume, also known as total hemoglobin concentration, THC.

Electroencephalography: To measure electrical activity in the brain, EEG was the method chosen, and specifically an OpenBCI device called the Cyton, an open source, 8-channel EEG processing platform was used along with gold electrodes and Ten20 Conductive Paste. This montage is shown in Figure 3a below. The Cyton uses a Bluetooth connection to send the data to a computer for display on an OpenBCI GUI. EEG is a current modality for monitoring electrical signals of the brain through the use of active electrodes on the scalp. The EEG system takes the electrical signal of the brain from the scalp and then graphs the data onto a chart as an electrical waveform. The intensity of these readings is typically in the microvolts range with each waveform having its own frequency range. An example of these waveforms is shown in the Figure 3b below.

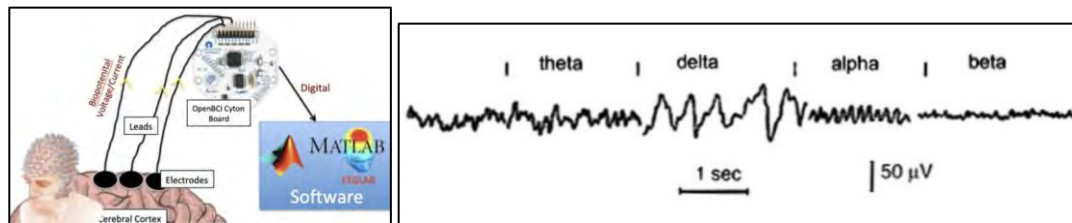


Figure 3. a) Diagram depicting electrodes collecting voltage differences from scalp to the CytonBoard which BT connects to MATLAB software. b) Electroencephalography waveforms with the four different stages labeled.

Abnormal events seen in the EEG are described as large signals with significantly higher voltages than those seen in the four primary waveforms. Specifically, EEG after TBI demonstrates a slowing of the posterior dominant rhythm and increased diffuse theta slowing, which may revert to normal within hours or may clear more slowly over many weeks [3]. This makes some abnormal events difficult to read and certain waveforms could act like another signal, making abnormality undistinguishable. Due to the difficulty in reading signals, there are trained professionals in clinical settings that can continuously read EEG graphs.

Combining the modalities: The two technologies would have been combined on a 3D printed casing with wells for the LED, detectors, and electrodes. This casing was designed on SolidWorks and printed out of NINJAFLEX flexible silicon material using a Craftbot Plus Printer. The design process and final printed casing is shown in Figure 4 below.

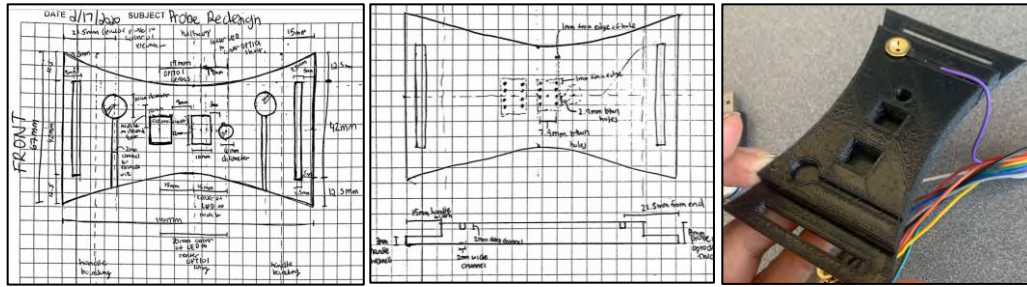


Figure 4. Hand-drawings for front, back, & width of casing, drawn in SolidWorks to be 3D printed by a Craftbot Plus Printer.

Characterizing blood flow and validating fNIRS: To characterize blood flow in controls and concussed subjects, the following protocol was followed. The premise is autoregulation changes in blood flow when the head changes elevation (30 degrees to 0 degrees) will differ between controls and subjects, with a focus on the rate of change of these parameters. This protocol also validates the fNIRS technology to monitor cerebral hemodynamics in real time and for clinical analysis.

Test-1: Baseline measurements. The subjects will lay on a hospital bed raised to a 30 degree angle and remain still for about 5 minutes with no measurements performed only rest. After the initial 5 minute rest period, continuous measurements will be performed at this same elevation for 5 minutes. This will measure basal brain function. There is no risk involved with this procedure.

Test-2: Head of Bed Manipulation. The head of the bed will lowered to an angle of 0 degrees at a rate of 1 degree/second so the subject is now in a supine position. This position will be held for 5 minutes. Optical measurements will be taken continuously. There is no risk involved with this procedure.

Results Obtained and Figures/Charts

Due to the COVID19 situation, testing on the integrated device was limited. Each component was tested separately and the integration was not able to occur; however each individual component was functional. In Figure 5a below, some preliminary testing using the EEG component is visible. The subject was asked to watch two videos while wearing the device, one for each mood listed. In the “happy” initial data, one can observe a steady trend of the two channels. In Figure 5b below, one can see the OpenBCI GUI was functional with the left showing the individual channels, and the right showing a Fourier transform plot depicting amplitude peaks at certain frequencies as well as accelerometer data.

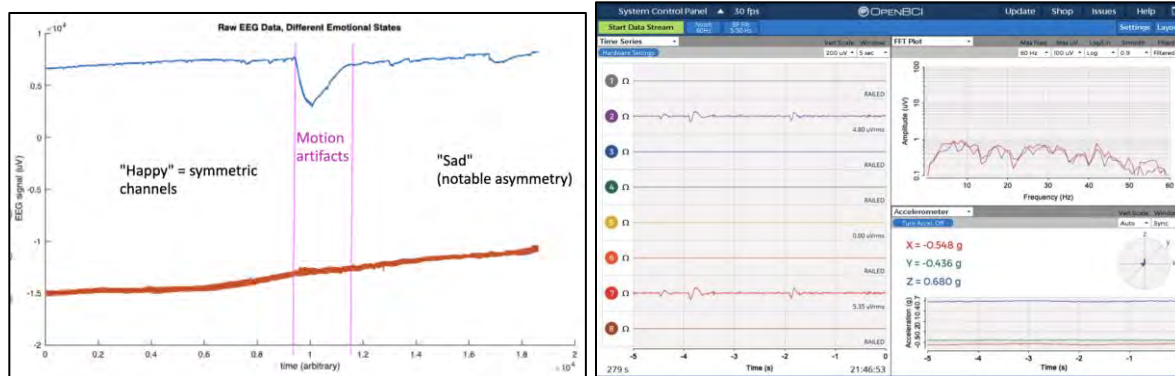


Figure 5. a) On the left, MATLAB plotted EEG signals obtained during preliminary testing. b) On the right, the GUI output displaying individual channels, FT transform, and accelerometer information.

In Figure 6 below, two trials of the fNIRS protocol are shown--a control (blue) and a concussed subject (red). An system called ISS was used, as the custom-built fNIRS system was not yet finalized. Going from a 30-degree elevation to a supine position, changes in HbO, Hb, and THC are visible in the control with the main observation being the consistent HbO increase back to steady levels. In the concussed subject, however, there is an irregularity in the HbO plot prior to, during, and even after the elevation change.

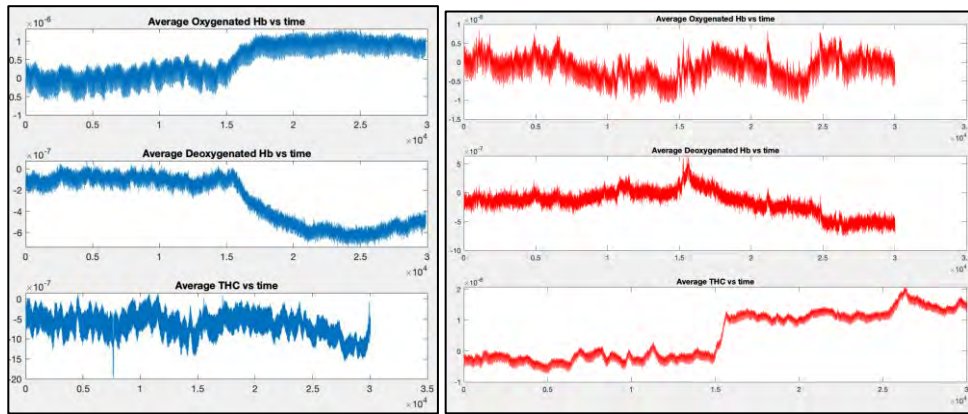


Figure 6. Data obtained during fNIRS protocol of head of bed elevation changes. Top shows changes in HbO, middle shows changes in Hb, bottom shows changes in THC. Blue is a control subject while red is a concussed subject.

Significance and Interpretation of Results

This project began creating an integrated probe for TBI monitoring. Even without integration, each component was tested individually to demonstrate functionality. The obtained waveforms and GUI output in Figure show that the EEG component of the design was functional and obtaining cerebral electrical activity. The significance of the data, however, warrants further study to ensure they are meaningful voltage values. The fNIRS protocol validates fNIRS as a technique for monitoring cerebral hemodynamics. By observing irregularity in the concussed subject compared to the control, this also validates fNIRS as a tool for furthering clinical research in traumatic brain injuries. This project still requires testing if the custom-built fNIRS device as it was halted due to COVID19. Overall however, the integration of fNIRS and EEG shows promise as a cerebral monitoring tool for traumatic brain injuries.

Acknowledgements and References

1. Faul, M., Wald, M. M., Wu, L., & Coronado, V. G. (2010). Traumatic brain injury in the United States: emergency department visits, hospitalizations, and deaths, 2002-2006. doi: 10.15620/cdc.5571
2. Leon-Carrion, Jose & Leon-Dominguez, Umberto. (2012). Functional Near-Infrared Spectroscopy (fNIRS): Principles and Neuroscientific Applications.
3. Ianof, J. N., & Anghinah, R. (2017). Traumatic brain injury: An EEG point of view. *Dementia & neuropsychologia*, 11(1), 3–5. doi:10.1590/1980-57642016dn11-010002
4. Gregori-Pla, C., et al., *Cerebral vasoreactivity in response to a head-of-bed position change is altered in patients with moderate and severe obstructive sleep apnea*. PLoS One, 2018. **13**(3).

Health and Wellness Testing Assessment

Student Researcher: Jordan A. Graves

Advisors: Dr. Rajeev Swami and Dr. Brandy Phipps

Central State University
Department of Education

Abstract

It is important for astronauts to maintain a healthy lifestyle because they have an increased risk of cardiovascular disease and muscle deterioration. Researchers study and monitor astronaut health for safety and disease prevention. Many of these methods are used in other health fields (e.g. exercise science, nutrition, medicine.) In this lesson students will be given the opportunity to learn and perform health assessment techniques, calculate risk factors, and make recommendations for “clients.” I will teach the assessment methods, healthy eating and exercise recommendations, and testing techniques and sample calculations on paper. Then, students will be divided into groups of three, with each student assigned a role (future astronaut, doctor/exercise scientist, and nutritionist.) Students will record height, weight, blood pressure, heart rate, and waist circumference. Calculations and standard risk charts will be used to evaluate “future astronaut” health risk. Students will then work in a group to determine nutrition and exercise recommendations for their “client.” By the end of the lesson, students will understand healthy eating practices, demonstrate ability to perform common health measurements and calculations of risk, and demonstrate ability to translate risk analysis into health recommendations.

Lesson

The common core standard for my lesson is the nature of science, these 8th grade students will be applying knowledge of science in real world challenges. I will begin the lesson by having students give their perspective and knowledge of a healthy diet is and what foods should you eat regularly. I will also ask students to guess what a normal blood pressure and heart rate is. Next students will watch a video about Nutrition from NASA astronauts. After the video, I will provide handouts including 1) detailed protocols for measuring height, weight, blood pressure, heart rate, and waist circumference; 2) standard risk charts relating measurements to cardiovascular disease and metabolic syndrome; 3) instructions for converting measurements into risk analyses; ad 4) standard nutrition recommendations for healthy individuals. I will demonstrate the measurements on a volunteer, and have students practice calculations, risk analyses, and action plan with data from two “sample clients,” The lesion is designed to provide a collaborative, “real world” learning opportunity for the students. To accomplish this, after the demonstrations and “sample client” practice, students will be divided into groups of three (deciding within the group which student will assume the roles of future astronaut, doctor/exercise scientist, and nutritionist.) The exercise scientist/physician will record height, weight, blood pressure, heart rate, and waist circumference of the future astronaut and perform calculations and risk analyses. The exercise scientist/ physician will work with the nutritionist to develop a written nutrition and exercise plan for the future astronaut based on the results of the risk analysis. Students will the switch roles, allowing each member of the group to assume each role. By the end of the lesson, students will have demonstrated 1) understanding healthy eating and exercise practices, 2) the ability to perform common health measurements and calculations of risk, and 3) the ability to translate risk analysis into health recommendations.

Resources

- Stadiometer with scale
- Sphygmomanometer
- Measuring tape
- Calculator
- Protocol handouts, standard risk analyses charts, and nutrition handouts
- [**STEMonstrations: Nutrition**](#)

Objectives

- Students will be able to understand and provide examples of healthy eating practices
- Students will demonstrate ability to perform common health measurements and calculations of risk.
- Students will demonstrate ability to translate risk analysis into health recommendations.

Methodology Used

In this lesson, the methodology used is the Lev Vygotsky Social Theory. He suggested that students learn best when they interact with their peers, teachers, and experts. This lesson provides a collaborative “real world” learning experience for students to take the information they are taught and apply it modeling expert behavior. They will work together, providing critique and suggestions to work of their group-mates, demonstrating their knowledge and ability to work in teams.

Results

Students will learn that nutrition is an important factor in life and specific steps they can take to create healthy eating habits in their life. This activity can influence students who do not care for health or science to be in an interactive lesson. Students will know how to take common body measurements and how they relate to health.

Assessment

I will do an informal and formal assessments of this activity. As students are working on this project I will walk around to monitor if they are on task and answer questions. I want to make sure students are accurately performing waist measurement, height and weight measurements, blood pressure, and heart rates, providing correction through demonstration as needed. Formally, students will submit their recorded measurements, risk analyses, and action plans for each “client” in their group. I will provide feedback and correction, if needed in the following areas: 1) calculations, 2) use of standard charts to correctly determine risk, and 3) translation of risk into appropriate action plans. Feedback will be used to provide handouts as a reference for corrections and feedback.

Optimized Supercritical CO₂ Compressor Design

Student Researcher: Matthew Ha

Advisor: Dr. Mark Turner

University of Cincinnati

College of Engineering and Applied Sciences

Department of Aerospace Engineering Gas Turbine Simulation Laboratory

Abstract

A new compressor design is studied using supercritical CO₂ as its working fluid in a heat pump to store energy. Specifically, the design of the first stator vein was investigated. This project utilized T-Blade3 to generate three dimensional blades which were then processed and solved by Mises. The solutions generated by Mises were interpreted by OpenMDAO to generate optimized blade geometry parameters which are fed back into T-Blade3 for the newly generated, optimized blade. By iterating this process, a blade may be designed using an objective function held to certain constraints. The details of this design process and the results of the study are discussed below.

Project Objectives

The objective of this study was to utilize an iterative design process using T-Blade3, Mises, and OpenMDAO to develop the first stage stator blade row geometry of a supercritical CO₂ compressor. This task includes the setup and familiarization of the Linux operating system, compiling and setup the design tools, configuration of the design environment, design of the optimization process, and interpretation of results.

Methodology Used

The environment setup for optimization was necessary to begin the optimization process. Ubuntu 18.04 was installed and configured in a dual boot desktop. T-Blade3 1.2.2 was obtained through the GTSL GitHub repository and source codes for Mises 2.70 were provided by Dr. Mark Turner. After obtaining T-Blade3 and Mises, the programs were compiled and added to the user path. OpenMDAO was installed through the python package manager in Anaconda. The initial input geometry supplied to T-Blade3 was downloaded from GitHub found as Reference 1.

Once the environment had been fully setup, the construction of the program structure began. T-Blade3, a parametric design tool, was used to generate the blade geometry. The provided LE55 file was modified to maintain a constant span for the initial in beta and out beta parameters for analysis. Following the construction of the blade row, Mises is next used to solve the flow field around the generated geometry. Supercritical CO₂ properties were approximated by controlling gamma in the Mises source code. From Reference 2 the gamma for supercritical CO₂ at the compressor inlet can be approximated as 1.8. Mises successfully grids, solves, and plots the solutions of the flow field around the blade geometry.

Finally, OpenMDAO is implemented into Mises and T-Blade3. OpenMDAO is a NASA developed python-based code for multidisciplinary optimization. The framework for OpenMDAO was designed by utilizing Reference 2, “Optimization of the Design of a Turbine Blade using OpenMDAO” by Tom Viars. A python script was developed to run T-Blade3, Mises, and OpenMDAO together; the outputs from Mises were taken by OpenMDAO and postprocessed to create a new, optimized input for T-Blade3. The OpenMDAO solver was instructed to minimize a zeta loss parameter while constraining S2, the exit flow angle. In this

study, S₂ was constrained to 0 degrees. A SLSQP optimization scheme was selected and a convergence tolerance of 1e-4 was selected. A 10-variable design space was designed by Tom Viars. This design space was modified to fit the objectives of this 9-variable optimization project. The full details of the construction of his design space may be found in Reference 3. The 9-variable constrained optimization was next completed.

Results Obtained

The project python script was able to successfully optimize the blade geometry using T-Blade3 as the blade generator, Mises as the flow solver, and OpenMDAO as the optimizing driver. The optimization was completed over 36 iterations and located a blade with a zeta loss parameter of 0.02382906 and exit angle S₂ of 5.155e-15, effectively zero. A plot of the optimized blade and Mach number vs X position along the blade is shown in Figure 1.

Significance and Interpretation of Results

The successful optimization of this blade proved the feasibility of a multi variable optimization-based design technique. An iterative method to create a blade geometry that has been optimized by a driver using a user defined objective function and constraint was demonstrated. Future work includes the further improvement of simulation accuracy and the application of the optimization design process to larger, multi-stage designs.

Figures and Charts

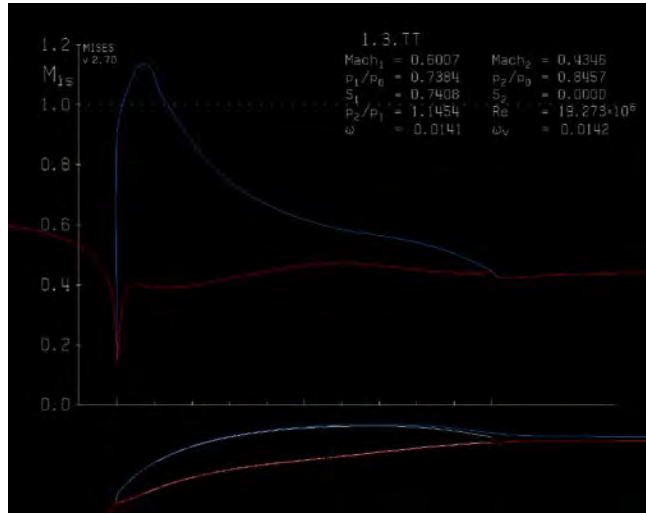


Figure 1. Mach number blade plot.

Acknowledgments

I would like to thank Dr. Mark Turner for his generous support and assistance in this project. Dr. Turner has been a fantastic advisor; through excellent mentoring and helpful documentation, the challenge of learning Linux, T-Blade3, Mises, and OpenMDAO was greatly reduced. I look forward to working with you in the future Dr. Turner!

References

1. Siddappaji, K., "GTSI-UC/T-Blade3," GitHub Available: https://github.com/GTSI-UC/T-Blade3/tree/master/inputs/NACA_thickness_cases/OGV_midspan_section/LE55.
2. Schroder, A., "Andy Schroder - Supercritical Carbon Dioxide Power Cycle Design Space Explorer," Andy Schroder - Supercritical Carbon Dioxide Power Cycle Design Space Explorer Available: <http://andyschroder.com/CO2Cycle/Explorer>.
3. Viars, T. "Optimization of the Design of a Turbine Blade using OpenMDAO", Mini-Thesis for a Master's of Science in Aerospace Engineering, 2019.

Remote Sensing of the US Virgin Islands Spring 2020

Student Researcher: Emilie Hardnock

Advisor: Dr. Joseph D. Ortiz

Kent State University
Department of Geology

Abstract

The goal of this project is to use remote sensing to monitor water quality in the coral reef areas around the US Virgin Islands. Suspended sediment, algae, cyanobacteria and other nutrients are measured in the water via water samples and satellite images to compare to coral health to see if these substances have a positive, negative, or no effect on the corals. Coral reefs are very important ecosystems and their continued health is important to many species and the ocean as a whole. Using these water quality monitoring methods helps give information on coral reef health over time and what substances are causing their health to degrade.

Work So Far

So far in my research I have been processing images of the US Virgin Islands from 2017 and 2018. I have taken Sentinel 3A satellite images and used the VPCA method in ENVI + IDL to produce images of the area. I have also been analyzing the amount of cloud cover in my study area. The large percent of cloud coverage over the island had been noted while looking for viable images to process, therefore it was something to look into. The large percent of cloud cover in the Caribbean proved to be a factor in the amount of usable images I could find per year.

Plans

Due to the campus shutdown, I have been working from home on analyzing USVI images from 2017 to continue determining amount of cloud coverage in the area. In addition to cloud coverage data, I have been looking at wind speeds, temperature and precipitation data from the area during 2017. This data will be compared to the images once produced to see if there is a correlation to show these factors affecting the water quality. I have also been searching for new images to process once I'm able to. I am also training on new software from home such as Google Earth Engine and ENVI which will be used to begin generating images. I am also planning on accessing the lab computers remotely once the setup has been configured to recover my previously processed 2017 & 2018 images. My plan for this time is to continue to collect cloud coverage and climate data of the area and then continue to create and analyze images once the software is fully configured to work from home.

Polymerized Liquid Metal Network Characterization for Stretchable RF Devices

Student Researcher: Christopher L. Hartnagel

Advisor: Dr. Alexander Watson

University of Dayton

University of Dayton Electrical Engineering Department

Abstract

Highly stretchable conductors are a necessary part of flexible and stretchable electronics, yet are not well developed or characterized, particularly in radio frequency (RF) electronics. Gallium metal alloys that are liquid at room temperature are appealing for stretchable RF devices because they are sufficiently conductive and are intrinsically deformable. Air Force Research Laboratory has recently developed a highly stretchable conductive material based on polymerized liquid metal networks (Poly-LMNs) which are especially well suited for stretchable RF devices¹. This material, which is deposited in an ink, can remain conductive at extreme strains greater than 500%. Additionally, AC and DC impedance is consistent over this strain range. These are important for stretchable RF devices because changes in impedance result in problematic energy reflections. Measurement with a laser profilometer is performed to reveal how the geometry of the conductor and substrate change under strain thus allowing us to predict impedance changes. Device activation conditions and sheet resistance are systematically investigated to see how they affect the properties of the device. This work paves the way for novel stretchable RF devices that can be reconfigured on-the-fly and is amendable to flexible structures and wearable devices[AW1].

Project Objectives

RF design requires very specific geometries and dimensions to achieve impedance matching. Perfect matching maximizes energy transfer, mitigates energy reflection, and minimizes general loss. Yet when stretching anything, all dimensions are changing especially for extreme strains. Thus, we need to understand how this strain will affect the material's intrinsic properties as well as the precise geometry needed for RF circuits. The scope of this project deals with two aspects of stretchable device characterization. The[AW2] first objective is understanding how characteristic impedance changes from varying signal line width and distance between signal line and the ground plane. This is possible because these geometries are proportional to the changes of the 3M™ VHB™ Tape substrate. The team wishes to understand the effects of keeping substrate width consistent as well as letting the width change with strain. This means utilizing a 3D laser profilometer to measure the desired geometries at different strains and computing how characteristic impedance changes as a result. The second objective is understanding how activation stretch axis effects DC sheet resistance of Poly-LMN as a dielectric. This means controlling which axis the device is stretched along to activate then applying a voltage and measuring the resistance seen in-between the voltage terminals.

Methodology

Grounded co-planar waveguides show the most promise for stretchable RF devices because both the signal line width, as well as the distance between the signal line and ground plane decrease as the device is elongated. This fact allows the impedance to stay relatively consistent over a large strain range. Commercially available 3M™ VHB™ Tape has been chosen as the substrate for these devices due to its low electrical loss and isotropic nature which allows the signal line width and the distance between the signal line and ground plane to change proportionally. Lastly, this tape is extremely durable allowing for more than 1,000 cycles at various strains greater than 300%.[AW3] Success means characterizing basic

microstrip and coplanar waveguide circuits (transmission lines, stub tuners, and filters) made from Poly-LMN on a stretchable substrate. [AW4] Manufacturing methodology for these devices entails placing a mask onto commercially available 3M™ VHB™ Tape and drop-casting the Poly-LMN ink. Once manufactured the ink must be stretch activated by stretching the tape[AW5].

In order to understand how the impedance changes by varying waveguide signal line width and distance between signal planes (height of the substrate), a basis for a microstrip transmission line geometry was needed. The industry standard characteristic impedance for radio frequency components is $50\ \Omega$ so that was the target basis. Given that the dielectric constant of the Poly-LMN dielectric is 2.68 and the height of the 3M™ VHB™ Tape substrate is 1 mm, the width of the micro-strip co-plainer waveguide signal line can be determined to achieve $50\ \Omega$. Characteristic impedance, independent of frequency, can be calculated with equation 1 below ². It was calculated that a width of 2.735 mm has a characteristic impedance of $50\ \Omega$.

The equation for a micro-strip transmission line with a width/height ratio greater than 1 can be approximated by equation 1 below ³.

$$Z_0 = \frac{120\pi}{\sqrt{\epsilon_{eff}} \left[\frac{W}{H} + 1.393 + \frac{2}{3} \ln \left(\frac{W}{H} + 1.444 \right) \right]}$$

Where ϵ_{eff} = dielectric constant; W = width of the signal line, mm; H = height of the dielectric, mm;

As 3M™ VHB™ Tape is strained, the thickness and width decrease due to the Poisson effect. During experimental measurements, width can be consistent by stretching the device along that axis. To observe this change accurately, a 3D laser scanning microscope was used. The width of the signal trace and the thickness of the substrate can be measured in the middle of the device at random strain increments up to approximately 300%. These strained height and width measurements were then normalized by dividing by the unstrained height and width. This normalized measurement was then multiplied by the width and height for the calculated $50\ \Omega$ microstrip to get an equivalent geometry at the various strain increments. Using the equivalent geometry, the characteristic impedance was re-calculated for each strain increment. To show how the device would perform with a consistent width, characteristic impedance was re-calculated for each strain increment keeping width at 2.735mm. Both sets of impedance measurements are plotted in Figure 1.

In order to understand how activation stretch axis effects sheet resistance of poly-LMN dielectric, resistivity was measured with a four-point probe method for X-axis only activation and X-axis then Y-axis activation. Five one square inch sheets of Poly-LMN dielectric material were patterned onto the stretchable substrate and each was tested with the same methodology. First, the X and Y axis was marked on the samples and hand strained to 200% and back to 0%, 10 times in a row, along the X-axis only. This process ensures consistent activation, ensuring each sample is conductive. The measurement probe, shown in Figure 2, was placed into the center of the sample along the X-axis and the resistance was sampled 10 times without lifting the probe. The probe was lifted and replaced in the same orientation two additional times for a total of 30 measurements along the X-axis shown in blue, light blue and purple. The probe was then aligned along the Y-axis and the process was repeated yielding 30 measurements shown in red, orange and pink. Secondly, the sample was hand stretched along the Y-axis in the same manner as X-axis only, equating to X-axis then Y-axis activation. Measurements were taken using the same methodology. All results from the sheet resistance testing are shown in Figure 3.

Results Obtained

The initial results from impedance calculations are promising for confirming that grounded co-planar waveguides that use 3M™ VHB™ Tape substrate, without adjusting the width, will work well as stretchable RF devices. Initially, as the substrate is strained beyond 0%, the impedance decreases by about 2Ω due to a change in the width/height ratio. After this initial impedance drop, the ratio then remains relatively consistent over the strain range. At the largest tested strain of 317% where the device would perform its worst, the device impedance is calculated at 47.16Ω as plotted in figure 2. To quantify the performance of the device we can look at the hypothetical impedance mismatches between the source and the load. The ratio of amplitudes of the reflected and incident voltage waves at the load is known as the voltage reflection coefficient².

The equation for voltage reflection coefficient (Γ) can be calculated using equation 2 below.

$$\Gamma = \frac{Z_{in} - Z_0}{Z_{in} + Z_0}$$

Where Z_{in} = impedance of source (50Ω); Z_0 = characteristic impedance of the load from equation 1.

A load is said to be matched to a transmission line if the load impedance is equal to the characteristic impedance of the line ($Z_{in} = Z_0$) because there will be no reflection by the load. This reflection coefficient can be used to calculate a more meaningful power loss in decibels by calculating the power reflection loss².

Using the calculated voltage reflection coefficient, the power reflection loss in decibels can be calculated using equation 3 below.

$$\text{Power Reflection Loss (dB)} = 10 * \log(\Gamma)$$

Where Γ = voltage reflection coefficient from equation 2.

At the worst case tested, 317% strain, the device has a power reflection loss of -15.34 Db. For example, if 1 watt was supplied to the device, just 0.029 watts would be reflected to the source as loss^[AW6], this shows these devices would be very efficient at a large range of strain. Device with consistent, adjusted, width yields a much lower impedance of 33.70Ω at 319% strain resulting in a reflection of -14.24 dB which is less efficient than the unadjusted width. From this data, we can conclude that both the height and width decrease during strain are beneficial to maintaining the impedance matching of a device. The width and height change are nearly proportional to one another for the 3M™ VHB™ Tape. This fact is an important trait for practical stretchable RF devices.

The initial results from the sheet resistance testing show that the DC resistivity is independent of activation and measurement axis. Data in figure 2 does not show a trend in the magnitude change when aligning the measurement probe along the x-axis versus the y-axis. Additionally, the data does not show a trend in the magnitude change when activating the device along the x-axis only versus x-axis then y-axis activation. This would indicate that the Poly-LMN material is isotropic. This fact allows Poly-LMN RF devices to be stretched along both the x-axis and y-axis during use without effecting the intrinsic resistivity of the dielectric. Maintaining this resistivity during operation is critical to proper matching.

Acknowledgments

The author of this paper would like to thank the Air Force Research Laboratory and UES Inc. for supplying the materials and equipment to conduct this research. The author would also like to thank Dr. Alexander Watson, Dr. Christopher Tabor, Dr. Michelle Yuen, and Dr. Carl Thrasher for their cooperation on the project^[AW7].

[AW8] **Figures/Charts**

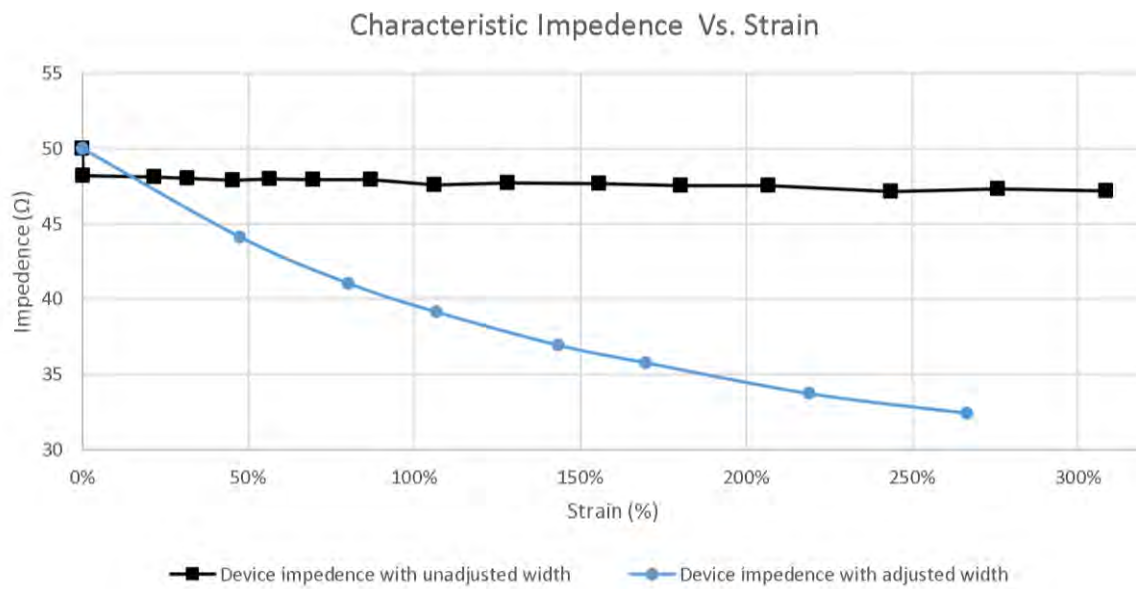


Figure 1. Characteristic impedance of a grounded microstrip line on 3M™ VHB™ Tape as it is strained.

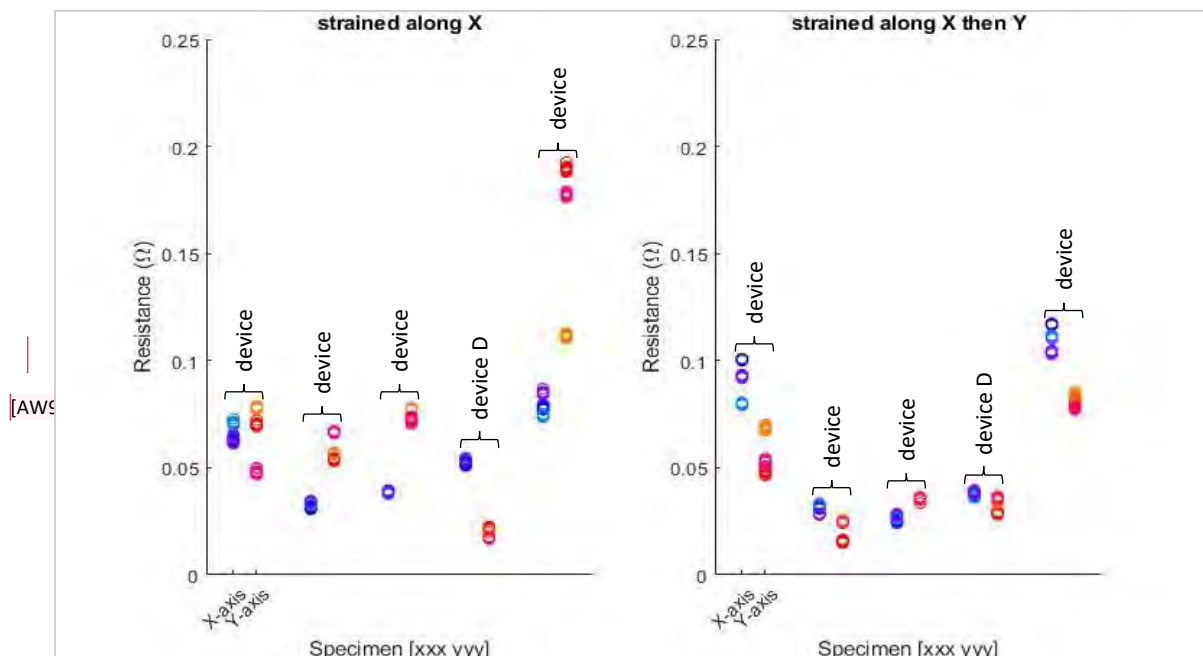


Figure 2. Resistivity of Poly-LMN dielectric based on activation axis and measurement axis.

References

1. Thrasher, C. J., Farrell, Z. J., Morris, N. J., Willey, C. L., Tabor, C. E., Mechanoresponsive Polymerized Liquid Metal Networks. *Adv. Mater.* 2019, 31, 1903864. <https://doi.org/10.1002/adma.201903864>
2. *Microstrip Calculator*, Pasternack, www.pasternack.com/t-calculator-microstrip.aspx.
3. Ulaby, Fawwaz T., and Umberto Ravaioli. *Fundamentals of Applied Electromagnetics*. 7th ed., Pearson, 2015.

The Neuroscience of Gender – Exploring the Link between Prenatal Hormone Exposure and Sex-Specific Neuroanatomy in a Rat Model

Student Researcher: Delenn R. Hartwick

Advisor: Clare Mathes

Baldwin Wallace University

Neuroscience Department

Abstract

Sexual differentiation of the brain may follow a different pattern in transgender individuals than in cisgender individuals, and this may be due to different prenatal hormone environments. Some brain areas that are sexually dimorphic, such as the bed nucleus of stria terminalis (BNST), present in transgender humans at a volume intermediate to that of cisgender male and female individuals (Zhou et al. 1995). This can be causally recapitulated in a rat model by using prenatal testosterone exposure – when female pups are exposed in utero and upon birth to testosterone, their BNST at 12 days of age display a volume in between that of male and female pups exposed to only vehicle prenatally (Chung et al. 1999). We seek to replicate and extend these findings by: 1) limiting testosterone exposure to prenatal only, 2) using a lower dose less likely to masculinize genitalia, and 3) assessing persistence of the effect on the BNST past early childhood. Thus we plan to, across 2 phases, mate 8 female rats with male rats, and, when the impregnated females reach gestational day 17, inject half of them subcutaneously with testosterone propionate (TP; 2 mg) and half with vehicle (0.1 ml 50/50 sesame oil + DMSO) to prenatally expose their pups. From this we plan to use 6 males and 6 female pups from each of the 8 litters, with brains of 1 male and 1 female offspring in each condition (TP and vehicle) harvested at postnatal day (PND) 12, 26, and 47, which are periods representative of infancy, adolescence, and early adulthood. Once perfused, the rats' brains will be sliced coronally on a freezing microtome (60 µm), Nissl stained, and the volume of the BNST stereologically quantified. Based on the findings of Chung et al. (1999), we would expect that males would have a larger BNST than females, but that the BNST of TP-exposed animals would be larger than those of vehicle-exposed animals within each sex at each lifespan time point. TP-exposed female rats would display a BNST volume intermediate to that of nonexposed males and females, thus neuroanatomically modeling some aspects of transgender humans and offering a possible mechanistic explanation for this phenomenon.

Project Objectives

The overarching goal of this project is to examine the neural and hormonal components that contribute to gender and gender differences, and it is based on the hypothesis that gender identity is influenced by the developing brain's exposure to sex hormones at certain critical periods (e.g., Savic et al. 2010).

According to this hypothesis, the brain will develop in response to the hormones it is exposed to later in prenatal development, rather than the hormones it was exposed to earlier, which were regulated by chromosomal arrangement and contribute to the masculinization or feminization of the gonads and genitals of the fetus. Therefore, when the brain of a XX fetus is exposed to masculinizing or defeminizing hormones, the brain will develop differently than that of a XX fetus not exposed to those types of hormones. This often results in differing sexually dimorphic neuroanatomy and behavior in both animal models (e.g., Chung et al. 1999; Goldman et al. 1966) and in humans (e.g., Zhou et al. 1995) and, potentially, in cognitive experiences including expression of gender identity. The present study will replicate and extend past research but by using methods that focus on prenatal exposure (which also should limit the masculinizing effects of testosterone on genitalia) and assess persistence of effect at critical periods across the lifetime.

Methodology To Be Used

16 rats (8 males, 8 females over two phases) will be bred one male to one female overnight to allow for accurate gestational day (GD) tracking. On GD 17, the dams will be treated with either a 0.1 ml subcutaneous injection of TP (2 mg; n=4, 2 in each breed phase) or its vehicle (0.1 ml of 50/50 sesame oil + DMSO; n=4, 2 in each breed phase). Immediately after birth, each litter will be culled to 6 males and 6 females. All pups will then be cross-fostered to the vehicle-injected dams (since TP injection may alter maternal behavior), such that each dam has 3 of each sex of TP-exposed pups and 3 of each sex of vehicle-exposed pups, none of which are of her own litter. One pup of each sex and each treatment will be randomly selected and removed from each foster dam at PND 12, 26, and 47 to be perfused for the collection of brain tissue. Brain tissue will be sliced, mounted, and Nissl stained with cresyl violet, and then BNST volume will be stereologically quantified. Volumes will be compared statistically to assess differences between treatment groups and sexes across time points.

Results Expected

A prior study showed that a concentrated dose of TP given both prenatally and postnatally resulted in PND 12 female offspring with BNST volumes intermediate to that of non-TP-exposed offspring of each sex, with control males presenting with larger BNST volumes than females (Chung et al. 1999). I expect that males will possess a larger BNST than females, and that exclusively prenatal exposure to a lower dose of TP (one that does not masculinize genitalia) will increase the volume of the BNST in rats as compared to non-TP-exposed rats of the same sex, and this effect will persist across developmental milestones and into sexual maturity.

Significance and Interpretation of Results

This study seeks to explore the hypothesis that prenatal sexual differentiation of the brain may follow a different pattern in transgender individuals than it does in cisgender individuals. Testosterone-exposed female rats possessing an intermediate BNST volume could neuroanatomically model some aspects of transgender humans and offer a possible mechanistic explanation for this phenomenon.

Acknowledgments

Research funding and support provided in part by the Edith Robinson Fund, the Joyce Evans Schanz Summer Scholars Endowment, the Baldwin Wallace Neuroscience Program, and the Ohio Space Grant Consortium. This research proposal was presented at the September 2019 Midwest and Great Lakes Undergraduate Research Symposium, Wooster, OH, and the October 2019 Faculty for Undergraduate Neuroscience poster session at the Society for Neuroscience conference, Chicago, IL, travel for which was supported in part by the Baldwin Wallace Office of Undergraduate Research and Creative Studies.

References

1. Chung, W. C., Swaab, D. F., De Vries, G. J. (1999) Apoptosis during sexual differentiation of the bed nucleus of the stria terminalis in the rat brain. *J. Neurobiol.*, 43: 234-243.
2. Goldman, A. S., Bongiovanni A.M., Yakovac, W.C. (1966) Production of congenital adrenal cortical hyperplasia, hypospadias, and clitoral hypertrophy (adrenogenital syndrome) in rats by inactivation of 3-beta-hydroxysteroid dehydrogenase. *Proc. Soc. Exp. Biol. Med.*, 121: 757-766.
3. Savic I. (2010) Sex differences in the human brain, their underpinnings and implications. *Prog. Brain Res.*, 186: 7-9.
4. Zhou, J., Hofman, M.A., Gooren, L.J.G., Swaab, D.F. (1995) A sex difference in the human brain and its relation to transsexuality. *Nature*, 378: 68-70.

Development of Flapping Winged Micro Air Vehicle Control Systems

Student Researcher: Joel A. Hauerwas

Advisors: Roger Quinn and Mark Willis

Case Western Reserve University

Mechanical Engineering

Abstract

Flapping Winged Micro Air Vehicles (FWMAV) are a promising field of robotics and aeronautics as an alternative more energy efficient form of flight. Compared to traditional stable winged aircraft flapping winged vehicles can fly at slower speeds and are generally more energy efficient. These robots typically use a yoke mechanism to flap their wings in a mirrored motion. This flapping motion can provide significant lift but limits the ability to independently control the wings for turning. Due to this limitation turning and steering the robot. Our lab has developed a novel control method by studying slow motion footage of moth flight and looking for movement patterns prior to turns or strafes. The moth appears to flex its abdomen in the opposite direction it intends to move. To prove this flexation causes turning we have developed a mechanical model which we can control and isolate this motion for testing in wind tunnels.

Keywords—*Flapping Winged, Controls, Prototyping, 3D printing, 3D Scanning, Mesh Editing, Biorobotics, Biomimicry, Moths, and Insects*

Introduction

In this paper we study a control mechanism for flapping winged micro air vehicles allowing for strafing and steering. Previous studies have demonstrated viability of flapping winged robotics [1],[2],[3],[4] and have shown that insects use their abdomen to manipulate flight [5],[6]. This work demonstrates a novel approach to control systems learned from biological study of moths in flight. To implement this technology rapid prototyping and 3D scanning were used to create effective test models.

Biological models have adapted very precise mechanisms to enable flight. *Manduca Sexta*, The Tobacco Hawkmoth, has been studied for its complex flight patterns [7]. The moth is capable of hovering midair, strafing, and turning quickly midair traits incredibly advantageous for aerial vehicles [8]. Slow motion footage of moths in flight suggests a correlation between abdominal rotation and the flight pattern of the insect. This rotation changes the passive flight plane of the moth to change flight direction.



Figure 1. *Manduca Sexta* adult stage.

In this paper, we investigate and test a method of flight control for future research in flapping winged robotics. This control system is based upon the abdominal rotation of *Manduca Sexta*, which has seven abdominal sections each of which rotates between two and five degrees about the neutral axis of the insect [9]. To test the effectiveness of our solution the insect was scanned in a neutral position and then digitally articulated into different natural body positions. The modified moths were 3D printed and then could be tested in a wind tunnel using smoke to visualize airflow.

Once proof of concept was established a mechanical system capable of articulating the abdomen was developed. The articulating abdomen was controlled by a stepper motor and an Arduino to turn the mechanical abdomen. This

model was also tested in a wind tunnel with smoke to visualize the airflow and then as the abdomen turns the change in airflow suggests that if untethered the moth would strafe in the direction of rotation. This control system can be applied to traditional aircraft as well as flapping winged models suggesting it could be promising for additional study.

Overview

Moth Anatomy

Manduca Sexta is a species of moth native to North America well known in research for its flying abilities. The species is capable of flying in intense winds, strafe while hovering, and feed on flower while hovering. The species experiences significant sexual dimorphism with the females of the species being ten to fifteen percent larger than their male counterparts. On average between the two genders the species has a wingspan a little over ten centimeters and has a mass of about 1.55 ± 0.5 g. Their large size makes them an ideal candidate for study as they can be more easily 3D scanned and manipulated. To simplify the testing only female moths were used for their larger size.

The species has four wings a set of primary wings and a set of hind wings. The primary wings generate the majority of the lift that keeps the moth airborn. The hindwings have been shown to generate relatively little lift and are likely involved in steering and flight control. Figure [2] shows the flight pattern of a moth during take off. There are four distinct phases of continuous flight two short phases supination and pronation where the moth changes the angle of its wing with its wing pivot to prepare for the next stroke. The downstroke generates lift and the upstroke returns the wing to the upward position. During the downstroke the moth's wing is perpendicular to gravity while during the upstroke it is much closer to parallel so less force is required to lift the wing then is generated in the downstroke.

The moth's body has three distinct sections: the head, the thorax, and the abdomen. The head contains the moth's sensory organs and is responsible for controlling the insect. The thorax is where the wings attach to the insect's body and where the flight control muscles are located. Moths have a fairly simple flight muscle system with one set of direct and indirect flight muscles. The direct flight muscles are attached directly to the wing and help pivot the wing for the up and down strokes. Conversely, the indirect flight muscles deform the thorax to cause the flapping motion. Lastly the abdomen has several distinct sections and holds the other organs.

Slow motion footage of the moths suggests that the abdomen likely plays a role in flight control as well. The moth has a significant degree of control over each individual segment and will curl them down to slow its' flight or rotate them it about the neutral X_b axis reference to Figure [4]. Early study has suggested that the moth can turn each individual abdominal section between three and five degrees. Rotating the

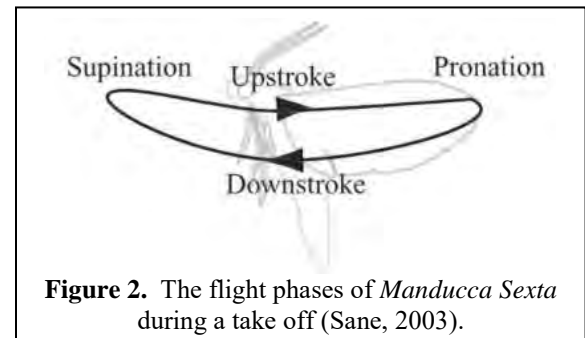


Figure 2. The flight phases of *Manduca Sexta* during a take off (Sane, 2003).

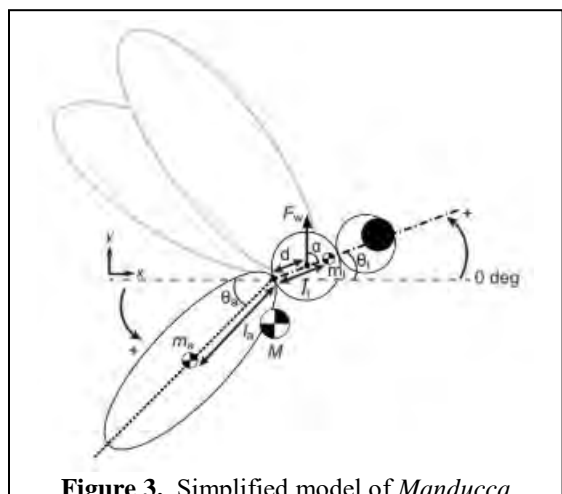


Figure 3. Simplified model of *Manduca Sexta* in flight with labeled forces and masses (Dyer et al, 2013).

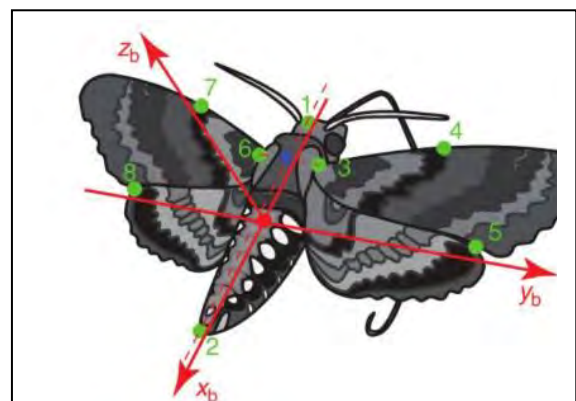


Figure 4. Moth in flight with overlaid axis (Cheng et al. 2011).

abdomen allows the pocket of air created underneath the moth to escape from one side or the other creating a small moment allowing the moth to strafe in the direction of rotation.

3D Scanning and Model Manipulation

In order to create a mechanical equivalent to the biological model a 3D scanner was employed. The machine developed by Hexagon Metrology uses laser light and a powerful camera to record position data and build a 3D model. The moth was prepared for scanning by removing its scales and wings to leave a clean scan surface. By combining several scans, a full 360-degree model of the moth could be developed. The original model was then digitally repaired to patch holes in the 3D mesh using Autodesk Meshmixer an open-source mesh editing software. The moth model was then smoothed using an algorithm to remove noise and artifacts from the scanning process. Careful attention was paid to not digitally alter the shape of the moth such that it would change how air flows around the model.

Once the moth model was repaired and smoothed it could be adjusted further for printing. The model needed to be scaled to one hundred and fifty percent scale to account for the size of the control stepper motor. To account for the increase in scale we increased the flow rate proportionally in the wind tunnel so that the flow acts as it would for a standard scaled moth. A support was also added to the back of the moth for the stepper motor in such a way that it wouldn't impact the airflow.

The stepper motor used to articulate the abdomen was the 28-BYJ48 Stepper motor. This motor was selected because it is easy to code and very cheap making it ideal for early prototyping. The stepper motor and the abdomen key were modeled in Solidworks before they were imported into Autodesk Meshmixer for final edits. Flat cuts were made through the moth model at each abdominal section so that they could be independently rotated and then a key slot with varying angles was cut through the center. The key was then attached to the stepper motor and then as it turned it engaged each abdominal section in series. Allowing the abdomen to rotate through its phases shown in Figure [5].

The model once tested digitally was 3D printed on the Objet350 Connex3 printer. This system has a resolution of 30 microns making it suitable for high precision biological models like the moth model developed by the 3D scanner. The Objet350 photopolymers also have a smooth surface finish which limited the effect of friction between each abdominal section which is essential to the rotation of the abdomen. Once the model was printed each abdominal section was placed on the key in order and then the final section was affixed with epoxy. The thorax and head were printed separately and the stepper motor was attached to the mounting plate with a pair of bolts. Once the two main assemblies were completed the abdomen was attached to the shaft of the stepper motor with epoxy ensuring the two pieces would hold together. To further reduce friction between the abdominal sections a lubricant was added and the surfaces were manually smoothed with sandpaper and cleaned.

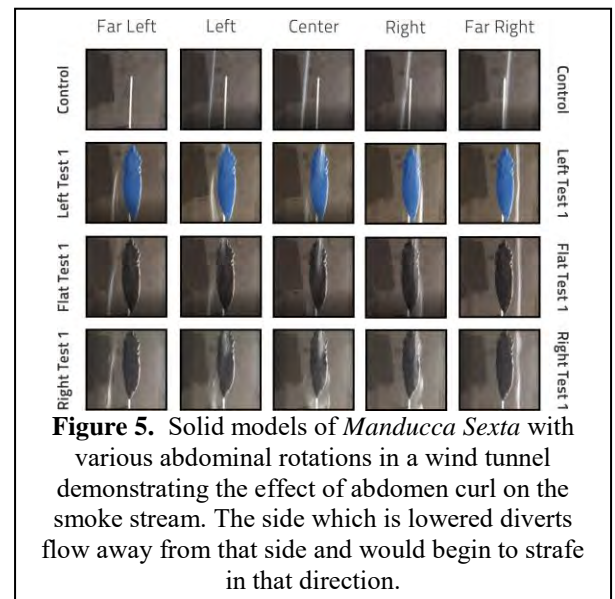


Figure 5. Solid models of *Manduca Sexta* with various abdominal rotations in a wind tunnel demonstrating the effect of abdomen curl on the smoke stream. The side which is lowered diverts flow away from that side and would begin to strafe in that direction.

Results

Once assembled the model was attached to a long connecting rod to limit interference from surrounding object. The completed assembly was affixed to an adjustable base and placed in a wind tunnel for testing. The model was placed down wind from a smoke source and as the abdomen moved the effect of the abdominal rotation could be observed. The test suggests very similar patterns with the stable bodied craft developed last year shown in Figure [6].

The dynamic rotation of the abdomen shifted the flow of air around the model noticeably and in such a way that if the model was free standing it likely would have begun to strafe. Unfortunately, the smoke flow in the wind tunnel was insufficient to capture on video. However, in person there was a clear distinction between the different abdominal positions.

Conclusion and Future Work

Conclusion

This test has proven incredibly promising and a clear impact of the model was demonstrated in the smoke flows. More tests however will be required to ensure accuracy of our results. In addition, the model of the moth has potential for improvement since despite attempt to limit friction abdominal sections still stick together. Sticking of the abdominal sections is a potential issue since it calls into question the effectiveness of the mechanical model presented in this presentation. One way to limit the effect of the friction would be to reduce the contact area of the sections but this could allow for air flow between the sections which would dramatically affect the results of the test. The moth could also be improved by integrating soft components like a sleeve to ensure a more gradual natural transition compared to the hard-plastic edges of the current model. Smaller stepper motors would also allow for smaller error since the effects of the top mounted motor can be mitigated.

The test bed itself can also be improved to get more laminar flow and PIV or particle image velocimetry techniques can be used to confirm the effects of the abdominal rotation on airflow. PIV provides a great opportunity to quantify the results that we obtain qualitatively currently and is likely the next step for this project.

Acknowledgments

I would like to thank Ken Moses for introducing me to moth bot and pushing my work and research. As well as my lab advisors Roger Quinn and Mark Willis for providing guidance and invaluable insight. Lastly, I would like to thank Kim Thompson for accommodating my tests and helping to prepare moths for study.

References

1. Moses, K. C., Michaels, S. C., Willis, M., & Quinn, R. D. (2017). Artificial *Manduca sexta* forewings for flapping-wing micro aerial vehicles: how wing structure affects performance. *Bioinspiration & Biomimetics*, 12(5), 055003. doi: 10.1088/1748-3190/aa7ea3
2. Cranston, B., & Palazotto, A. (2014). Evaluation of the Thorax of *Manduca Sexta* for Flapping Wing Micro Air Vehicle Applications. *International Journal of Micro Air Vehicles*, 191–210. <https://doi.org/10.1260/1756-8293.6.3.191>
3. “Experimental and Computational Investigation of Flapping Wing Propulsion for Micro Air Vehicles,” *Fixed and Flapping Wing Aerodynamics for Micro Air Vehicle Applications*, pp. 307–339, 2001.
4. R. Sahai, “Direct Sensing of Wing Flapping and Rotation Parameters for a Hawkmoth-Sized Flapping Wing Micro Air Vehicle,” *Volume 1: Advances in Aerospace Technology*, Nov. 2016.



Figure 6. Repaired 3D scan and finished mounted 3D model with mounted servo motor.

5. Zhao, J., Wu, J., & Yan, S. (2015). Movement Analysis of Flexion and Extension of Honeybee Abdomen Based on an Adaptive Segmented Structure. *Journal of insect science (Online)*, 15(1), 109. doi:10.1093/jisesa/iev089
6. N. Stead, "The Abdomen: The Secret To Stabilising Flight," *Journal of Experimental Biology*, vol. 216, no. 9, pp. i-ii, 2013.
7. Hedrick, T. L. (2006). Flight control in the hawkmoth *Manduca sexta*: the inverse problem of hovering. *Journal of Experimental Biology*, 209(16), 3114–3130. doi: 10.1242/jeb.02363
8. T. Hedrick, "Hawkmoth flight in unsteady flows," *2016 International Congress of Entomology*, 2016.
9. Dyhr, J.P., Morgansen, K.A., Daniel, T.L. and Cowan, N.J. (2013). Flexible strategies for flight control: an active role for the abdomen. *J. Exp. Biol.* **216**, 1523-1536.
10. J. Gau, N. Gravish, and S. Sponberg, "Indirect actuation reduces flight power requirements in *Manduca sexta* via elastic energy exchange," Jul. 2019.
11. D. Tom, "Decoding the independent and synergistic roles of flight muscles for control of turning in the hawkmoth, *Manduca sexta*," *Frontiers in Behavioral Neuroscience*, vol. 6, 2012.
12. "Correction: Robotic Moth Reveals Key to Insect Flight," *Science News*, vol. 151, no. 3, p. 35, 1997.
13. M. Fuchiwaki, T. Kuroki, K. Tanaka, and T. Tabata, "Vortex Ring Formed over the Wings of a Flapping Butterfly and a Small Flapping Robot," *41st AIAA Fluid Dynamics Conference and Exhibit*, 2011.
14. H. Duan, Z. Li, and Q. Li, "Model and control of Micro Flapping-wing Aerial Robot," *2010 International Conference On Computer Design and Applications*, 2010.
15. H. R. Vejdani, "Dynamics and stability of Bat-Scale Flapping Wing Hovering Robot," *2019 IEEE 15th International Conference on Automation Science and Engineering (CASE)*, 2019.
16. Sane & Dickinson, 2001, 2002; Truppel & Rossi, 2011; Usherwood & Lehmann, 2008;
17. Cheng et al., 2011; DeLeón & Palazotto, 2011; Z. A. Khan & Agrawal, 2007, 2011; Z.

3D-Printed Poly (lactic acid) Scaffolds for Regenerative Medicine: Does PLA Degrade, Support Osteoblastic Cellular Growth?

Student Researcher: Brevin F. Henninger

Advisor: Dr. Tim Norman

Cedarville University
School of Engineering and Computer Science

Abstract

A major challenge facing researchers in the field of regenerative medicine is the ability to repair tissue defects and stimulate healing. Today, bone is often replaced with biologically inert materials such as titanium. Often the more desirable tissue engineering approach would be to provide a scaffold seeded with the osteogenic capability for cell proliferation and growth eventually leading to tissue restoration. The overall goal of our research is to develop a method using three-dimensional (3D) printing to create biodegradable scaffolds of customizable stiffness which promote bone (osteoblasts) ingrowth. Using Finite Element Analysis (FEA), we also found favorable scaffold strain magnitudes which should stimulate bone modeling. These results provided confidence in implant designs ability to repair bone. It was concluded that further studies were required to examine the *in vivo* behavior of the implants: i.e. PLA sustainability (i.e. how long can it provide a suitable stable scaffold), and the ability of osteoblastic cells to attach and proliferate on PLA scaffolds.

Project Objectives

The X scaffold was selected for this project due to its customizable stiffness and demonstrated culturability. Utilizing this 3D printed PLA scaffold specimen, the objectives of the project were to:

- 1) assess PLA's sustainability in a physiological-like environment, i.e. does PLA degrade with soak time;
- 2) observe if bone precursor cells (osteoblasts) can attach and survive on PLA.

Methodology Used

Assessment of PLA Sustainability

Eight X scaffold specimens were selected for the assessment of PLA sustainability due to soaking in cell culture media. Specimens were weighted, measured and mechanically tested at the onset of the protocol ($t = 0$ weeks) and at weeks 1-7 and week 10 while continuously soaking in cell culture media in well plates. Three measurements were made for each specimen including the width, depth and height. Mechanical testing was conducted in compression at a displacement rate of 1.27 mm/min using a Mark-10 electromechanical testing machine (Copiaque, NY). Compression test were made between steel plates and specimens were only loaded within the elastic region of the material. Following testing the structural stiffness (Load/displacement) was calculated form the slope of the load-displacement curve within the linear elastic region. Statistical analysis using JMP (SAS institute, Cary, NC) was performed to detect degradation in weight and stiffness with soak time. A significant difference is indicated by $P < 0.05$.

Osteoblast Attachment on PLA

A total of eight PLA specimens were placed in the cell culture protocol. Four of the specimens were cultured with fibroblast as a control and four were cultured with large T transfected human osteoblasts as the test group according to the following protocols. After printing, the X scaffolds were sterilized in

70% isopropyl alcohol for 24 hours then air-dried in a HEPA filtered BL-2 Biosafety cabinet. The last step in sterilization included a two hour UV irradiation in the biosafety cabinet. At the time of plating and co-incubation with sterile scaffolds, cells were viable and proliferating. For both cell lines throughout the study, all recommendations for culturing and passaging of large T antigen transfected human osteoblasts (CRL-11372) by the ATCC and normal human fibroblasts were followed. Individual 3D printed scaffolds were placed in a 12-well plate with five mL of complete growth media, and 5,000 cells/cm² then incubated at 37°C with new media added every two days. After four days of culture the scaffolds were removed from media, fixed in freshly prepared 2% PBS-buffered paraformaldehyde for 15 minutes at room temperature. Scaffolds with attached cells now fixed to the scaffold were rinsed with PBS twice, for five minutes. To assess cell attachment scaffolds were submersed in trypan blue solution, which binds cell structures and allows visualization under light microscopy, then rinsed with PBS for five minutes.

Results Obtained

Results and comparisons are presented here for week 0 and week 10 where the magnitude of the differences should be the greatest of all weeks recorded. Eight scaffolds weights at time = 0 weeks were pooled and compared using ANOVA to their weights at time = 10 weeks (Fig. 1). There was a significant drop in weight, but the drop was small, resulting in a weight reduction of nearly 4 % of the scaffolds average starting weight.

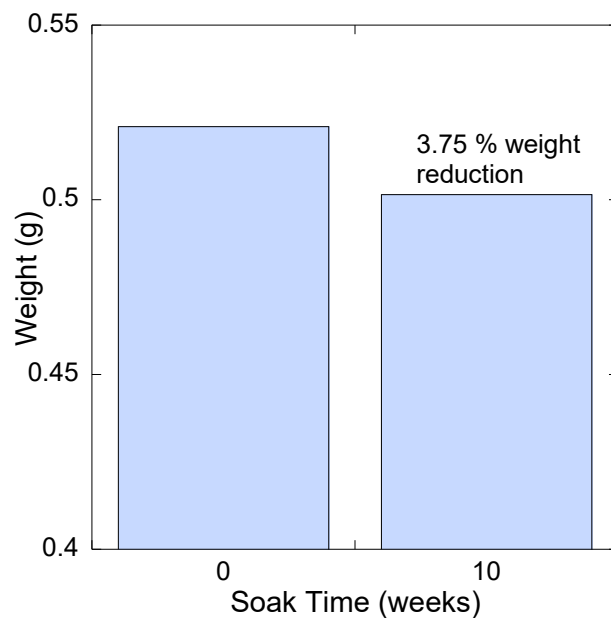


Figure 1. Scaffold weight vs. soak time.

Load and deflections curves were constructed and fits of the linear portions where made. The stiffness values of the scaffolds at time = 0 weeks were compared to the same specimen's stiffness after 10 weeks of soak time. The 0 week scaffold average stiffness was 696 N/mm (± 95 N/mm) while the scaffold with at 10 week soak time had an average stiffness of 750 N/mm (± 87 N/mm). When the two groups were compared using ANOVA, the difference was not significant ($p < 0.26$) (Fig. 2). Increased stiffness with soak time is indicated by increasing slope in the load and deflection curve (Fig. 3).

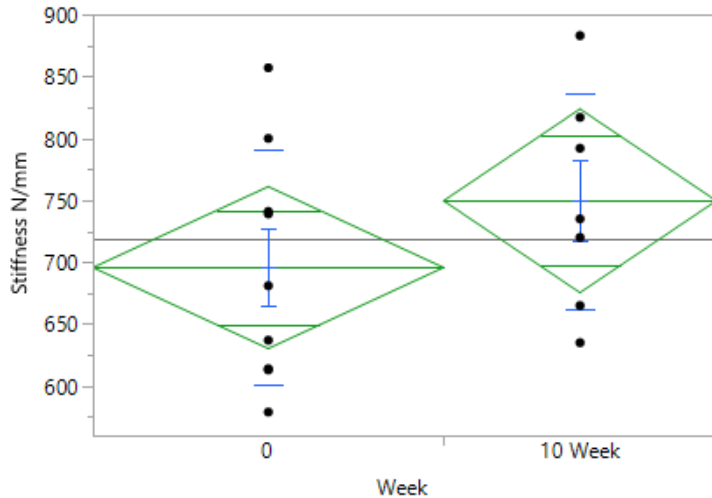


Figure 2. ANOVA of scaffold stiffness showed NSD

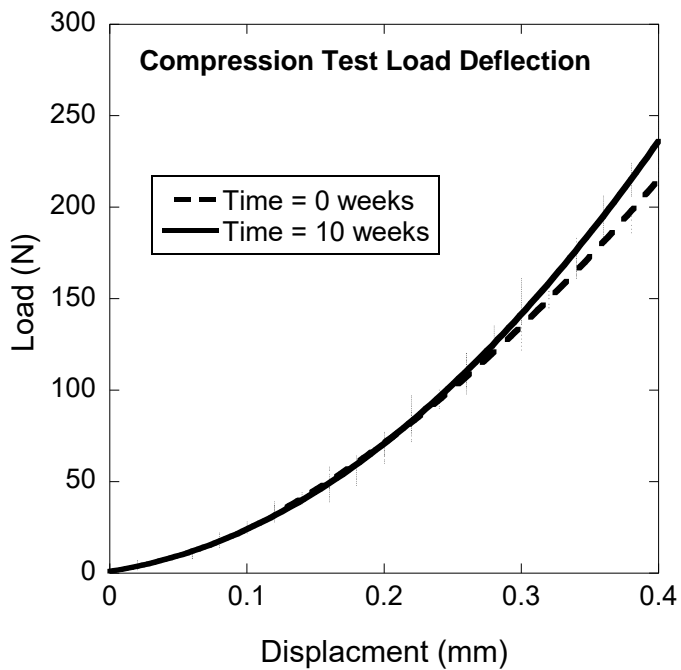


Figure 3. Load-Displacement of scaffolds.

Significance and Interpretation of Results

The first objective of this project was to determine if PLA scaffolds degrade with time while soaking in cell culture media. Results indicated that although minimal weight loss occurs, it appears as though PLA scaffolds tend to get stiffer with soaking. This observed behavior is not fully understood at this time. The second objective of this project was to observe if bone precursor cells (osteoblasts) could attach and survive on PLA. Microscopic evidence showed that large T antigen transfected human osteoblasts attached and survived on 3D printed PLA scaffolds. The frequency and locations mimicked that of fibroblasts which is known to survive and proliferate on PLA.

Acknowledgments

The author would like to acknowledge his co-workers on this project: Sarah Seman, Dr. Rocco Rotello, and Dr. Tim Norman. I would also like to thank the Ohio Space Grant Consortium for the funding that helped make this project possible.

References

1. Cole, J., Martinelli, T., Ryan, M., Seman, S., Sidle, D., Smith, S., Rotello, R., and Norman, T. L., "3D Printed PLA Scaffolds to promote healing of Large Bone Defects," *Research and Scholarship Symposium*, Cedarville University, Cedarville, OH April 2018.

Understanding and Comparing Stars

Student Researcher: Elainie C. Huncik

Advisor: Karen L. Henning

Youngstown State University

Department of Physics & Astronomy, Department of Teacher Education

Abstract

This lesson is based on Ohio's Learning Standards for a high school physical science class. Students will learn how astronomers categorize stars based on their color, temperature, luminosity, size, and mass. Students will also become familiar with Hertzsprung-Russell diagrams. Each student will be assigned a star from a predetermined list of stars and will be tasked with doing research about the properties of the star and compiling the information to share with their classmates. Students may create a poster, presentation, paper, model, etc. to compare their star with others and answer questions about how stars with different properties share some similarities but also have many differences.

Lesson

This three-part lesson does not need to be taught with sessions immediately following one-another and will likely work better if sessions are spread out over a few days/weeks so that students have time to process the new information and work on their project. Sessions can also be broken into multiple parts to allow flexibility with different types of scheduling. In a high school class, this lesson should be done in one to two weeks, depending on the amount of time spent in class.

Session 1 will begin with a student-focused lecture, where the instructor asks the students questions to gauge what they already know about stars. Students will learn what stars are, why we study them, the lifecycles of stars, how to read Hertzsprung-Russell diagrams, and how astronomers categorize stars. If time allows, students should complete the HR Diagram activity attached (with guidance from the instructor) to enforce their understanding of HR Diagrams.

In Session 2, students will begin their projects. This is in-class time for students to work on their projects and receive guidance from the instructor, but students are encouraged to complete their projects outside of class. For the project, students will be assigned a star from a predetermined list of stars and will be tasked with doing research about the properties of the star and compiling the information to share with their classmates. Students may create a poster, presentation, paper, model, etc. to compare their star with others and answer questions from their peers (and their instructor).

Session 3 is the final session, in which students will present their project and be expected to answer questions and compare their stars with other students. This can be done in a similar manner to a poster session, where students are free to move around and look at other projects, or students can present to the entire class. There are benefits to both methods, so the instructor is free to choose based on the capabilities of the class.

Resources & Supplemental Materials

Science mission directorate info:

<https://science.nasa.gov/astrophysics/focus-areas/how-do-stars-form-and-evolve>

HR Diagram activity:

<http://www.mrsgeology.com/wp-content/uploads/2015/08/HR-Diagram-What-Types-of-Stars-are-in-our-Universe.pdf>

<http://www.mrsgeology.com/wp-content/uploads/2015/08/HR-Diagram-Star-Circles.pdf>

<http://www.mrsgeology.com/wp-content/uploads/2014/04/HR-Diagram-Lab-Handout.pdf>

Objectives

Students will understand life cycles of stars and be able to interpret HR Diagrams.

Students will understand the correlation between properties of stars i.e. a star's temperature can be determined by its color and cool, small stars have longer lifespans than hot, massive stars.

Students will practice communicating and comparing scientific information.

Alignment

Ohio Learning Standards: Science – PS.U.3: Stars

NASA Science Mission Directorate: Science

Underlying Theory

This lesson utilizes Universal Design for Learning (UDL) to effectively teach to a wide variety of learners. The lesson plan can easily be modified to accommodate almost any group of students. Because students can use their own approach to the project, they can choose their strongest method so that they can focus on the content of the project rather than struggling with the format or presentation. This lesson can be mostly student-led, so students can stay engaged and explore new information with some guidance from their instructor.

Assessment

Students will be assessed in session 3 when presenting and sharing their projects. Students will be assessed on how well their project meets the requirements set by the instructor, and how well they understand the content of their project based on their presentation and answers to questions.

Conclusion

At the end of this lesson, students will have gained many skills, including interpretation of diagrams, comparison of scientific information, and communication skills. They will understand the lifecycles of stars, how to read HR Diagrams, and what can be learned from properties of stars.

**The Influence of Interfacial Properties on the Propulsion of Active Janus Particles
Near an Air-Water Interface**

Student Researcher: Marola W. Issa

Advisor: Christopher L. Wirth

Cleveland State University
Department of Chemical and Biomedical Engineering

Abstract

Self-propelled or “active” micrometer scale particles are capable of supplying local mechanical work necessary for micro-scale cargo delivery and useful in other applications within bio imaging and sensing [1]. These particles, typically with chemical or geometric anisotropy, have the potential to transform applications in chemical, and medical drug delivery as analogous for molecular scale phenomena and in consumer products [2]. Additionally, they could also be used as models to study the dynamics of biological systems such as bacterial colonies at interfaces [3]. Research in the last decade focused on developing, measuring and manipulating the locomotion mechanisms of active particles in simple environments. However, most applications will be in complex environments with nearby boundaries or variations in physiochemical cues such as viscosity and density. The objective of this project is to measure the impact of interfacial forces on the propulsion of catalytic active Janus particles near boundaries. This report summarizes my work on catalytic active Janus particles consisting of polystyrene beads with a platinum cap. Initially, I will summarize some of my previous work showing the impact of charged nanoparticles on the propulsion of active colloids at a fluid-solid interface. I found the addition of charged nanoparticles and polymers to reduce the speed of propelling particles as a consequence of both changes in conductivity and the mobility of the active particle. Additionally, the report will summarize work from the current project, which seeks to analyze the swim dynamics of active particles near an air-water interface populated with a surface-active agent “surfactant”. Surfactants, such as Sodium dodecyl sulfate (SDS) are analogous to microbially produced substances that are secreted by *Pseudomonas aeruginosa* as anionic amphiphilic molecules. The presence of these naturally occurring surfactants are thought to influence the way microorganisms swim and interact with water-air interfaces. Analysis of particle sedimentation patterns showed the degree of sedimentation decreased with increasing surfactant concentration. Additionally, an increase in propulsion speed was also observed to cause the suspension to mildly or strongly mix and further decreased the sedimentation strength.

Project Objectives

The objective of this project is to measure the impact of interfacial forces on the propulsion of catalytic active Janus particles near boundaries.

Methodology

The fabrication process of Janus particles involved the formation of a monolayer of polystyrene particles, which were deposited onto a silicon wafer using a spin coater (Figure 1A). The next step of fabrication utilized physical vapor deposition (PVD) in which a 20 nm platinum layer was deposited onto the polystyrene spheres (Figure 1B). Finally, the Janus particles were re-dispersed by first submerging the wafers in ultrapure water using a 50 mL centrifuge tube. The tubes were sonicated for ~45 minutes to ensure maximum desorption of particles (Figure 1.C). Lastly, the suspension containing the Janus particles was then centrifuged, and the supernatant was removed. The process was repeated twice, and the finally collected volume was concentrated into a 1 mL suspension consisting of Janus particles and ultrapure water.

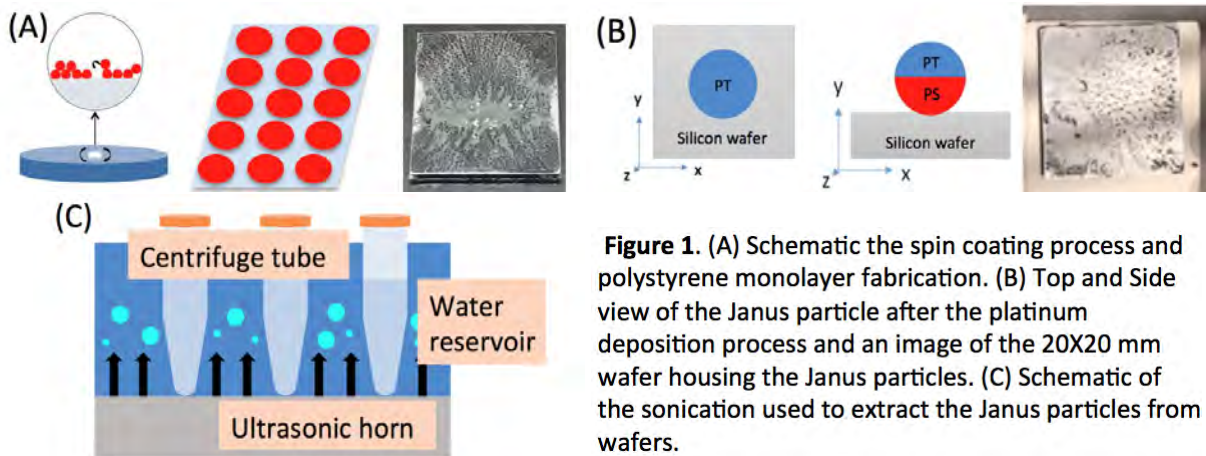


Figure 1. (A) Schematic the spin coating process and polystyrene monolayer fabrication. (B) Top and Side view of the Janus particle after the platinum deposition process and an image of the 20X20 mm wafer housing the Janus particles. (C) Schematic of the sonication used to extract the Janus particles from wafers.

Preparation of Fluid Cell and Image Collection

At solid-fluid interface: Experiments at solid-fluid interface were conducted in a fuel cell, which was installed onto a microscope slide using a secure-seal spacer with a 9mm diameter and a 0.12 mm depth and coverslip on top as can be seen in Figure 2 (A). Images were collected and analyzed at a frame rate of between 2.6 and 16.2 frames per second of an infinitely dilute suspension of particles settled near a boundary. A total of 81 videos at various conditions were obtained, with the majority containing >1000 frames or more and between 1 and 5 particles in the region of interest for the entire video. The 5 μ m diameter particles were initially identified and processed using ImageJ software and particle trajectories were then tracked using an existing algorithm executed in MATLAB. Figure 2 (B) and (C) show micrographs of tracked particles coupled with their corresponding trajectories.

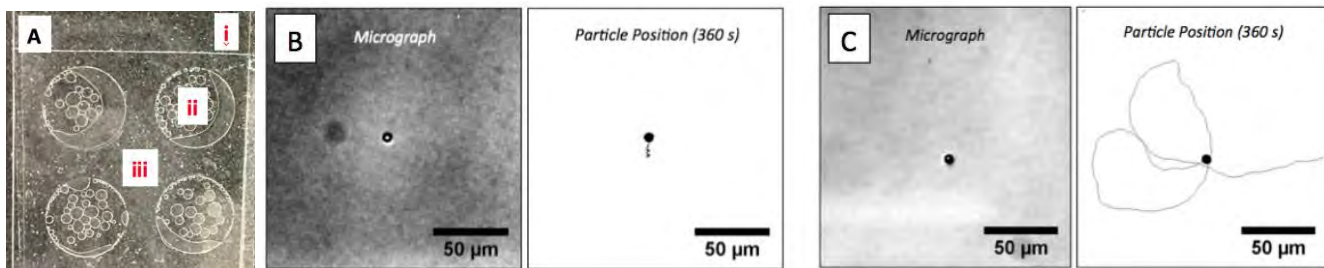


Figure 2. (A) An image of fluid cell with (i) Microscope slide, (ii) Fluid cell, and (iii) Cover slip. (B) ~5 mm non-Janus polystyrene particle in the absence of fuel. (C) ~5 mm Janus polystyrene particle in 5% H₂O₂ fuel.

At fluid-fluid interface: Initially, the 50 mm capillary tubes were cleaned with a methanol-water mixture followed by ultrapure water to ensure no contaminants are left on the surface. This is important because impurities could potentially alter the chemistry or composition of the suspension. Next, the tubes were partially submerged in a salinizing agent in order to coat ~80% of the inner walls. The colloidal suspension was first transferred to 1 mL centrifuge tube where the desired amount of hydrogen peroxide was added and the constituents were vortex mixed for ~3 seconds to ensure proper integration of components. Lastly, the suspension was pipetted into the region of capillary tube not treated with salinizing agent and the tube was sealed with wax to prevent the suspension form escaping once the tube is inverted (Figure 3). Images were collected and analyzed at a frame rate of 1 frame per second for all experiments. A total of 31 videos at various conditions were obtained, with the majority containing ~1000 frames. The collected videos were then processed using ImageJ software and particle trajectories were plotted for each experiment.

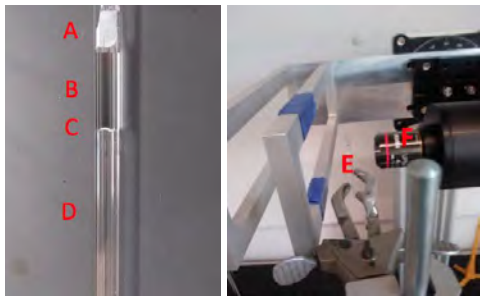


Figure 3. Capillary tube and experimental set up.

- (A) Wax
- (B) Colloidal suspension
- (C) Liquid-Liquid interface
- (D) Atmospheric air
- (E) Capillary tube
- (F) Microscope objective

The obtained results were further classified in order to analyze the effects of SDS on active particle dynamics. The classification of particle sedimentation patterns has three subsections: strong sedimentation, mild convection, and strong convection. Sedimentation was considered to be strong with little to no mixing, if the observed trajectories were seen to be straight and with minimal crossing. Moreover, suspensions were considered to have strong convection if the trajectory lines were observed to mix and recirculate in the suspension. As for the mild convection classification, it included all experiments that didn't fall into either of the two extreme cases. Below is a figure (Figure 4) denoting an example of each of the three classifications. The black region, which is seen in the lower portion of the images, is the atmospheric air. The gray region above it is the colloidal suspension. Note: Sedimentation is occurring in the downward direction similar to direction of gravity and the particle trajectories are seen as streaks (lines) throughout the suspension.

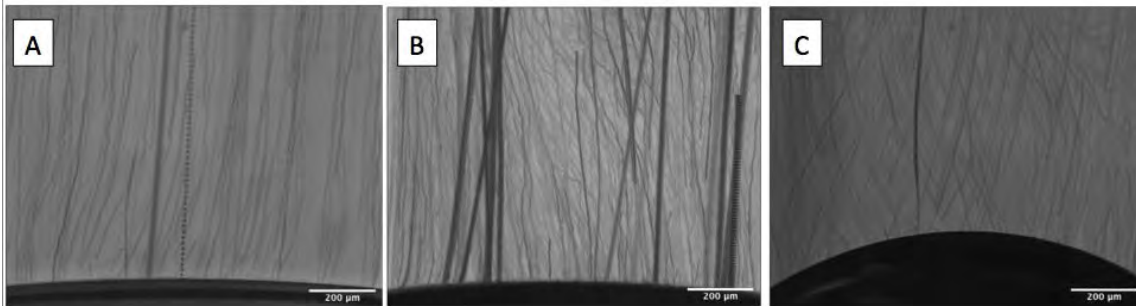


Figure 4. Particle sedimentation classifications (A) strong sedimentation. (B) Mild convection. (C) Strong convection.

Results for Analysis at Solid-fluid Interface

It was observed that an increase in fuel concentration (H_2O_2) has a direct impact on the propulsion speed of active Janus colloids. Note: Our platinum-coated polystyrene Janus particles can actively swim via a propulsion method known as self-diffusiophoresis. Diffusiophoresis is defined as the spontaneous motion of colloidal particles in a fluid, induced by a concentration gradient of a different substance, which in this case is air bubbles. Moreover, the platinum cap acts as a catalyst and breaks down hydrogen peroxide (H_2O_2) into oxygen bubbles and water allowing for the active motion to transpire. Moreover, the acquired speed data for 0.1%, 0.5%, 1% and 5% concentration of H_2O_2 showed that the apparent propulsion speed increased linearly with increasing fuel concentration (Figure 5). Additionally, negatively charged nanoparticles were introduced to the media to study the effects of depletion attraction on the propulsion of active Janus particles. A depletion force is an effective attractive force that arises between large colloidal particles that are suspended in a dilute solution of depletants, which are smaller solutes that are preferentially excluded from the vicinity of the large particles [4]. This was accomplished by introducing 20 nm diameter sulfate-modified polystyrene particles to the suspension of active particles. The addition of depletants caused the Janus particles to move closer to the solid boundary because of increased attractive interactions between the particle and wall. The decrease in average separation distance was nonmonotonic, which could result from structural forces that arise in suspensions of strongly charged nanoparticles (Figure 6). Similarly, the

diffusion coefficient, which is an indicator of swimming activity, was also analyzed and seen to decrease with increasing depletant volume fraction.

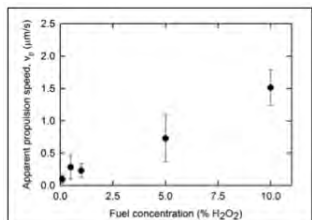


Figure 5. Apparent speed for various H₂O₂ concentrations.

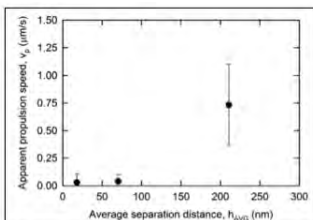


Figure 6. Apparent speed for various separation distances

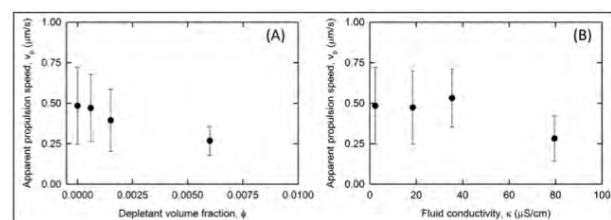


Figure 7. (A) Apparent propulsion speed for Janus particles in uncharged depletant poly(ethylene glycol) (PEG) and (B) NaCl.

Additionally, the agent based simulations using separation distances inferred from experimental findings further showed a similar trend in decreasing propulsion speed after the addition of nanoparticles. However, the reduction in speed was smaller which suggested some influence of hydrodynamic interactions on the swim speed when the particles were brought closer to the boundary. Supplementary control experiments were conducted in order to separate the effect of conductivity and depletant concentration on particle speed. It was observed that the addition of polyethylene glycol (PEG) particles with low conductivity < 10 um/cm resulted in decreased propulsion speed which validated the effects of depletion attractions as a method for quenching. Similar experiments were conducted utilizing various concentrations of sodium chloride (NaCl) thus varying the conductivity of the suspension. Data analysis showed that an increase in fluid conductivity resulted in decreased active particle motion (Figure 7).

Results for Analysis at Fluid-Fluid Interface

The analyzed data has shown that the Janus (Non-active) particles with 0mM SDS were all observed to have strong sedimentation. Additionally, an increase in the surfactant concentration for non-active particles was seen to reduce the sedimentation strength and introduce some degree of particle mixing. As for the active particles, it was concluded that an increase in propulsion speed, in comparison with non-active particles, had also introduced some degree of mixing which varied between mild and strong convection. The strongest convection (mixing) was observed for active particles with the highest percent concentration of SDS. The figure below (Figure 8) represents a phase diagram of the analyzed data.

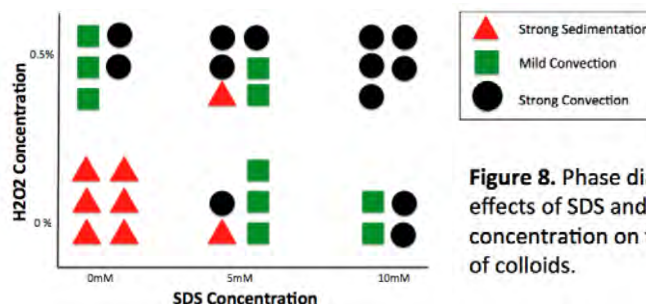


Figure 8. Phase diagram representing the effects of SDS and Hydrogen peroxide concentration on the sedimentation dynamics of colloids.

Acknowledgments

Research described in this report, was supported by the National Aeronautics and Space Administration (NASA), through its National Space Grant College and Fellowship Program, and Cleveland State University. Special Thanks to Dr. Christopher Wirth for guidance in carrying out the project and data analysis.

References

1. Issa, M. W.; Baumgartner, N.; Kalil M.; Shawn, D. R.; Wirth, C. L. Charged Nanoparticles Quench the Propulsion of Active Janus colloids. *ACS Omega* 2019, **4**, 13034–13041.
2. Rashidi, A.; Issa, M. W.; Martin, I. T.; Avishai, A.; Razavi, S.; Wirth, C. L. Local Measurement of Janus Particle Cap Thickness. *ACS Appl. Mater. Interfaces* 2018, **10**, 30925–30929
3. Toner, J.; Tu, Y. Long-Range Order in a Two-Dimensional Dynamical XY Model: How Birds Fly Together. *Phys. Rev. Lett.* 1995, **75**, 4326–4329.
4. Mao, Y.; M.E. Cates; H.N.W. Lekkerkerker (May 1995). "Depletion force in colloidal systems". *Physica A*. **222** (1–4): 10–24.

The Effect of Diabetes Mellitus on Bone Fracture

Student Researcher: Laura R. Jackam

Advisor: Dr. Anne Loucks

Ohio University
Department of Biological Sciences

Abstract

The mechanical property of bone strength cannot be measured directly *in vivo* because the gold standard method for measuring bone strength and stiffness, known as Quasi-static Mechanical Testing (QMT), requires the bone to be removed from the body and fractured. Mechanical Response Tissue Analysis (MRTA) was developed in the 1980s to measure the flexural rigidity (EI) of long bones *in vivo* in a non-invasive manner, but MRTA measurements were found not to be accurate or reproducible. Dr. Anne Loucks and colleagues at Ohio University identified sources of error in MRTA and corrected them in Cortical Bone Mechanics Technology (CBMT). This technology provides a clinical way of measuring ulna's EI *in vivo*, which can then be used to accurately predict the ulna's bending strength (i.e., the peak moment before fracture, M_{peak}). For this study, CBMT and QMT data were compiled on ulnas in nine pairs of diabetic and non-diabetic male cadaveric human arms and ImageJ software was used to measure their interosseous diameter (IOD). The CBMT and QMT data include ulna EI and M_{peak} . Statistical analyses were performed comparing the effects of ulna IOD, body mass index (BMI) and age on M_{peak} , EI_{CBMT} , EI_{QMT} , bone stiffness (K_b), and bone damping (B_b) between diabetic and non-diabetic male cadaveric human arms.

Project Objectives

Diabetes mellitus is a disease characterized by insulin deficiencies which affect the metabolism of glucose and if uncontrolled, this disease can lead to retinopathy, neuropathy, nephropathy, and death. The disease is divided into multiple classes, with type 2 being the most prevalent diagnosis. Over half a billion of the global population suffers from type 2 diabetes. (Kharroubi, et al 2015) Although medicine today has improved the survival rate of diabetes patients, they must be aware of diabetic complications as well as osteoporosis and their increased bone fracture risk (Poiana, et al 2017). The micro architectural changes of the bone due to diabetes which decrease structure quality and strength is known as diabetic osteopathy. Most type 2 diabetes patients have an elevated bone mineral density (BMD). BMD is the current technology used for osteoporosis diagnosis. A high BMD would suggest that the patient is at low risk for osteoporosis and therefore bone fracture, yet type 2 diabetes patients continue to fracture at increased rates. (Moayeri, et al 2017) Although an osteoporosis diagnosis is based on BMD, studies are beginning to show that the mechanical properties and micro architecture of bone need to be considered when predicting fracture risk (Bowman, et al 2019).

The goal of this study is to test the hypothesis that diabetes changes the effects of IOD, BMI, and age on M_{peak} . It will be concluded that diabetes changes these effects, if the slopes and/or Y-intercepts of the regression lines relating IOD, BMI, and age to EI_{CBMT} , EI_{QMT} , K_b , B_b , or M_{peak} are different in ulnas from diabetic and non-diabetic arms. If so, in future clinical settings, diabetes patients could be made more aware of their risk of bone fracture by using CBMT to measure ulna EI .

Methodology

In 2013, 35 fresh-frozen cadaveric arms of large men and small women were obtained from the human tissue bank (Science Care, Inc. Phoenix, AZ). Arms needed to have a history free of bone cancer or cancer that could metastasize to bone, bone breaks, or a freeze date later than nine days post-mortem. (Bowman, et al 2019) In 2018, eight additional pairs of fresh frozen male cadaveric arms were obtained from the same human tissue bank used in 2013. Donors needed to weigh over 79.5 kg and have a no history of arm fracture or cancer affecting the bone.

In 2013 and 2014, the cadaveric arms were stored at -20 °C until CBMT testing. The arm was thawed, and the upper arm was defleshed. The hand was removed from the arm and the forearm defleshed, exposing the ulna bone. In addition, the radius bone was cut at the radial tuberosity to prevent the loss of mechanical integrity and axial rotation of the ulna. The ulna was positioned horizontally, with the distal radius directly beneath it and support at the elbow and wrist. The styloid process of the radius rested on a vertical block at the wrist and the humerus was secured vertically with a bone clamp. Wide rubber strips were placed over the ulna and used to substitute for skin because the tissue had been removed. A load was applied onto the ulna at its midpoint. The blunt probe with a mechanical shaker was placed over this point so that when it lowered, it applied a static load, limited to 24 N, and shook once contact was made with the forearm. An acceleration frequency response function (FRF) was generated at each site in a transit across the midpoint of the ulna. The location and shape of this function were determined by mechanical properties of skin and bone, as well as the static load applied at the midpoint. (Bowman, et al 2019)

The CBMT data collection and analysis in 2018 were similar to the guidelines used in 2013 and 2014 except that the automated Prototype 3 was used instead of the manual Prototype 2. The ulna was supported on the proximal end by the humerus and the distal end by a metal platform. The humerus was held in place by an apparatus with a pin placed through the humeral epicondyles. The ulna was checked repeatedly for levelness. Loads of 10, 15, and 20 N were applied at 50% of the ulna length. The humerus was wedged to reduce excessive vibrations. One of each pair was soaked in saline for 39 hours while the other was soaked in a KOH solution. The arms soaked in the KOH solution were not included in this study due to collagen degradation from KOH. (Custer, 2019).

After CBMT testing, QMT data were collected using an MTS QTest-Elite load frame from the MTS Systems Corporation in Minnesota to control displacement. Before the ulna was fractured at its maximum strength, loading cycles of 0 to 100 N were performed on it to record the load-displacement slopes at 50% of the peak load. This process was repeated until the coefficient of variation in the last 5 cycles was less than 1%. The fracture cycle was then performed where the load was increased until the ulna fractured. The ulna bending strength known as the peak moment (M_{peak}) was found from QMT using the formula { $M_{peak} = F_{peak} \times L/4$ } where L was the length of the ulna measured by the calipers and F_{peak} was the force required to fracture the ulna. The maximum value of tangent stiffness, plotted as a function of load, provided a measure of K_b . (Bowman, et al 2019) In 2018, QMT used the same humerus holding device as CBMT. The procedure on the second day of testing, after the soak, did not differ from the 2013 and 2014 cadaveric arms. Graphs of load versus displacement were generated and the peak stiffness was used to calculate EI. To calculate ulna flexural rigidity (EI) the following formula { $EI = K_b \times L^3/48$ } was used where L was the length of the ulna. Since CBMT was modeled after MRTA, the forearm was modeled as a 7-parameter mechanical skin-bone system. The parameters used were the mass, stiffness, and damping of the skin (M_s, K_s, B_s) and ulna bone (M_b, K_b, B_b), and damping of the peripheral soft tissue (B_p). These values were estimated by fitting them onto stiffness and compliance frequency response functions (FRF). (Custer, 2019).

To obtain images of the ulna for IOD calculations, a μ CT scan of a segment of the ulna or a CT scan of the arm was made as described previously (Hausfeld, 2015). The program ImageJ was used to visualize the μ CT scans of 2013 and 2014, and the CT scans of 2017 and 2018. (Bowman, 2019) The greatest diameter of the ulna was used as the IOD.

Each male diabetic cadaveric arm was paired with a male non-diabetic cadaveric arm based on the closest match, or lowest difference, of IOD, body mass index (BMI), and age. If multiple diabetic arms shared the same non-diabetic comparison arm, the diabetic arm with the greatest difference when compared to all non-diabetic arms was selected for the pairing. This selection process repeated until all diabetic arms had an unshared non-diabetic comparison arm. The effect of diabetes on the influence of IOD, BMI, and age on M_{peak} , EI_{QMT} , EI_{CBMT} , and K_b was determined by regression analysis. The differences of the means and slopes were determined by paired and unpaired T-tests.

Results

After analyzing Figure 1, one can see that overall, as IOD increased, M_{peak} or bone strength increased. When comparing the Standard Error of Estimates (SEEs) and slopes between the diabetics and non-diabetics, it became apparent that diabetes does have a reducing effect on the influence of IOD on M_{peak} or bone strength. Figures 2, 3 and 4 also showed diabetes's reducing effect on the influence of IOD over EI_{QMT} , K_b , and B_b respectively. IOD is an aspect of bone geometry unlike BMI or age. This means that the ability of bone geometry to predict M_{peak} is lost in diabetes. Diabetes had the largest effect on bone damping (Figure 4). Additional analysis showed that CBMT measurements of ulna damping were 25% lower in ulnas of nine donors with Type 2 diabetes than in ulnas of the same size in arms of donors without diabetes ($p=0.03$). Bone damping is a property of bone protein, and the elevated fracture risk in patients with Type 2 diabetes is attributed to the decoration of collagen with advanced glycation end products (AGEs) (Acevedo, et al 2018). In addition to IOD, BMI and age were analyzed. With BMI, no effect of diabetes was observed except that diabetes reduced the influence of BMI on EI_{QMT} and B_b respectively. An increase in BMI generally led to an increase in M_{peak} , EI , and K_b . Age had similar results where diabetes did not affect the influence of age on M_{peak} , EI , and K_b except that diabetes had a reducing effect on the influence of age on B_b . As age increased, M_{peak} decreased while age had the opposite effect on EI and K_b . This enforces that age was a very weak predictor of ulna strength, along with high SEEs, because of the many different sizes and body types associated with every age. The next step of this study would be to obtain a larger sample size than 9 of type 2 diabetic male cadaveric arm specimens with a wider range of IODs and rerun regressions to see how diabetes affects the influence of IOD on M_{peak} , EI , K_b , B_b .

Figures

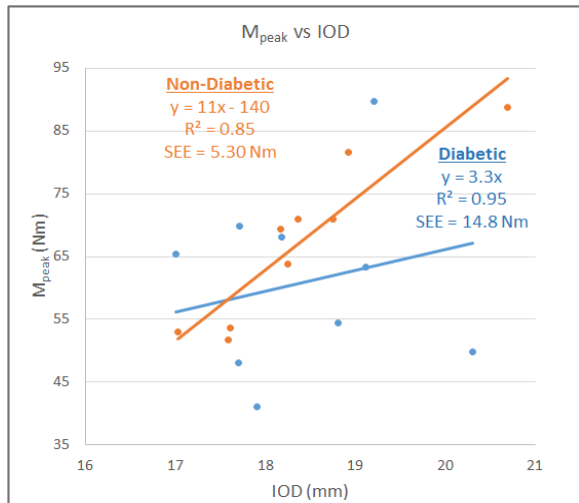


Figure 1. The Effect of Diabetes on the Influence of IOD on M_{peak}.

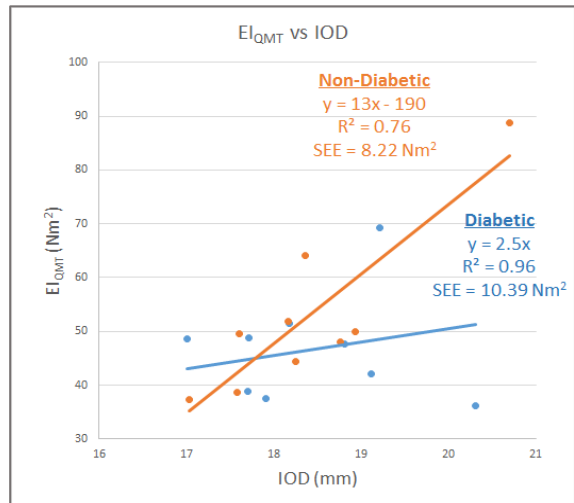


Figure 2. The Effect of Diabetes on the Influence of IOD on EI_{QMT}.

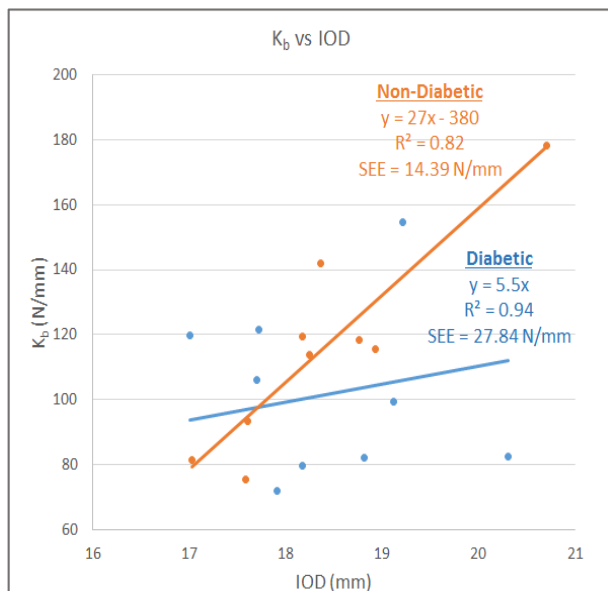


Figure 3. The Effect of Diabetes on the Influence of IOD on K_b.

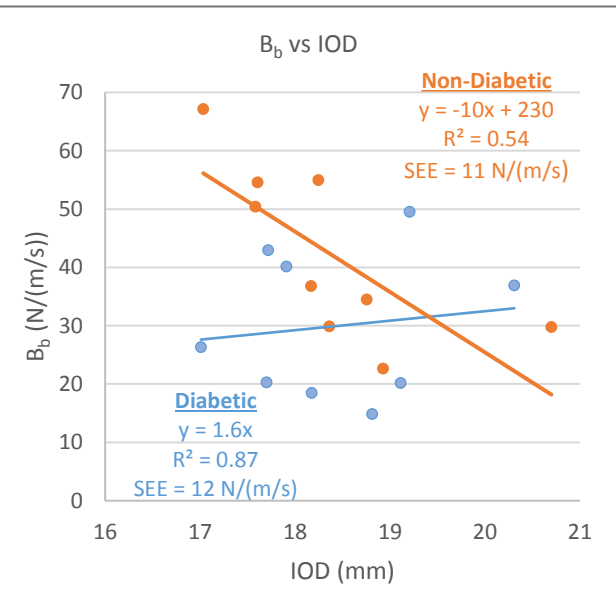


Figure 4. The Effect of Diabetes on the Influence of IOD on B_b.

Acknowledgments

The author of this paper would like thank Ohio Space Grant Consortium, Dr. Anne Loucks, Lyn Bowman, and Erica Custer for their guidance and support during this project.

References

1. Acevedo C, Sylvia M, Schaible E, Graham JL, Stanhope KL, Metz LN, et al. Contributions of material properties and structure to increased bone fragility for a given bone mass in the UCD-T2D rat model of type 2 diabetes. *J Bone Miner Res.* 2018;33(6):1066–75.
2. Bowman, L., Ellerbrock, E. R., Hausfeld, G. C., Neumeyer, J. M. & Loucks, A. B. A new noninvasive mechanical bending test accurately predicts ulna bending strength in cadaveric human arms. *Bone* 120,336–346 (2019).
3. Custer, EM. (2019). Cortical bone mechanics technology and quasi-static mechanical testing sensitivity to bone collagen degradation (embargoed thesis). Ohio University, Athens, Ohio.
4. Hausfeld, G.C., 2015. Comparison of Cortical Porosity, Diameter, and Stiffness as Predictors of Ulna Bending Strength, Electronic Thesis. OhioLINK Electronic Theses and Dissertations Center, Ohio University.
5. Kharroubi, A. T. Diabetes mellitus: The epidemic of the century. *World Journal of Diabetes* 6,850–867 (2015).
6. Moayeri, A. et al. Fracture risk in patients with type 2 diabetes mellitus and possible risk factors: a systematic review and meta-analysis. *Dove Press Journal: Therapeutics and Clinical Risk Management* 13,455–468 (2017).
7. Poiana, C. & Capatina, C. Fracture Risk Assessment in Patients With Diabetes Mellitus. *Journal of Clinical Densitometry: Assessment & Management of Musculoskeletal Health* 20,432–443 (2017).

Uncovering the Recipe for Synthetic Mineral Water

Student Researcher: Mystal Jackson

Advisor: Dr. Regan Silvestri

Lorain County Community College
Associate of Science Program

Abstract

Mineral waters may contain various salts including sodium chloride, potassium chloride, calcium chloride and magnesium chloride. Furthermore, mineral waters may contain various sulfates and bicarbonates. Atomic Absorption (AA) spectroscopy and Inductively Coupled Plasma (ICP) spectroscopy are being used to identify and quantify the various minerals in selected commercially available mineral waters. Further, blind taste tests are being conducted on the mineral waters to identify user preference for flavor. Ultimately, a statistical correlation will be drawn between the analytical data and user preference, identifying what minerals are preferred for taste and in what quantities.

Project

Sodium, commonly known as salt, comes in many forms including but not limited to table salt, Himalayan pink salt, kosher salt, sea salt and Celtic salt. Sodium is a common element that is important to the human body, needed to control fluid levels, maintain blood pressure and for nerve and muscle function. The flavor of mineral water is important because people will repeatedly choose what tastes good to them. Taste tests are being carried out by multiple test subjects on campus and the data is being recorded; this tells us which water the majority think tastes better. Spectroscopy is being used to analyze and quantify the minerals in various water samples, -to tell us what's in it and specific amounts. The analytical data is being compared to the taste test results and a correlation drawn, which in turn tells us what people prefer to taste in their water. We are de-formulating the recipe for the best tasting mineral water and using this information to create our own synthetic mineral water.

Effect of DNA Methyltransferase Inhibition in Hypoxic and Normoxic Conditions on Cellular Proliferation and Potential Growth Regulators in Human Diffuse Intrinsic Pontine Gliomas

Student Researcher: Madison M. Jewell

Advisor: Dr. Robert Lober, M.D., Ph.D.

Wright State University
Neuroscience, Cell Biology, and Physiology

Abstract

Diffuse intrinsic pontine gliomas (DIPGs) are aggressive, infiltrative pediatric brain tumors that contain an abysmal survival rate of less than 1-year. A distinct and abnormal genetic profile of DIPG is evident in which the most commonly observed mutation occurring in over 80% of DIPGs is a methionine substitution at lysine 27 on histone H3 (H3.3K27M), resulting in observed global reduction of H3K27me2/3 and central gain of H3K27me3. In particular, variations in expression of p16/ink4A, a tumor suppressor and critical cell cycle regulator of the G₀-G₁ to S-phase transition, have been observed and a mechanism of H3.3K27M-induced repression of p16/ink4A has been proposed in which a DNA methyltransferase inhibitor rescued p16/ink4A expression, thus restoring cell cycle regulation and tumor suppression capabilities. Regions of hypoxia are evident within the solid tumor microenvironment of DIPGs and are associated with the distinct epigenetic profile and therapeutic resistance observed. Despite the global hypomethylation observed in DIPGs, hypoxic regions are classically hypermethylated, highlighting the importance of determining the efficacy of a DNA methyltransferase inhibitor in both normal and low oxygen states. This study sought to investigate the effects and treatment efficacy of DNA methyltransferase inhibition on the overall proliferation of H3.3K27M expressing DIPG cells as well as the expression of p16/ink4A in both normoxic and hypoxic regions.

Project Objectives

The objective of this project was to investigate the epigenetic changes and overall cellular proliferation that occurs upon treatment of human diffuse intrinsic pontine glioma cell lines with increasing concentrations of a DNA methyltransferase inhibitor, decitabine. Prior studies utilizing murine models displayed evidence at the p16 promoter for increased levels of H3K27me3 in conjunction with H3.3K27M induced targeted repression of p16/ink4a, a tumor suppressor and critical cell cycle regulator of the G₀-G₁ to S-phase transition. Loss of p16/ink4a is associated with accelerated tumorigenesis and thus it was suggested rescuing p16/ink4a with decitabine as a potential therapeutic avenue in treatment of DIPG tumors harboring p16/ink4a repression. We sought to investigate the effect of a DNA methyltransferase inhibitor on epigenetic changes shown to promote tumor growth and disease progression as well as evaluate the overall cellular proliferation in both normoxic and hypoxia-induced human DIPG cells.

Methodology

A line of human DIPG X cells were utilized in the evaluation of protein expression through western blot analysis. The cells were treated in ten-fold increasing concentration of decitabine ranging from 0.001 micromolar to 10 micromolar in addition to a DMSO treated vehicle. One set of cells were treated in 24 hour pulse hypoxia (0.5% O₂) while another were incubated in a normal oxygenated environment. Lysates were then collected and BCA calculations ensued utilizing the Pierce BSA kit. Western blot results for cells treated in normoxic conditions are shown below in Figure 1, and western blot results for cells treated in hypoxic conditions are shown below in Figure 2.

To evaluate the viability and cellular proliferation following treatment in ten-fold increasing concentration with decitabine as performed prior, a dose response curve over a five day period was obtained utilizing Trypan Blue Assay on human DIPG IV cells. Three trials were performed in normoxic conditions and the analyzed results are shown in Figure 3. Due to logistical difficulty attaining the necessary gas for the hypoxic chamber, only one trial of Trypan Blue Assay pulse-hypoxia (0.5% O₂) and decitabine treated DIPG IV cells was able to be performed. The un-analyzed results are shown below in Figure 4. A comparison of the percent viability between decitabine treated human DIPG IV treated in hypoxia and normoxia occurred and is shown in Figure 5.

Results

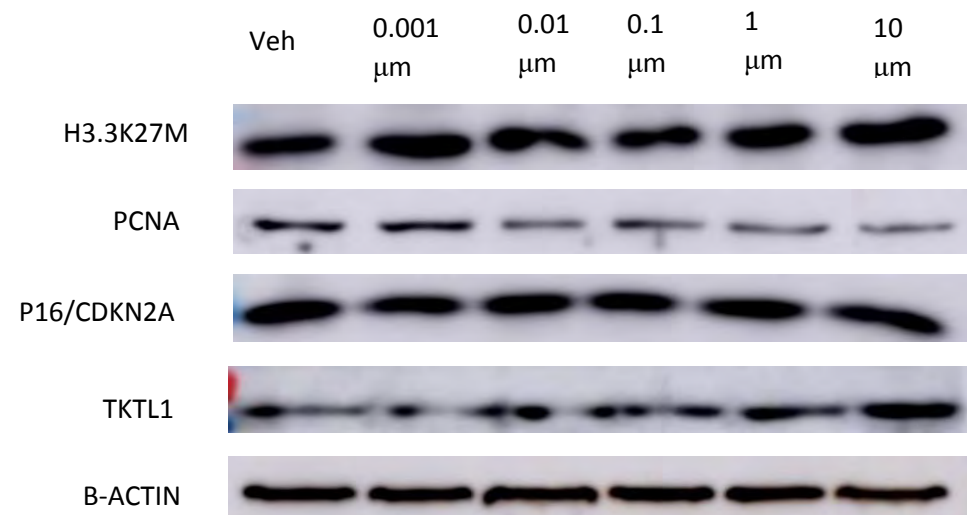


Figure 1. Protein expression with increasing decitabine concentration in human DIPG X cells treated in normoxic conditions.

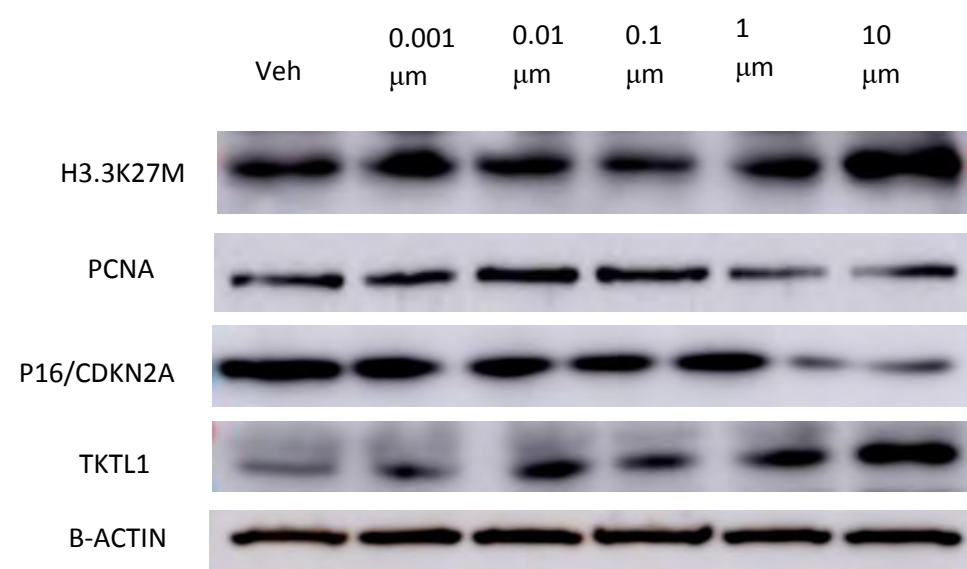


Figure 2. Protein expression with increasing decitabine concentration in human DIPG X cells treated in hypoxic conditions (0.5% O₂ 24 hr).

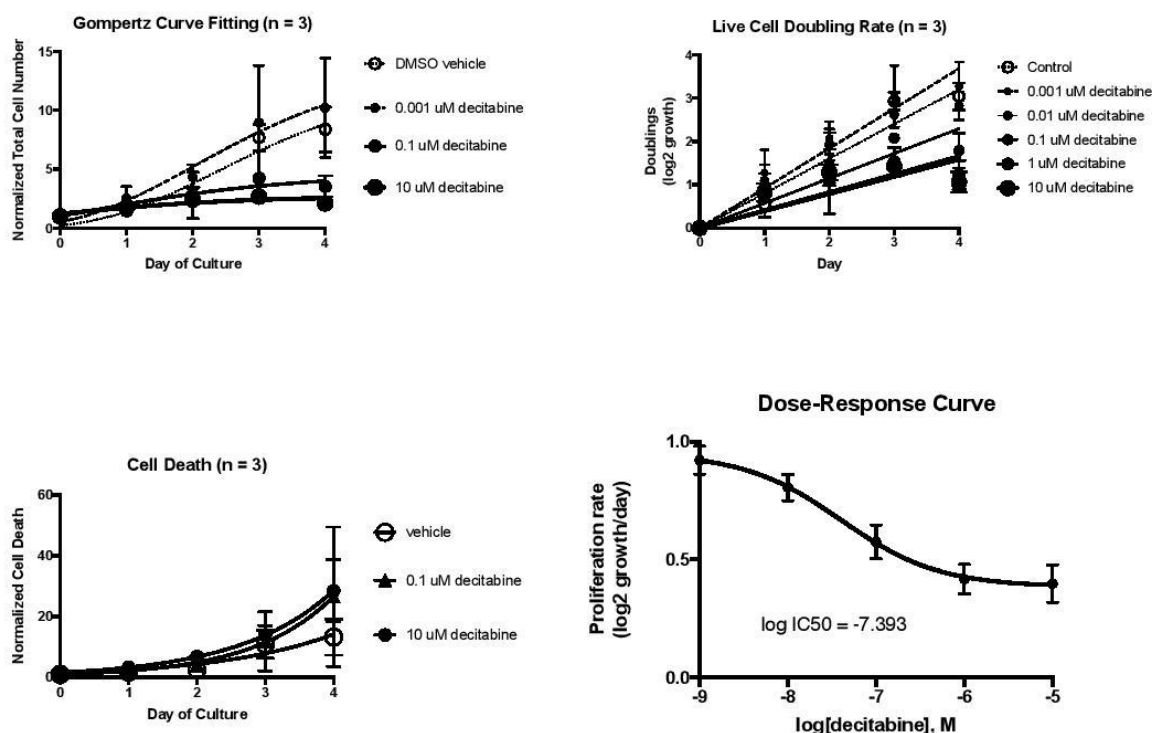


Figure 3. Analyzed trypan blue assay data of total cell number, cell death, live cell doubling rate and dose-response curve for human DIPG IV cells (n=3).

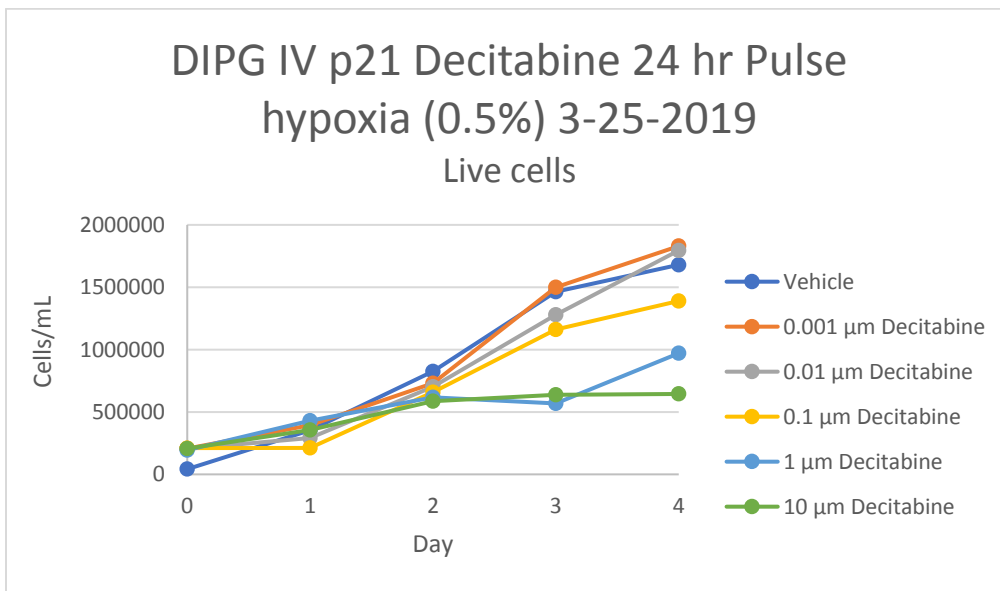
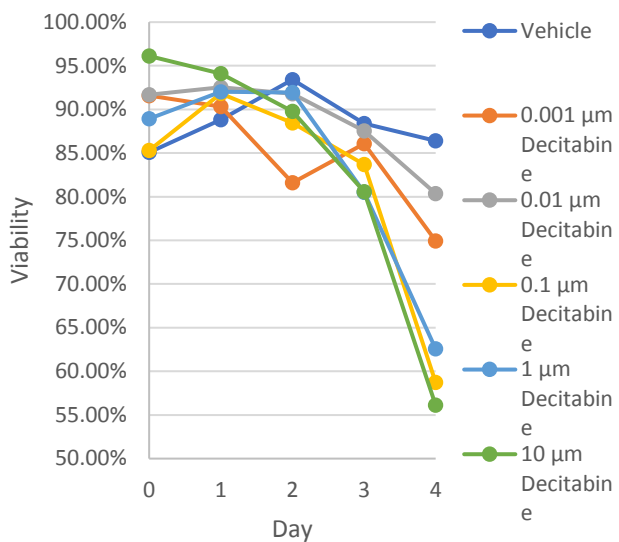


Figure 4. Un-analyzed data for trypan blue assay dose-response of pulse hypoxia (0.5% O₂ for 24 hr) and decitabine treated human DIPG IV cells (n=1).

DIPG IV Decitabine Dose Response Normoxia Viability



DIPG IV Decitabine 24 Hr Pulse Hypoxia(0.5%) Dose Response Viability

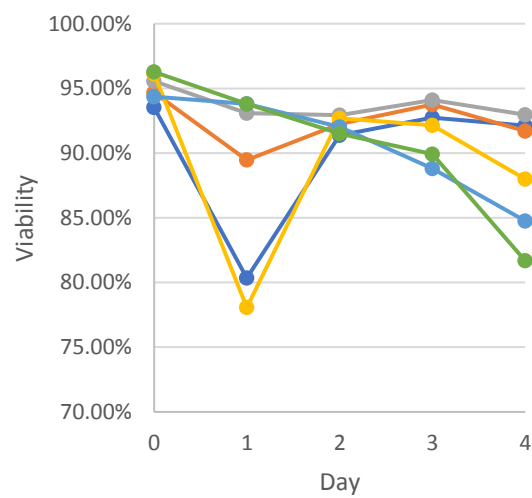


Figure 5. Viability comparison for decitabine treated human DIPG IV cells in hypoxic and normoxic conditions.

Significance and Interpretation

Upon western blot analysis, p16 expression was shown in human DIPG X lines with no considerable changes in expression following decitabine treatment in a normoxic environment. However, expression of p16 appeared to decrease with increasing decitabine concentration in hypoxic conditions. Additional trials will follow to confirm this result. Whether or not the observed expression of p16 is considered repressed compared to normal brain tissue is yet to be determined and could be a possible explanation for the repression observed in prior studies.

The expression of proliferating cellular nuclear antigen (PCNA), which is associated with cellular proliferation and DNA replication, was found to decrease in both normoxic and hypoxic cells, with less decreased repression in hypoxia-treated cells. Decreased DIPG IV cell viability was observed in the trypan blue assay for cells treated in the normoxic conditions as opposed to a higher percent viability of cells treated in hypoxic conditions. This proposes the possibility of decreased efficacy of DNA methyltransferase inhibition in hypoxic conditions, suggesting varying methylation patterns occur between hypoxic and normoxic environments. The variation in methylation pattern was further investigated with the expression of TKT1, a protein responsible for sensitizing cells to hypoxia and is activated by hypomethylation. Increased expression of TKT1 was observed in both normoxia and hypoxia treated cells with increasing decitabine concentration. A greater increase of TKT1 expression was observed in hypoxia-treated cells and suggests a possible role in cellular adaptation to a low oxygen environment, thus offering a possible explanation for decreased efficacy of DNA methyltransferase inhibition observed in a hypoxic environment. However, this relationship warrants further investigation.

Increasing the concentration of decitabine poses possible increased effectiveness due to the higher decrease in cellular viability upon the 72-hour mark following treatment. The upper limit of decitabine treatment concentration remains unknown warranting the capability for further investigation. The next steps in this project are to continue examining the resulting epigenetic changes induced by DNA methyltransferase inhibition as well as the overall cellular proliferation rate with increasing decitabine concentration in both normoxic and hypoxic environments.

References

1. Bertoli C, Skotheim JM, de Bruin RA. Control of cell cycle transcription during G1 and S phases. *Nat Rev Mol Cell Biol.* 2013;14(8):518–528. doi:10.1038/nrm3629.
2. Cordero FJ, Huang Z, Grenier C, et al. Histone H3.3K27M Represses p16 to Accelerate Gliomagenesis in a Murine Model of DIPG. *Mol Cancer Res.* 2017;15(9):1243–1254. doi:10.1158/1541-7786.MCR-16-0389.
3. Fang D, Gan H, Cheng L, et al. H3.3K27M mutant proteins reprogram epigenome by sequestering the PRC2 complex to poised enhancers. *eLife.* 2018;7:e36696. Published 2018 Jun 22. doi:10.7554/eLife.36696.
4. Hashizume R. Epigenetic Targeted Therapy for Diffuse Intrinsic Pontine Glioma. *Neurol Med Chir (Tokyo).* 2017;57(7):331–342. doi:10.2176/nmc.ra.2017-0018.
5. Heller S, Maurer GD, Wanka C, et al. Gene Suppression of Transketolase-Like Protein 1 (TKTL1) Sensitizes Glioma Cells to Hypoxia and Ionizing Radiation. *Int J Mol Sci.* 2018;19(8):2168. Published 2018 Jul 25. doi:10.3390/ijms19082168.
6. Mackay A, Burford A, Carvalho D, et al. Integrated Molecular Meta-Analysis of 1,000 Pediatric High-Grade and Diffuse Intrinsic Pontine Glioma. *Cancer Cell.* 2017;32(4):520–537.e5. doi:10.1016/j.ccr.2017.08.017.
7. Saratsis AM, Kambhampati M, Snyder K, et al. Comparative multidimensional molecular analyses of pediatric diffuse intrinsic pontine glioma reveals distinct molecular subtypes. *Acta Neuropathol.* 2013;127(6):881–895. doi:10.1007/s00401-013-1218-2.
8. Strzalka W, Ziemienowicz A. Proliferating cell nuclear antigen (PCNA): a key factor in DNA replication and cell cycle regulation. *Ann Bot.* 2010;107(7):1127–1140. doi:10.1093/aob/mcq243.
9. Thienpont B, Steinbacher J, Zhao H, et al. Tumour hypoxia causes DNA hypermethylation by reducing TET activity. *Nature.* 2016;537(7618):63–68. doi:10.1038/nature19081.

Robust, Solvent-Free Anion Exchange Membranes for Fuel Cells

Student Researcher: Jason W. Kahn

Advisor: Dr. Matthew Liberatore

The University of Toledo

Department of Chemical Engineering

Abstract

Fuel cells are a promising development in energy technology as they can convert fuel to electricity with a minimal carbon footprint. Through electrochemical processes, fuel cells can be twice as energy efficient as the internal combustion engine. While proton exchange membrane (PEM) fuel cells are relatively common, hydrogen availability and cost of the platinum catalyst have been a major concern for PEM fuel cells. One way to overcome these challenges is by using Anion Exchange Membrane (AEM) fuel cell. The essential function of an anion exchange membrane is to conduct anions while being impermeable to the oxidants and fuel used in the fuel cell. While the benefits of fuel cells are understood and sought after, the polymeric membrane poses hindrance for widespread growth.

Project Objectives

This research project explores a solvent-free approach to the synthesis and characterization of anion exchange membranes for use in a wide variety of industrial applications ranging from fuel cell operation to water purification. Anion exchange membrane synthesis utilizes a patent-pending, cross-linking reaction of two water miscible constituents known as polyacrylamide-co-diallyldimethylammonium chloride copolymer and glutaraldehyde reacted with hydrochloric acid (HCl). A temperature-controlled variable speed micrometer-adjustable film coater was used to control desired film thickness and size.

Methodology Used

To determine how heat-controlled variables impacted our films we studied the following parameters: water uptake, ion exchange capacity (IEC) and film thickness. IEC determines how effective of a membrane the film is, the higher the IEC the more ions are being transferred. Water uptake is important as higher water uptake is responsible for things like dimension swelling and stability of the film. Thickness is important as a thinner film allows for a higher IEC but at the cost of stability for the film.

Results Obtained

Final membrane thicknesses ranged from 50 to 90 μm . Chemical characterization of ion exchange capacity (IEC) and water uptake measurements are completed for each film to measure conductivity levels and swelling behavior of the membranes. Measured IEC values ranged from 0.8 to 1.20, similar to state-of-the-art membranes. The membrane water uptake ranged from 30 to 50 wt%.

Significance and Interpretation of Results

From the results we were able to conclude that heat during the process of making the films has a logarithmic relationship in terms of thickness, there is a maximum amount of time that the film can dry on the heated surface before it has diminishing returns. Whereas with IEC and water uptake they seemed to have either no correlation or a slight correlation to the results. What can be gathered is that while it does play a role in affecting the IEC and water uptake, it does not play an impactful role.

Figures/Charts

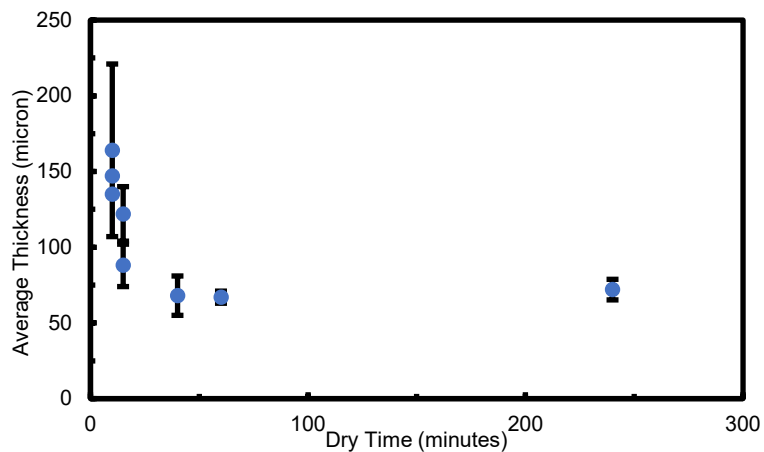


Figure 1.

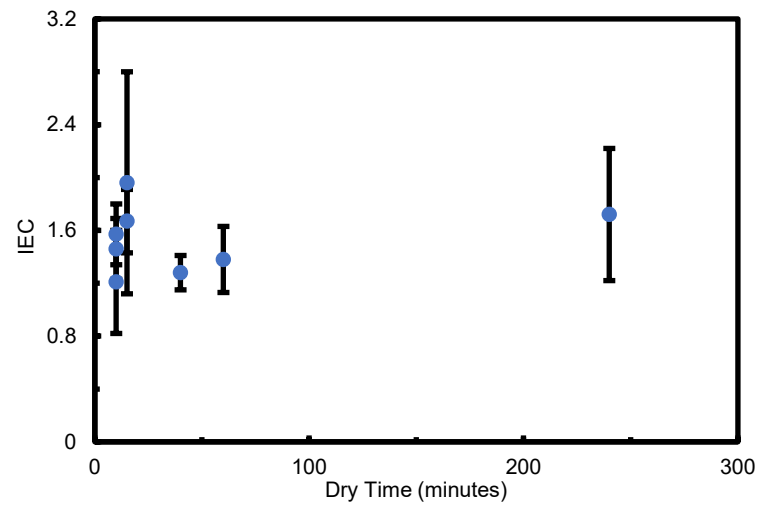


Figure 2.

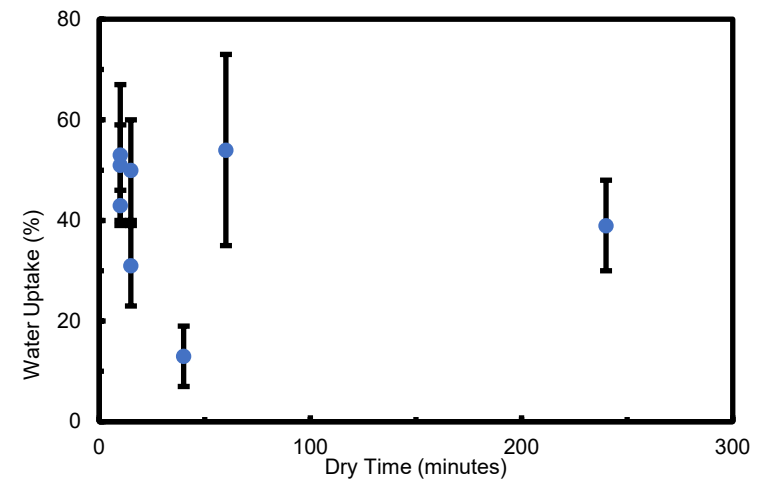


Figure 3.

We Are Going on a Road Trip, Exploring Exoplanets and Life in Space

Student Researcher: Margaret M. Kaminski

Advisor: Julie Wilcox

Kent State University
Department of Education

Abstract

My students are planning a trip to outer space and to our new home. They will do all of this while playing along to the project topic which is: our Earth is dying so we need to find a new planet and figure out a way to get there. Hopefully by the end of this project the groups of students will have chosen an exoplanet, designed a spaceship and figured out the means of survival for their journey to our new home. We will accomplish this with a mix of lectures, group work, and hands on activities.

Lesson

My lesson plan includes the use of human exploration and operations mission directives. I thought this could provide an interesting project at the end of an Earth science or Life science class. My objectives for this two to three-week project is for students to be able to identify and articulate what an exoplanet is and why they are important to humankind. Through this lesson students will debunk artificial gravity in famous space movies, work to better understand the price and difficulties of deep space travel, design and build a space travel vehicle and discuss the many essential human needs on a deep space trip.

Objectives

The first objective I will accomplish is a brief lesson on exoplanets. We will describe what an exoplanet is and why they are important. I will encourage the groups to visit NASA's site on exoplanets and they will then choose an exoplanet they want to travel to and establish a new Earth colony. In this part of the lesson we will also calculate how long it will take to get to this exoplanet so the groups can know how many resources they need for their spaceships. I will ask for a description of their planet and why they chose it. By completing this lesson my students will be able to list three types of exoplanets and be able to calculate space travel through light years.

The second objective will focus on is how we will travel to their newly chosen planet. I want to focus on different aspects of travel in deep space. One thing I want to focus on is artificial gravity. I will have my students read articles and watch videos like "can we create artificial gravity" by real engineering on YouTube. We will discuss the myth of artificial gravity in the film industry so students can understand how it is accomplished. The students will then read an article from NASA about "Top five technologies needed for a spacecraft to survive in deep space". From this lesson my students will be able to describe 2 different types of force, the harms of zero gravity on the human body and be able to articulate why we have not yet explored deep space travel.

The third and final objective will focus on life in space. To achieve the final objective, I will have my students study life in space. This will be accomplished by using the International Space Station as a model for our aircraft. As a class we will read and watch videos on farming, oxygen recycling and solar energy in space to better understand space life. These videos include astronauts Chris Hadfield's video about water recycling, a NASA article about farming in space and finally an article from the Department of Energy about solar space power. After completing this and some thought questions the students we

will construct their spaceships. I will ask the groups of students to consider in their design the oxygen and water recycling systems, energy, gravity and food resources. Each group will choose one choice for each topic on the chart below. The students will then use mixed media to make a design a representation of their spacecrafts.

Farming	Fresh food farming More space/cheaper	Freeze dried food Less space/costs more
Energy	Laser satellites Costs less/needs many to be effective	Microwave satellites Costs more/only a few needed but installed by astronauts
Oxygen	Already installed	
Water	Already installed	
Gravity	Ring structured ship Costs less/worse for the body	High tech artificial gravity Costs more/better for the body.

Results

At the end of this lesson I will have the groups present on their planet, the ship they made and any other relevant information. After completing this lesson students will be able to identify 5 essential resources for human survival in space and will be able to provide supporting evidence for their choices. Some challenges I anticipate for this project is having to adjust the time period for the project if my students need more time or if we move through material faster than anticipated. I also anticipate maybe some difficulty building models or drawing them. In order to address this issue, I will find resources for them that they will be able to use for this portion of the project.

Since the pandemic of COVID-19 I can see this project transition somewhat easily to online learning. Some of the strategies would include performing classes with PowerPoint lectures, forming the groups and having them meet during class time and work on their project. I would still include quizzes for the lectures and other topics we discuss. Instead of making 3D models I could have my students submit a collaborative document about what they will include in their craft and a drawing or spaceship design online.

References

1. "Exoplanet Exploration: Planets Beyond Our Solar System." NASA, NASA, 17 Dec. 2015, exoplanets.nasa.gov/.
2. Garcia, Mark. "Top Five Technologies Needed for a Spacecraft to Survive Deep Space." NASA, NASA, 30 July 2018, www.nasa.gov/feature/top-five-technologies-needed-for-a-spacecraft-to-survive-deep-space.
3. Hadfield, Chris, director. *Water Recycling on the ISS*. Water Recycling on the ISS, 26 Apr. 2013, www.youtube.com/watch?v=BCjH3k5gODI.
4. Heiney, Anna. "Growing Plants in Space." NASA, NASA, 9 Apr. 2019, www.nasa.gov/content/growing-plants-in-space.
5. McManus, Brian, director. *Can We Create Artificial Gravity?* Can We Create Artificial Gravity, 29 June 2016, www.youtube.com/watch?v=im-JM0f_J7s.
6. Wood, Daniel. "Space-Based Solar Power." Energy.gov, 6 Mar. 2014, www.energy.gov/articles/space-based-solar-power.

A Machine Learning Framework for Drop-in Volume Swell Characteristics of Sustainable Aviation Fuel

Student Researcher: Shane T. Kosir

Advisor: Dr. Joshua Heyne

University of Dayton

Department of Chemical and Materials Engineering

Abstract

A machine learning framework has been developed to predict volume swell of non-metallic materials commonly found in commercial aircraft fuel systems submerged in neat molecules. Volume swell, a material compatibility concern, serves as a significant impediment for the minimization of the environmental impact of aviation. Sustainable aviation fuels, the only near and mid-term solution to mitigating environmental impacts, are limited to low blend limits with conventional fuel due to material compatibility/O-ring swell issues. A neural network was trained to predict volume swell for neat molecules found in conventional jet fuel. Subsequent blend optimization incorporated swell predictions for cyclo- and *iso*-alkanes to create a high-performance jet fuel within ‘drop-in’ limits. Aircraft performance analysis was performed on a Boeing 737-800 to quantify the payload increase and fuel savings conferred by the high-performance jet fuel. Optimization considering nitrile rubber O-ring volume swell achieved median specific energy [MJ/kg] and energy density [MJ/L] increases of 1.9% and 5.1% respectively relative to Jet A, resulting in a 5.4% reduction in fuel volume and a 2.5% payload increase for a Boeing 737-800 flying from New York City to San Francisco.

Introduction and Objectives

Although aviation currently contributes a relatively small percent of global anthropogenic CO₂ emissions at ~2% [1], air travel is expected to double by the year 2037 [2], with associated particulate matter (PM) and radiative forcing (RF) emissions nearly doubling the current climate impact of aviation transportation. This growth could make aviation transportation account for a significant fraction of total anthropogenic carbon emissions. Sustainable aviation fuel (SAF) is the only near and mid-term opportunity for the minimization of aviation emissions. Currently, SAF adaption is limited by both the approval of novel fuels and the cost of currently approved fuels. Of the five SAFs currently approved, four are limited to a max blend ratio of 50% with conventional jet fuel due to material compatibility issues (e.g., O-ring swell) [3]. Specifically, aircraft have been found to leak significant quantities of fuel over the timescale of hours when volume swell is not sufficient [4].

Aromatics provide the majority of volume swell character to conventional jet fuel but are generally undesirable due to their low energy and tendency to form soot. Prior work [5] has illuminated a novel path for the approval of SAFs beyond 50% materials compatibility. This study indicated that blends of 30% cycloalkanes in synthetic paraffinic kerosene (SPK) exhibit volume swell properties similar to conventional jet fuel despite the lack of aromatic content, as can be seen in Figure 1. The dashed lines in the figure represent the lower volume swell limits of the 90% confidence intervals of 12 Jet A fuels. Many cycloalkanes are close to or exceed the lower limits, indicating that they can confer similar volume swell to a low-aromatic Jet A. It is expected that higher concentrations of cycloalkanes would confer further volume swell benefits. Moreover, these cycloalkane compounds have been found to increase the value of SAFs via aircraft operation improvements by increasing the fuel energy content [6].

In this study, volume swell was predicted for neat molecules via a neural network. These predictions were subsequently implemented into the optimization of high-performance jet fuels (HPFs), which represent a subset of SAFs that improves the performance of aircraft while remaining within ‘drop-in’ limits. This optimization illuminates a path for maximizing the value of SAFs by minimizing PM emissions, maximizing energy content, meeting previously reported SAF operability and safety constraints, and satisfying novel swell requirements. Subsequent aircraft performance analysis was performed using HPFs to determine fuel volume reductions and payload capacity increases achievable relative to Jet A. Combined, these results will guide current and ongoing research and development efforts of novel SAFs towards eclipsing the cost-benefit threshold of HPFs.

Methodology

Volume swell measurements used for this work consist of a single set of optical dilatometry measurements from literature [5]. Volume swell was measured for 10 non-metallic materials commonly found in commercial aircraft fuel systems submerged in compounds from seven molecular groups. Non-metallic materials included nitrile rubber, extracted nitrile rubber, fluorosilicone, low temp fluorocarbon, lightweight polysulfide, polythioether, epoxy (0.2mm), epoxy (0.04mm), nylon, and Kapton. Each material had volume swell measurements for one *iso*-alkane, 10 monocycloalkanes, one dicycloalkane, six aromatics, one diaromatic, three cycloaromatics, and one diamondoid, with a total of 230 observations. The materials were submerged in an aromatic-free SPK blended with neat compounds to examine the effect of the compounds on volume swell. The volume swell data was split into training and test frames.

Principal component analysis (PCA) was performed on the training frame, and the resulting principal components were used to train the neural network. 10 k-fold cross-validation was used to validate the neural network. After the neural network was generated, the PCA model was applied to the test frame and volume swell predictions were made to provide additional model validation. The prediction frame consisted of 24 cyclo- and *iso*-alkanes that did not have volume swell data in literature but were of interest for HPF optimization. The PCA model was applied to this frame and volume swell was predicted via the neural network. Molecules that met feature importance screening criteria were subsequently incorporated into HPF optimization. The rest of this paper will focus on HPF optimization and subsequent aircraft performance analysis applied to optimized HPFs.

HPF optimization done in this study leveraged code from previous efforts [6][7]. The approach was to use blending rules from literature coupled with ant colony optimization to maximize performance and value-added properties -specific energy (SE) [MJ/kg] and energy density (ED) [MJ/L]- for blends of molecules in the jet range while remaining within operability limits. Operability and safety limits are required to ensure novel fuels have no associated deleterious risks. A total of eight operability and safety properties served as constraints for optimization: volume swell, derived cetane number (DCN), density, kinematic viscosity at -20°C, flash point, freezing point, 10% recovered temperature, and final boiling point. The result of optimization was a Pareto front indicating the best performance properties achievable via blends of molecules without violating operability limits.

Nitrile rubber volume swell values were used for optimization because of the commonality of nitrile rubber in commercial aircraft fuel systems and the low mean absolute error achieved for neural network predictions. The optimization started with 1,000 random initial guesses that met operability limits. The totality of these solutions underwent an initial optimization run, with subsequent optimization revisions guided by 2σ convergence criteria for ΔSE and ΔED across the Pareto front. Solutions that fell outside

the 2σ range underwent further optimization for 10 consecutive revision rounds, with σ here being the physical uncertainty associated with the neat molecule SE and ED values used for optimization.

Volume swell was predicted for blends of cyclo- and *iso*-alkanes under the assumption that their interaction effects would be sufficiently weak due to their lack of hydrogen bonding and low polarity. It follows that volume swell should vary linearly with the concentration of cyclo- and *iso*-alkanes within the blending limits provided in literature [5]. This assumption may not hold for aromatics because they exhibit dipole-dipole interactions and hydrogen bonding which can affect molecular solubility and shift equilibrium concentrations, resulting in unpredictable blending behavior. Assuming a linear correlation between volume swell and the concentration of cyclo- and *iso*-alkanes allowed for the creation of a blending rule:

$$\text{swell}_{\text{blend}} = \sum (\text{swell}_i \times \varphi_i) \quad (1)$$

where φ_i represents the individual volume fraction of each molecule. This blending rule was coupled into the optimization framework as a constraint.

Aircraft performance analysis was performed on a Boeing 737-800 flying 2,150 nautical miles using the Environmental Design Space (EDS) [8]. A Design of Experiments was created to maximize the information learned from a computationally inexpensive number of EDS run cases. SE and density were varied from -15% to +15% of that of Jet A, while off-design mission ranges were evaluated in 500nm increments until the maximum design range and payload was reached. Performance parameters of interest were the change in fuel volume and weight as a function of SE, density, and flight range. The statistical package, JMP, was used to develop surrogate models for the aircraft performance metrics as functions of the SE, density, and flight range. Fuel volume decrease was taken as the reduction in fuel volume relative to Jet A using Equation 2.

$$\text{volume} = \text{weight}/\rho \quad (2)$$

Equation 3 was derived via the EDS analysis. Payload capacity increase was taken as the difference in fuel weight between the HPF and Jet A per Equation 3, where R represents the flight range.

$$\text{weight} = 2.71 \times 10^4 + 59.64\rho - 1.37\text{SE} + 12.05R + (\rho - 1.01)[-530.77(\rho - 1.01)] + (\rho - 1.01)[-1.30 \times 10^{-3}(\text{SE} - 1.88 \times 10^4)] + (\text{SE} - 1.88 \times 10^4)[1.04 \times 10^{-4}(\text{SE} - 1.88 \times 10^4)] + (\rho - 1.01)[0.278(R - 1500)] + (\text{SE} - 1.88 \times 10^4)[-8.59 \times 10^{-4}(R - 1500)] + (R - 1500)[4.06 \times 10^{-4}(R - 1500)] \quad (3)$$

Results

Figures 2 and 3 show the specific energy plotted against energy density with the Pareto front consisting of 7,196 optimized blends of 10 molecules. The red markers represent conventional jet fuels, which serve as the origin for the plot. Green, brown, and pink markers represent molecules used for optimization. The 2D kernel density plot represents the distribution of conventional jet fuels taken from the Petroleum Quality Information System (PQIS), a Department of Defense database dedicated to fuel quality information. The dark blue line represents the highest values from the PQIS. Fuels that exceed the SE and ED values of this line and meet operability requirements have been deemed high-performance jet fuels. The HPF region is indicated by the yellow-purple colormap, with percent fuel reduction by volume and percent payload increase by weight relative to Jet A displayed in Figures 2 and 3 respectively.

Median specific energy and energy density values across the Pareto front are 43.9 MJ/kg and 36.3 MJ/L respectively, representing 1.9% and 5.1% gains relative to Jet A. Comprehensive performance statistics across the Pareto front are displayed in Table 1. The Pareto front is fairly constrained relative to previous optimization efforts which spanned the majority of the density region represented by the straight blue lines. The Pareto front is limited on the right because it cannot achieve a higher specific energy than the set of molecules used for optimization. Specifically, the highest specific energy was that of *cis*-1,2-dimethylcyclooctane and farnesane at 43.95 MJ/kg. The Pareto front is constrained on the left because it violates the upper density limit. The Pareto front does not appear to reach the upper density limit in Figures 2 and 3 because ASTM D1298 reproducibility uncertainty is incorporated into the optimization constraints to provide a factor of safety.

Median Pareto front SE and ED increases correspond to a 5.4%/857L decrease in required fuel and a 2.5%/315kg increase in payload capacity. The increased payload capacity can add roughly five passengers per flight. In general, fuel volume reduction increases with increasing ED. Volume reductions from increasing SE were negated by decreasing density per Equation 2. Payload increases correlate strongly with increasing SE, with higher ED values reducing the payload capacity due to increased density per Equation 3. In general, percent fuel reduction and percent payload capacity increase with longer range.

Compositions and functional groups for solutions across the Pareto front can be seen in Figure 4, with blue lines representing mean blend values. Solutions consisted primarily of monocycloalkanes blended with either dicycloalkanes or farnesane, with a critical point existing at 43.91 MJ/kg. Despite its low volume swell, farnesane appeared in solutions toward the right of the Pareto front because of its high SE. Amongst dicycloalkanes, *cis*-decalin was favored, likely because of its low freezing point and higher DCN than *trans*-decalin. Amongst monocycloalkanes, *cis*-1,2-dimethylcyclooctane was favored despite having a high viscosity and low DCN because of its high SE and ED.

Operability and safety properties of solutions across the Pareto front can be seen in Figure 5, with dashed lines representing operability limits. Volume swell did not serve to constrain optimization, with the lowest volume swell solutions occurring where the concentration of farnesane was the highest. The minimum volume swell value was 5.5%, well above the 3.7% v/v lower limit for nitrile rubber. DCN remained consistent across the Pareto front, with a standard deviation of 0.008. Molecules with low DCN values, such as methylcyclohexane and *trans*-decalin, were generally avoided. Density served to bound the left of the Pareto front, hindering the addition of more dicycloalkanes. It scaled with volume swell, decreasing linearly as dicycloalkanes were replaced by monocycloalkanes and as farnesane was added. Viscosity remained close to its upper limit, indicating that it was a limiting constraint. This is likely because of the high viscosity of *cis*-1,2-dimethylcyclooctane, which was favored across solutions. Flash point remained well above its limit of 38°C, decreasing as dicycloalkanes were removed and subsequently increasing as farnesane was added. Freezing point decreased between 43.90 and 43.91 MJ/kg due to the addition of light monocycloalkanes and increased as farnesane was added from 43.91 to 43.93 MJ/kg. The 10% recovered temperature remained well below its limit, increasing as *sec*-butyldecalin and subsequently farnesane were added. The final boiling point also remained well below its limit, following a stepwise pattern because it was determined by the highest boiling point molecule in the solutions. Molecules that determined final boiling points across the Pareto front were *sec*-butyldecalin, heptylcyclohexane, and farnesane from left to right. High boiling points could serve as an impediment to the use of large cyclo- and *iso*-alkanes.

Significance

A framework has been developed to predict volume swell of non-metallic materials commonly found in commercial aircraft fuel systems due to neat molecules and subsequently optimize blends of molecules that swell within the range of conventional jet fuel. This study indicates that cycloalkanes are a suitable replacement for aromatics considering volume swell requirements. Optimized solutions achieved a median nitrile rubber volume swell of 6.2% v/v, well above the 3.7% v/v lower limit. The emissions reduction from replacing aromatics with cycloalkanes would be significant: cycloalkanes produce 88% less soot on average compared to aromatics [9]. It is estimated that direct radiative forcing from aviation-related soot emissions is $\sim 9.5 \text{ mW/m}^2$ [10], approximately 12% of the total RF associated with aviation [11]. It follows that the replacement of aromatics with cycloalkanes could reduce RF associated with aviation by roughly 10.6%. Value and performance gains are also conferred by replacing aromatics; median specific energy and energy density gains of 1.9% and 5.1% were achieved in this study, which can decrease fuel requirements by 5.4% or increase payload capacity by 2.5%, conferring environmental and monetary benefits to airlines.

Figures

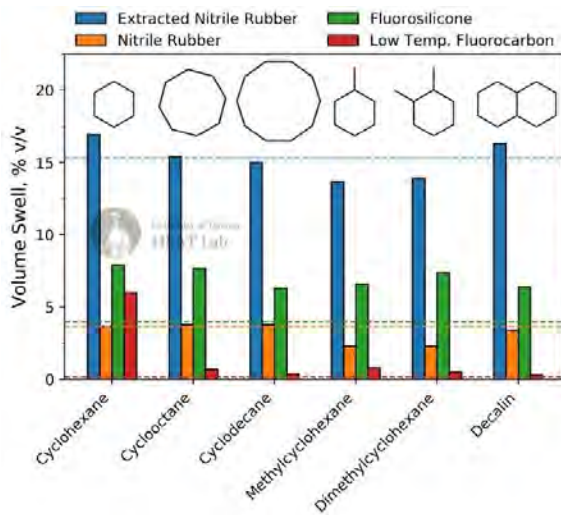


Figure 1. Volume swell of four O-ring materials submerged in cycloalkanes blended at 30% v/v with zero-aromatic synthetic paraffinic kerosene. Dashed lines represent conventional jet fuel lower limits, which many cycloalkanes exceed.

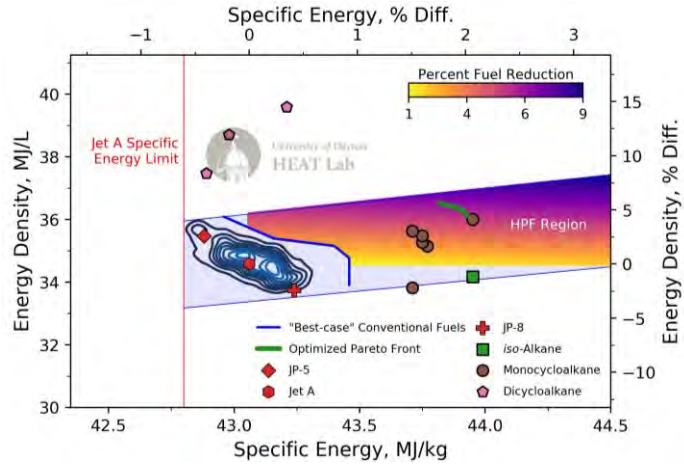


Figure 2. Specific energy plotted against energy density with the optimized Pareto front representing blends of cyclo- and *iso*-alkanes meeting nitrile rubber volume swell requirements in addition to other operability limits. Color gradient represents percent fuel reduction from HPF performance benefits.

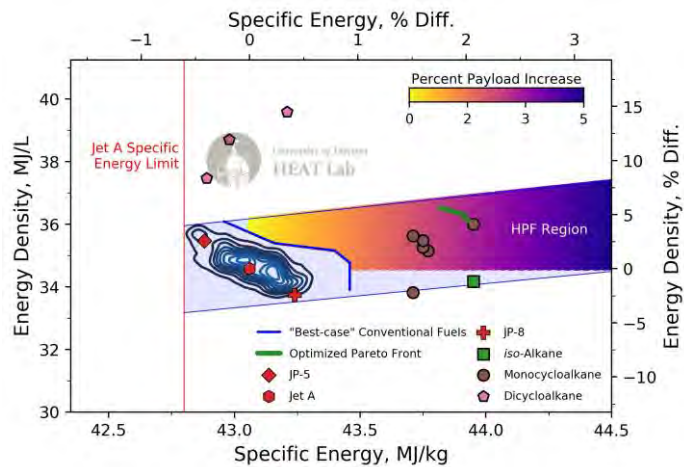


Figure 3. Specific energy plotted against energy density with the color gradient representing percent payload increase from HPF performance benefits.

Table 1. Performance statistics across the HPF Pareto front relative to Jet A.

Property	Min	Median	Max
SE [%]/[MJ/kg]	1.76/43.82	1.94/43.90	2.02/43.93
ED [%]/[MJ/L]	4.43/36.11	5.11/36.34	5.61/36.52
Fuel Reduction [%]/[L]	4.75/752.6	5.41/857.2	5.88/932.0
Payload Increase [%]/[kg]	2.25/286.7	2.48/315.3	2.56/326.7

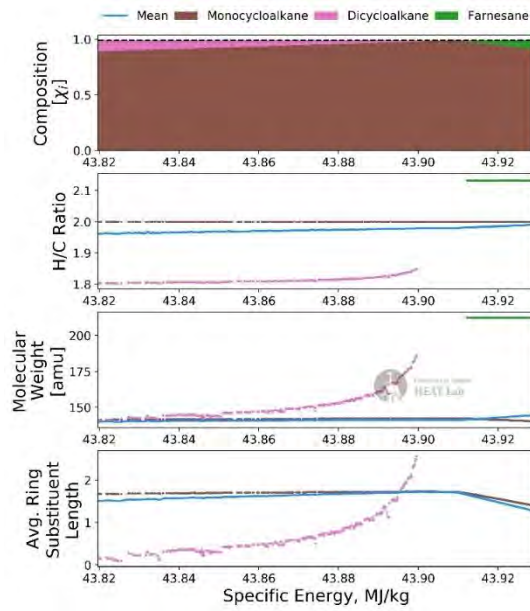


Figure 4. Composition and functional groups of solutions across the HPF Pareto front.

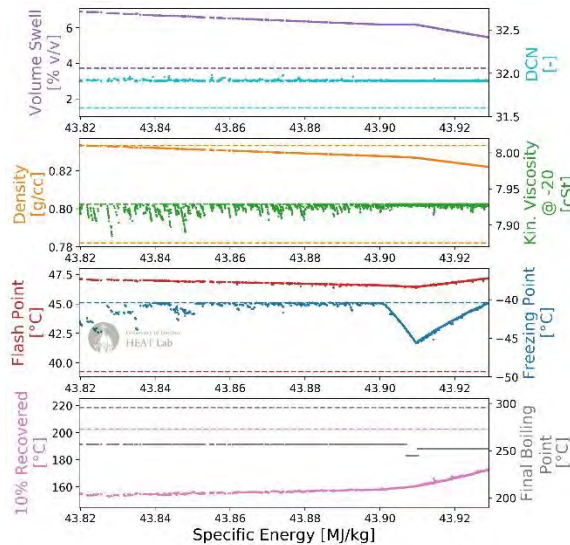


Figure 5. Operability and safety properties of solutions across the HPF Pareto front.

Acknowledgments

The authors would like to thank the Ohio Space Grant Consortium for providing funding for this work. Additionally, this work would not have been possible without Michelle Kirby offering her assistance with the aircraft performance analysis, John Graham lending his expertise regarding volume swell, and Kevin Hallinan helping with machine learning efforts using H₂O Flow.

References

1. Climate Change & CORSIA. Int Air Transp Assoc 2018.
2. IATA Forecast Predicts 8.2 billion Air Travelers in 2037. Int Air Transp Assoc 2018.
<https://www.iata.org/pressroom/pr/Pages/2018-10-24-02.aspx>.
3. Alternative Aviation Fuels: Overview of Challenges, Opportunities, and Next Steps. US Dep Energy 2017.
4. Klingshirn, C. D., DeWitt, M., Striebich, R., Anneken, D., Shafer, L., Corporan, E., et al. Hydroprocessed Renewable Jet Fuel Evaluation, Performance, and Emissions in a T63 Turbine Engine. J Eng Gas Turbines Power 2012;134.
5. Graham, J. L. Impact of Alternative Jet Fuel and Fuel Blends on Non-Metallic Materials Used in Commercial Aircraft Fuel Systems. Dayton: 2011.
6. Kosir, S., Behnke, L., Heyne, J., Stachler, R., Flora, G., Zabarnick, S., et al. Improvement in Jet Aircraft Operation with the Use of High-Performance Drop-in Fuels. AIAA SciTech Forum, San Diego: AIAA SciTech; 2019.
7. Flora, G., Kosir, S., Behnke, L., Stachler, R., Heyne, J., Zabarnick, S., et al. Properties Calculator and Optimization for Drop-in Alternative Jet Fuel Blends. AIAA SciTech Forum, San Diego: 2019.
8. Barros, P. A., Kirby, M. R., Mavris, D. N. An approach for verification and validation of the environmental design space. 26th Congr Int Counc Aeronaut Sci 2008:1–15.
9. Ladommato, N., Rubenstein, P., Bennett, P. Some effects of molecular structure of single hydrocarbons on sooting tendency. Fuel 1996;75:114–24.
10. Stettler, M. E. J., Boies, A. M., Petzold, A., Barrett, S. R. H. Global civil aviation black carbon emissions. Environ Sci Technol 2013;47:10397–404.
11. Lee, D. S., Fahey, D. W., Forster, P. M., Newton, P. J., Wit, R. C. N., Lim, L. L., et al. Aviation and global climate change in the 21st century. Atmos Environ 2009;43:3520–37.

Alternatives to Decommissioning Offshore Infrastructure: Artificial Reefing

Student Researcher: Johnathan L. Kungle

Advisor: Craig Rabatin

Marietta College

Department of Petroleum Engineering and Geology

Abstract

Water covers 70% of the Earth, yet hydrocarbon discoveries are still made on land despite continuous exploration for the past 150 years—meaning unfathomable amounts of undiscovered oil and gas likely exist beneath Earth’s oceans. Two decades ago, 5,000 ft of water was considered an “ultra-deep” offshore well; now, a large majority of offshore rigs are rated for at least 10,000 ft of water. Needless to say, offshore technology in the oil and gas field is rapidly growing and will continue to do so as demand increases and operators push into deeper water to find more hydrocarbons. Thus, offshore infrastructure is and will continue to become outdated quickly, resulting in a lengthy and expensive decommissioning project for operators. With the ever-growing amount of obsolete offshore structures, it is time the industry investigates alternatives to the standard decommissioning process. This study considers artificial reefing, wind and wave power, tourism, and fisheries as alternatives. It investigates feasibility, potential cost savings and/or profit, and real-world examples to find that artificial reefing is the best option, and then further investigates this alternative method.

Project Objectives

Determine the best alternative to traditional decommissioning of offshore infrastructure on the basis of three criteria: economics, feasibility, and environmental friendliness. Then, gain a deeper understanding of the artificial reefing process including its benefits and challenges.

Methodology Used

The driving force behind this whole project is my 2018 summer experience working for a large upstream oil and gas operator as a drilling engineering intern in their Gulf of Mexico operations. Throughout the summer, which included a trip to an offshore drillship, I realized how many offshore structures are decommissioned each year—a trend that will continue well into the future. This prompted further investigation on my part and I spent considerable time researching this topic, interviewing industry experts, analyzing my findings, and compiling all of the data I had collected.

Results Obtained

The idea of harvesting either wind or wave energy (see **Figure 1: Oscillating Column Diagram**) from retired platforms certainly meets the last of the three criteria, environmental friendliness, as it would provide a source of clean, renewable, and sustainable energy. However, the economics are questionable as no such projects have been completed on a commercial scale, and the feasibility is quite low given current technology in these fields. Tourism remains neutral regarding environmental impact as it has no major positive or negative impact. It is a justified economic decision since it is cheaper than standard decommissioning and can provide a small revenue stream, and it has been done across the world (see **Figure 2: Malaysia Sea Adventures Center**). However, its large-scale feasibility is low given its small market combined with the high amount of decommissioning that will likely take place in the coming decades. Fisheries do have promising economics if developed correctly, but the feasibility is very much in question with many obstacles remaining before this alternative can be advanced. Its environmental

impact is neutral since the fish are domestic and do not interact with the surrounding ecosystem. This leaves artificial reefing as the only viable option meeting all three criteria. Although some argue over its environmental impact, studies have proven its positive effects which is why it has support from a majority of interested scientists (see **Figure 3: Marine Life Flocking to a Man-Made Structure**). Economics and feasibility have been proven through hundreds of projects as it is an easier process than standard decommissioning that guarantees cost savings through the Rigs-to-Reefs program. Several of these alternatives may have potential in the future, but artificial reefing is a sure bet for operators looking for alternatives in the next decade and maybe beyond.

Artificial reefing is prolific in the Gulf of Mexico, with between 500 and 600 reefed rigs in the region (see **Figure 4: Offshore Texas Artificial Reef Map**). Other areas are somewhat behind this trend due primarily to legal obstacles, with Thailand just recently getting permission to complete its first artificial reefing project. Offshore California still has no reefed rigs despite a legal process being rolled out for these projects in 2010 (much more complicated and less financially beneficial when compared with Gulf of Mexico regulations). The general process for reefing a rig involves removing the topside of the rig (see **Figure 5: Barge Removing the Topsides of Retired Platforms**) which is almost always sent back to shore so as not to pollute the water. Then the steel legs are cut off 80 ft below the water line and usually toppled over so as to not interfere with any passing vessels. There are large areas in the Gulf of Mexico specifically designated for artificial reefing based on a variety of factors, so this reduces further complexities with these projects.

Artificial reefs work so well because the galvanized steel which was already in place below the water line has no negative impacts on the environment and conversely provides a fantastic ecosystem for marine life. A typical eight-leg structure can support up to 14,000 marine animals. In fact, the vertical orientation of the structure is particularly beneficial because it would naturally take a very long time for a reef to build up this high, and it also provides multiple equivalent acres of habitat with a minimal impact on seafloor real estate. Many natural reefs close to the shore are polluted from runoff, so artificial reefs farther offshore provide much healthier ecosystems than most traditional near-shore reefs. Additionally, this is also very beneficial for stakeholders, primarily divers and fishermen. Luckily, there is a program called Rigs2Reefs which specializes in these projects and even serves as a consultant for smaller companies who do not have the personnel to devote to these projects. This allows for more artificial reefing, and through this program the companies in the Gulf of Mexico also donate 50% of their cost savings back to the state's artificial reefing program (this number is much higher in California, one of the main problems for companies there). All in all, there is no denying the studies that show artificial reefs are some of the most productive ecosystems, so this decommissioning alternative not only helps operators save money but is also extremely environmentally friendly.

Figures

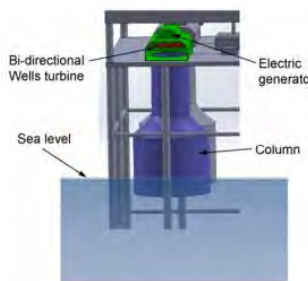


Figure 1. Oscillating Column Diagram.
Basic outline of how waves can be used to create energy.



Figure 2. Malaysia Sea Adventures Center.
An old rig converted to a dive center off the coast of Malaysia.



Figure 3. Marine Life Flocking to a Man-Made Structure.
An eight-leg structure can support 14,000 fish, and this vertical orientation is particularly beneficial to marine ecosystems.

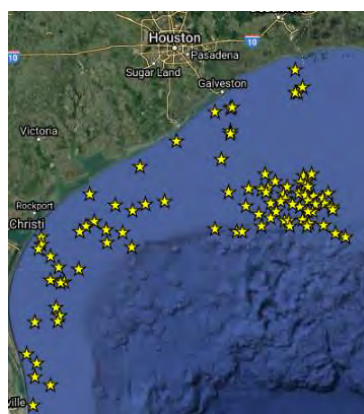


Figure 4. Offshore Texas Artificial Reef Map.
The artificial reefs in place off the shore of Texas; a portion of the many artificial reefs in the Gulf of Mexico.

Acknowledgments and References

1. Azimov, U. and Birkett, M. 2017. Feasibility study and design of an ocean wave power generation station integrated with a decommissioned offshore oil platform in UK waters. *International Journal of Energy and Environment* 8(2): 161-174.
2. Dexter, C. and Ghorashi, J. 2016. What do you do with an obsolete oil rig?. *The Chemical Engineer*: 38-39.
3. Evans, I. Can we repurpose decommissioned oil rigs for environmental gain?. PacificStandard, psmag.com/environment/rejiggering-the-rigs. Downloaded 3 November 2018.
4. Gaskill, M. Gulf coast oil platforms: save the rigs?. PacificStandard, psmag.com/environment/leave-those-rigs-alone-42598. Downloaded 3 November 2018.
5. How Does Decommissioning Work? Rigzone, www.rigzone.com/training/insight.asp?insight_id=354&c_id=. Downloaded 5 November 2018.
6. Kaiser, M.J. and Narra, S. A hybrid scenario-based decommissioning forecast for the shallow water U.S. Gulf of Mexico, 2018-2038. ScienceDirect, www.sciencedirect.com/science/article/pii/S0360544218316645. Downloaded 5 November 2018.
7. Khan, J. Decommissioned rigs: Precious marine habitats or giant lumps of ocean waste?. ABC, www.abc.net.au/news/science/2018-06-13/decommissioned-rigs-precious-marine-habitat-or-more-ocean-waste/9833084. Downloaded 3 November 2018.
8. McKinney, J. After the oil runs out: rigs to reefs. PacificStandard, psmag.com/environment/after-the-oil-runs-out-rigs-to-reefs-19272. Downloaded 3 November 2018.
9. Newman, N. The sharp rise of platforms decommissioning. Eniday, www.eniday.com/en/sparks_en/platforms-decommissioning/. Downloaded 3 November 2018.
10. Offshore decommissioning. PetroWiki, petrowiki.org/Offshore_decommissioning. Downloaded 4 November 2018.
11. Rigs to Reefs. Bureau of Safety and Environmental Enforcement, www.bsee.gov/what-we-do/environmental-focuses/rigs-to-reefs. Downloaded 5 November 2018.
12. Texas Artificial Reefs Interactive Mapping Application. Texas Parks & Wildlife, <https://tpwd.texas.gov/gis/ris/artificialreefs/>. Downloaded 20 March 2020.

High-Temperature, Flexible, Piezoelectric Transducers Based on Nylon-11 Nanowires

Student Researcher: Niccolo D. Lemonis

Advisor: Dr. Ryan C. Toonen

The University of Akron
Electrical and Computer Engineering Department

Abstract

Ceramic piezoelectric transducers are rigid and relatively expensive, and they typically contain heavy metals (such as lead) that are harmful to the environment. Polymer-based piezoelectric transducers are cost-effective and flexible but are not stable at temperatures that are even as high as 85°C [1]. There is a critical need for cost-effective, flexible piezoelectric transducers that meet aerospace and military temperature specifications (-55°C to 125°C).

We propose the innovation of a high-temperature, flexible piezoelectric transducer that is based on nylon-11 nanowires. Nylon-11 nanowires (synthesized in rigid substrates) have been shown to exhibit the unique feature of self-polarization, which results in resilience to temperatures approaching 200°C [2]. The self-poling property is especially significant because conventional piezoelectric materials, in both bulk and thin-film form, require poling in relatively high electric fields. Self-polarization will reduce the complexity in manufacturing in addition to eliminating the need for periodic re-poling of transducers that have experienced degradation due to aging.

Project Objectives

The objective of the proposed research is to innovate a flexible transducer that can be used for mechanical-sensing and energy-harvesting applications while operating at higher temperatures than are achieved by current state-of-the-art, polymer-based piezoelectric transducer technologies. To achieve this objective, we will build a customized system for synthesizing nylon-11 nanowires in flexible, track-etched polycarbonate (TEPC) templates. Nanowires produced from this apparatus will be physically characterized using scanning electron microscopy (SEM) and X-ray diffraction (XRD) analysis. SEM will allow for the average length and diameter of the nanowires to be determined. XRD will allow for the characterization of the nanowire crystallinity. The materials will be evaluated for piezoelectric responses at temperatures ranging from 20°C (near room temperature) to 125°C.

Methodology Used

The procedure used for creating the piezoelectric transducer is known as “template wetting”. Essentially the procedure involves creating a soluble Nylon-11 solution, then dripping the solution onto the templates after it is created. Template wetting allowed for the polymer solution to infiltrate the pores of the templates. Once the polymer solution solidifies in the templates the nanowires were formed.

Initially the Nylon-11 used in the experiment was attached to an aluminum sheet. The first obstacle was to separate the Nylon-11 polymer from the aluminum so the polymer mixture could be created. The procedure involved encasing the aluminum sheet in tape and making a small slit in the middle of the tape; therefore, only a small strip of the aluminum was exposed. Figure 3 fully shows how the slit was made. Once the aluminum was unprotected by the tape, chemical etching was used to remove the aluminum.

Trial and error studies were conducted for optimizing a method for preparing Nylon-11 solution. Previous preparations resulted in undissolved nylon-11 pellets. Figure 1 shows the clear solution that resulted from an optimized recipe in which solution temperature and mixing speed and duration were the experimental controls. A test was conducted to determine if the hydrophilic track-etched polycarbonate (PCTE) and track-etched polyester (PETE) nanopores naturally absorb or repel the nylon-11 / formic acid solution. Droplets of the solution, which was observed to quickly crystallize when removed from the 90°C hotplate, were placed on a PCTE and PETE templates. As shown in Figure 2, the meniscus contact angle appears shallow, which should indicate a hydrophilic characteristic.

Preliminary tests conducted on synthesizing nylon-11 nanowires in PCTE and PETE nanoporous templates. As shown in Figure 5, a customized apparatus was constructed to enable gas-flow assisted template wetting as described in prior work (*Energy Environ. Sci.*, 2017, 10, 2180). The apparatus can provide gas-flow speeds of up to 11 m/s. Inspection of initially synthesized materials indicates that the templates should be held at elevated temperatures while the nylon-11 / formic solution is permeating the nanopores.

Results Obtained

Originally we began seeking to characterize our templates by measuring a voltage response. As shown in Figure 4, the template was held down using copper tape to help decrease interference. The leads were used by oscilloscope to measure for any voltage response when pressure was physically applied on the template. However, it was observed that after the nylon-11 / formic acid puddles crystallized, the solidified nylon-11 did not adhere well to the surface of the templates. This observation does not indicate that nylon-11 nanowires did not form in the nanopores. It does indicate that the templates should be held at elevated temperatures while the nylon-11 / formic solution is permeating the nanopores.

The laminar flow chamber displayed more promising results compared to conventional template wetting. The flow chamber proved advantageous because it applied a force to solution when it was placed on the template. The added velocity from the laminar flow chamber allowed for the nylon-11 polymer solution to permeate the nanopores fully. Further characterization of the templates was beginning amidst the COVID-19 epidemic which was put temporarily on hold involving scanning electron microscopy, and x-ray diffraction analysis.

Figures and Charts



Figure 1. Nylon-11 solution prepared by dissolving nylon-11 pellets in formic acid at a temperature of 90°C.

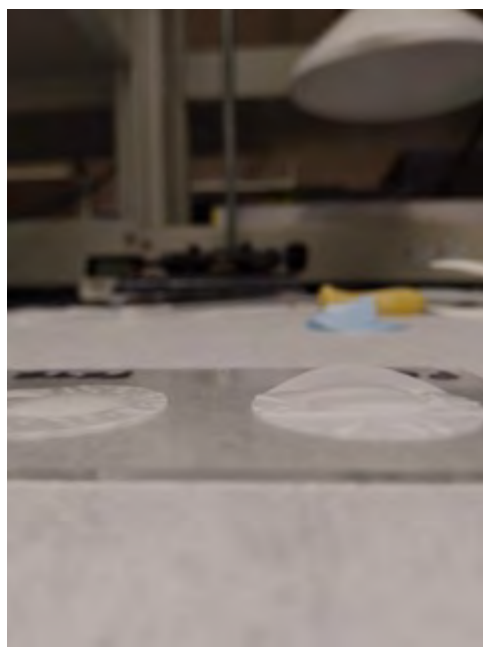


Figure 2. Nylon-11 / formic acid solution droplets placed on PETE (left) and PCTE (right) nanoporous templates.



Figure 3. Nylon-11 attached to aluminum sheet, encased in tape. The slit in the middle allowed for chemical etching.



Figure 4. Finalized template attached to copper tape. Initial monitor voltage response related to physical pressure applied to template.



Figure 5. Laminar flow chamber designed to enable gas-flow assisted template wetting.

Acknowledgment

The author of this paper would like to note their sincere gratitude to Dr. Ryan Christopher Toonen without whom the author would have not been informed of this project. Dr. Toonen provided and continues to provide assistance and unyielding support, thank you.

References

1. L. L. Blyler Jr, G.E. Johnson, and N. M. Hylton. "Characterization of biaxially-oriented polyvinylidene fluoride-film for transducer applications." *Ferroelectrics* **28(1)**, 303-306 (1980).
2. A. Datta, et al. "Piezoelectric Nylon-11 Nanowire Arrays Grown by Template Wetting for Vibrational Energy Harvesting Applications." *Advanced Functional Materials* **27(2)**, 1604262 (2017).
3. Y. Takase, et al. "High-temperature characteristics of nylon-11 and nylon-7 piezoelectrics." *Macromolecules* **24.25**, 6644-6652 (1991).
4. Nalwa, Hari Singh. *Ferroelectric polymers: chemistry, physics, and applications*. CRC Press, 1995.
5. Whiter, Richard A., Vijay Narayan, and Sohini Kar-Narayan. "A scalable nanogenerator based on self-poled piezoelectric polymer nanowires with high energy conversion efficiency." *Advanced Energy Materials* **4.18**, 1400519 (2014).
6. Y. S. Choi, et al. "A Triboelectric generator based on self-poled Nylon-11 nanowires fabricated by gas-flow assisted template wetting" *Energy Environ. Sci.* **10**, 2180-2189 (2017).

A Numerical Study of a Cyclone Separator at Reduced Operating Pressures

Student Researcher: Nathan E. Lin

Advisor: Dr. Kevin Disotell

Youngstown State University

Department of Mechanical, Industrial and Manufacturing Engineering

Abstract

Cyclone separators are air filtration devices that use inertia as a means of separating particles from fluid flow. These devices are being studied by the Particulate Filtration Laboratory at NASA Glenn Research Center as a potential pre-filter stage to extend the life of conventional air filters in Martian and Lunar environments. As part of a State of Ohio STEM Scholarship during Spring Semester 2020, the current work used computational fluid dynamics (CFD) to analyze and solve various flow configurations in a pre-designed cyclone separator.

Project Objectives

The objective of the research was to use numerical methods, in particular the Reynolds Stress Model (RSM), to simulate the flow field in a pre-designed cyclone separator at reduced operating pressures of 13.8 Torr, 134 Torr, 268 Torr, and 570 Torr.

Methodology

SolidWorks was used to model the cyclone separator geometry and the ANSYS 19.2 package (specifically ANSYS Meshing and Fluent) were used to generate poly-hex core meshes. These were grid- and time-step converged to a 1.87M mesh (Figure 1), using a time step of 0.001 second. The RSM, with default coefficients, was used to solve for turbulence in the flow. This turbulence model was chosen due to the success it has shown in modeling swirling flow and flow in cyclone separators [1]. The boundary conditions for the CFD cases were set based on experimentally measured pressure drops.

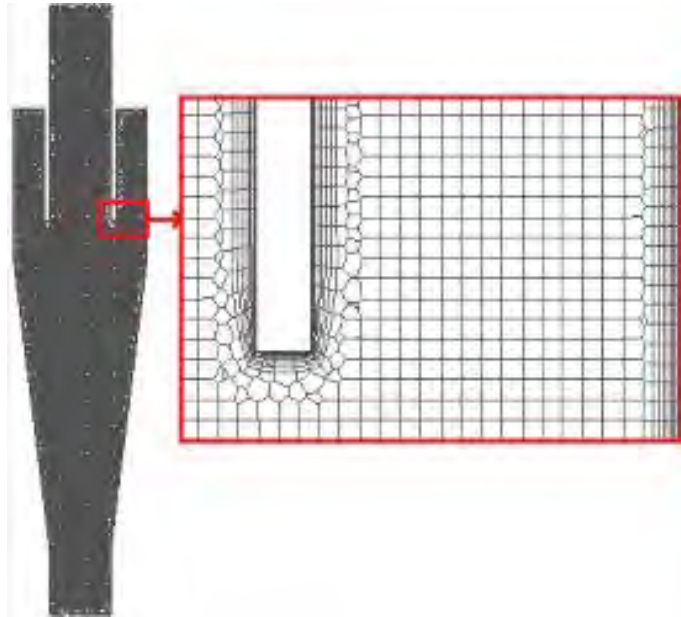


Figure 1. Section view of mesh with magnified cylinder section.

Results Obtained

Before further refinement of the operating pressures from experimental work, cases were run with operating pressures of 10 Torr, 140 Torr, 150 Torr, 300 Torr, and 600 Torr. A contour of tangential velocity is

helpful when analyzing the flow field of a cyclone separator. This contour, for the 140 Torr case, is shown in Figure 2. The higher tangential velocity in the contour leads to particles in the air having greater momentum; thus, they tend to follow the initial direction of flow down the cone section and into the collector. As the flow reverses and forms a forced vortex, indicated by the region of near-zero tangential velocity in Figure 2. The particles remain in the collector and cleaner air is ejected from the outlet.

The pressure drop across a cyclone separator is an important parameter, which is linked to the collection efficiency. The predicted pressure drop and specified inlet velocity for each of the initial set of cases is shown in Table 1, below.

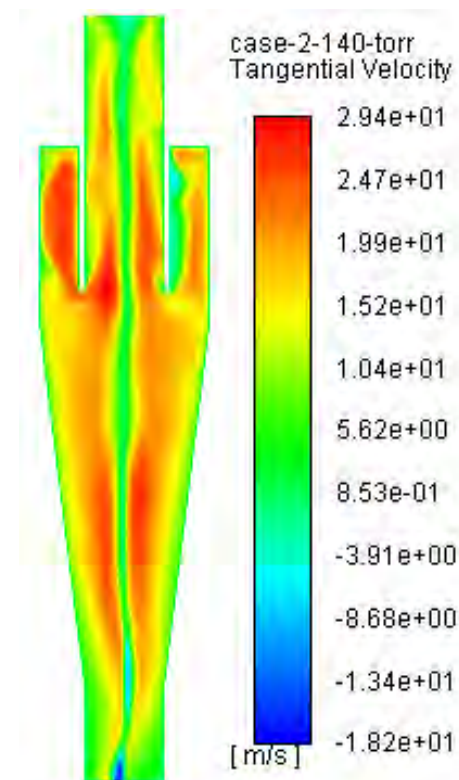


Figure 2. Midplane contour of tangential velocity for 140 torr case.

Table 1. Pressure drop results for the initial set of CFD cases.

Operating Pressure (Torr)	Inlet Velocity (m/s)	Pressure Drop (Torr)
10	13.2	0.051
140	15.85	1.426
150	14.5	1.257
300	6.38	0.476
600	2.20	0.107

The pressure drop for these cases was much lower than expected. The revised set of operating conditions slightly increased the pressure drop for each case, but not sufficiently to trust the prediction by the solver for the given set-up. Further investigation is needed to track the cause of this under-prediction of the pressure drop. A change of boundary conditions may be necessary to more accurately model the physical setup of the cyclone separator.

References

1. A. J. Hoekstra, J. J. Derksen, H. E. A. Van Den Akker. "An experimental and numerical study of turbulent swirling flow in gas cyclones" Chemical Engineering Science, Vol. 54 No. 13-14, (1999): pp. 2055-2056. doi.org/10.1016/S0009-2509(98)00373-X.

Our Solar System

Student Researcher: Margaret A. Lorenz

Advisor: Jon Breiner

University of Cincinnati
College of Education

Abstract

This lesson, designed intentionally for Middle School Students, focuses on the scale of our solar system and its planets. Part one of this lesson focuses on students' gaining an introduction to our Solar System's Planets. Student will use the NASA app to research each planet and complete a fact sheet on them. To accomplish part two of this lesson, the class will utilize three of the NASA classroom activity plans: Planetary Travel Time, Kinesthetic Radial Model of the Solar System, and Solar System Scroll. From these activities, student will be able to understand the diversity and vastness of our Solar System. Students will also be able to express the proportion of distance and size of planets to one another and the Earth.

Activity Plan

There are two parts of this plan that students will complete. The combination of these activities pulls aspects of technology, hands on experiences, and groupwork. All of these activities are available through the NASA resources for educators.

Part 1: Activity 1 NASA App with Planet Fact Sheet	Part 2: Activity 1 Solar System Scroll Activity	Part 2: Activity 2 Planetary Time Travel Activity	Part 2: Activity 3 Kinesthetic Radial Model of the Solar System
Students will use the NASA app <i>Featured Section</i> and then the <i>Planets</i> Module to guide them through exploring each planet. Students should be given a worksheet that allows them to track information from the <i>in-depth</i> and <i>missions</i> ' tabs within the module. Students will then hold a class discussion over their discoveries.	Individually, or in pairs of two, Students will first use their strip of paper to estimate how far they think the planets are from one another. Students will then follow along with the instructions for folding and draw in marker where planets actually are. This activity will help students grasp the misconceptions they had about the scale of distances in space. This should be followed up with a discussion.	As a whole class the students and teacher will work though the guided worksheet. Students will first share their guess for how long it would take to travel to the planet. Next the class will work together to find the actual time for them to travel there if they were on a "mission". After talking about the expected vs actual. From this, student will also be using Mathematical calculations so make sure to walk through these steps as a class very clearly.	Since this is a more advanced activity for 5 th grade, have the model set up before the class so that the students can just utilize the visualize and moving parts of the model. Walk the students through the model in small groups and have them answer the questions from the activity. Address any misconceptions. They can use their fact sheet from Part 1 Activity 1 to help them answer the questions.

Learning Objectives

The learning objectives for the lesson are as followed: Students will understand the diversity of our solar system, and Students will understand the proportion of planets and their distance from one another and earth. These Learning objectives align with the Ohio Learning standard for 5th grade 5.ESS.1. These objectives ensure that students are gaining understanding rather than just knowledge of our solar system. Looking for understanding has also guided the activity plan to ensure there are multiple means of representation in the activities. These objectives also leave room for scaffolding of the curriculum and for further exploration by the students into this topic of our solar system.

Standards

This Standard addressed in these activates for the middle age grade band, specifically 5th grade. The standard is, **5.ESS.1** The solar system includes the sun and all celestial bodies that orbit the sun. Each planet in the solar system has unique characteristics (Ohio Department of Education). This standard asks students to look into the characteristics of planets, how they all play a role in our solar system, and how all planets still have differences. This standard also introduces how planets are centered around the sun. This grows to teach the understanding that different planets hold varying distances away from the sun and that stays consistent throughout their orbits.

Pedagogy

The pedagogy behind this lesson stems from the Constructivist look at education. The constructivist view is that students get to explore the world around them to formulate their understanding of a topic. This is present in the lesson through the introductory lesson questions, allowing varying methods of instruction in the classroom and the wrap up questions that provoke questioning to then further the lesson and engage the student. There is also crossdisciplinarity components to this lesson that pull off of the Constructivist model of teaching. This is present during the Planetary Travel Time Activity and its use of mathematic processes. This lesson also pulls off of the structure for the Universal Design for Learning. This calls for multiple means of expression and inclusion in the lessons. This can be seen throughout the lesson in many different ways. The first in the inclusion of technology throughout the use of the NASA app. Through this app students will be able to explore at their own pace and can also use technology accessibility settings if needed through technology that is available in the classroom. Universal Design for Learning is also present in the hands-on activity of the Kinesthetic Radial Model of the Soral System Activity and the Solar System Scroll Activity. Overall, this lesson is hands on, allows for exploration, and uses multiple means of expression by using the NASA educational tools.

Student Engagement

The student engagement in this lesson is high and there is a wide range of activates that show similar concepts in a variety of ways. Students are asked to create, discover, and report their findings. All of these concepts fall in a high level on the Bloom's Taxonomy and call for high levels of engagement. Additionally, students also have the option to explore further into these concepts and they are also applying strategic thinking by planning throughout the activities. This type of thinking in the classroom means that they are high on the level of Webb's Depth of Knowledge. When all of these things work together along with Constructivism and the Universal Design for Learning it creates a highly engaging activates with a dynamic environment for the students to learn and discover in.

Resources

1. Nasa App (downloadable from the app store)
2. Fact sheet with each planet listed and key characteristic fill in the blanks
3. Planetary Travel Time Activity (<https://www.jpl.nasa.gov/edu/teach/activity/planetary-travel-time/>)
4. Kinesthetic Radial Model of the Solar System Activity (<https://www.jpl.nasa.gov/edu/teach/activity/kinesthetic-radial-model-of-the-solar-system/>)
5. Solar System Scroll Activity (<https://www.jpl.nasa.gov/edu/teach/activity/solar-system-scroll/>)
6. Ohio's Learning Standards and Model Curriculum (5th grade)
7. Basic school supplies needed: paper, scissors, calculators, markers/crayons

Results

By the end of these activity plans a student should have a full understanding of the different characteristics of planets that make up our solar system. Additionally, students will be able to show their understanding of the proportion/scale of our solar system. They will have physical work to show their progress through this learning process. First, they will be able to share their fact sheet that was filled out using the NASA app. Students will also be able to share their Solar System Scroll to help them describe the scale and proportion of our solar system. Lastly, students should be able to share about their experience doing the Planetary Travel Time Activity and also the Kinesthetic Radial Model of the Solar System Activity. These could be collected in a variety of forms that work best for the teacher. Some suggested options are a portfolio of work that could be turned in or a video of the students expressing what they have learned.

Critique and Conclusion

Though this lesson students got to experience and discover concepts about the planets in our solar system. After the foundational lesson using the NASA app students were prepared to work with their classmates and teacher through the other activities. Overall, students ended up gaining a learning experience that allowed them to build understanding of our solar system while fostering communication, groupwork, and critical thinking skills in the classroom.

Effect of Airfoil-Preserved Undulations on Wing Performance

Student Researcher: Faith A. Loughnane

Advisor: Dr. Sidaard Gunasekaran

University of Dayton

Department of Mechanical and Aerospace Engineering

Abstract

Most leading-edge tubercles studies involve serrated-type or undulated leading edges where the airfoil cross-section is destroyed unintentionally. Experimental investigations were performed at the University of Dayton Low Speed Wind Tunnel (UD-LSWT) on undulated wings where the NACA 0012 airfoil cross-section is preserved along the wingspan. Sensitivity study was done on the number of undulations along the span (6, 9 and 12) and undulation placement (leading edge, trailing edge, and both leading and trailing edge). The effect of the undulations on the wingtip vortex was also investigated through Particle Image Velocimetry (PIV). The wing with trailing edge undulations showed better aerodynamic performance and lower parasitic drag when compared to the baseline and other undulated wings at higher angles of attack. The aerodynamic coefficients were found to be independent of the number of undulations. For the same coefficient of lift, the undulated wing cases reduced the wingtip vortex circulation by 25% which in turn affected the balance of induced and parasitic drag. Investigation into the wingtip vortex core RMS and aerodynamic efficiency revealed a direct relationship where higher vortex core RMS resulted in a higher aerodynamic efficiency and vice-versa.

Background and Literature Review

Even with major advancements in aviation technology, an effective reduction of induced drag has remained a topic of study for many years. The lift-induced drag is responsible for more than 70% of the total drag of the aircraft during take-off and landing and about 5-15% of the total drag during cruise [1]. So far, no universal mathematical relation exists which relates the physics and properties of the wingtip vortex roll-up process, its evolution and the induced drag. Over the years, numerous methods to reduce induced drag have been conceived and implemented. Methods such as installing end plates at wingtips, winglets (most common), lift distribution tailoring (by changing the deflection of flaps on the wing), active/passive flow control methods (blowing or suction of air at the wingtip), etc. have been employed to affect the aerodynamic efficiency of the wing. Of all the methods mentioned above, the total reduction in drag so far has only been 5-7% [1]. The non-satisfactory performance of these methods is due to the insignificant influence by the devices on the wingtip vortex roll-up process.

Recent studies have shown the strength of the wingtip vortex can be significantly affected by enhancing the free shear layer interaction with the wingtip vortex [2], [3], [4]. The blockage of spanwise flow along the surface of the wing using active and passive flow control methods such as stall fences, dimples, bumps, riblets, etc. has been shown to have a strong influence on the growth and evolution of the wingtip vortex as well [5], [6], providing motivation for this study.

Historically, investigations into leading edge protrusions and surface features on wings was primarily bioinspired. Wings with unusual contours and undulations appear many places in nature, including the humpback whale [7], bats [8], and birds [9]. The humpback whale flipper has tubercles along the leading edge and on the trailing edge towards the tip of the flipper. Deriving similar motivation from wings found in nature, the main focus of this research will be to investigate the changes in aerodynamic performance

of wings with leading and trailing edge undulations, the effect of the undulations on the wingtip vortex, and the balance of lift induced and parasitic drag. This combination of these features was achieved by preserving the thickness to chord ratio of the airfoil along the span of the airfoil while changing the chord as a function of span.

Van Nierop et al. [10] investigated wing models with leading edge tubercles and found that the tubercles alter the pressure distribution resulting in boundary layer separation behind the tubercles, ultimately leading to a more gradual onset of stall and a higher stall angle. Shorbagy et al. [11] also performed a low-Reynolds number study on wings with leading edge tubercles and found that there was an increase in C_L/C_D for wings with sinusoidal leading edge tubercles and trailing edge tubercles at the wingtip. Hansen et al. [12] investigated the changes in wing performance with leading edge tubercles of varying wavelength and amplitude for distinct airfoil profiles and found that the tubercle parameters do not make a major impact in the pre-stall angle of attack, but there is a very noticeable impact in the post-stall range. One major difference between the previous studies mentioned above and the present is that in the previous literature, the airfoil cross-section is destroyed along the wingspan when the leading or trailing edge tubercles are incorporated into the wing design. Preserving the airfoil along the span while creating the undulations is hypothesized to provide better aerodynamic performance and predictability at both pre- and post-stall angles of attack. It is also hypothesized that the undulations created by preserving the airfoil will change the balance of induced and parasite drag of the wing.

Methodology

All experiments were conducted at the University of Dayton Low Speed Wind Tunnel (UD-LSWT) in the open jet configuration (Figure 1). The UD-LSWT has a 16:1 contraction ratio, 6 anti-turbulence screens and 4 interchangeable 76.2cm x 76.2cm x 243.8cm (30" x 30" x 96") test sections. The test section is convertible from a closed-jet configuration to an open-jet configuration with the freestream range of 6.7 m/s (20 ft/s) to 40 m/s (140 ft/s) at a freestream turbulence intensity below 0.1% at 15 m/s measured by hot-wire anemometer. The contraction feeds into a pressure/air sealed room where the test section is located. The effective length of the test section in the open jet configuration is 182 cm (72"). A 137 cm x 137 cm (44" x 44") collector collects the expanded air on its return to the diffuser. The velocity variation for a given RPM of the wind tunnel fan is found using a Pitot tube connected to a TSI T600 Micromanometer.

Nine different airfoil-preserved undulated wing cases (3 with trailing edge undulations, 3 with leading edge undulations and 3 with both leading and trailing edge undulations) were considered for the sensitivity study. The three cases for each undulation placement have different number of undulations on the wing surface (6, 9 and 12). The different cases are depicted in Figure 1. The baseline wing has a chord length of 12.7 cm and a wingspan of 25.4 cm resulting in a semi-span AR of 2 (full span AR 4). The undulated wings have a mean chord of 11.43 cm (4.5 in) and an effective full-span AR of 4.5. The test models shown were generated in SolidWorks and printed using the University of Dayton Gorilla Maker 3D Printer.

Undulation Placement

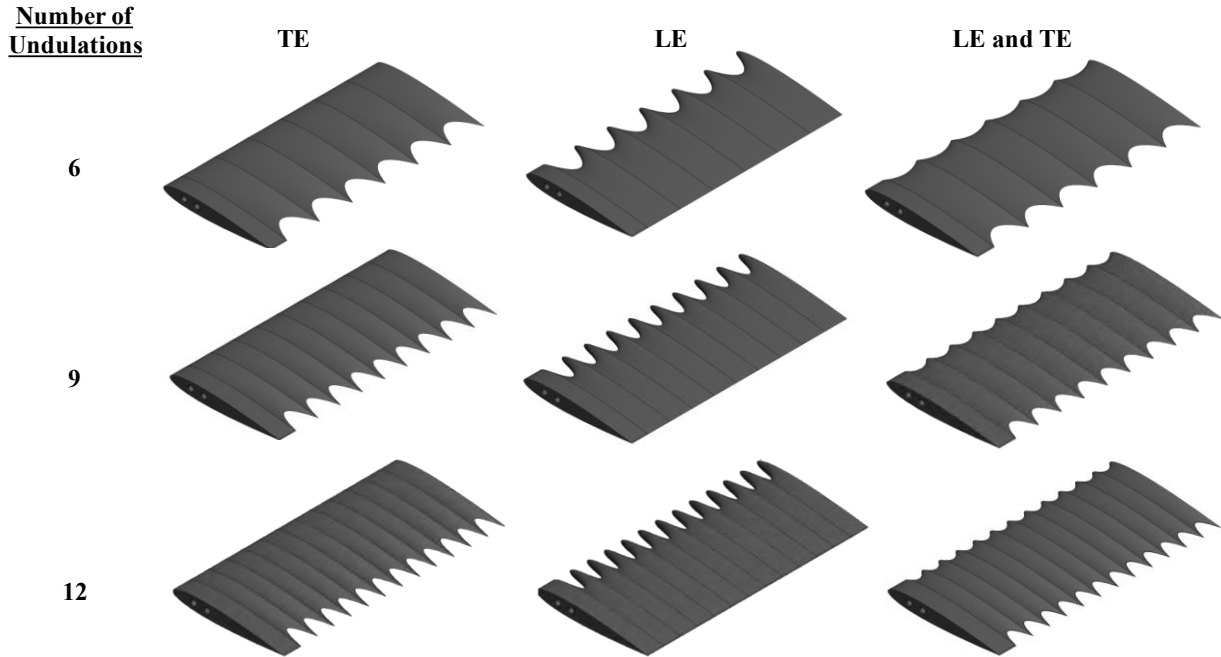


Figure 1. Schematic of wing models with varying undulation numbers and locations.

The ATI Gamma Sensor was used to measure the normal force (N) and axial force (A) on the wing which were transformed into lift and drag forces which were later converted to lift and drag coefficients, C_L and C_D . The sensor was located underneath the splitter plate along with the Griffin motion rotary stage which was used to control the angle of attack. The rotary stage was controlled using Galil motion software. All undulated wings and the baseline NACA 0012 wing were tested at a freestream velocity of 35 m/s which corresponds to a Reynolds number of approximately 282,000. The experiments were conducted at an angle of attack range of -17° to 17° in 1° increments. Two trials of each case were conducted to ensure repeatability.

Cross-stream Particle Image Velocimetry (PIV) was conducted to analyze how the undulations affected the wingtip vortex compared to the straight NACA 0012 wing. The PIV experiment was conducted using a Vicount smoke seeder with glycerin oil, a 200 mJ/pulse Nd:YAG frequency doubled laser (Quantel Twins CFR 300) and an Imperx B2021 camera with 200 mm lens. A plano-convex and plano-concave lens were used in series to open the laser beam into a sheet. The laser sheet was placed 3 chord lengths behind the wing. The laser and camera were triggered simultaneously using a Quantum composer pulse generator. In each test case, 500 image pairs were obtained and processed using ISSI Digital Particle Image Velocimetry (DPIV) software. Two iterations were performed in DPIV processing with 64-pixel interrogation windows in the first iteration and 32-pixel interrogation windows in the second iteration. The cross-stream PIV experiment was conducted at a Reynolds number of 201,000. The camera was located more than 10 chord lengths downstream from the trailing edge of the wing to reduce the effects of the camera disrupting the flow. The time delay between the laser pulses was changed at each angle of attack to obtain 8 to 10-pixel particle displacement at the wingtip vortex core boundary.

Force-Based Experiment Results

The coefficient of lift results from the force-based experiments are shown in Figure 2. It can be seen that there is not a strong correlation between the number of undulations and lift performance, however the placement of the undulations has a distinct effect. Trailing edge undulated (TEU) wings show improved lift over the baseline and other undulated wings until stall, leading edge undulated (LEU) wings show decreased lift as compared to the baseline and other undulated wings up until higher angles of attack. The LEU wings show a more gradual onset of stall and a higher stall angle which was also observed in previous literature. The leading and trailing edge undulated (LETEU) wings show characteristics of both the TEU wings and LEU wings with a slight increment in lift over the baseline at lower angles of attack and then a more gradual onset of stall.

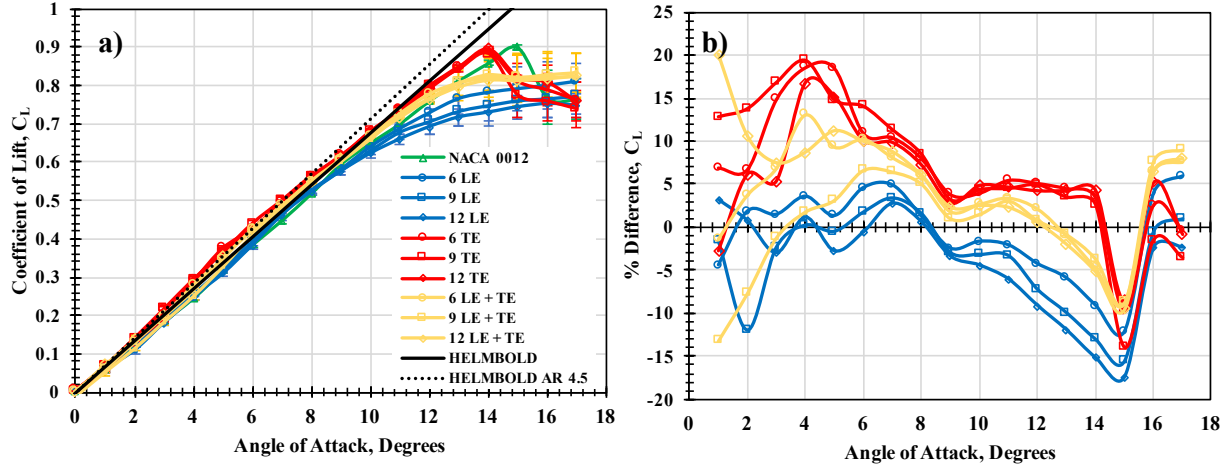


Figure 2. Variation of C_L a) comparison of all cases and b) percent difference from baseline NACA 0012 wing.

The coefficient of drag results from the force-based experiments are shown in Figure 3. Again, the number of undulations does not show a strong correlation to the drag performance while the placement of the undulations does have an effect. The TEU wings and LETEU wings show the most favorable drag performance as most cases show a slight decrement in drag as compared to the baseline from about 7 to 12 degrees. The LEU wings show a large increment in drag at most points, especially at high angles of attack.

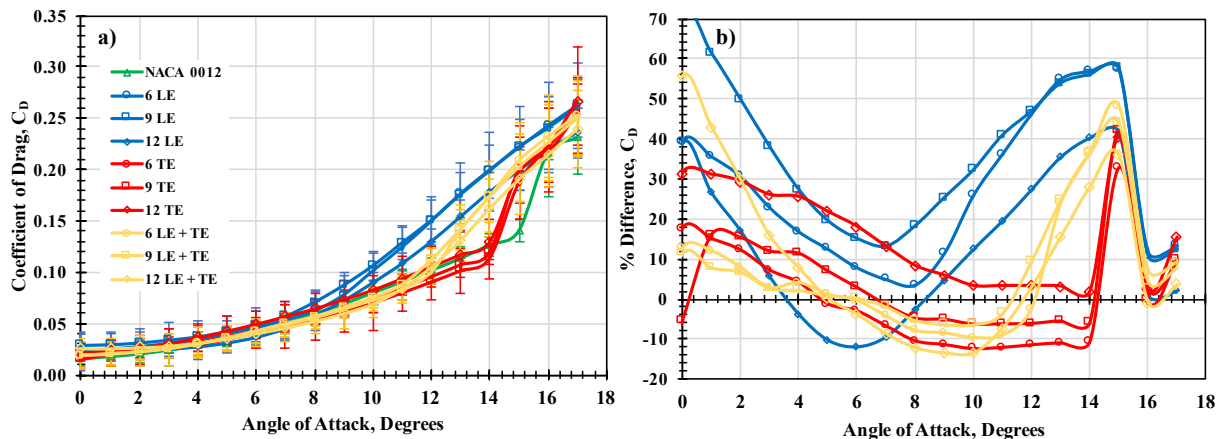


Figure 3. Variation of C_D a) comparison of all cases and b) percent difference from baseline NACA 0012 wing.

The coefficient of induced drag and parasitic drag was also calculated for each case to see how the undulations affected the balance of induced and parasite drag. These results can be seen in Figure 4. It can be seen that the undulations do, in fact, affect the balance. The TEU wings show consistently lower parasite drag however slightly higher induced drag at all angles of attack until stall. The LEU wings show consistently higher parasite drag and lower induced drag especially at higher angles of attack. The LETEU wings show consistently lower parasite drag until the gradual stall begins, at which point parasite drag begins to dominate induced drag.

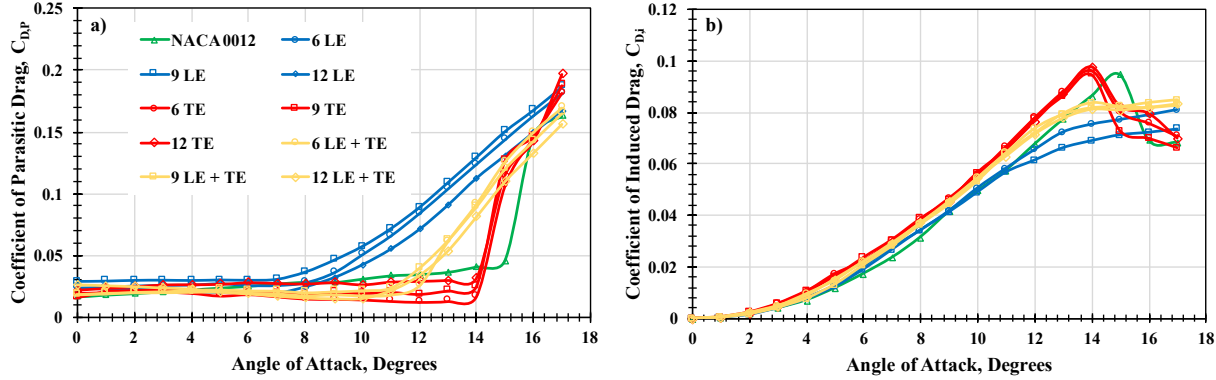


Figure 4. VARIATION OF a) INDUCED DRAG AND b) PARASITE DRAG WITH ANGLE OF ATTACK.

The aerodynamic efficiency quantified by the ratio of C_L and C_D for the different wing cases are shown in Figure 5. It makes sense that the TEU and LETEU wings show improved aerodynamic efficiency especially at lower angles of attack as more lift and less drag was produced in these cases. Similarly, it is expected that the LEU wings show poorer aerodynamic performance as consistently less lift and more drag was produced for these cases.

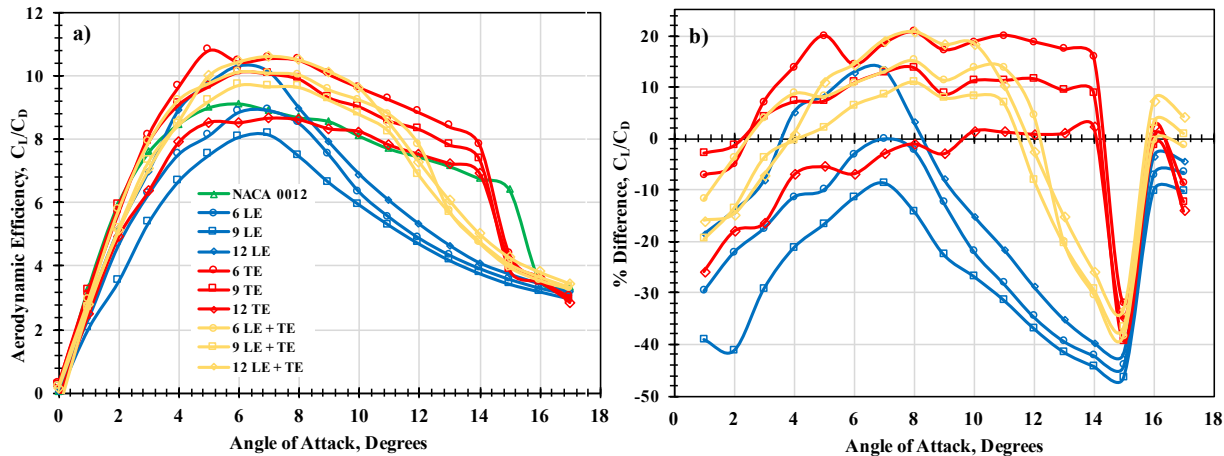


Figure 5. VARIATION OF C_L/C_D a) COMPARISON OF ALL CASES AND b) PERCENT DIFFERENCE FROM NACA 0012 WING.

Wingtip Vortex PIV Results

In order to quantify the effect of undulations on the wingtip vortex growth and evolution, the wingtip vortex normalized azimuthal velocity profiles of the baseline and the undulations wings are compared against the well-known Batchelor's wingtip vortex model given by

$$\frac{U}{U_{Max}} = \left(1 + \frac{1}{2\alpha_L}\right) \frac{1}{\eta} (1 - \exp(-\alpha_L \eta^2)) \quad (1)$$

where U_{Max} is the maximum velocity in the X direction, α_L is Lambs constant: 1.256, η is r/r_c where r is the radial location in the wingtip vortex and r_c is wingtip vortex core radius determined by the radial location where maximum azimuthal velocity occurs. For most cases shown in Figure 6, it can be seen that the velocity distribution follows the Batchelor's model trend very well at r/r_c greater than 1. However, inside the wingtip vortex core, deviations from the Batchelor's model can be observed, especially at lower angles of attack. This due to the non-mature status of the wingtip vortex at lower angle of attack cases and similar behavior is documented abundantly in literature. The wings with undulations also show similar behavior as the baseline but doesn't show higher deviations from the model at lower angles of attack (2°) as observed in the baseline case.

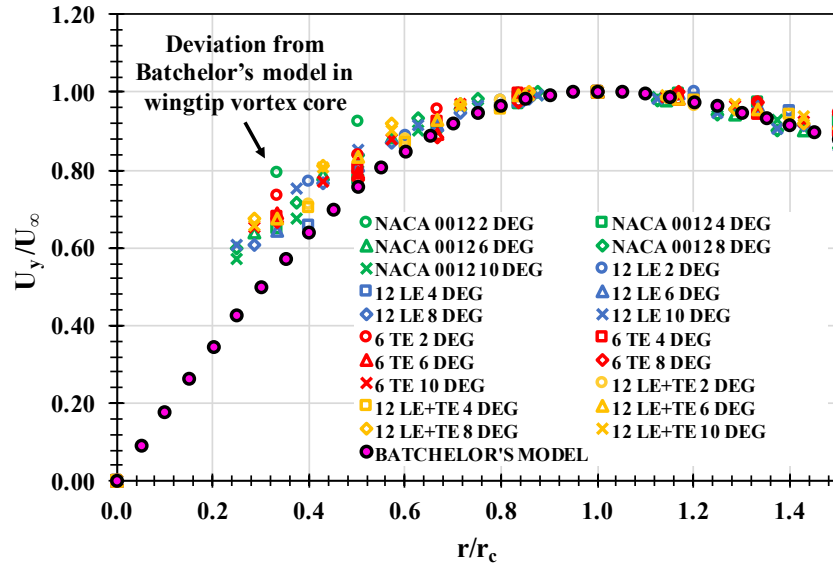


Figure 6. Variation in normalized u-velocity with respect to radial location.

The normalized z-vorticity of the wingtip vortex was determined for the baseline and undulated wings (Figure 7). It can be seen that the magnitude of the vorticity increases with an increase in angle of attack for all cases considered. A quick visual investigation of the contours reveal no significant variations between the vorticity contours with the exception of 12 LEU wing case. The wingtip vortex was found to be smaller at each angle of attack when compared to the other cases. This indirectly indicates a reduction in lift as observed in the lift coefficient plot shown in the previous section.

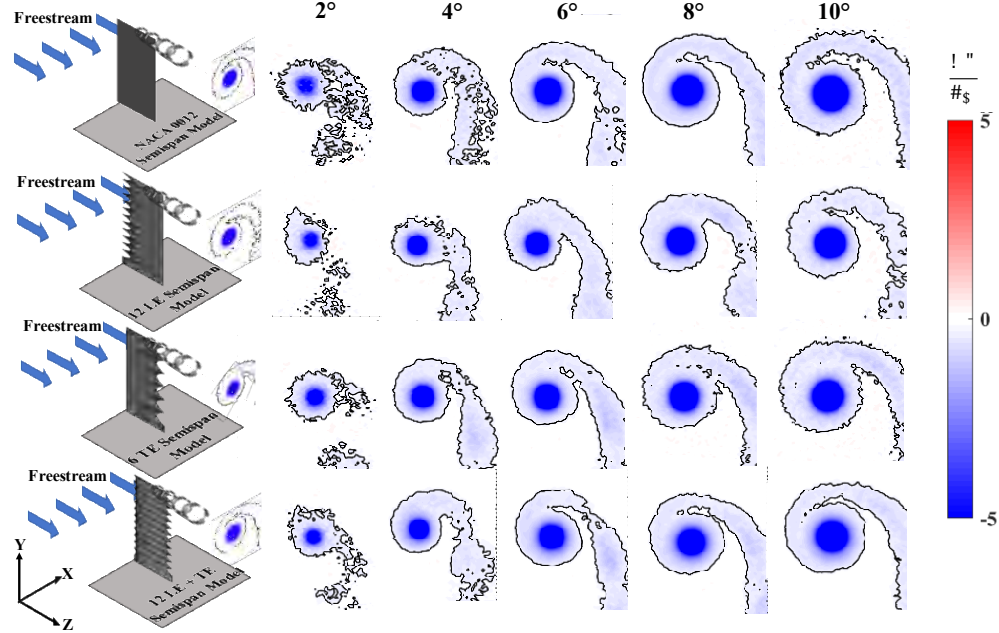


Figure 7. Normalized vorticity from 2° to 10° angles of attack for baseline and undulated wings.

To quantify the reduction in wingtip vortex strength, the circulation of the wingtip vortex was obtained by integrating the vorticity as shown in Eq. (2).

$$\Gamma = \iint \Omega \cdot ds \quad (2)$$

where Γ is the circulation, Ω is vorticity, and ds is the incremental surface area. After determining the vortex center through Q-criterion, the wingtip vortex circulation was determined as a function of wingtip vortex radius. This wingtip vortex circulation as a function of vortex radius obtained from the experimental data is then compared to the ideal Lamb-Oseen vortex model described by Eq. (3)

$$\Gamma(r) = \Gamma_0 \left(1 - \exp \left(-\frac{r^2}{r_c^2} \right) \right) \quad (3)$$

The Γ_0 in Eq. (3) was changed until a good fit was achieved between the model and the experimental data. This method of determining wingtip vortex circulation was developed by Stevens [13] and has been employed in Corkery et al. [14] and Stevens and Babinsky [15]. The Lamb-Oseen model is fitted with the experimental data by finding the Γ_0 which results in the highest R^2 value. The average R^2 value for all cases was 0.985.

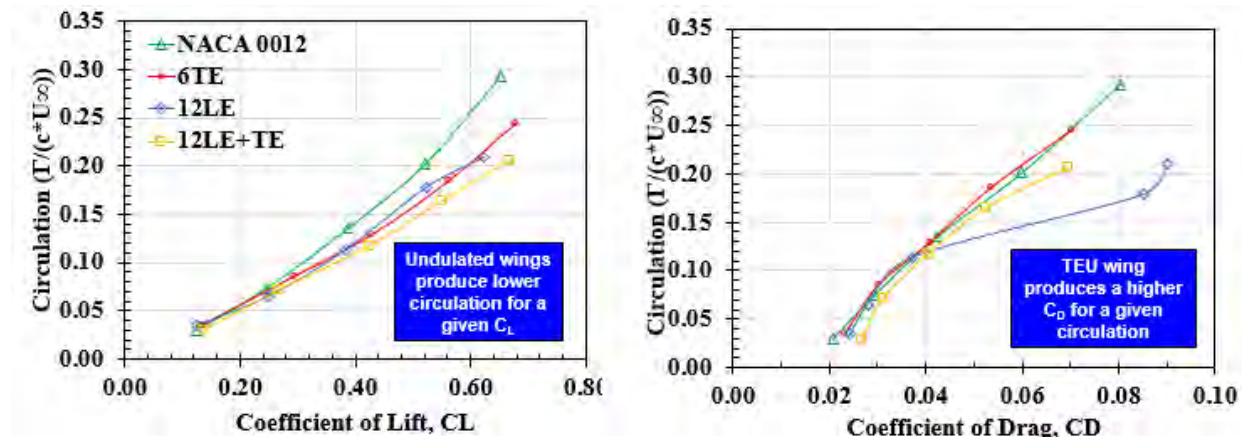


Figure 8. Variation of circulation as a function of a) coefficient of lift and b) coefficient of drag.

Figure 8 shows the normalized circulation as plotted against C_L and C_D . For the same value of C_L , the undulated wings produce lower circulation than the NACA 0012 wing with as high as almost 33% difference in the LETEU case at a C_L of about 0.64. This shows that the undulated wings are producing the same C_L with a lower circulation. This violates the Kutta-Joukowski theorem of linear variation between the C_L and circulation. However, it should be noted that the Kutta-Joukowski theorem was derived under the assumptions of inviscid and irrotational flow. It is possible that the undulations increased the viscous interactions of the wingtip vortex when compared to the baseline leading to a lower wingtip vortex circulation value for the lift coefficient condition. The change in normalized circulation with C_D is also shown in Figure 8. The undulated wings and NACA 0012 wing trend together with the exception of the LEU case. Given a certain circulation value, the LEU case produces a higher C_D than the NACA 0012 wing, TEU case, and LETEU case. This trend is in excellent agreement with the increase in C_D is observed for the LEU case in the force-based data.

The RMS of the velocity is calculated by

$$U_{RMS} = \sqrt{u'^2} \quad (4)$$

where u' is the fluctuating velocity about the x-axis. The variation of the freestream normalized peak U_{RMS} with coefficient of drag is shown in Figure 9.

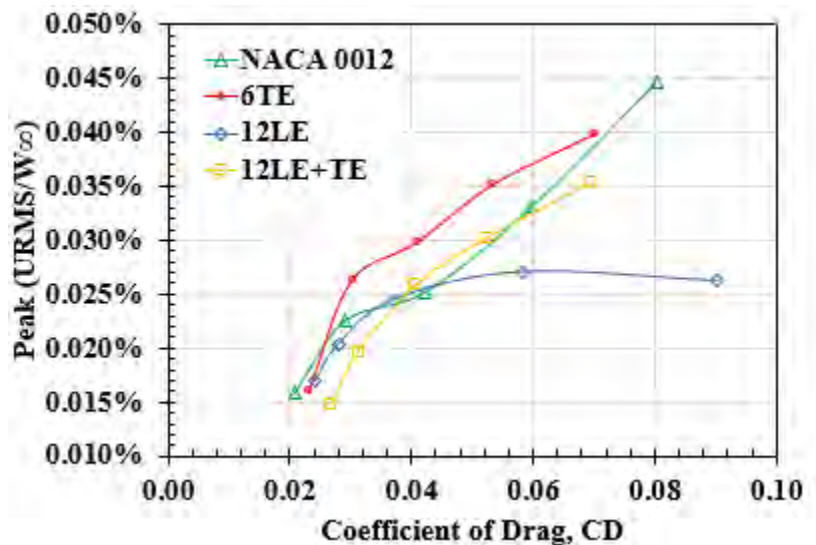


Figure 9. Variation of the normalized peak U_{RMS} as a function of C_D .

A trend is seen in the peak RMS vs with C_D where the 6TEU wing shows greater RMS at a given coefficient of drag condition when compared to all the other cases. Coincidentally, the 12LEU wing case shows lower RMS when compared at a given C_D condition. All these correlations indicate that the vortex RMS is a good indicator of the aerodynamic performance of the wing.

Conclusions

Wings with airfoil preserved undulations were investigated to determine its effect on the aerodynamic performance and on the balance of induced and parasite drag of the wing.

- The force-based aerodynamic coefficients show clear differences in aerodynamic performance between the TEU, LEU, and LETEU cases even at lower angles of attack. The TEU wing cases performs better than the LEU and LETEU wing cases, especially at lower angles of attack. At higher angles of attack however, the LEU and LETEU wing cases hint the post-stall benefits observed in the previous literature. It was observed that the changes between the TEU, LEU and LETEU cases were due to the way the wings change the balance of induced and parasite drag.
- The lift coefficient seems to be independent of the number of undulations on the TEU, LEU and LETEU wing cases. However, subtle changes were observed between the number of undulations in drag coefficient and in the aerodynamic performance. However, no discernible trends were observed.
- The top performing candidates of each category: 6 TEU, 12 LEU and 12 LETEU cases were chosen for PIV investigations, to provide insight to the way it affects the balance of induced and parasite drag of the wing. Relationship is observed in the LEU wing case which showed poor aerodynamic performance at low angles of attack and resulting in a lower RMS in the wingtip vortex core and a higher RMS in the wingtip vortex core for the better performing 6 TEU wing. This relationship indicates that vortex RMS has an inverse relationship with the aerodynamic performance and the wingtip vortex RMS plays a key role in affecting the balance of induced and parasite drag of the wing.

References

1. Hefner, Jerry N., and Dennis M. Bushnell. "An overview of concepts for aircraft drag reductions." (1977).
2. Gunasekaran, Sidaard, and Aaron Altman. "Better Insight into the Wingtip Vortex-Free Shear Layer Interaction." 55th AIAA Aerospace Sciences Meeting, AIAA 2017-1705.
<https://doi.org/10.2514/6.2017-1705>
3. Gunasekaran, Sidaard, and Tim Gerham. "Effect of Chordwise Slots on Aerodynamic Efficiency and Wingtip Vortex." AIAA Journal 56, No. 12 (2018): 4752-4767. <https://doi.org/10.2514/1.J057073>
4. Gunasekaran, Sidaard and Nathan Thomas. "Affecting Aerodynamic Efficiency by Influencing Wing Surface-Flow Direction." 2018 AIAA Aerospace Sciences Meeting, AIAA 2018-0344.
<https://doi.org/10.2514/6.2018-0344>
5. Walker, Michael M., and Jeffrey P. Bons. "The Effect of Passive and Active Boundary-Layer Fences on Swept-Wing Performance at Low Reynolds Number." In 2018 AIAA Aerospace Sciences Meeting, p. 0793. 2018. <https://doi.org/10.2514/6.2018-0793>
6. Solfelt, Daniel, and Raymond Maple. "CFD analysis of a T-38 wing fence." In 46th AIAA Aerospace Sciences Meeting and Exhibit, p. 331. 2007. <https://doi.org/10.2514/6.2008-331>
7. Fish, Franke E., D. S. Miklosovic, F. E. Fish, Jack Durham, Michael McDonald, AskNature Team, and Nature Kidd. "Flippers Provide Lift, Reduce Drag: Humpback Whale." AskNature, February 24, 2005. <https://asknature.org/strategy/flippers-provide-lift-reduce-drag/>
8. Bryce, Emma. "Behind the Scenes of the World's Largest Bird Wing Collection." Audubon, July 14, 2016. <https://www.audubon.org/news/behind-scenes-worlds-largest-bird-wing-collection>
9. "Bat Wings Images." Shutterstock. Accessed December 2, 2019.
<https://www.shutterstock.com/search/bat wings>
10. Van Nierop, E., Alben, S & Brenner, M. P., How bumps on whale flippers delay stall: an aerodynamic model, Physical review letters, PRL 100, 054502, February, 2008
<https://doi.org/10.1103/PhysRevLett.100.054502>
11. Shorbagy, Mohamad A., Bamsan El-hadidi, Gamal El-Bayoumi, Osama Said, and Moatasem Fouda. "Experimental Study on Bio-Inspired Wings With Tubercles." In AIAA Scitech 2019 Forum, p. 0848. 2019. <https://doi.org/10.2514/6.2019-0848>

12. Hansen, Kristy L., Richard M. Kelso, and Bassam B. Dally. "Performance variations of leading-edge tubercles for distinct airfoil profiles." AIAA Journal 49, No. 1 (2011): 185-194
<https://doi.org/10.2514/1.J050631>
13. Stevens, P. R. R. J., "Unsteady Low Reynolds Number Aerodynamic Forces," Ph.D. Dissertation, Univ. of Cambridge, England, U.K., 2013.
14. Corkery, S. J., Stevens, P. R. R. J., and Babinsky, H., "Low Reynolds Number Surge Response of a Flat Plate Wing at 90 Degrees Incidence," AIAA SciTech Forum-55th AIAA Aerospace Sciences Meeting, AIAA Paper 2017-0330, 2017. doi:10.2514/6.2017-0330 <https://doi.org/10.2514/6.2017-0330>
15. Stevens, P. R. R. J., and Babinsky, H., "Experiments to Investigate Lift Production Mechanisms on Pitching Flat Plates," Experiments in Fluids, Vol. 58, No. 1, 2017, <https://doi.org/10.1007/s00348-016-2290-x>

An Application of Modal Decomposition to Supersonic Flow Over a Wall-Mounted Turret

Student Researcher: Mikala J. Malkus

Advisor: Dr. Datta Gaitonde

The Ohio State University
Aerospace Engineering

Abstract

Data driven modal decomposition techniques provide a means for extracting physically important features from time-resolved dynamic systems. While these methods are well-developed, the interpretation of the obtained modes to understand complex unsteady flow physics can be difficult. In this research, the Proper Orthogonal Decomposition (POD) and Dynamic Mode Decomposition (DMD) techniques were employed to study the unsteady behavior of supersonic flow over a wall-mounted turret. This flow contains a variety of time-dependent features including multiple unsteady shock waves. The POD method was used to objectively rank the dominant features in the system while the DMD method highlighted structures based on their dynamics and their evolution with time. The analysis indicates that unsteady shock waves dominate many aspects of the unsteadiness in this flow, since the top POD mode contained over 40% total energy. The DMD modes revealed that the unsteady shock waves were oscillating at a peak nondimensional frequency of $St_L \sim 0.3$. Modal decomposition was shown to be a useful tool for characterization of unsteady flows, which is vital for flow control techniques to be developed.

Project Objectives



Figure 1. Hemispherical turret mounted on an aircraft. [1]

This research aims to expand our knowledge on how modal decomposition can be used as a tool to study fluid problems with a variety of complex features, as well as provide useful information for developing flow control strategies. An interesting example of such a problem is supersonic flow over a wall-mounted protuberance, such as a turret on an aircraft. Hemispherical turrets are optimal platforms for projecting and receiving laser beams due to their large field-of-view. When placed on airborne vehicles moving at transonic to supersonic speeds, the flow-physics become unsteady and complicated. The features that evolve, including multiple shock waves and regions of separation, cause distorting aero-optic effects on the laser projected from the turret. The unsteadiness and complexity of the physics increase in intensity with Mach number. As a result, the application of these laser systems has seemed impractical for supersonic aircraft.

The techniques used in this research, the Proper Orthogonal Decomposition (POD) and Dynamic Mode Decomposition (DMD), decompose data into characteristic spatial “modes” based on things like energy content, frequency, and growth rate. This flow contains broadband, multiscale features that lent themselves well to be extracted using modal decomposition.

Flowfield Data Description

The flow analyzed in this research was from a Large Eddy Simulation (LES) of Mach 2 flow over a wall-mounted cylinder. This simulation was completed at the Ohio State University. This flow is a 2D representation of the full 3D hemispherical turret. The various unsteady features can be found outlined in Figure 2. The data for the flow domain was recorded for a series timesteps, taking in snapshots. The spatial dimension was $N = 1.2$ Million points. The temporal dimension was $M = 7000$ snapshots.

Methods

A. The Proper Orthogonal Decomposition (POD)

The Proper Orthogonal Decomposition (POD) is a modal decomposition technique which aims to decompose data into a minimal number of basis vectors or modes that contain the most energy in the system over time. In POD, the temporal mean is subtracted so you are left with the unsteady components, $U'(x, t) = U(x, t) - \bar{U}(x)$. Through an algorithm called the Snapshot POD method, which can be found in reference [1], the data is decomposed in the following way:

$$U'(x, t) \approx \sum_{i=1}^M a_i(t) \Phi_i(x)$$

where Φ_i are the spatial POD modes and a_i are the corresponding temporal coefficients. These are obtained by solving the eigenvalue decomposition of the data's covariance matrix, defined as:

$$C = \frac{1}{M-1} U'^T U$$

In which case you obtain eigenvalues, λ_i , for each eigenvector (POD modes), ordered from largest to smallest. These values tell you how well each mode captures the variance of the data. The modes that are capturing the most unsteadiness in the data will be ordered first. The POD method gives you an objective way to rank the flow structures it extracts.

B. The Dynamic Mode Decomposition (DMD)

The Dynamic Mode Decomposition (DMD) is a modal decomposition technique that extracts spatial coherent structures with a single temporal frequency and growth/decay rate. With this method, we assume a linear operator $[A]$ is evolving our data from one snapshot to the next in the following way:

$$\mathbf{x}_{k+1} = A \mathbf{x}_k$$

An equation of this form has a well-known solution, =

$$\mathbf{x}_k = \sum_{j=1}^n \phi_j \lambda_j^k b_j = \Phi \Lambda^k b$$

where Φ are the eigenvectors and λ_i are the eigenvalues of the operator $[A]$. If solved directly, this matrix is of the size $[N \times N]$, which is computationally infeasible. The DMD algorithm, which can be found in reference [2], provides a computationally feasible approach to solving for these eigenvalues and eigenvectors. These eigenvectors, also called DMD modes, approximate the dynamical shapes of features in the data. The eigenvalues tell you the frequency and the growth/decay rate of the corresponding modes.

Results Obtained

The top POD mode contained the motion of the two upstream unsteady shock waves and captured over 40% of the density variation in the flow. Similar shock shapes were found in the top modes of the velocity field, but with higher magnitudes also in the separated regions. This suggested that the oscillations in the separation regions could be contributing to the shock unsteadiness. Overall, the POD analysis gave evidence that the shock motion was dominating the unsteadiness in the flow. These modes can be seen in Figures 2 and 3 below.

The DMD analysis extracted modes that approximated how features in the flow were evolving, with each mode separated by a characteristic frequency. The unsteady shock motion was captured in the lowest-frequency mode, for both the density and velocity fields, at a non-dimensional frequency of $St_L \sim 0.3$. This low frequency motion agreed well with the trends normally seen in shock wave/turbulent boundary layer interactions. These modes can be seen in Figures 4 and 5 below.

The POD and DMD analysis both extracted modes that contained the motion of the separation and reattachment shock waves. The shapes captured in both methods agreed well with one another and both revealed the two shocks moving out of phase. While the POD analysis was able to objectively identify that shocks were the most dominant unsteady feature, it was not able to provide information regarding dynamics. The DMD analysis was able to complement the POD analysis by providing detail about the dynamics of the shock motion, revealing a low frequency that could be targeted for future flow control techniques. Although the flow application contained a variety of unsteady, multiscale features evolving at different frequencies, modal decomposition was able to characterize the dominant physics.

Figures and Tables

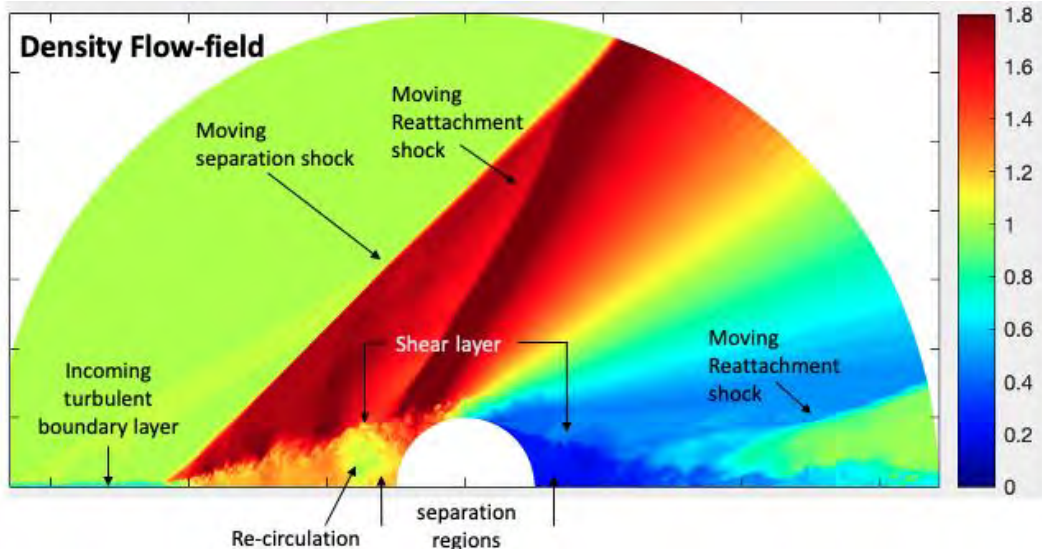


Figure 2. 2D Flow over a wall-mounted turret, instantaneous density field with unsteady features marked.

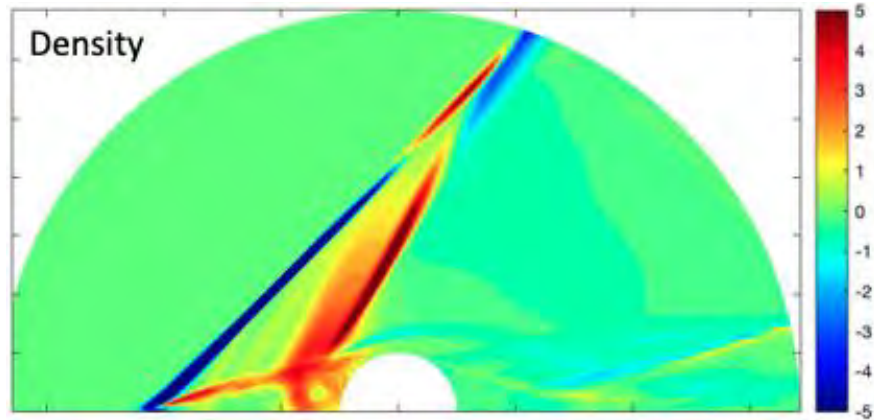


Figure 3. Density field, leading POD mode, contains > 40% of total density fluctuation.

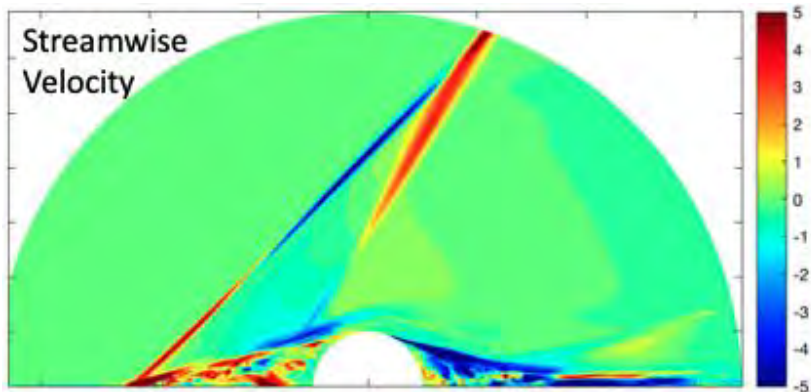


Figure 4. Streamwise velocity field, leading POD mode, contains 12% of total velocity fluctuation.

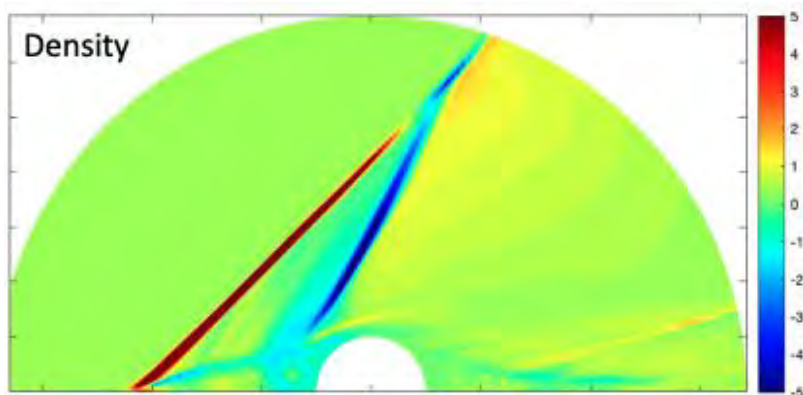


Figure 5. Density field low-frequency DMD Mode $StL \sim 0.3$.

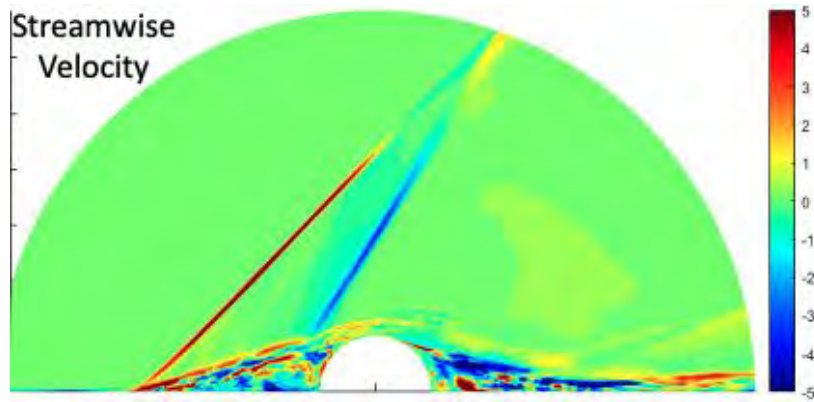


Figure 6. Streamwise Velocity field low-frequency DMD Mode StL ~ 0.3 .

Acknowledgments

I would like to sincerely thank my advisor, Dr. Datta Gaitonde, for providing me with the opportunity to develop, conduct, and own my research as an undergraduate student. In addition, I want to thank Dr. Mohammad Samimy for recommending me to this scholarship. Finally, I would like to thank my family and friends for supporting and guiding me throughout all my endeavors in life.

References

1. Lockheed Martin, Air Force Research Laboratory (AFRL). (2015).
2. Lawrence Sirovich. "Turbulence and the dynamics of coherent structures. I - Coherent structures". In: *Quarterly of Applied Mathematics* 45 (1987)
3. J. N. Kutz et al. "Chapter 1: Dynamic Mode Decomposition: An Introduction". In: SIAM, 2016, pp. 1–24.

Determining the Influence of a Novel Mutation located in the C-terminal Cytoplasmic Domain of the CCR5 Gene on Infectivity of Primate Lentiviruses

Student Researcher: Sara A. Martin

Advisor: Dr. Harry W. Kestler

Lorain County Community College
Biology Department

Abstract

The subjects of this study are from a family of 6 from Florida, including a mother and her 5 children. The mother contracted HIV before she gave birth to her first child in the early 1980's, and unknowingly exposed all 5 children to the virus. All but one child, the second born, contracted HIV. Genetic analysis was consistent with the mother being the source of the virus, as her children's birth order was inversely correlated with the degree of relatedness between her HIV and her children's. A missense point mutation in the carboxyl terminal (TG5) was discovered in the uninfected child's *ccr5* gene, changing a lysine codon to an arginine codon at position 314. The allele containing the TG5 mutation was amplified using polymerase chain reaction. This study aims to sub-clone TG5 into pLenti puro HA-Ubiquitin, a retroviral plasmid vector. Clones made from pLenti-TG5 will be used to transfect the cell packaging line 293FT. The 293FT cell line will assemble viral particles containing the TG5 mutation. The retroviral particles will then be used to determine if CCR5-TG5 has a negative effect on surface expression of CXCR4 or wild-type CCR5.

Project Objectives

To determine if the TG5 allele containing a lysine to arginine mutation is capable of altering the infectivity of T lymphocytes.

Methodology Used: Cell culturing, DNA splicing, polymerase chain reaction, DNA cloning

The subjects of this study are from a family of 6 from Florida, including a mother and her 5 children. The mother contracted HIV before she gave birth to her first child in the early 1980's, and unknowingly exposed all 5 children to the virus. All but one child, the second born, contracted HIV. Genetic analysis of the virus obtained from the HIV positive family members was consistent with the mother being the source of the virus, as her children's birth order was inversely correlated with the degree of relatedness between her HIV and her children's. A genetic explanation for the second child's lack of infection was investigated, and a missense point mutation in the carboxyl terminal (TG5) was discovered in the uninfected child's *ccr5* gene, changing a lysine codon to an arginine codon at position 314 located in the carboxyl terminal end of the final cytoplasmic domain of the protein. The ability of the *ccr5* gene containing the lysine to arginine mutation was investigated, and the allele containing the TG5 mutation was amplified using polymerase chain reaction. The amplified TG5 sequence was sub-cloned into pLenti puro HA-Ubiquitin, a retroviral plasmid vector. Clones made from pLenti-TG5 are used to transfect the cell packaging line 293FT. Retroviral particles containing the TG5 mutation are assembled by the 293FT cell line. The retroviral particles are used to determine if CCR5-TG5 has a negative effect on surface expression of CXCR4 or wild-type CCR5 in cells expressing both.

Evaluating the Effect of Electrode Configuration in Electrostatic Actuators for Increasing the Intensity of Vibrotactile Feedback

Student Researcher: Taylor W. Mason

Advisor: Dr. Jeong-Hoi Koo

Miami University

Department of Mechanical and Manufacturing Engineering

Abstract

The vibrational sensation felt on the surface of a screen, known as vibrotactile feedback, is a key feature of many modern touch displays. This sense of touch enhances user feedback and improves object usability. Today, there exist several actuators used for generating vibrotactile feedback in touch displays, such as eccentric rotary motors, linear resonant actuators, piezoelectric actuators, and electrostatic actuators. These actuators are primarily used for small displays in hand-held devices to effectively create touch feedback. However, the current actuators are not suitable for large touchscreen displays because they cannot produce sufficiently large vibrotactile sensations. Devices such as tablets, information kiosks, and automotive dashboard panels are examples of large touchscreens that typically lack the capability to generate vibrotactile feedback for the users. To address a growing need for actuators used in large touch displays, this research studies the effectiveness of a new electrostatic actuator design that utilizes a moving mass to generate greater vibrotactile feedback. Two actuators were compared, studying the effect that electrode configuration has on the actuators' maximum vibration. The initial results showed that the dual-electrode actuator produced larger vibrations, generating a maximum of 11.97 g-forces compared to the single-electrode actuator's maximum of 8.27 g-forces. More research is needed to validate these initial results.

Introduction

Touchscreens have become increasingly popular in everyday electronics, but the market is expanding beyond handheld devices. The vibrational sensation felt on the surface of a touchscreen, known as vibrotactile haptic feedback, is most commonly used in small consumer electronics, such as cell phones, to create engaging user interfaces without the need for mechanical buttons [1]. Studies have shown that the implementation of such haptic modules in touch displays increases input speed and input accuracy, as well as tactile feedback and user satisfaction [2]. Many small touchscreen devices utilize vibrotactile feedback, however, this feedback is lacking in the developing market for large touch displays (10-inch or larger). This is because most of the current haptic actuators used in touch displays are small and lightweight, allowing them to fit in mobile devices, but they fail to create sufficiently large vibrational sensations when used in bigger screens. Devices such as tablets, information kiosks, and automotive dashboard panels are examples of large touchscreens that typically lack the capability to generate vibrotactile feedback for the users.

In an effort to develop a new actuator for large touch display applications, this study proposes a new haptic module based on an electrostatic actuator. Unlike traditional electrostatic actuators, it intends to incorporate a moving mass in the module to increase vibration intensity. The mass is driven by an electrostatic force generated by electrodes in the actuator. The working principle of the proposed actuator can be seen in Figure 1 (a). A vibrating mass in the center of the actuator is connected to a grounded base through thin radial beam springs. The addition of the moving mass greatly increases vibrational performance, making it useful for large touch screen applications. The proposed module and

proof-of-concept design prototype are based on previous research [3]. *Figure 1 (b)* shows a prototype electrostatic actuator that utilizes one bottom electrode to generate vibration. The long-term target application of using the actuator in large touchscreens can be visualized in *Figure 1 (c)*, where four actuators are used in combination to generate the required vibrations.

This study helps to further advance the research done in the field of electrostatic actuators for vibrotactile haptic feedback. The current conventional haptic actuators cannot create sufficient vibrotactile sensations in large screens. To address this need, a new actuator design that uses a moving mass to create strong vibrations is proposed. This project studies and characterizes the existing prototype actuators' single degree of freedom vibrational performance when using one electrode compared to two electrodes. The performance evaluation will be used to improve the prototype actuators, as well as determine which electrode configuration produces the optimal results.

Project Objectives

The primary goal of this research was to evaluate and compare the vibrotactile haptic potential of two actuators with different electrode configurations. To accomplish this goal, vibrational testing was done with the actuators to determine their maximum steady-state peak to peak acceleration (this study's metric for vibrational output) and resonant frequency. The results were plotted together and compared to see which electrode configuration produced the strongest vibration on the actuator's mass.

Methodology Used

The movable mass on the actuator was modeled as a single degree of freedom mass, spring, and damper system with an electrostatic force as an input. The first step was to identify the critical parameters of the actuator prototypes (see *Figure 2*) such as resonant frequency, damping ratio, and spring stiffness. These parameters were found experimentally through the use of a function generator and accelerometer and dynamic mechanical analysis (DMA) testing on the single-electrode actuator, shown in *Figure 3*. Using Hooke's Law, the spring stiffness of the mass' radial beam springs was calculated for the actuator. The Fourier transform of a chirp signal was used to estimate the actuator's resonant frequency, and the half-power method was used to estimate the damping ratio. The experimentally determined resonant frequency and spring stiffness were then used to calculate the actuator's mass using the simple harmonic oscillation natural frequency formula. Both actuators were made to be identical, but due to the very high manufacturing precision required, it was suspected that they might have different critical parameters.

After the system identification was complete, an experimental study was conducted to test the actuators' vibrotactile performance. In the performance testing, the steady-state peak to peak acceleration was measured using an accelerometer and oscilloscope across a frequency range of 80-200 Hz. The sampling frequency was increased near the actuator's resonant frequency to provide a more accurate result. To power the electrodes, a custom controller and high voltage amplifier were used. In the first experiment, the single-electrode actuator with a bottom electrode was used. In the next experiment, the dual-electrode actuator was used. A hole was made in the dual-electrode actuator's top electrode, which allowed the accelerometer to be mounted directly onto the actuator's mass. This resulted in an approximate 20% reduction in area, which was expected to proportionally lower that electrode's performance by 20%.

Results

After taking the Fourier transform of the time response chirp data, the estimated resonant frequency was found to be 129.1 Hz for the single-electrode actuator. Using Hooke's Law on the DMA testing data, the single-electrode actuator spring stiffness was calculated to be 16.62 kN/m. The mass on the actuator was then calculated as 25.26 grams using the experimental resonant frequency and spring stiffness. The dual-electrode actuator parameters were estimated to be approximately equal to the single-electrode actuator.

The single degree of freedom vibrational performance experiments were conducted and plotted together, seen in Figure 4. Based on the acceleration experiments, it is clear that the resonant frequencies of the two actuators are not equal. The dual-electrode actuator produced a higher maximum acceleration of 11.97 g-forces, compared to the single-electrode actuator which produced 8.27 g-forces.

Despite the actuator performance testing only providing initial results, it is clear that the dual-electrode actuator produces greater vibrotactile feedback compared to its single electrode counterpart. These results show promising potential for the use of this actuator in generating vibrotactile feedback for large touch displays. Future studies will be conducted to validate these initial results and to evaluate the actuator's two degree of freedom vibrational performance when mounted onto a touchscreen panel.

Figures

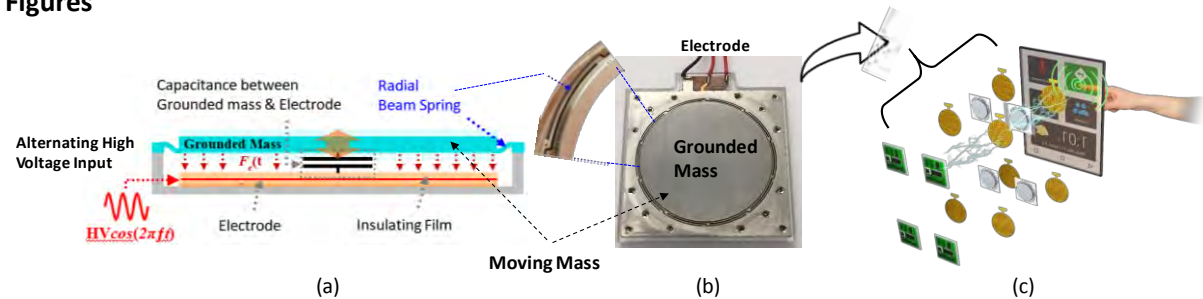


Figure 1. (a) Working principle of the proposed actuator (b) Constructed prototype actuator (c) Exploded view of the actuator's incorporation in large display panels.

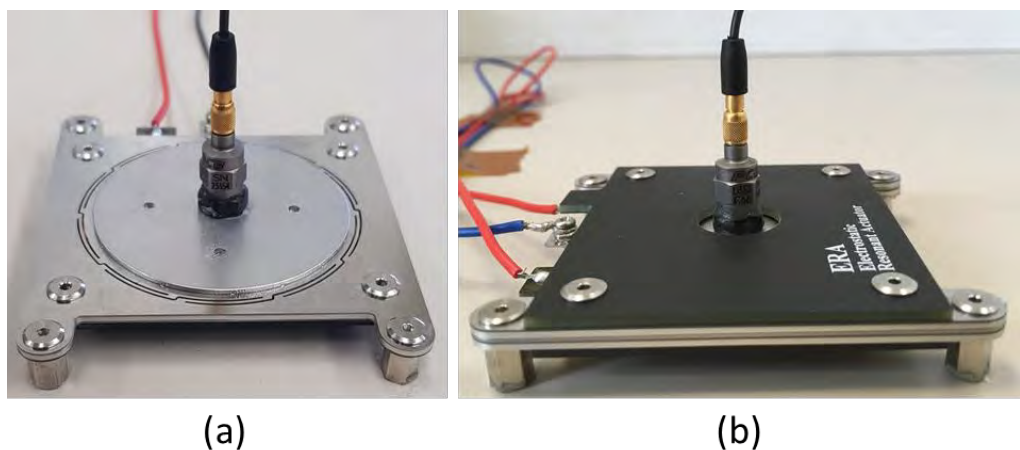


Figure 2. (a) Single-electrode actuator with an electrode below the mass (b) Dual-electrode actuator with electrodes below and above the mass.

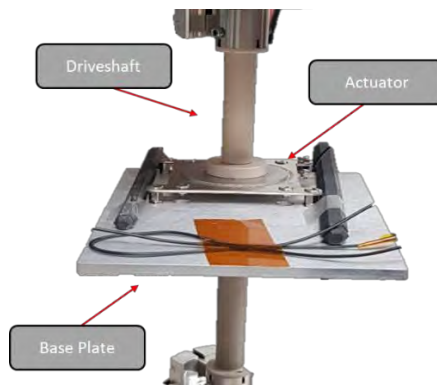


Figure 3. DMA testing setup used to measure the actuator's spring stiffness.

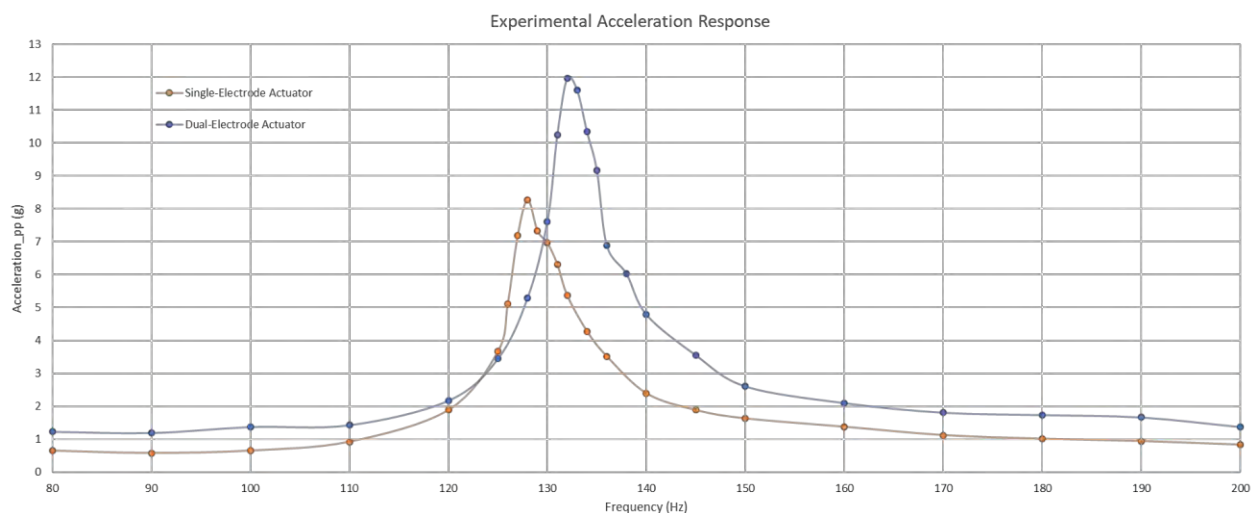


Figure 4. Experimental acceleration response of single-electrode actuator (orange) and dual-electrode actuator (blue). The dual-electrode actuator produces a larger maximum vibration of 11.97 g-forces compared to the single-electrode actuator's 8.27 g-forces.

References

1. M. Silfverberg, "Using Mobile Keypads with Limited Visual Feedback: Implications to Handheld and Wearable Devices," *Mobile HCI 2003*, ed. L. Chittaro, LNCS 2795: 76-90 (2003).
2. Banter, Bruce. "Touch Screens and Touch Surfaces Are Enriched by Haptic Force-Feedback." *Information Display*, vol. 26, no. 3, 2010, pp. 26–30.
3. Schuster, Jeremy. "Modeling and Simulation of a Novel Electrostatic Beat Actuator for Haptic Feedback in Touch Screens." Electronic Thesis or Dissertation. Miami University, 2018. *OhioLINK Electronic Theses and Dissertations Center*. 02 Oct 2019.

GC-MS Analysis of Spirits

Student Researcher: Clayton R. Mastorovich

Advisor: Dr. Regan Silvestri

Lorain County Community College
Department of Math and Sciences

Project Description

Gas Chromatography-Mass Spectroscopy (GC-MS) can be readily utilized to generate the analytical profile of flavor compounds in spirits. In the Republic of Ghana, gin is commonly flavored with herbs including garlic, ginger and various nuts producing a drink known as "bitters". Application of this GC-MS method will generate the flavor profile of Ghana spiced gin bitters.

In addition, the GC-MS method is being applied to generate the flavor profile of moonshine twice distilled from bananas. Fruity ester flavors were anticipated a priori from the bananas, however our previous work has shown that the twice distilled spirit is unfortunately lacking in any fruit flavors. Comparisons of the flavor profiles between the banana mash, the once distilled spirit, and the twice distilled spirit will pinpoint where in the process the fruity ester flavors are lost, in an effort to recommend changes to the distillation process which could retain the fruit flavors.

Current Research

We are currently using our GCMS to test the flavor compounds found in Ghana spiced gin bitters. The data from the Ghana gin bitters is then compared to data from normal unflavored gin. The preliminary data shows that there are differences between the Ghana spiced gin bitters and the unflavored gin. At the moment we are also running preliminary GCMS trials on the banana flavored moonshine. The preliminary for the banana flavored moonshine shows there is a distinct difference between the banana mash, once and twice distilled moonshine.

Millimeter-Wave Polarimetry for Non-Contact Investigations of Aluminum Alloy Microstructure

Student Researcher: Spencer T. Matousek

Advisor: Dr. Ryan Toonen

The University of Akron
Department of Electrical Engineering

Abstract

This study looks for a way to detect sensitization of alloys with a contactless method. Sensitization of aluminum surfaces can lead to intergranular corrosion. Many times, with industries like military sea vessels, it is beneficial to know if a material has been sensitized so that it can be addressed at an appropriate time. The current industry standard for testing for sensitization is bulk resistivity measurements. Although simple, this process is inconvenient because it can require a piece of material to be cut out for testing.

Project Objectives

The project objective is to remotely collect magneto-optic Kerr effect (MOKE) data from aluminum alloy surfaces. This will be accomplished using millimeter-wave (mmW) reflection polarimeter to detect slight changes in the mmW polarization before and after contact with the MUT.

Methodology

The millimeter wave is generated at 15.3125GHz which is converted to 61.25GHz using a frequency multiplier. The wave is focused with a spherical reflector and two convex lenses before it contacts the Material Under Testing (MUT). By using an XYZ stage the MUT is positioned at the focal point of the millimeter wave where the wave is planar. Directly behind the MUT is positioned an electromagnet that is powered from 0 to 2 amps. The setup of the experiment is shown in Figure1.

The reflection of the mmW off of the MUT passes through a convex lens so that the wave can be measured at a focal point. A dual Polarized Horn Antenna (DPHA) is used to measure the polarization of the wave. Equation 1 solves for polarization given the amplitude of the vertical and horizontal components of the millimeter wave from the DPHA.

$$|\cos(n\theta_R) \sin(n\theta_R)| = \delta\theta \propto \frac{< V_V - V_H >}{< V_V > + < V_H >}$$

Equation 1 describes the relation between the polarization and the vertical and horizontal magnitudes.

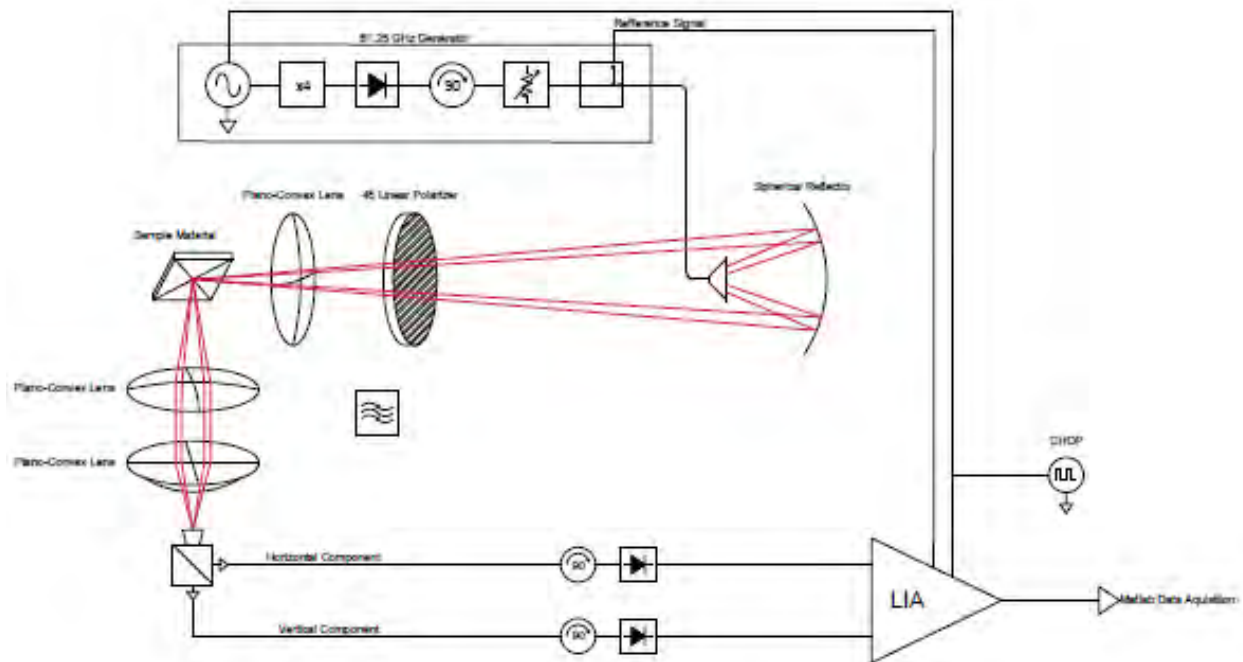


Figure 1 illustrates the setup for this experiment.

The electromagnet was experimentally measured at the focal on the MUT and is characterized by the Equation 2 in terms of the current sourced to the magnet.

$$EMag\ Field\ at\ Sample\ (mT) = 1.8565 * I - 0.0434\ (A)$$

Equation 2 describes the relation between the current source and the magnetic field at the MUT.

Due to the heating characteristics of the electromagnet, it is run at a duty cycle of 50%. Figure 2 shows the control of the electromagnet to measure one cycle. Only measurements were taken when the electromagnet was high.

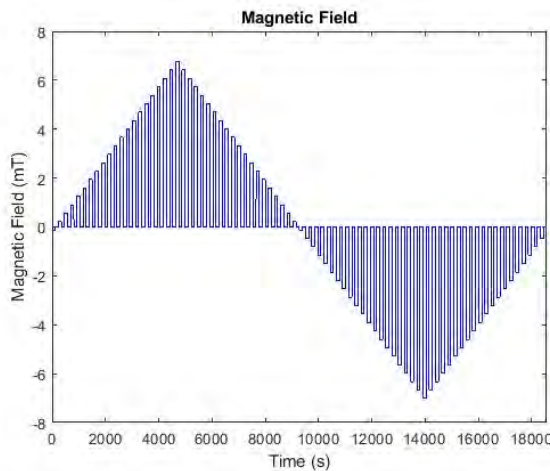


Figure 2 shows 1 cycle of varying magnetic field at the MUT.

The MUT started with no sensitization and was gradually sensitized by baking in an oven at 150C. Each set of measurements was taken after one or two days of sensitizing and consisted of 5 cycles shown in Figure 2. For each cycle of measurements, the magnet was sourced current from 0 to 2 amps, from 2 amps to 0, from 0 to -2amps and finally from -2amps to 0 all at an increment of 0.1amps as shown if Figure 2. The first two cycles gave the MUT time for its electromagnetic characteristics to settle. Due to the sensitivity of the measurements the final three cycles were averaged together.

Results

Figure 3 shows the polarization of all sets of data. This plot shows the different hysteresis plots shifted to be on top of each other. This is only representative of the different shapes and there seemed to be no correlation between the levels that they were shifted to and the amount of sensitization.

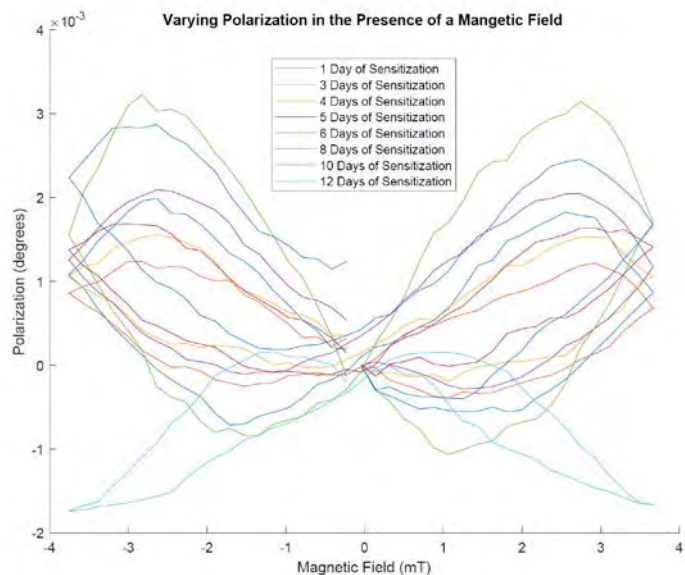


Figure 3 shows the polarization of the mmW in the presence of a varying magnetic field with respect to sensitization.

Although the hysteresis plots show varying shapes that seem to have no trend, the area within the hysteresis plots may have an upward trend as shown in Figure 3. This plot looks at the area inside the hysteresis curves and is plotted across levels of sensitization. Due to issues in the lab, the setup needed to be reconstructed after the sixth day of sensitization. This may be the cause of the drastic dip in data in Figure 3 after the 6th day of sensitization.

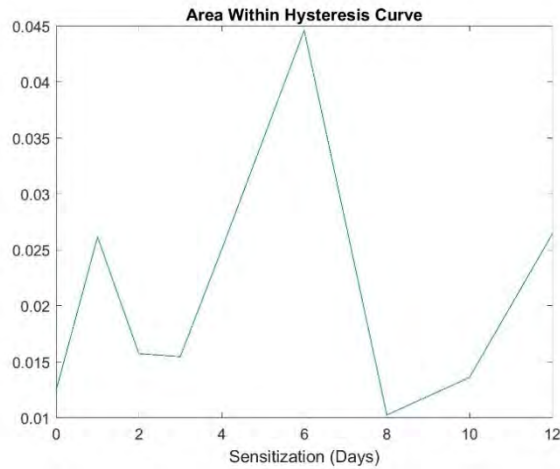


Figure 4 shows the area within the hysteresis curves plotted against sensitization.

Figure 5 shows data that has been modified from Figure 4. In this new data set, the point after which the setup was reconstructed, was replaced by the average of the slope of data between 4-6 and 8-10 days of sensitization. Proceeding data points were shifted by the same amount.

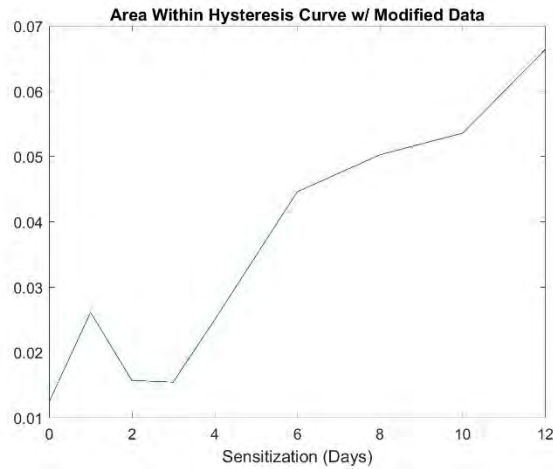


Figure 5 shows the area within the hysteresis curves plotted against sensitization with reconstructed data.

Conclusion

A dual beam MOKE setup was designed and implemented to watch the hysteresis characteristics of sensitized and un-sensitized aluminum. With the level of precision used, there is no correlation between the amount of sensitization and the magnitude of the horizontal and vertical components when the horizontal and vertical components are looked at independently. There is possible correlation in the hysteresis characteristics of the polarization of the millimeter wave and the amount of sensitization. Due to the extreme sensitivity of the experiment and the unfortunate that the setup needed to be rebuilt halfway through, it is hard to posit that there is a trend. This experiment can be improved upon by adding a resonator screen on top of the MUT which would cause more interaction with the millimeter wave and the MUT and create a more pronounced shape. There were also minor inconsistencies in the holder of the MUT. In conclusion, there is possible correlation between the characteristics of the polarization and the levels of sensitization of the material under testing.

Channel Detection and Synchronization in Ultra-Wideband Communication Systems

Student Researcher: Stephen M. Matz

Advisor: Dr. Moncef Tayahi

Cleveland State University
Electrical Engineering and Computer Science

Abstract

This project analyzed the characteristics of an optimal ultra-wideband communication system to provide adequately high data rates while using significantly less power than traditional narrowband systems. While some ultra-wideband systems are currently in use, technical challenges like signal detection, estimation, and synchronization pose technical challenges to the widespread deployment of these communication systems. An end-to-end system model was developed and used to evaluate the performance of ultra-wideband communication systems. MATLAB was used to specifically study the properties and characteristics of channel detection and synchronization in these systems.

Project Objectives

An ultra-wideband communication system model was developed in MATLAB. This model simulated the parameters required for detection, estimation, and synchronization for communication channels with predominantly multi-path characteristics. By changing different model parameters, like the number of paths or type of multi-path environment, characteristics were gathered and exploited to improve the model, and suggestions were provided for future ultra-wideband system implementation. To evaluate the performance of the system model, metrics such as Bit-Error-Ratio (BER) and calculated timing offsets were used.

Project Methodology

A basic end-to-end communication system model was developed based on the block diagram shown in **Figure 1** [1]. Because ultra-wideband systems use very large bandwidths in the range of a few Gigahertz (GHz), the model has a time step size of 125 picoseconds (ps) to support frequency resolution up to 8 GHz. At a data rate of 1 megabit per second, 1000 bits of simulated data were transmitted and analyzed at the receiver.

To test the system performance, an array of binary digits was randomly generated with an equal probability distribution. These bits were converted to a bipolar Non-Return-to-Zero Line-Inverted (NRZ-L) modulation format so that a one was represented as a positive square wave, and a zero was represented as negative square wave. To match the time resolution of the simulation, the NRZ-L data was up-sampled and filtered with an interpolation filter. The data stream was then modulated with a Gaussian monocycle pulse with a pulse duration of 1 nanosecond (ns). The Gaussian monocycle, shown in **Figure 2**, is the first derivative of a Gaussian pulse and has a large bandwidth suitable for ultra-wideband communications [2]. To implement this modulation, the NRZ-L formatted data was pulse shaped by the convolution function with the Gaussian monocycle. The resulting waveform was a baseband modulated signal; no heterodyning to passband frequencies was done.

Typical communication systems model the propagation channel as an Additive White Gaussian Noise (AWGN) channel, in which random noise with a Gaussian distribution is added to the signal [1]. At large bandwidths with many signal reflections, the AWGN model is not adequate, because the distortion by

noise is solely added; no multi-path reflections are modeled. To account for the multiple electromagnetic path reflections, attenuations, and group delay, a modified Saleh-Valenzuela channel model proposed in the IEEE 802.15.4a technical report was used instead of the AWGN channel model [3]. The Saleh-Valenzuela model is a commonly used model for wideband and ultra-wideband systems, as it accurately models the random delays, amplitudes, and phases of multi-path reflected rays within multiple delayed clusters [4]. An example of a single randomly generated multipath channel impulse response using the Saleh-Valenzuela channel model is seen in **Figure 3**. Two specific models used from the IEEE report were for Non-Line-Of-Sight (NLOS) residential environments, such as office spaces and homes with signal attenuation through walls and reflections through hallways and rooms. The effects of such an environment were accounted for by convolving the transmitted signal through multiple paths of a randomly generated Saleh-Valenzuela impulse response.

Signal detection of the channel-impaired signal was done with a bank of matched filters, one for a positive pulse, and another for a negative pulse. These filters were matched to the estimated Gaussian monocycle after transmission through the channel. By subtracting the difference of the two matched filters, a signal estimate was produced. A hard-decision decoder was used to decode whether a binary one or zero was sent, based on the signal estimate. The hard-decision decoder output a binary one if a positive pulse was estimated and a binary zero if a negative pulse was estimated. The data output remained in this format for a BER calculation.

Results and Discussion

The modulation of choice for this ultra-wideband simulation was an impulse radio scheme using very short duration pulses for a wide bandwidth. The data was directly modulated using a Gaussian monocycle pulse. It was determined that the Gaussian monocycle was an effective waveform to use for an ultra-wideband communication system. However, the first attempt at modelling was not successful. Unlike the familiar AWGN channel impairments, the typically used matched filter was not adequate. Due to the multi-path environment from the Saleh-Valenzuela channel, the impulse response resulted in a delayed and severely distorted signal that was not able to be demodulated by the matched filter if the Gaussian monocycle was used as a reference signal. For proper demodulation, a modified reference signal was needed.

The modified reference signal was generated by transmitting a single Gaussian monocycle pulse through the channel. The time-reversed and delayed version of the received signal was then used as the new reference. **Figure 4** shows the received signal after transmission through the Saleh-Valenzuela channel. By using this distorted signal as the reference signal, the transmitted pulses could be accurately matched and demodulated. This may be implemented in further research by using an initial training sequence known by both the transmitter and receiver. As the expected training sequence is received, the receiver may use an adaptive filter to match the pulses transmitted through the channel after an initial estimate.

A simple form of data synchronization was done based on the number of samples in the symbol period and received signal using the mathematical equivalent of a ‘stolen clock’. This was done by aligning the received data with respect to the start of the simulation. Methods for true synchronization were theorized while troubleshooting simulation issues, because the Saleh-Valenzuela channel may cause delays in the signal from the first major peak of the impulse response. True symbol synchronization may be possible based on the symbol spacing of a training sequence.

Changing parameters like the type of multi-path environment and the number of reflections received did not change the calculated BER. For simulations tested with 1, 100, and 500 multi-path channel

impulse responses, the BER remained zero, indicating that no errors occurred. Similarly, using two different NLOS residential environment models from the IEEE 802.15.4a report, the BER remained zero with 100 multipath impulse responses.

Figures

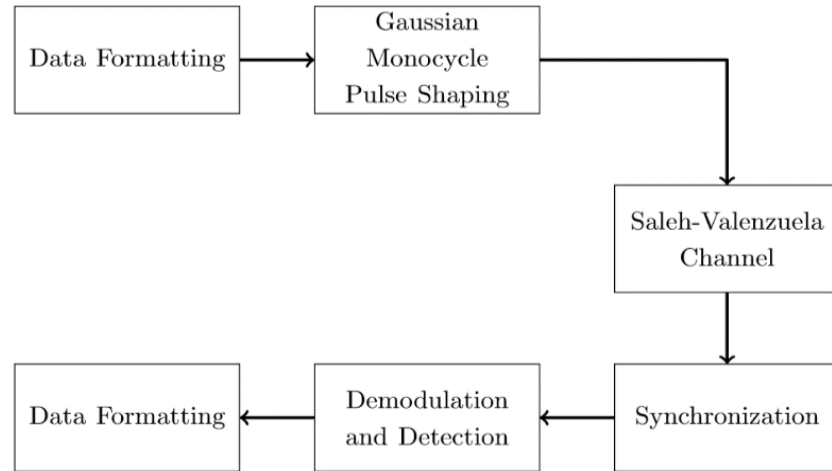


Figure 1. Ultra-Wideband Communication Model.

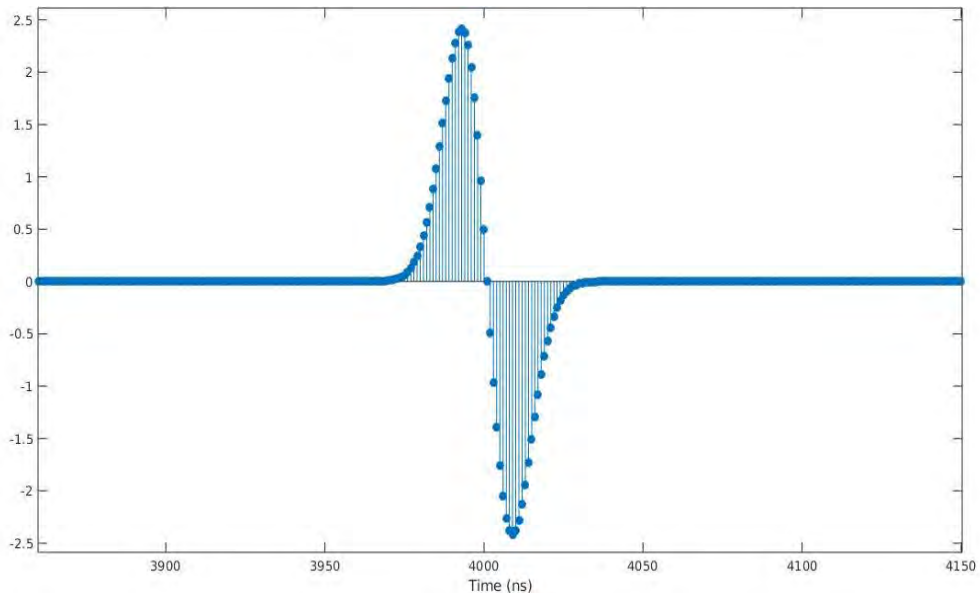


Figure 2. Gaussian Monocycle Pulse.

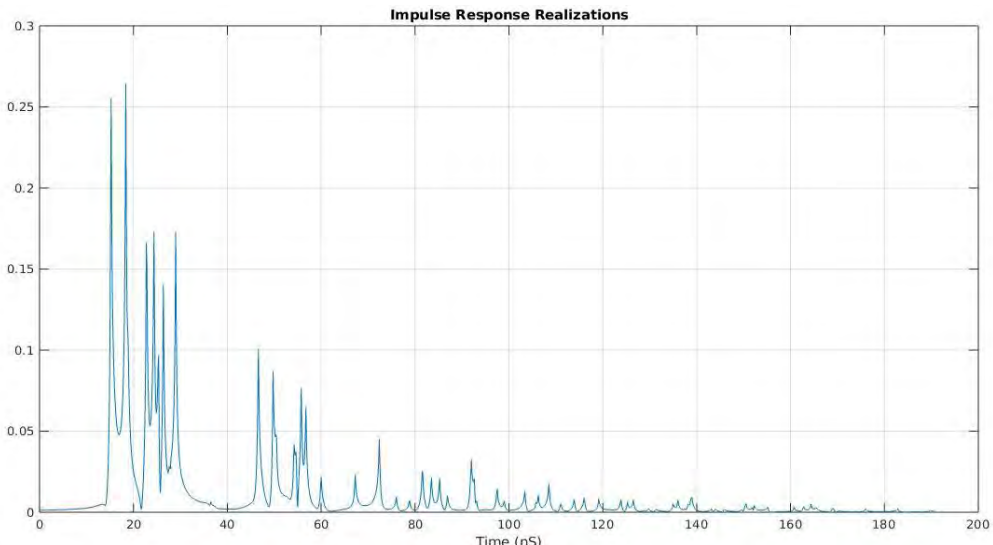


Figure 3. A Single Multi-Path Saleh-Valenzuela Channel Impulse Response.

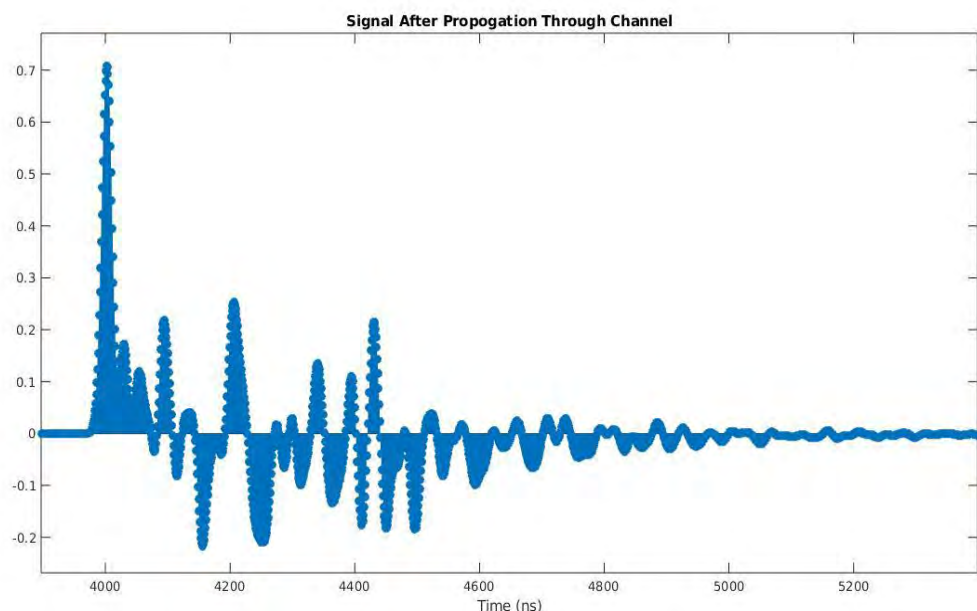


Figure 4. Received Gaussian Monocycle Pulse after Saleh-Valenzuela Channel Distortion.

References

1. B. Sklar, *Digital Communications: Fundamentals and Applications*, 2nd ed. Prentice Hall PTR, 2001.
2. M.-G. D. Benedetto, T. Kaiser *et al.*, Eds., *UWB Communication Systems A Comprehensive Overview*. Hindawi Publishing Corporation, 2006.
3. A. F. Molisch, K. Balakrishnan *et al.*, “IEEE 802.15.4a Channel Model – Final Report,” IEEE 802.15 WPAN Low Rate Alternative PHY Task Group 4a (TG4a), Tech. Rep., Nov. 2004.
4. Meijerink and A. F. Molisch, “On the Physical Interpretation of the Saleh-Valenzuela Model and the Definition of Its Power Delay Profiles,” *IEEE Trans. On Antennas and Propagation*, Vol. 62, Sep. 2014.

Classifying Clouds through Inquiry

Student Researcher: Madison M. McBryer

Advisor: Dr. Bridget Mulvey

Kent State University
Education Department

Abstract

This lesson is geared towards 11th grade students taking an Environmental Science course. This lesson focuses on learning how to classify clouds based on their formations and coverage. In this lesson, the students are provided with the opportunity to use their devices in conjunction with NASA's GLOBE Observer system to capture images of different clouds outside. The students will then submit their images to NASA's database, and try to classify their cloud images by comparing them to satellite images from the database. After exploring the satellite images, the students will develop a visual aid to help them identify the different types of clouds based on their appearance.

Objectives/Alignment

Students should be able to identify the four types of clouds (cirrus, stratus, cumulonimbus, cumulus). Students should be able to visually represent the different cloud formations.

This lesson is based primarily on the following Ohio Environmental Science standard (2018):
ENV.ES.5: Movement of matter and energy through the hydrosphere, lithosphere, atmosphere and biosphere

- Weather
- Climate

Lesson/Methodology

This lesson would ideally span 4 or 5 days, so that the students can collect cloud images over the course of many days. The students will start out with their data collection. Each student will be asked to use their device to download the NASA GLOBE Observer application. Students who do not have a personal device should either be provided one or asked to pair up with a student who has one. Once the students have downloaded the application, the teacher will give the students a tutorial on how to use the application outdoors. The students will go outside each day and take pictures of the clouds with their devices.

Each day, the students will collect their images and upload them to the NASA database once they return to the classroom. Then, the students will visit NASA's GLOBE Observer database to compare their cloud images to NASA's satellite images. The students will use a cloud classification chart to aid them in identifying the different cloud types.

At the end of the data collection and comparison, the teacher will review the different cloud types and formations in the form of a whole class discussion. Then, the students will be asked to create a visual representation of the cloud classification system. The students will be provided with the materials to create colorful posters or infographics depicting the different cloud formations. The visual representation will serve as the formative assessment for this lesson, and will also help the students identify the different types of clouds in the future.

This lesson incorporates a wide variety of engaging activities that allow different types of learners to be successful in the classroom. This lesson was designed based on the theory that there are three different types of learners that must be supported; visual, auditory, and kinesthetic. There are learning opportunities in this lesson that support all three of the different types of learners. Visual learners will benefit from the cloud images that they get to explore (both from NASA's database and from their own images). In addition, the cloud classification chart will incorporate images to help the students match cloud names with their formations. Auditory learners will benefit from the teacher-facilitated class discussion about the different types of clouds and their respective forms. Kinesthetic learners will benefit from the activity in which they use their personal devices to go outside and collect images of the clouds in the sky. The formative assessment at the end (designing a poster or infographic) will benefit all of the different types of learners by allowing them to express their knowledge creatively.

Results Obtained

Due to the outstanding global circumstance that ensued in the midst of the academic year, I did not have the opportunity to implement this lesson plan into the classroom. Ideally, I would have used this lesson over the course of a week this Spring with weather that would permit capturing images of the clouds outdoors. After completing the lesson, I would document student engagement and formative assessment performance to determine the effectiveness of this lesson plan. I would use those results to determine what could be improved for further implementation in the classroom setting.

Reference

1. NASA GLOBE Observer: "GLOBE Observer." *GLOBE.gov*, observer.globe.gov/do-globe-observer/clouds.

Wireless Mesh Networking for Swarm Robotics

Student Researcher: Cameron McCaskey

Advisor: Dr. Brian Trease

The University of Toledo

Mechanical Industrial and Manufacturing Engineering

Abstract

Swarm robotics are robotics in which multiple robots are deployed, often with different sensor packages. In this case, the robotic swarm takes shape in the form of small boats that are deployed on Lake Erie to study harmful algae growth patterns. Swarm robotics are a complicated subject because any small increase in cost or complexity exponentially increases the cost or complexity of the entire robotic swarm. One of these key areas of interest is telemetry. Telemetry in the robotic swarm allows for the robots to be controlled from a central base station and also communicate with each other their exact location to avoid collisions.

Project Objectives

The objective of this research project is to use and adapt off the shelf wireless transceivers to implement the telemetry system for these swarm robotics. These off the shelf solutions allow for other labs to implement the same robotic swarm without investing in building custom electronic hardware.

Off the shelf radio transceivers are consistent, widely available, and significantly lower cost than developing custom radio hardware for a project. The radio modules being tested in this research are the Wemos D1 Mini Pro (ESP8266), LoRa 32u4 (SX1276), XBee Pro S1, and the XBee Pro S3B.

Methodology Used

Multiple range tests of each radio module were conducted. These range tests took place over a long straight length of road in front of the engineering college. In order to facilitate the range test, firmware was written for each radio module, that transmitted it's current GPS coordinates available from a discrete GPS device. An identical radio module was held stationary in a parking area directly linear with the road. This receiving radio ran firmware that communicated the received GPS coordinates from the transmitter to a laptop computer where the results were recorded. The transmitter was driven down and back along the road to generate the GPS test data. This GPS data was later analyzed to calculate the range of the radio module being tested.

Results Obtained

The GPS data was ran through GPS Visualizer, a free utility that generates map data of GPS coordinates. This was a great tool for visualizing the collected GPS data. The distance of each test was then found using this map data shown in Figure 1.

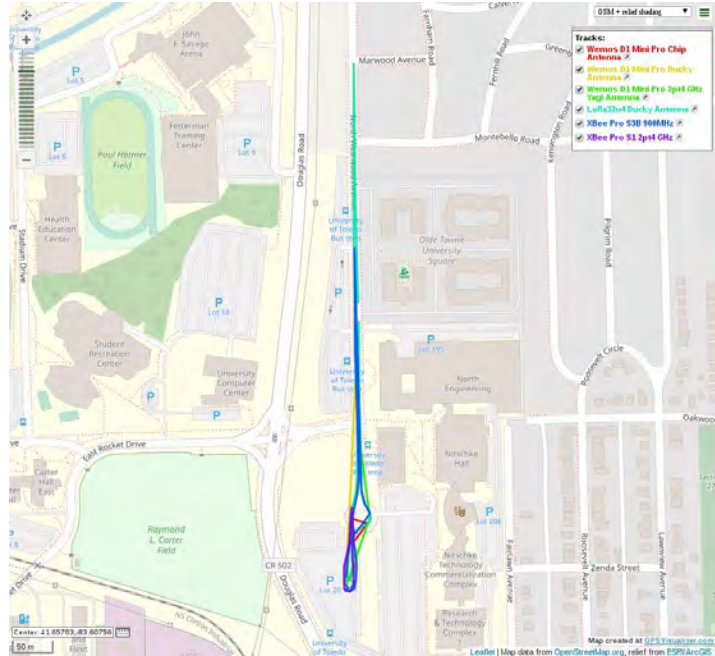


Figure 1. Range Test Map.

Figure 2 shows the range test data. The LoRa32u4 board offered the best range, followed by the XBee Pro S3B. This is no surprise since the transmit power and receiver sensitivity is similar for all of the modules, however the Lora32u4 board and XBee Pro S3B are 915 MHz and 900 MHz transmitters respectively. The Wemos D1 Mini Pro was the next best performing option especially with the ducky antenna. The Yagi antenna should have performed better than the ducky antenna due to the higher gain, however it is possible that the Yagi was not properly tuned to 2.4 GHz.

Board	Frequency (MHz)	Tx Antenna Type	Rx Antenna Type	Typical Cost (USD)	Ease of Use	Range (m)
XBee Pro S3B	900	1/4 Wave	1/4 Wave	\$43.00	Easy	408
XBee Pro S1	2400	1/4 Wave	1/4 Wave	\$45.00	Easy	96
Wemos D1 Mini Pro (ESP8266)	2400	Chip	Chip	\$12.00	Medium	83
	2400	Ducky	Ducky	\$12.00	Medium	243
	2400	Ducky	2.4 GHz Yagi	\$12.00	Medium	192
LoRa32u4 (SX1276)	915	Ducky	Ducky	\$20.00	Medium	625

Figure 2. Range Test Data.

It is important to choose the radio module that suits the need for its intended application. In cases where ease of use is supreme, the XBee Pro S3B is best. For low cost applications the Wemos D1 Mini Pro is a good choice. For best range, the LoRa SX1276 is a good choice. The Wemos D1 Mini Pro and LoRa SX1276 both require programming which is available on Github @3MDL. For swarm robotics, where many robots are built, the individual cost of each radio module rapidly adds up. Moving forward, due to the range and low cost the LoRa32u4 based on the SX1276 transceiver is a good choice for 3MDL especially compared to the XBee Pro S3B that are currently used.

Future Advancements in the Field of Programmable Logic Controllers

Student Researcher: Molly M. McCullough

Advisor: Jeffery M. Woodson

Columbus State Community College
Electro-Mechanical Engineering Technology

Abstract

If the machines in a manufacturing facility are the body and organs of a living animal then the Programmable Logic Controller (PLC) is the brain. Ever since the PLC was developed in the 1960's it has allowed the manufacturing field to grow exponentially. Programmable Logic Controllers have become an imperative part of any successful assembly line. How exactly have PLCs accomplished this and what does the future look like for PLCs?

Project Objectives

What exactly is a Programmable Logic Controller? Before PLCs were developed, the systems implemented by production facilities were Relay Logic Systems. Manufacturing components, (relays, timers, etc.), were hard-wired to a control panel and directly connected to each other in a specific sequence in order to perform a task. (*"Future of the PLC."* *Control Engineering*, 26 Aug. 2014, www.controleng.com/articles/future-of-the-plc/.) The issues with this system were that it required a lot of wiring, it was hard to troubleshoot, and making any changes to the switchboard were so difficult it sometimes was easier to just start wiring from scratch. (*"Future of the PLC."* *Control Engineering*, 26 Aug. 2014, www.controleng.com/articles/future-of-the-plc/.) This was not cost-effective nor efficient so a new system was developed, the Programmable Logic Controller.

Methodology Used

The PLC was superior in many ways to the old Relay Logic System. In the PLC's simplest form it is only made up of five parts; the CPU for processing, memory for storage, I/O section to read operation commands and carry out commands, power supply, and an expansion slot to be able to increase the PLC's operational limit. (*PanelShop.com. "The Potential Future of PLC's."* *The Potential Future of PLC's*, info.panelshop.com/blog/the-potential-future-of-plcs.) Complex logic sequences were much easier to create and could be altered with ease. The cost of components and the time dedicated to wiring the switchboards greatly decreased. With the absence of mechanical relays in lieu of digital components maintenance and replacements became few and far between. Monitoring and troubleshooting could be done from one location and easily diagnosed. (*"Future of the PLC."* *Control Engineering*, 26 Aug. 2014, www.controleng.com/articles/future-of-the-plc/.) A side-effect of the control center of a factory being simplified is that the hardware and setup of automation systems could be simplified as well.

The technology field is ever-growing and with this comes high competition between developers to come up with the next new and better product. Programmable Logic Controllers are able to reap the benefits of technology with smaller and faster electronic components. These include smaller and faster processors in order to create more memory space and newer ways to access the PLCs and the machinery they control. (*"Future of the PLC."* *Control Engineering*, 26 Aug. 2014, www.controleng.com/articles/future-of-the-plc/.) USB technology started to be utilized by PLCs, thus increasing the ease of getting online and monitoring factory systems. Having the ability to add more memory space will be as simple as plugging a drive into the PLC. With these advancements the cost of

certain components will decrease so these resources will also become available to smaller manufacturing facilities. More advanced PLCs will no longer be only available to bigger production facilities.

Results Obtained

The future of Programmable Logic Controllers will include the development of remote monitoring, virtualization, and real-time monitoring. (*"PLCs of the Future: Are They Still PLCs?" Automation.com, www.automation.com/en-us/articles/2017/plcs-of-the-future-are-they-still-plcs.*) However, with these additions to PLCs the need for added security will have to be developed and implemented as well. (*"Future of PLC in Industrial Automation." Plant Automation Technology, 7 Mar. 2018, www.plantautomation-technology.com/articles/future-of-plc-in-industrial-automation*). The biggest risks to these additions include improper data encryption, weak online protection, and poor asset tracking. (*"Remote Access Security Risks." SolarWinds MSP, www.solarwindsmsp.com/content/remote-access-security-risks.*). Data encryption of certain client products could be considered a breach of any Non-disclosure agreements that may have been included in a manufacturing contract. Internet malware will be able to overcome basic protection when technicians need to access PLCs from remote locations. As PLCs networks' capacity increases the ease of connecting more and more machine's increases and the necessity to be able to keep everything organized becomes even more important. Even with these potential problems the benefits greatly outweighs the risks and PLCs will continue with these improvements none the less.

Just as the Programmable Logic Controller can continue to improve thus reaffirming its place within the manufacturing field, there is also the possibility that it can be replaced by a different system. Manufacturing facilities traditionally place a PLC at every machine, however a PC network could put all of the machines onto one network to be operated from one place. (*Kalmar, Javan. "Beyond the Present of the PLCs." Beyond the Present of the PLCs, info.panelshop.com/blog/beyond-the-present-of-the-plcs.*). At the moment the cost of this kind of system is still exponentially higher than that of a PLC and has its own set of risks to a production facility. Everything comes down to cost and efficiency, both of which the Programmable Logic Controller is currently leading so it will not be replaced anytime in the near future.

Significance and Interpretation of Results

There is no doubt that the field of manufacturing would not be what is today without the use of the Programmable Logic Controller. With its minimal parts and its adaptation to ever-changing technology the future of the PLC looks to have no limitations in what it can do to a facility's production capabilities. With smaller, faster, and cheaper parts this "brain" of the assembly line is essential in the past, present, and future of manufacturing.

Direct Numerical Simulation of Cavity Flow

Student Researcher: Joseph W. Mileski

Advisor: Jed E Marquart, Ph.D., P.E.

Ohio Northern University
Mechanical Engineering Department

Abstract

Direct Simulation is used to model turbulent flow, without the use of a turbulent model. To achieve this a structured grid must adequately fine to completely capture even the smallest eddy produced by the geometry. This is achieved using the Kolmogorov microscale of length. Cavity flow focuses on introducing a cavity into an existing geometry, focusing on the flow inside and around that cavity. This work-in-progress project investigated a rectangular cavity with a length/height ratio of 4 and a Reynolds number of 5000.

Project Objectives

The Objective of this project is to: Use Direct Numerical Simulation to model the turbulent flow over a cavity, without the use of turbulent models. The purpose of which is to Illustrate the concepts used in turbulent models to continue to validate the results produced in other Computational Fluid Dynamics work.

Methodology Used

First, a geometry was selected, based on previous work. By using the geometry used in previous work, intermediate results could be compared to ensure that solutions were valid, leading to logical conclusions being drawn. The geometry selected was a rectangular cavity with a width to height ratio of 4, which was used by Pope and Hardin [1]. Also following the work of Pope and Hardin, a Reynolds number of 5000 was originally selected to compare results to those published by them.

Using the dimensions of using 4 in. by 1 in. for the cavity, and the desired Reynolds number, a length scale was able to be calculated. This was accomplished using the Kolmogorov microscale of length [2]. This length scale, η , has been determined to be the length of the smallest eddy produced by flow, as shown in Equation 1.

$$\eta = \left(\frac{v^3}{\epsilon} \right)^{1/4} \quad (1)$$

Where v is the kinematic viscosity of air at standard Temperature and Pressure, and ϵ is the dissipation rate of that air at the given velocity. The dissipation rate was defined by Tennekes and Lumley as equation 2, where V is the free-stream velocity and L is the characteristic length, in this case the depth of the cavity.

$$\epsilon = \frac{V^3}{L} \quad (2)$$

Using the Reynolds number, the velocity was determined, allowing for the previous calculations to produce a length scale of 0.0135 in. However, the length scale itself was not fine enough to determine the grid spacing. The length scale was used to determine the size of the smallest eddy, in order to

capture this eddy, the grid spacing would need to be a factor of the length scale. It was determined to use a grid spacing of one fifth of the length scale. This grid spacing was used to produce the 2D model created to run the Mathematical Model.

A two-dimensional geometry was selected to reduce computational timing. The project was time restricted, not allowing for the processor time necessary to produce a 3-D model. Work from Olsman and Colonius state that a 2-D model, though having some draw backs, produces acceptably accurate results [3]. Figure 1 shows the model produced using Pointwise grid generation.

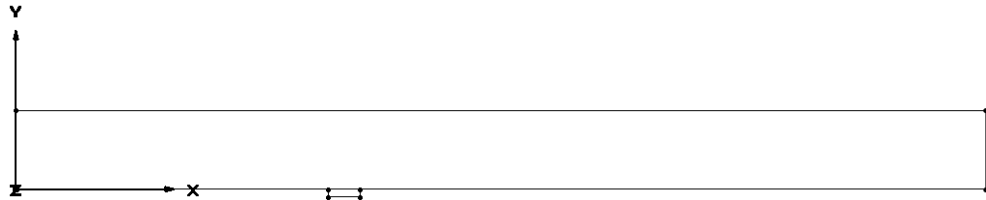


Figure 1. Geometry of Model.

To produce the grid, the three connectors of the cavity itself were assigned a spacing of 0.0027 in. as determined above. The two bottom connectors were given an initial spacing of 0.00027 in., a hyperbolic tangent growth function, and a growth rate of 1.2. The top connector of the flow box was determined by the number of nodes produced below it. The two vertical connectors of the flow volume were selected to produce an adequate grid, but minimize computational timing.

Boundary conditions for the geometry were then assigned. The cavity itself was assigned as solid adiabatic no-slip walls. The floor of the flow box were both assigned to be slip-walls, and the rest were assigned as Modified Riemann Sum Farfields. Using the grid and boundary conditions as described, the flow-solver, Cobalt, was used to evaluate the mathematical model. This mathematical model used Laminar Navier-Stokes equations to solve for the flow at each node in the grid.

The model was run through Cobalt with a CFL of 1.0e6 for the first 6000 iterations, then slowly reduced to 10 in 1000 iteration intervals. This was performed to increase the stability of the solution [4] to ensure the Direct Numerical Simulation was as accurate as possible. This solution was then compared to a geometry with wider grid spacing and a turbulent Navier-Stokes model used in the solver.

Results Obtained

After Cobalt was used, the x-forces were used to determine if the solution was adequately converged, which produced Figure 2.

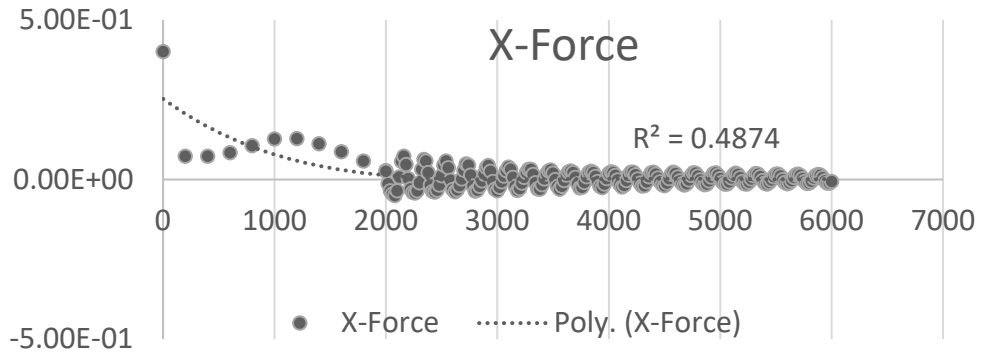


Figure 2. Convergence of x-forces.

Though the convergence does not have a true steady state value, the nature of modeling turbulent flow with direct numerical simulation, is that it is an unsteady solution, causing the oscillation shown in Figure 2. When the CFL was changed, there was no noticeable change to the pattern, other than having a tighter spacing.

Post-Processing was accomplished using Fieldview. First, the velocity of the flow around the cavity was evaluated to ensure that the cavity was behaving as expected. This is shown in Figure 3.

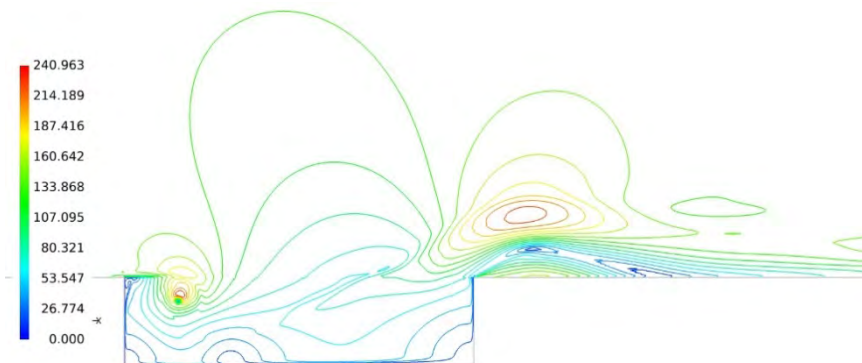


Figure 3. Velocity distribution around cavity.

Recognizing that the solution appears to be following the anticipated pattern, the pressure produced was compared to Pope and Hardin, as shown in Figure 4.

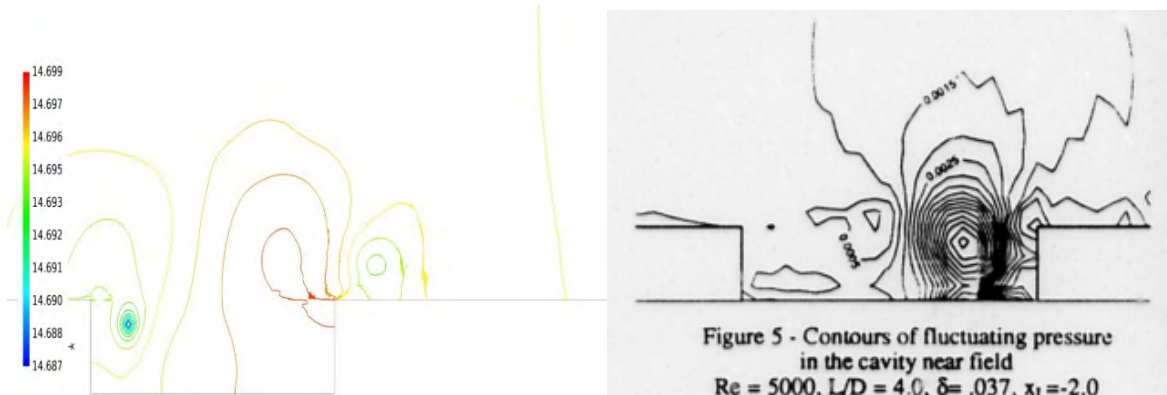


Figure 4. a) (left) Pressure distribution of project. b) (right) Pressure produced by Pope and Hardin [1]

Visually inspecting Figure 4, it was determined that the basic pattern of the two results agree. The greatest fluctuation in pressure is centered around the eddy formed and along the slip wall of the trailing edge. The discrepancy between the two is due to the difference in Reynolds number, though patterns are maintained.

Significance and Interpretation of Results

The results shown above illustrate, that though this project used laminar Navier-Stokes equations for calculating flow, turbulent flow behavior is indeed able to be modeled. Using a Direct Numerical Simulation to model may be more time intensive compared to a simulation using built in turbulent models, but is able to function equally in the ability to properly model turbulent behavior. When the grid of a model is determined by a fraction of the Kolmogorov microscale of length [2], even the smallest eddies are able to be modeled in a Direct Numerical Simulation. Using this method turbulent flow within a grid cell, the flow is able to be treated as laminar.

Acknowledgments

The author would like to thank the Ohio Space Grant Consortium for funding this work. He would like to also acknowledge the great assistance and encouragement of Dr. Jed E Marquart, which without this work not be possible.

References

1. D. S. Pope and J. C. Hardin, "A Numerical Investigation of Two-Dimensional Cavity Flow," *SAE Technical Paper Series*, Jan. 1995.
2. H. Tennekes and J. L. Lumley, *A first course in turbulence*. Cambridge, Mass. u.a.: MIT Press, 1985.
3. W. F. J. Olsman and T. Colonius, "Numerical Simulation of Flow over an Airfoil with a Cavity," *AIAA Journal*, vol. 49, No. 1, pp. 143–149, 2011.
4. *Cobalt Manual, Version 8*, Cobalt Solutions, LLC, Dayton, OH, 2018.

Investigations of Radiohalos from the Galway Batholith in Ireland

Student Researcher: Sara A. Mitchell

Advisor: John H. Whitmore

Cedarville University

Department of Science and Mathematics

Abstract

Granite often has an abundance of biotite. Zircon crystals can be embedded within the biotite, and these crystals can have a high percentage of uranium in them. This makes them highly susceptible to radioactive decay. As the uranium undergoes alpha decay, the alpha particles scar the surrounding biotite and leave a spherical ring around the parent material. Radiohalos (sometimes called pleochroic halos) are, then, these radioactive scars on grains of biotite. The radiohalos, though, can only form at temperatures less than 150° C. If the temperature of the rock rises above this, the radiohalos will be essentially erased. Thus, all of the scarring must take place after the granite has cooled sufficiently. The granite under study is from a batholith near Galway, Ireland and is late-Caledonian. Under a petrographic microscope, different types of radiohalos will be counted and logged. Then a statistical analysis will be done to understand the abundance and distribution of these radiohalos.

Project Objectives

The objective of this research is to better understand the Galway Batholith and the granites attributed to it. This study could have implications for the speed of cooling of the studied plutons, the nature of radioactivity, and the history of heating of the granite.

Methodology Used

Seven granite samples have been collected from their respective locations in Ireland, as labelled in Figure 1, which all represent a part of the vast batholith in Galway. Names and descriptions of each sample are described in Table 1. Each sample was crushed into small particles. Under a binocular microscope, the flakes of biotite were picked out and set aside. Each sample had fifty slides associated with it, and each slide had approximately twenty flakes of biotite on it. Then, the twenty flakes were placed on a transparent piece of tape. Using another piece of tape on top of them, the biotite was separated into thinner sheets. This process was repeated until the flakes were sufficiently thin, or only one layer thick. Once this was complete, the tape with the flakes was placed on a slide and labelled. Under a petrographic microscope, different types of radiohalos were counted and logged by measuring the diameters of the bullseye-like scars. Then an analysis was done to understand the abundance and distribution of these radiohalos.

Results Obtained

All of the samples were found to have at least one radiohalo in them, however the numbers were lower than perhaps expected. GBMMZG-2 and GBETG-1 primarily had micaceous minerals that had a greenish tint (as can be seen in image B), which could be due to alteration. GBMMZG-1 and GBLG-1 also had some, but were still predominantly biotite. The greenish micas tended to have less radiohalos in them. Additionally, it was difficult during the crushing process to extract flakes of a large enough size to be used, which could contribute to the smaller numbers of halos found. Different disaggregation methods might yield better flakes, which would also show more halos. See Figure 2 for distribution of the types of halos found.

Significance and Interpretation of Results

The reason for a lack of halos (especially in GBMMZG-2, GBMG-1, AND GBETG-1) could be, in part, due to the fact that the region has been quite active in its past. There could have been a lot of low-grade metamorphism occurring which could have erased the halos, so that they would be found in less abundance. Both GBMMZG-1 and -2 are Mixing-Mingling Zone Granodiorite, so it is likely that temperatures would have risen above 150 ° C in some areas of the body that would have erased some of the previously-formed halos. Indeed, some of the granites studied have been observed to have foliation, possibly giving credence to that hypothesis. Of interest is that sometimes ^{214}Po and ^{210}Po are found with ^{238}U , even though they have vastly different half-lives—164.3 μs , 138.4 days, and 4.6Ga, respectively. This could be due to the mingling of the different granites. Hydrothermal fluids moving through the granites could also play a factor as they transport radioactive elements like uranium or polonium and their daughter products. More research needs to be done to better understand this batholith, to determine why these different halos are occurring, and how they could be used in the study of the cooling rates of the batholith.

Figures/Charts



Figure 1. Locations of collected samples near Galway, Ireland. Note that GBMMZG-1 overlaps with GBMG-1 on map.

Table 1. Sample names and descriptions.

Sample	Name	Description
GBLLG-1	Lough Lurgan Granite	grayish-pink granite with approximately 1-6mm crystals
GBMMZG-1	Mixing-Mingling Zone Granodiorite	gray granodiorite with approximately 1-4mm crystals
GBMMZG-2	Mixing-Mingling Zone Granodiorite	gray granodiorite with approximately 1-8mm crystals
GBCMG-1	Costeloe Murvey Granite	pink granite with small, approximately 1-4mm crystals
GBCG-1	Carna Granite	light-colored granite with small, approximately 1-3mm crystals
GBMG-1	Megacrystic Granite	gray granite pegmatite with large distinctive K-feldspar crystals
GBETG-1	Errisberg Townland Granite	grayish-pink granite pegmatite with large (>1cm) K-feldspar crystals

Table 2. Distributions of the halo types by sample.

Sample	# of Slides	^{210}Po	^{214}Po	^{238}U
GBLLG-1	30	15	7	14
GBMMZG-1	30	3	2	4
GBMMZG-2	30	0	1	0
GBCMG-1	30	5	2	3
GBCG-1	30	14	5	9
GBMG-1	30	2	1	2
GBETG-1	30	1	1	2

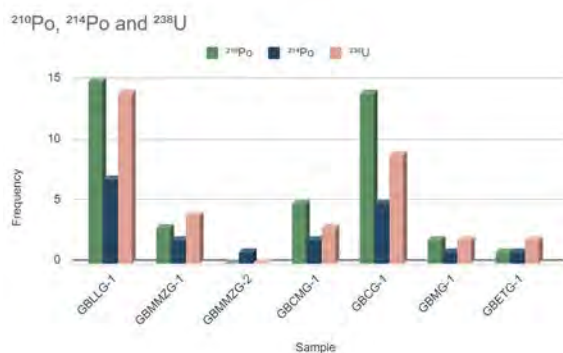


Figure 2. Histogram that shows the distribution of the various isotopes of interest and their frequencies per sample. Data indicates a lower frequency of ^{214}Po in all samples in relation to the other isotopes.

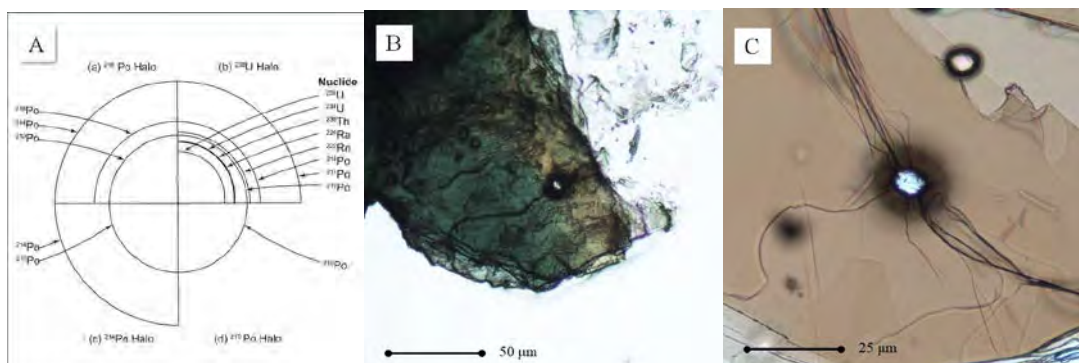


Image Description: A) Figure from Gentry (1967) that shows halo type and the nuclides that are responsible for the decay rings, B) ^{238}U halo encircling a zircon from sample GBMMZG-1, C) ^{238}U halo encircling a zircon next to a smaller ^{210}Po halo from sample GBCG-1.

Acknowledgments

I would like to thank my advisors Dr. John Whitmore and Dr. Andrew Snelling for their invaluable counsel and direction as well as Jordan Oldham for his helpful guidance. Additionally, I would like to thank the 2020 Historical Geology class for helping with slide preparation.

References

1. Baxter, S., & Feely, M. (2002). Magma mixing and mingling textures in granitoids: examples from the Galway Granite, Connemara, Ireland. *MINERALOGY AND PETROLOGY*, 76(1–2), 63–74.
2. Feely, M., Costanzo, A., McNulty, E., Gaynor, S. P., & Selby, D. (n.d.). A review of molybdenite, and fluorite mineralisation in Caledonian granite basement, western Ireland, incorporating new field and fluid inclusion studies, and Re-Os and U-Pb geochronology. *Lithos*, 354–355.
3. Feely, M., Selby, D., Hunt, J., & Conliffe, J. (2010). Long lived granite-related molybdenite mineralization at Connemara, western Irish Caledonides. *Geological Magazine*, 147(6), 886–894.
4. Gentry, R. V. (1967). Extinct radioactivity and the discovery of a new pleochroic halo. *Nature* (London), 213(5075), 487–489.

Drone Equipped Temperature Probing Hardware (DEPTH)

Student Researcher: Zane R. Myers

Advisor: Jed E. Marquart, Ph.D., P.E.

Ohio Northern University
Department of Mechanical Engineering

Abstract

The concern for harmful algal blooms (HABs) in Lake Erie has peaked in recent years. The bloom in the western basin of Lake Erie in 2014 reached such a severe level that it triggered the State of Ohio to declare a state of emergency [1]. The purpose of this project is to design and build an unmanned aerial vehicle (UAV) mountable data acquisition module for studying Lake Erie algae blooms and their relation to water temperature. Project DEPTH is a piece of flight hardware designed to capture temperature and Global Positioning System (GPS) data at different points in a body of water. With this data, maps will be created to show temperatures across the water column at different locations. These data maps could then be used to help further understand the relation of temperature in the water column to algae blooms. The long-term goal of DEPTH is to help predict when and where algae blooms are going to occur.

Project Objectives

The goals of the DEPTH kit are to be flyable on a DJI Phantom 3, collect temperature and corresponding GPS data, and that data shall be written to an external storage device capable of being read on a PC.

Methodology Used

The basis of collecting temperature data across the water column is based on several research findings in the field of cyanobacteria in relation to HABs. It has been found that water temperature is a significant and independent predictor of cyanobacterial biomass (CBB) [2]. The levels of CBB are a major factor in triggering swimming and drinking water restrictions because of the hazard imposed on human health. Furthermore, a warmer, more stable water column also favors cyanobacteria [3]. This adds to the benefit provided by the device in measuring the temperature across the column. The data obtained can also give an idea of the amount of vertical mixing that is occurring. Warm summers with little vertical mixing provide ideal conditions for surface blooms of harmful cyanobacteria [3]. Therefore, a basis for the proposed data to be collected is justified.

The available UAV system for this project was a DJI Phantom 3. There are no commercially available payload charts for this UAV. Therefore, a test was created to establish a baseline for the flight characteristics that could be expected at different payloads. This was done so that a maximum weight for the DEPTH kit could be established. The setup can be viewed in Figure 1. The test was conducted by setting markers 20ft apart and flying the UAV at full speed from one marker to the next before letting off the pitch and allowing the UAV to auto level to a complete stop.

Results Obtained

From the results of the Payload test shown in Figure 2. It was established that the DEPTH kit shall weigh no more than 1.25lbs. This constraint was then considered in selecting the electronics for the kit.

Significance and Interpretation of Results

From the results of the Payload test shown in Figure 2. It was established that the DEPTH kit shall weigh no more than 1.25lbs. The kit is composed of an Arduino Mega, LCD, Keypad, SD Card Reader/Writer, LED indicator light, Thermistor Probe, and a NEO 6M GPS Module all mounted in a waterproof case.

To use DEPTH, the user inputs flight altitude, probing depth, frequency of readings, and number of data points into the user interface before starting the survey. DEPTH is then fastened to the landing gear of the UAV using $\frac{1}{2}$ inch cable clamps that are fixed to the kit. The UAV is flown around the survey area stopping to take a reading each time the red indicator light comes on in view of the camera. Once the survey is complete. The SD card is removed, and the data can be uploaded to Excel for processing. The final configuration of DEPTH is shown in Figure 3.

Figures/Charts



Figure 1. Setup for UAV Payload Test.

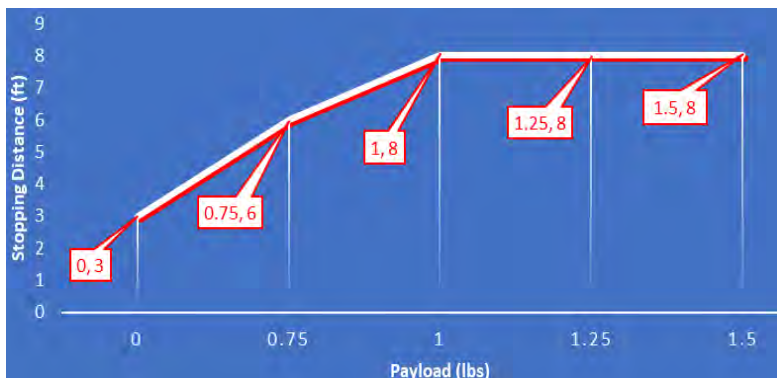


Figure 2. Payload (lbs) vs. Stopping Distance (ft).

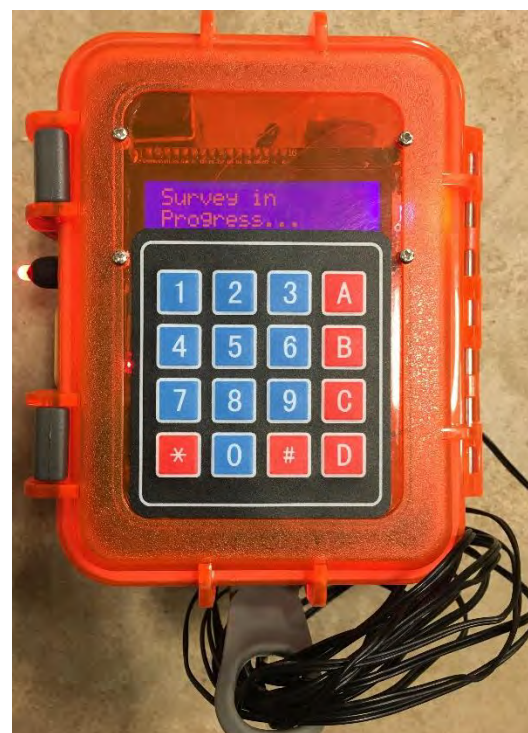


Figure 3. Completed DEPTH Kit.

References

1. Lekki, John, et al. "Airborne hyperspectral and satellite imaging of harmful algal blooms in the Great Lakes Region: Successes in sensing algal blooms." *Journal of Great Lakes Research*, Vol. 45, No. 3, 2019, pp. 405-412. OhioLINK Electronic Journal Center, doi:10.1016/J.JGLR.2019.03.016.
2. JÖHNK, KLAUS D., et al. "Summer heatwaves promote blooms of harmful cyanobacteria." *Global Change Biology*, Vol. 14, No. 3, 2008, pp. 495-512. OhioLINK Electronic Journal Center, doi:10.1111/j.1365-2486.2007.01510.X.
3. Beaulieu, Marieke, Pick, Frances, Gregory-Eaves, Irene, (2013), Nutrients and water temperature are significant predictors of cyanobacterial biomass in a 1147 lakes data set, *Limnology and Oceanography*, 58, doi: 10.4319/lo.2013.58.5.1736.

Determination of Menthol in Peppermint Oil

Student Researcher: Roneishah S. Nixson

Advisors: Ann Fallon, Michele Mangels

Cincinnati State Technical College
Chemical Technology

Abstract

Peppermint was first brought to the USA in the late 1700s where it became the main focus of a chemist named Hieronymus David Gaubius. With intensive studies and lab time he was able to identify and isolate the compounds responsible for peppermint unique characteristics. He was the first chemist to isolate menthol from peppermint and synthesis it. Peppermint is widely known for its many uses in culinary applications for flavoring teas and dishes, in hygiene for fighting bad breath and in medicine for calming digestive complaints and minor muscle tension.

Menthol is also known as Menta and has the IUPAC name 5-methy—2-Propan-2-yl cyclohexan-1-ol. The chemical formula is $C_{10}H_{20}O$ with a molecular mass of 156.269 g/mol and has a white crystalline structure. There is a wide range of products with menthol like Bengay, Halls, Vicks that each have their own amount of active menthol. Menthol can be considered a drug depending on the use of purpose and combination of other medicinal purpose.

Project Objective

The objective is to research the chemical compounds, uses, impacts and methods of menthol in peppermint oil. The experiment is designed to determine the quality of menthol between two different brands, Brand 1 (Now) and Brand 2 (Aura Cacia). Each brand is pure 100% pure peppermint oil that was distilled. The quality of essential oils can vary depending on the nature of the plant it was extracted from. Analyzing different brands will be beneficial to Americans that are seeking alternative ways to improve their health.

Materials and Method

Extracting menthol out of a plant naturally can yield very low results and with wide range concentration. Past research has measured the concentration of menthol using different types of gas chromatography. The best way to ensure the most menthol can be extracted is synthetically using fraction columns. Gas chromatography is the best way to measure the different components in a plant according to "Uses of Gas Chromatography-Mass Spectrometry (GC-MS) Technique for Analysis of Bioactive Natural Compounds of Some Plants". GC can measure the different compounds with complex solutions like an essential oil. This research will examine the composition of several commercial peppermint oils and determine the variability in menthol using gas chromatography.

Determining the Solvent

To determine a good solvent for the experiment a test tube rack was set up in the hood. Nine solvents were used before deciding on a good solvent. The solvents were water, hexane, cyclo-hexane, isopropyl, ethanol, methanol, tetra- butanol, Toluene, and ethyl alcohol. The solvents that were closer to the polarity of menthol made the best solvents for each sample. The most efficient solvent tested was ethyl alcohol. Once the best solvent was chosen, sample preparation is the next step.

Sample Preparation

Create a 1000ppm by weighing .0645 grams of menthol and diluting it in 10mL flask with ethyl alcohol. Use serial dilution to create a 500, 250, 125, 62.5, 37.25ppm. Create a separate stock solution the same as 1000 ppm to create a 250 and 62.5ppm check standard. A 5mL flask diluted with ethyl alcohol will be used for blanks.

Mock Experiment

Create 1000 ppm solution and 5 established standards in 10mL flasks, sample solutions in 5 mL flasks, Create 2 check standards and a blank. Run the samples with the established GC method, collect results The 1000 ppm gives the range of concentrations needed to be made in order to create the 5 standards that will be used in the calibration curve to determine the menthol concentration in the samples. The GC machine will be used to measure the components in my matrix's (Brand 1 and 2 and make any necessary changes).

Gas Chromatography Settings

Run the stock solution through the GC machine. Start with the column being 180 degrees Celsius, the oven 225 degrees Celsius, set to heat 12 degrees/ minute as prepared in the method for measuring horsetail in "Determination of bioactive compounds of equisetum arvense by Gas Chromatograph mass spectrometry method "^a. The chromatography showed two peaks. One could be my solvent and one menthol. It took 30 mins to run the sample.

This would conclude the end of lab work performed due to the Coronavirus pandemic.

Significance and interpretation of Results

The two brands behaved very differently while determining a best solvent. Brand two reacted with the more alcohol solvents. Due to the COVID-19. I was unable to complete the experiment that would decide the level of menthol concentration of each brand.

Collecting more data on essential oils and its many benefits to humanity and environment could produce more natural and healthier results in the body.

The human body is a complex system and maintaining a healthy body is essential to life longevity and quality. Most people enjoy being healthy, full of energy and ready to take on the challenges of the day. This experiment was conducted to prove presence of the chemical compound responsible for the peppermint unique abilities. Even though there are many more active compounds contributing to the plants characteristics it's nice to know peppermint can contribute to help maintain a healthy body.

References

1. S. Yilmaz, S. Ekinci and B. Yilmaz. 2013, December 07. Determination of Bioactive Compounds of Equisetum Arvense By Gas Chromatography-Mass Spectrometry Method. <http://ijpjurnal.com/bft-article/determination-of-bioactive-compounds-of-equisetum-arvense-by-gas-chromatography-mass-spectrometry-method/?view=fulltext>
2. <https://www.knowyourotcs.org/ingredient/menthol/>
3. Al-Rubaye, A., Hameed, I., Kadhim, M. www.ijtpr.com. Uses of Gas Chromatography-Mass Spectrometry (GC-MS) Technique for Analysis of Bioactive Natural Compounds of Some Plants. (2017).

Active Flow Control in an Aggressively Offset High-Speed Inlet/Diffuser Model

Student Researcher: Collin J. O'Neill

Advisor: Dr. Mo Samimy

The Ohio State University
Mechanical and Aerospace Engineering Department

Abstract

Offset diffusers are becoming increasingly prevalent in both commercial and military aircraft. The compact, offset shape reduces radar cross section, increases the integration of the propulsion system, and improves the thrust-to-weight ratio [1]. Despite these benefits, the curves in the inlet also introduce a variety of problems. The main problems are total-pressure loss and the development of secondary flow structures where the inlet meets the engine fan face, which is called the aerodynamic interface plane (AIP) [2]. The concentrated regions of total-pressure loss produced by these secondary flows result in unsteady loading on engine turbomachinery components [1]. This unsteady loading decreases engine performance and results in a shorter propulsion system lifespan [3]. Recent research has shown that the secondary flows and resulting distortion can be modified by affecting the separated flow region downstream of the second turn [4]. High-frequency, high-amplitude actuators, called localized arc-filament plasma actuators (LAFPAs), have been successfully used for flow control in several high-speed and high-Reynolds number shear layers similar to the one that exists over the separated region in an offset inlet [5]. The low power use, scalability, and adaptability provided by LAFPAs make them perfect for high-speed inlet flow control. In order study this flow, a new, modular offset diffuser facility was designed and constructed. This facility was then thoroughly characterized without excitation to create a baseline performance profile. The final step of this project is to investigate the application of LAFPAs to improve the aerodynamic performance of an offset inlet.

Project Objectives

There have been several efforts to mitigate the negative performance aspects of offset inlets in the past. These efforts fall into the categories of passive flow control, active flow control, and hybrid flow control. Passive methods, such as vane-type vortex generators, have been found to be effective, but they are typically designed for one condition and cannot adjust for off design conditions [6, 7]. They also produce total pressure loss. The primary active flow control tested so far is microjets, which are small, high velocity jets that inject momentum into sensitive regions of the flow [2]. These microjets can adjust for off-design conditions, but supplying them with air typically involves costly engine bleed systems that reduce the power available to downstream engine components. Hybrid control blends these two control strategies, allowing for similar levels of control across a range of conditions with much less air required [8, 9]. These systems, however, still do require engine bleed.

The ultimate goal of this project is to assess the efficacy of a new form of active flow control for offset diffusers that does not require air from other engine components. This active flow control method is a class of plasma actuators called localized arc-filament plasma actuators (LAFPAs) that have been shown to be effective in controlling several similar flows [5]. A single LAFPA consists of two tungsten electrodes with a small gap between them. A high voltage with a controlled frequency is imposed across the

electrodes, creating a repeated plasma breakdown in the air. The rapid, localized heating produced by this breakdown generates a thermal perturbation that propagates throughout the flow. By introducing perturbations at frequencies that match the natural instability frequencies in the flow, plasma actuators can exert significant flow control with minimal power usage [5].

The specific objective of this investigation is to design and fabricate a new inlet/offset-diffuser facility and to use it to obtain baseline, unexcited results to assess flow distortion and pressure loss. The main metrics of distortion and total pressure loss will be measured using a pressure rake at the AIP, while the flow physics will be studied using centerline surface pressure taps, and oil flow visualization (OFV).

Methodology

One of the high speed wind tunnel facilities at the Gas Dynamics and Turbulence Laboratory (GDTL) at The Ohio State University is being used for this experiment. This is a high mass flow, blowdown-type wind tunnel. A modular offset inlet/diffuser test section was designed in SolidWorks and constructed. This facility is shown from the side in Figure 1.

The facility has three main sections. The upstream section is machined aluminum that smoothly transitions from the rectangular outlet of the settling chamber to the inlet throat. This transition allows the inlet geometry of interest to interface with the high-speed wind tunnel facility.

The main test section of the facility is a modular, 3D printed design. The geometry was provided by Boeing. The inlet geometry of interest has a throat area of 100.15 cm^2 and an AIP area of 126.62 cm^2 with a 12.7 cm inch diameter at the AIP. There are 38 streamwise pressure taps along the top and bottom of the diffuser to observe separation of the flow. These streamwise pressure taps are aligned along the center of the facility with one inch spacing between each adjacent tap. There are also four windows to allow for particle image velocimetry measurements (PIV) and OFV at the upstream and downstream turns. When PIV is not being performed, the windows are replaced by 3D printed blanks that are exactly contoured to match the internal geometry. These blanks are installed in Figure 1. The main test section contains an actuator insert that houses 19 LAFPAs. Each LAFPA is composed of two 1 mm tungsten electrodes flush mounted in a small groove. This groove stabilizes the arc and prevents it from being stretched and carried downstream by the flow. This is critical as it allows the frequency to be precisely controlled [5]. The LAFPAs are connected to a custom-built power supply capable of producing microsecond pulses of several kV. The typical pulse used in this experiment is approximately 4 microseconds at 5 kV. This actuator block is just upstream of the second turn to maximize the LAFPAs' control authority over the separated region nearest to the AIP. This insert is also contoured to match the internal geometry of the diffuser. The facility also contains an opening to allow for an actuator insert at the upstream turn. For the present investigation, this opening is filled with a 3D printed blank that matches the internal geometry of the diffuser.

The downstream section is constructed of machined aluminum. This downstream section houses the AIP pressure rake assembly. The rake assembly contains 40 stagnation pressure probes located in centroids of equal area and 8 equiangularly spaced static pressure probes in total. Beyond the AIP, the downstream section contains a smooth diffusion section that allows the flow to be vented outdoors with minimal losses.

Results Obtained

Centerline pressure measurements along the top and bottom of the inlet were obtained at Mach numbers of 0.5 and 0.8. These pressure measurements were then graphed against streamwise tap location to show the variations in pressure in the streamwise direction. This is shown in Figure 2. OFV was performed on the top surface of the diffuser just downstream of the second turn. This captured the dynamics of the separated region and the surrounding area. The OFV for Mach 0.5, 0.6, 0.7, and 0.8 is shown in Figure 3. AIP total pressure contours were created for Mach 0.5 and 0.8. These are shown in Figure 4. The windows used for PIV and OFV are flat for optical measurements. This introduces a nonuniformity into the internal contour of the facility, which affects the flow. Figure 5 shows AIP total pressure contours with and without the windows in place. The distortion and total pressure recovery across all Mach numbers tested and in every tunnel configuration is shown in Figure 6.

Significance and Interpretation of Results

Figure 2 shows the coefficient of pressure in the streamwise direction. The region of interest in Figure 2 is the inside of the second turn. This corresponds to streamwise coordinates 10-19 on the top of the diffuser. As the flow enters the second turn, it experiences an adverse streamwise pressure gradient along the top of the diffuser. This adverse pressure gradient leads to local separation, which would present as a plateau in the streamwise pressure. This separation is marked in Figure 2 as a highlighted section of line. Interestingly, it appears that the separation actually shrinks with increasing Mach number. The other feature of note in Figure 2 is the radial pressure gradient at each turn. This radial pressure gradient, combined with the low speed of the boundary layer, creates the secondary flows responsible for sweeping low momentum fluid from the separation towards the duct centerline. OFV from the separated region is shown in Figure 3. The separation line near the top of the image is curved, showing the highly three-dimensional nature of the flow. The separated region is visible in the center of the images, appearing as regions with minimal oil movement. The crossflow created by the diffuser turns is clearly visible on either side of the separated regions. At the bottom of the separated region, there are signatures of two counter-rotating streamwise vortices. The separation gets smaller with increasing Mach number, especially in the spanwise direction. This suggests that the secondary flows are the dominant flow feature. Figure 4 shows AIP total pressure contours for Mach 0.5 and Mach 0.8. The contours are qualitatively similar, with a concentrated region of high total pressure loss along the top and a more diffuse region of lower total pressure loss along the bottom. These total pressure loss regions are produced by the turns, with the region along the bottom being more diffuse due to the greater distance between the first turn and the AIP. Although qualitatively similar, the total pressure loss rapidly increases with increasing Mach number. Figure 5 shows the effects of the downstream window inserts on the total pressure recovery contour at Mach 0.8. The bottom window does not make a large difference, but the side window introduces a concentrated region of total pressure loss directly downstream. This is visible in the bottom right of the windows-in contour in Figure 5. Figure 6 shows the total pressure recovery and distortion of all test section configurations tested and across all Mach numbers of interest. Figure 6 also shows the results of Burrows et al. (2017) working in the same inlet geometry [4]. The total pressure recovery and distortion worsen with increasing Mach number for all cases. The windows decrease total pressure recovery, which is expected from Figure 5. The windows also decrease distortion. This is because the distortion metric in this study is circumferential distortion, which is calculated on a ring-by-ring basis and then averaged across the AIP face. The total pressure loss produced by the windows actually makes the outer ring more uniform, which results in decreased overall distortion. The actuator block does not have any significant effect on either metric. The results

match Burrows et al. (2017) qualitatively, but the flow in this investigation is slightly higher quality. This is likely due to a difference in the facilities driving the test sections.

Figures



Figure 1. Side view of Offset Diffuser Facility.

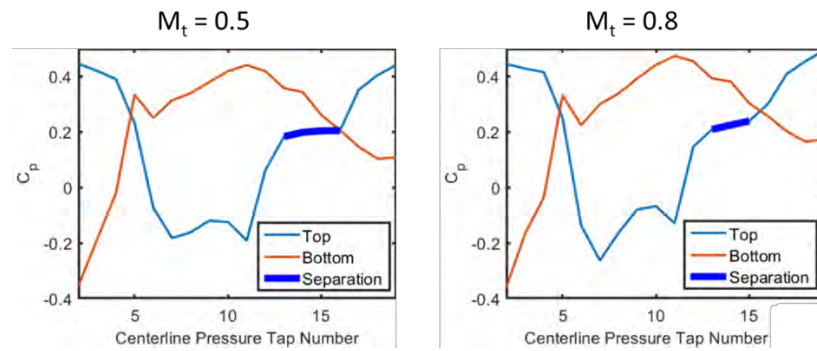


Figure 2. Centerline Pressure Coefficients along Top and Bottom of Diffuser with Separated Region
Highlighted at (a) Mach 0.5 and (b) Mach 0.8.

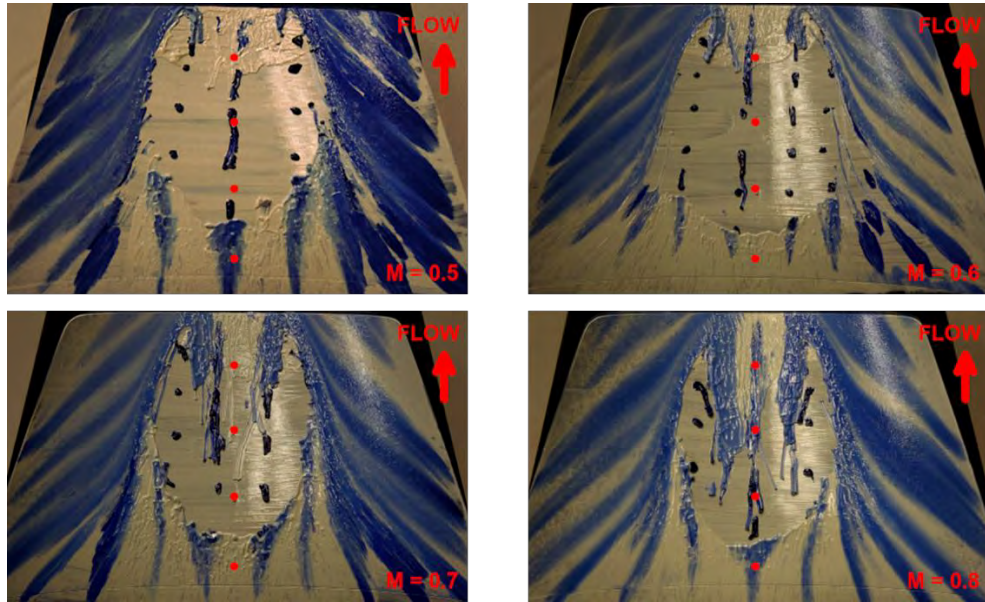


Figure 3. OFV of Separated Region at Mach 0.5, 0.6, 0.7, ad 0.8.

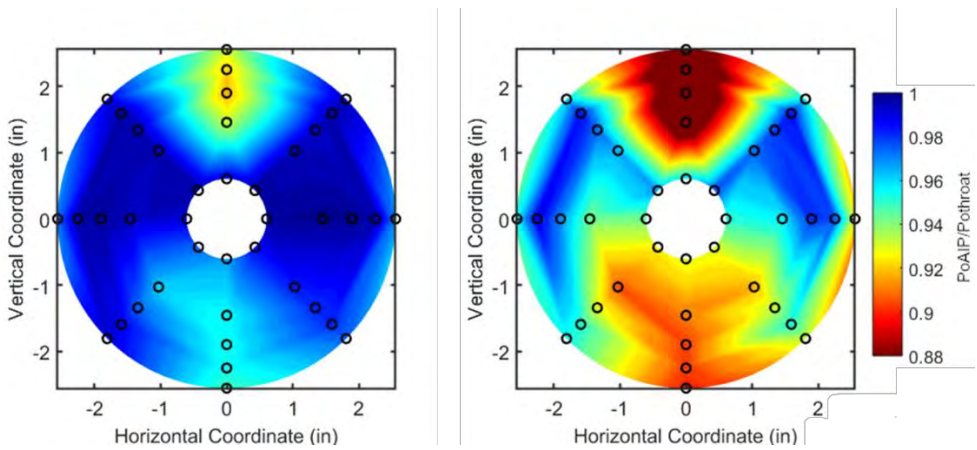


Figure 4. Total-Pressure Loss Contours at AIP at a) Mach 0.5 and b) Mach 0.8.

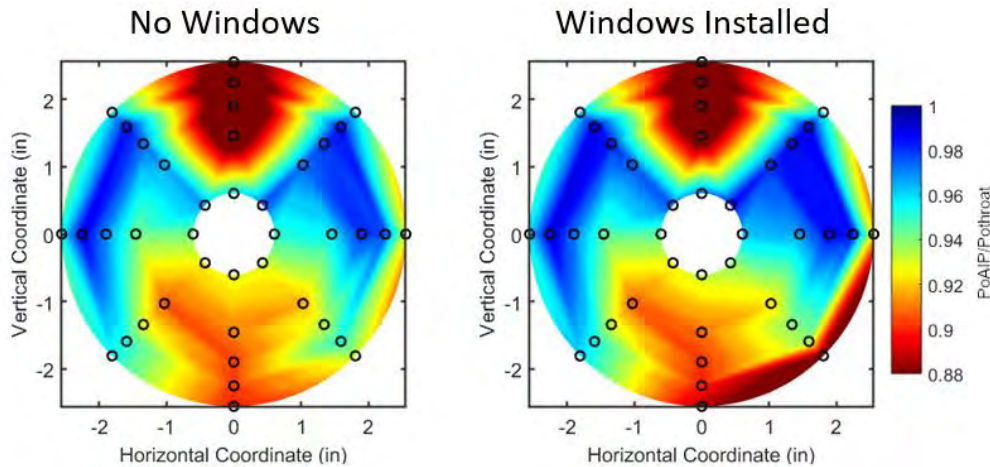


Figure 5. Total-Pressure Loss Contours at AIP at Mach 0.8 without and with Window Inserts.

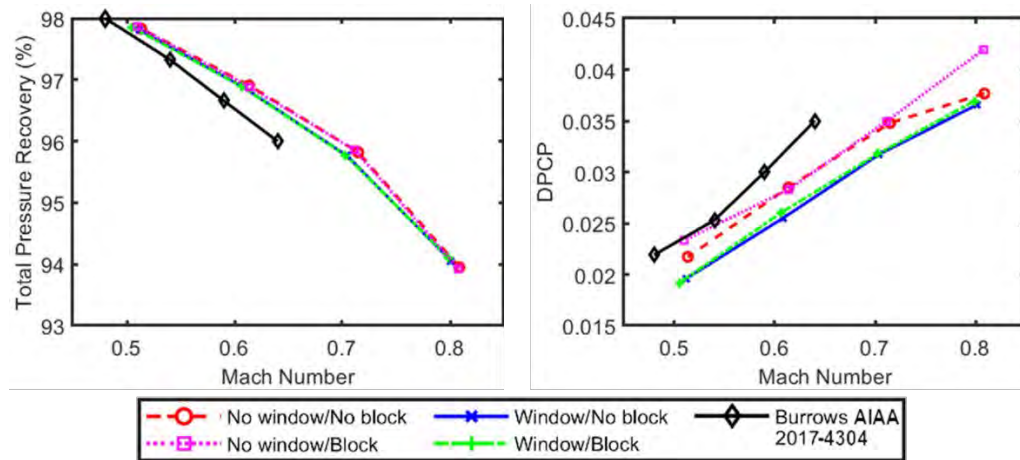


Figure 6. Total Pressure Recovery (left) and Distortion (right) with all Test Section Configurations across a Range of Mach Number.

Acknowledgments

The author would like to thank Dr. Nathan Webb and Dr. Mo Samimy. Their guidance and work was instrumental in completing this research. The author would also like to thank the Office of Naval Research (ONR), Ohio Space Grant Consortium (OSGC), and The Ohio State University for providing funding to make this research possible.

References

1. Rabe, A. C., "Effectiveness of a Serpentine Inlet Duct Flow Control Scheme at Design and Off-Design Simulated Flight Conditions," Ph.D. Thesis Virginia Polytechnic Institute and State University, 2003.
2. Anderson, B. H., Baust, D. H., and Agrell, J., "Management of Total Pressure Recovery, Distortion and High Cycle Fatigue in Compact Air Vehicle Inlets," NASA/TM. 2002-212000, 2004a.
3. Luers, A. S., "Flow Control Techniques in a Serpentine Inlet: An Enabling Technology to Increase the Military Viability of Unmanned Air Vehicles," Master's Thesis Massachusetts Institute of Technology, 2003.
4. Burrows, T. J., Vukasinovic, B., and Glezer, A., "Fluidic Control of an Aggressive Offset Diffuser for a Supersonic Inlet," AIAA Paper 2017-4304, 2017.
5. Samimy, M., Webb, N., and Crawley, M., "Excitation of Free Shear-Layer Instabilities in High-Speed Flows," AIAA Journal, March 2018. <https://doi.org/10.2514/1.J056610>.
6. Anderson, B.H., and Gibb, J., 1993, "Study on Vortex Generator Flow Control for the Management of Inlet Distortion," AIAA/SAE/ASME/ASEE 28th Joint Propulsion Conference and Exhibit, AIAA-92-3177.
7. Reichert, B. A., and Wendt, B. J. "Improving curved subsonic diffuser performance with vortex generators," AIAA Journal Vol. 34, No. 1, 1996, pp. 65-72. doi: 10.2514/3.13022.
8. Owens, L. R., Allan, B. G., and Gorton, S. A. "Boundary-Layer-Ingesting Inlet Flow Control," Journal of Aircraft Vol. 45, No. 4, 2008, pp. 1431-1440. doi: 10.2514/1.36989.
9. Gissen, A. N., Vukasinovic, B., McMillan, M. L., and Glezer, A., "Distortion Management in a Boundary Layer Ingestion Inlet Diffuser Using Hybrid Flow Control," Journal of Propulsion and Power, Vol. 30, No. 3, May-June, 2014.

Optimized Compressor Stator Design with Supercritical CO₂

Student Researcher: Rokas Ogorodnikas

Advisor: Dr. Mark G. Turner

University of Cincinnati
Aerospace Engineering

Abstract

The University of Cincinnati is working on a new compressor design project using supercritical CO₂. The application for this compressor is to work as the compressor in a heat pump that will act on the supercritical CO₂ to store energy. Specifically, Dr. Turner is leading a project to design the first three stages of the larger machine using several programs including OpenMDAO, Mises, and T-Blade3.

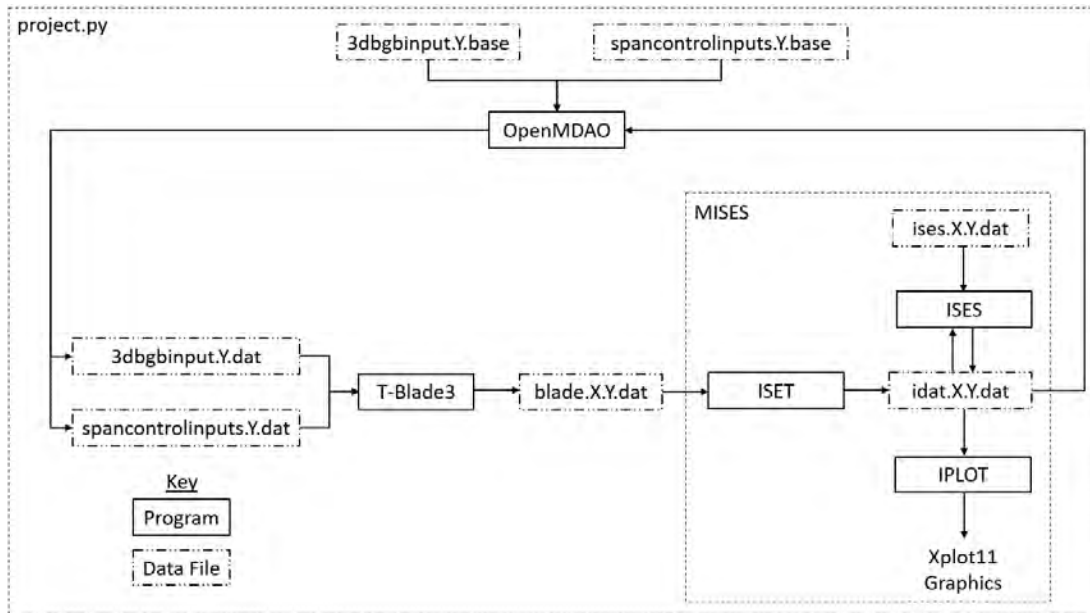
In this project a python script was setup to optimize a vane design using supercritical CO₂. To do so, a ten variable python script, created by Tom Viars, was modified for an Outlet Guide Vane (OGV) with a Leading Edge (LE) of 5.5. This script uses T-blade3 (a parametric 3D blade geometry builder), Mises 2.70 (a Newton's method flow solver with machine precision), and OpenMDAO (a python-based optimization platform) to minimize the vane's loss coefficient (Zeta), while constrained to an exit flow angle (S2).

Project Objectives

The objective of this undergraduate research study was to first become familiar with process of compressor blade design and to understand the capabilities of OpenMDAO, Mises, and T-Blade3. Furthermore, the methodology of how each program interacts with each other was studied as well. These programs were run on a Linux operating system on a virtual machine. A research study completed at the University of Cincinnati by Tom Viars, Optimization of the Design of a Turbine Blade using Open MDAO will be used as a general guideline on how to use the programs.

After gaining experience in OpenMDAO, Mises, and T-Blade3, these programs were used to investigate the first vane optimization of the 3rd stage of a blade row in a stator design. In separate projects, a blade optimization study is completed using T-Blade3. With the designed blade, the three stages of the rotor will be designed with both rotor and stator vanes. This research project will focus specifically on the design of the first three stages of the rotor in the compressor using supercritical CO₂ with the programs OpenMDAO, Mises, and T-Blade3.

Methodology Used



There are three inputs that are needed for the optimization script to work; 3dbgbinput.Y.base, spancontrolinputs.Y.base, and ises.X.Y.dat. The .base files are copied and left unchanged through the optimization, for easier comparison. Once OpenMDAO has optimized, it writes an out file for the vane's loss coefficient (Zeta), exit flow angle (S2), and a case result file. This file contains the value of all the variables that are specified in the input file, after every iteration.

Results Obtained

The Figures below show the results of an optimization run done on the first OGV LE 5.5 vane of 33 vanes, constrained to one degree of exit flow angle and gamma set to 1.8 to simulate supercritical CO₂ flow.

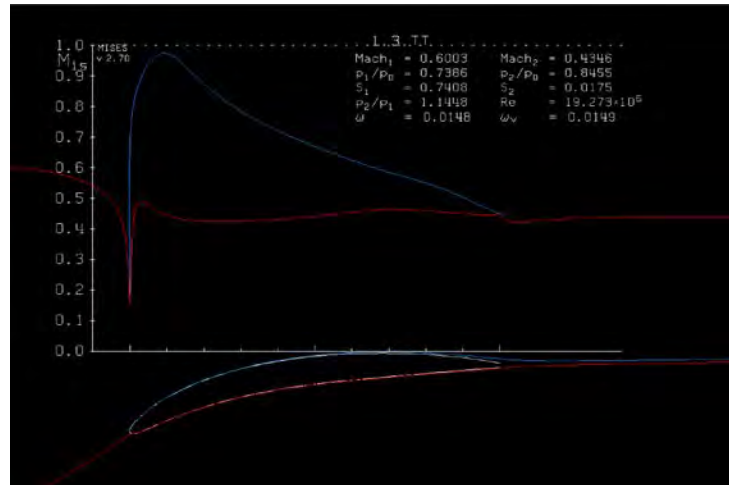


Figure 1. 9 Variable Optimized Vane and Surface Mach Number.

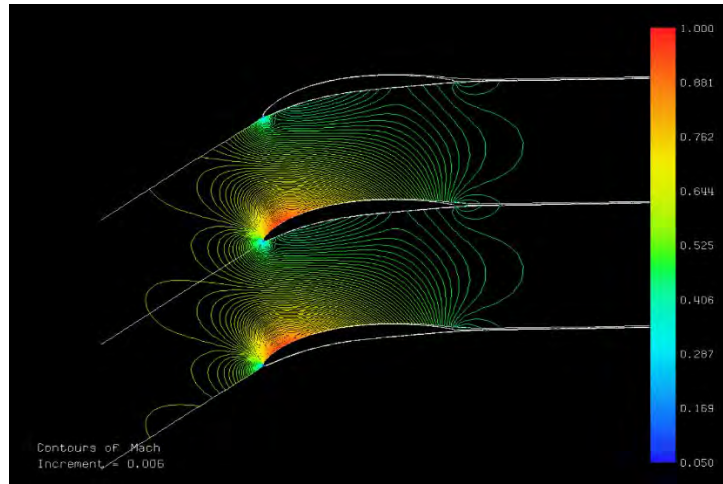


Figure 2. 9 Variable Optimized Vane Mach Number Contour.

Significance and Interpretation of Results

These results show that this script can optimize a 2D blade design to satisfy a given constraint, while using multiple variables and in a supercritical CO₂ environment.

Acknowledgments

Without the help and guidance of my mentor, Dr. Mark G. Turner, and the support from the Ohio Space Grant Consortium, this project would have not been possible.

References

1. Drela, M., Youngren, H., "A User's Guide to MSES 2.63", <http://web.mit.edu/drela/Public/web/mises/mises.pdf>, Accessed April 20, 2020.
2. Viars, T., Turner, M. G., Orkwis, P. D., "Optimization of the Design of a Turbine Blade using OpenMDAO" Tech. rep.

An Investigation on Kernel Growth Variations between Conventional Spark Discharges and Nanosecond-Pulsed High-Frequency Discharges

Student Researcher: Katherine C. Opachich

Advisors: Joshua S. Heyne, Timothy Ombrello, Joseph K. Lefkowitz, Robert J. Leiweke, Kenneth Busby

University of Dayton
Department of Mechanical and Aerospace Engineering

Abstract

Depositing energy using nanosecond-pulsed high-frequency discharges (NPHFD) has been shown to lead to successful fuel-lean ignition. Despite these observations, questions remain regarding how the NPHFD ignition system will perform against the conventional ignition system on shorter timescales and in a flowing environment. This work provides a comparison between the NPHFD ignition system and a conventional, capacitive discharge system in a flowing environment where the total energy deposited, and average power is matched. The results show that matching these characteristics result in similar trends in radius growth, time to minimum growth rate, and radius at which minimum growth rate occurs between the two systems. In utilizing these results as a baseline, it was found that decreasing the average power of the NPHFD system while maintaining the total energy deposited resulted in a ~38% increase in streamwise radius due to advective effects. This larger kernel size comes at the expense of the kernel taking ~20% longer to transition to a self-propagating flame that occurs at a radius that is ~72% larger than the baseline condition. This behavior can be explained by the long duration of the discharge and the low energy density per unit volume in the fluid. Ultimately, the convenience of the larger kernel size comes at the cost of reliability. Therefore, in combustor conditions with strong external quenching physics, depositing the most energy in the shortest time will be optimal in preventing kernel extinction. Conversely, for kernels developing in the presence of mild turbulence, the average power can be decreased, and flow advection can be utilized to grow the kernel over a longer duration without risk of extinction.

Nomenclature

ϕ	= Equivalence Ratio
I	= Current [Amps]
V	= Voltage [Volts]
E	= Energy Deposition of a Single Discharge [mJ]
t	= Time [ms or μ s]

Introduction

A challenge regarding engine design is the development of a combustion system that is both fuel and thermally efficient. One way of achieving this is through fuel lean combustion which, however, makes ignition increasingly difficult [1]. Therefore, the research and development of adequate ignition techniques is required. One technique that is promising involves ignition by nanosecond-pulsed high-frequency discharges (NPHFD). An overview of the research that worked to broaden the understanding of NPHFD is discussed below.

Research conducted by Lovascio [1], Pancheshnyi [2], and Lefkowitz [3], demonstrated the success of NPHFD systems in igniting lean fuel-air mixtures in quiescent and flowing environments. This research will focus on NPHFD in convective environments. A benefit of NPHFD systems is the ability to control the repetition frequency of the pulses, hence, the energy deposition timescale. The work of Lefkowitz et al. [4] illustrated that increasing the time between pulses increases the volume of gas exposed to the discharge in a flowing environment. Therefore, it was determined that for a given flow speed, there is an ideal pulsation frequency at which advection can be utilized to maximize kernel growth while maintaining a 100% ignition probability [4].

Although the ability of NPHFD systems to ignite lean fuel-air mixtures has been documented, little research has been done involving a direct energy and timescale comparison to how this system performs as compared to conventional spark discharges. Work conducted by Xu et al. [5] provided an initial comparison regarding how the two ignition devices perform relative to each other in a quiescent environment. Nanosecond repetitive pulses were generated using an FID pulse generator and discharges from the conventional system were produced using a coil [5]. Both the repetitive pulsed discharge ignition system and the conventional ignition system provided approximately 55 mJ of energy with an average power value of approximately 16-20 Watts (time of discharge on the order of 3.5 ms). Results showed that at a pressure of 2 bar, the flame radii of the systems were approximately identical [5]. In spite of these observations, questions remain regarding how the NPHFD ignition system will perform against the conventional ignition system on shorter timescales and in more engine-relevant, flowing environments.

This work provides a comparison between the NPHFD ignition system and a conventional, capacitive discharge system in a flowing environment under matching total energy and average power conditions as well as ignition probability. The time and size at which the kernel transitions into being a self-sustained, self-propagating flame are utilized to differentiate the performance of the two systems. Lastly, this study will explore how decreasing the pulsation rate while maintaining total energy will influence the kernel growth of the NPHFD system compared to the conventional system.

Experimental System

A. Flow Tunnel Setup

The experimental setup was centered around a small flow tunnel that utilized in previous ignition work [4,6,7]. Dimensionally, this flow tunnel has a constant cross-sectional area of 3.81 cm by 3.81 cm. A pre-mixed fuel/air inflow was introduced at one end of the tunnel through the utilization of two Bronkhorst calibrated mass flow controllers. The uncertainty of these controllers was $\pm 2\%$ of the flow setting. The fuel utilized in all experiments was chemical grade methane with 99% purity and the air utilized was filtered and dried. The flow velocity was measured in a previous effort [14] to be approximately 12.5 m/s with a turbulence intensity less than 0.5%. The equivalence ratio (ϕ) was maintained at 0.7, and the static pressure and temperature within the tunnel was maintained at ambient room conditions (approximately 100 kPa and 294 K).

At the entrance of the tunnel, the premixed flow of fuel and air passed through three screens separated by 1.27 cm each. These screens and their corresponding mesh sizes worked to create a uniform flow throughout the tunnel. Approximately 5.18 cm downstream of the screens, two 1.6 mm diameter lanthanated tungsten electrodes are oriented in a pin-to-pin fashion. The electrodes were sharpened to a 10° half angle cone and were electrically isolated from the tunnel using alumina sheaths and Teflon inserts. Each electrode could be moved independently with micrometers to set the gap distance and the

location of the gap in the flow. For all experiments, the electrode gap distance was maintained at 1.7 mm and oriented in the center of the flow tunnel. Optical access was achieved with UV grade fused silica windows and allowed for the discharge and subsequent kernel development to be imaged.

B. Ignition Systems

Both ignition systems discussed in this section received signals from a Quantum Composers 9520 pulse generator. The NPHFD power system was a custom exciter from Transient Plasma Systems (TPS). Voltage and current waveforms were obtained from a TPS Systems custom in-line voltage and current monitor. A schematic of the NPHFD ignition system is shown below in Fig. 1. The energy of the nanosecond discharges was calculated using the obtained waveforms and Eq. (1) where I is the current, V is the voltage, and E is the energy deposition of a single discharge.

$$E = \int IV dt \quad (1)$$

The voltage and current monitor utilized in this work produced waveforms and energy results that were in accordance with the findings of Lefkowitz et al. [4,8]. Again, the energy per pulse was found to be a function of inter-pulse time (IPT). At the IPTs of 3.33, 4, 6, 20, 50 and 100 μ s, the energy of each pulse was approximately 3.3 ± 0.26 , 3.3 ± 0.26 , 3.25 ± 0.26 , 3.2 ± 0.23 , 3.0 ± 0.23 , and 2.8 ± 0.23 mJ, respectively, for all pulses in the train excluding the first [8]. The first pulse in the train deposited approximately 0.4 mJ less energy than all subsequent pulses. The sum of the energies of the individual pulses equated to the total energy deposited by the train.

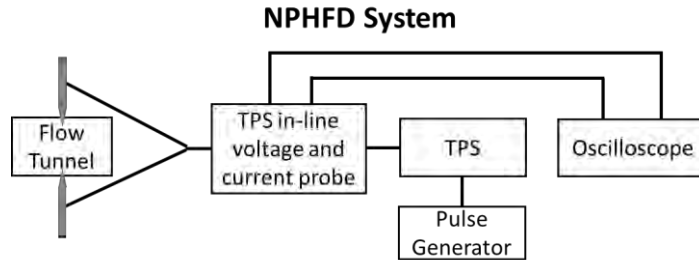


Figure 1. Schematic illustration of the NPHFD ignition system experimental setup.

The conventional ignition system exciter produces discharges that are similar in design to those of commercial turbine engines, although the pulse width is shorter and the energy deposited is smaller. Internal capacitors can be added or removed from the exciter, and/or the operating voltage can be adjusted to deliver a range of igniter energies. In addition, an internal inductor can be chosen to provide a desired pulse width. The energy delivered to the igniter was calculated by using a method identical to that of the NPHFD ignition.

The voltage waveform was measured by a North Star high voltage probe and the current waveform was measured by a Pearson current monitor. A schematic of the conventional ignition system is provided in Figure 2.

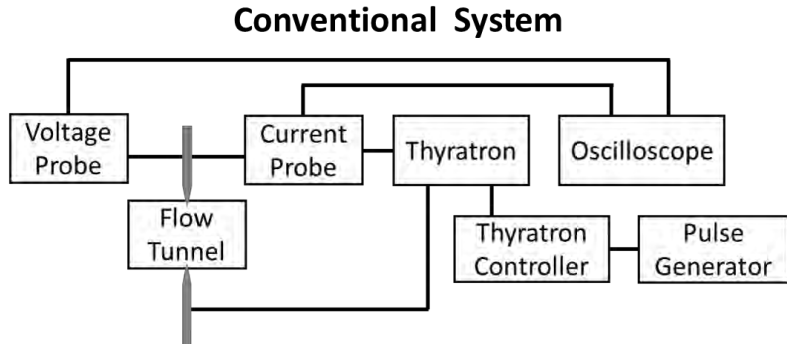


Figure 2. Schematic illustration of the conventional ignition system experimental setup

The energy deposition with respect to time for each ignition system is shown in Fig. 3 for the conditions in the current experiment. The IPT used to generate the NPHFD system waveforms was 4 μ s. These waveforms illustrate that the energy deposition is frontloaded for the conventional system as compared to the NPHFD system.

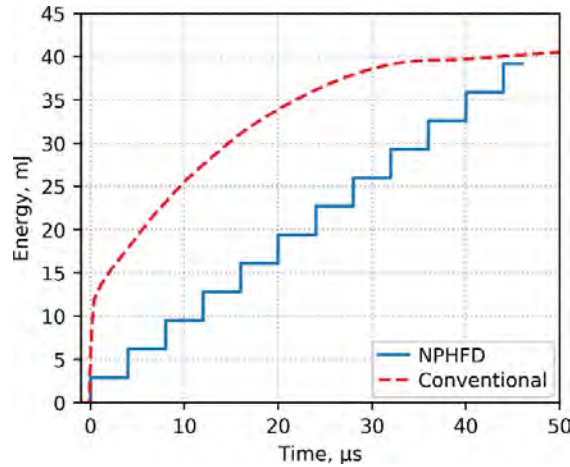


Figure 3. Energy deposition over time for the NPHFD and conventional ignition systems.

High frame rate schlieren imaging was utilized to capture the discharge, kernel growth, and flame propagation processes. For this, a Hg-Xe lamp, two concave mirrors, a knife-edge, and a Photron FASTCAM SA-Z high-speed camera were utilized. Photron FASTCAM viewer software was utilized to capture and save high-speed videos and images. ImageJ software was used to post-process and analyze the schlieren images [9].

Kernel geometries and minor and major ellipsoid radii, were determined with a MATLAB Canny edge detection program [10] and an ellipse fitting algorithm [11]. A description of the algorithms within this program can be found within work conducted by Lefkowitz et al. [8].

Results and Discussion

The total energy deposition of both ignition systems was set to approximately 40 mJ. To reach this amount of deposited energy, the NPHFD system produced 12 pulses. In order to increase the potential for advective coupling between pulses, a range on IPT were tested. Table 1 outlines the test conditions of both systems, their total energy, total deposition time, and average power.

Table 1. Test conditions for the NPHFD and conventional ignition systems.

Test Condition	Total Energy, mJ	Total Time, μ s	Avg. Power, W
3.33 μ s IPT	39.20 \pm 2.86	36.6	1071.0
4.00 μ s IPT	39.20 \pm 2.86	44.0	890.9
50.00 μ s IPT	35.60 \pm 2.53	550.0	64.7
100.00 μ s IPT	31.20 \pm 2.53	1100.0	28.4
Conventional	40.36 \pm 0.66	42.0	961.0

Ten ignition trials were taken at each test condition and the average growth rates and standard deviations of the major and minor radii were obtained. Figure 4 displays the major and minor radii of the elliptical kernel plotted with respect to time. Based on this figure, it is shown that matching the average power between the two systems results similar kernel growth performance. As IPT is increased between pulses (avg. power decreased), the advective effects begin to aid kernel growth specifically in the 50 μ s and 100 μ s IPT cases.

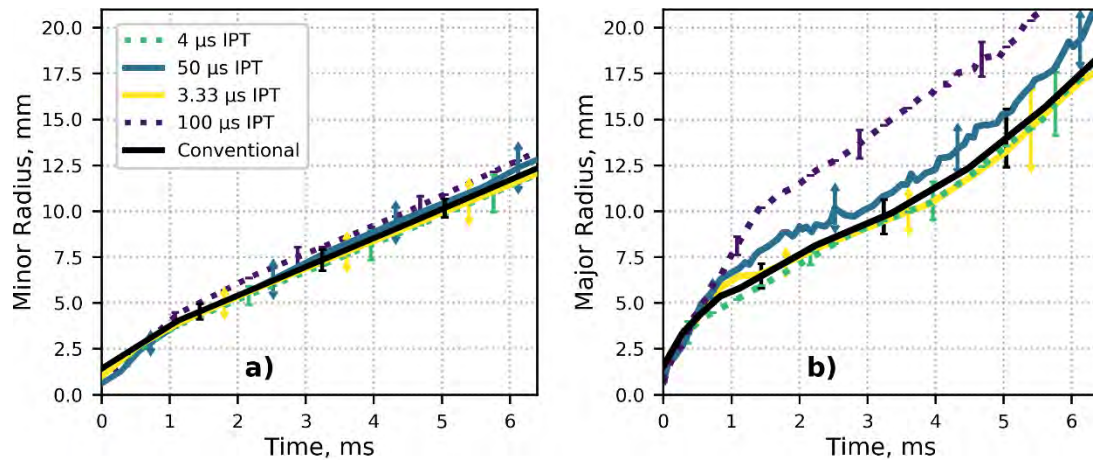


Figure 4. a) Minor radius and b) major radius of the elliptical kernel as a function of time for the NPHFD and conventional ignition systems.

In addition to these findings, dr/dt was plotted as a function of time. Figure 5 displays the results for the major radii alone since the minor radii data follow a similar trend, only less profound. This figure reveals that the 100 μ s IPT condition takes a longer amount of time to reach self-sustained growth as compared to the other test conditions. The radii listed next to each test condition show that the major radius at which sustained kernel growth begins has the trend of increasing with increasing IPT, with the 50 and 100 μ s IPT cases having the largest radii where this transition occurs.

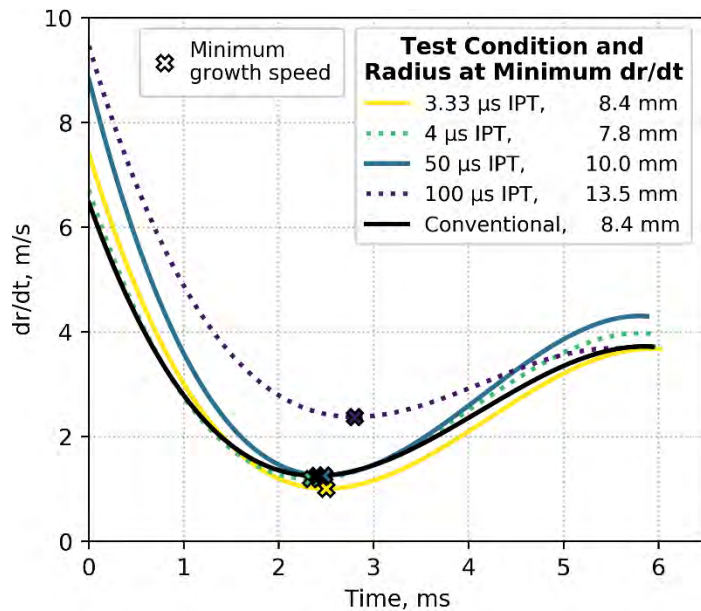


Figure 5. dr/dt for the major radius plotted as a function of time. Legend lists the major kernel radius at the minimum dr/dt point.

The major radius dr/dt plot was time shifted for each test condition such that time-zero was the time immediately after the end of the energy deposition timescale. In Fig. 6, the 100 μ s IPT test condition has a lower dr/dt value due to the lower energy per unit volume and correspondingly slower rate of thermal expansion that occurs after the last pulse in the train. Although the growth rate is slower, the time to reach the minimum dr/dt value around which self-sustained growth initiates is shorter. This is a result of flow advection enhancing streamwise kernel growth throughout the pulse train, resulting in a large size of the kernel after the pulse train terminated.

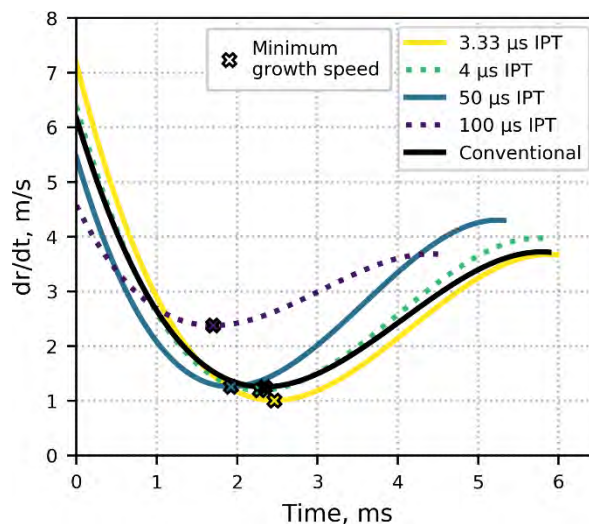


Figure 6. dr/dt for the major radius plotted as a function of time, where time-zero is the time after the last discharge.

By using the NPHFD test condition where total energy and average power is approximately matched to the conventional system as a baseline, the effects decreasing average power has on kernel size and dr/dt can be summarized on a percent-difference basis. In Table 2, the 4.00 μs IPT test condition was utilized as a performance baseline to compare all other test conditions. The values in Table 2 are related to the major radii data alone. Here, it is shown that the 3.33 μs IPT and conventional test conditions have similar average power values as the baseline, and correspondingly have similarly sized radii, time to minimum dr/dt , and radius at which minimum dr/dt occurs. As average power is decreased, the effects of flow advection become apparent. As it is shown in Fig. 5, the 100.00 μs IPT test condition has the fastest growth in the streamwise (major radius) direction. Furthermore, a ~38% increase in the major radius size after 6 ms is observed compared to the baseline value. Seemingly counterintuitive to this, it takes the 100.00 μs IPT test condition ~20% longer to reach the *minimum* dr/dt that occurs at a radius that is ~72% larger than the baseline condition. The need for a longer time and larger radius can be explained by the long duration of the discharge and the low energy density per unit volume of the fluid, respectively.

Ultimately, decreasing the average power is advantageous in that it results in larger kernel sizes. This increase in size comes at the expense of requiring more time to achieve a larger radius at which self-propagation occurs.

Table 2: Results related to the major radius are recorded on a percent-difference basis using the 4.00 μs IPT test condition as a baseline.

Test Condition	Average Power, W	% Increase in Time to Minimum dr/dt	% Increase in Time to Minimum dr/dt after Last Discharge	% Increase in Radius at Minimum dr/dt	% Increase in Radius at 6.00 ms
3.33 μs IPT	1071.0	6.8	7.9	7.7	-1.1
4.00 μs IPT	890.9	0.0	0.0	0.0	0.0
50.00 μs IPT	64.7	6.0	-15.8	27.7	13.4
100.00 μs IPT	28.4	19.7	-25.4	72.1	37.6
Conventional	961.0	2.5	2.6	6.6	1.4

Conclusion

The kernel growth rate and self-propagation flame radius were utilized as metrics of comparison between NPHFD and conventional, capacitive discharge ignition systems. Results of this work have shown that matching total energy and average power resulted in similar trends in radius growth, time to minimum dr/dt , and radius at which minimum dr/dt occurs between the NPHFD and conventional ignition systems. Lowering the average power of the NPHFD system allowed kernel growth to be aided by flow advection. As a result, the kernel radius measured at the end of the flow tunnel was larger than that of the conventional system. The total increase in the streamwise radius was found to be over 70% while only needing 3% of the total power, equating to a power reduction of approximately a factor of 40. However, the larger kernel size comes at the expense of needing a larger radius at which self-propagation initiates in an extended period of time due to the low energy density per unit volume of fluid.

Based on the results of this work, it can be inferred that in combustor conditions where there are influences such as turbulence, shear, and radiative losses that work to extinguish the kernel, depositing the most energy in the shortest time would be optimal towards achieving successful kernel growth and

ignition. This is because quenching would be mitigated since it would take less time to reach the self-propagation radius. In contrast, if conditions are similar to that of a mildly turbulent linear flow, the average power can be decreased, and the flow can be utilized to grow the kernel over a longer duration without risk of extinction. Ignition timing is a key parameter in the development and operation of ignition systems. Therefore, knowledge of the aforementioned phenomena can be utilized to tailor the energy deposition timescale to best fit specific combustor requirements.

References

1. Lovascio, S., Ombrello, T., Hayashi, J., Stepanyan, S., Xu, D., Stancu, G. D., and Laux, C. O., "Effects of pulsation frequency and energy deposition on ignition using nanosecond repetitively pulsed discharges," *Proceedings of the Combustion Institute*, 2017. DOI: 10.1016/j.proci.2016.07.065.
2. Pancheshnyi, S. V., Lacoste, D. A., Bourdon, A., and Laux, C. O., "Ignition of Propane-Air Mixtures by a Repetitively Pulsed Nanosecond Discharge," *IEEE Transactions on Plasma Science*, vol. 34, Dec. 2006, pp. 2478–2487. DOI: 10.1109/TPS.2006.876421.
3. Lefkowitz, J. K., Guo, P., Ombrello, T., Won, S. H., Stevens, C. A., Hoke, J. L., Schauer, F., and Ju, Y., "Schlieren imaging and pulsed detonation engine testing of ignition by a nanosecond repetitively pulsed discharge," *Combustion and Flame*, 2015. DOI: 10.1016/j.combustflame.2015.02.019.
4. Lefkowitz, J. K., and Ombrello, T., "An exploration of inter-pulse coupling in nanosecond pulsed high frequency discharge ignition," *Combustion and Flame*, 2017. DOI: 10.1016/j.combustflame.2017.02.032.
5. Xu, D. A., Schneider, M. N., Lacoste, D. A., and Laux, C. O., "Thermal and hydrodynamic effects of nanosecond discharges in atmospheric pressure air," *Journal of Physics D: Applied Physics*, vol. 47, Jun. 2014, p. 235202. DOI: 10.1088/0022-3727/47/23/235202.
6. Ombrello, T., "Pulse-to-Pulse Coupling for Ignition in Cross-Flow Using Nanosecond-Pulsed High-Frequency Discharge," *54th AIAA Aerospace Sciences Meeting*, Reston, Virginia: American Institute of Aeronautics and Astronautics, 2016. DOI: 10.2514/6.2016-1210.
7. Bonebrake, J. M., Blunck, D. L., Lefkowitz, J. K., and Ombrello, T. M., "The effect of nanosecond pulsed high frequency discharges on the temperature evolution of ignition kernels," *Proceedings of the Combustion Institute*, vol. 37, Jan. 2019, pp. 5561–5568. DOI: 10.1016/j.proci.2018.06.027.
8. Lefkowitz, J. K., and Ombrello, T., "Reduction of flame development time in nanosecond pulsed high frequency discharge ignition of flowing mixtures," *Combustion and Flame*, 2018. DOI: 10.1016/j.combustflame.2018.04.009.
9. Schneider, C. A., Rasband, W. S., and Eliceiri, K. W., "NIH Image to ImageJ: 25 years of image analysis," *Nature Methods*, vol. 9, Jul. 2012, pp. 671–675.
10. Canny, J., "A Computational Approach to Edge Detection," *IEEE Transactions on Pattern Analysis and Machine Intelligence*, vol. PAMI-8, Nov. 1986, pp. 679–698. DOI: 10.1109/TPAMI.1986.4767851.
11. Halir, R., Europe, J. F.-P. 6th I. C. in C., and 1998, undefined, "Numerically stable direct least squares fitting of ellipses," Citeseer.

Genetic Fuzzy Based Tetris Player

Student Researcher: Lynn K. Pickering

Advisor: Dr. Kelly Cohen

University of Cincinnati
Aerospace Engineering

Abstract

Tetris is a single player game, the objective being to place four-piece blocks and clear as many rows of blocks as possible. The game requires quickness and flexibility in its decision making, which makes it a good candidate for Fuzzy Logic decision making [1]. To train the Fuzzy Logic Tetris Player (FLTP), a genetic algorithm is used. The genetic algorithm trains the input and output membership functions, along with the rules of the fuzzy logic system. Previously the FLTP was created by playing the game repeatedly, creating input functions and rules and iterating upon these parameters by identifying faulty decisions from previous runs. The genetic algorithm is able to search a bigger solution space, exploring this complex problem and the many parameters to tune; therefore achieving higher game scores than the FLTP not trained by a genetic algorithm.

Project Objectives

In this project the objective was to build upon a Fuzzy Logic Tetris Player previously created by training the FLTP using a genetic algorithm. The goal was for the Fuzzy Logic Player to achieve higher scores than when the FLTP was created using expert knowledge.

Methodology Used

A fuzzy logic controller was initially designed using expert knowledge, and a three input, one output controller is used. The Tetris game was played many times to identify the top three identifiers of a good move in Tetris [2][3]. These identifiers are the number of holes created by a move, the number of rows cleared by a move, and the balance of the board created by a move. The first input, holes, is the number of holes created for each spin of the block and each position of the block. The membership functions for the FLTP designed using expert knowledge are shown in Figure 1. The second input, balance, is the height the blocks will reach for each spin of the block and each position of the block. The final input, rows, is how many rows will be cleared for each spin of the block and each position of the block.

A falling Tetris block can be rotated four times and positioned across the board in 10 locations, so there are 40 possible options for a block placement each time. The fuzzy system takes the three inputs described and calculates the membership value for each input. The membership functions are limited to triangles and trapezoids for the input membership functions to keep the controller calculations simple. The output in this system is simply a score, on how good a move is determined to be. The center of area method is used as the defuzzification method [4].

A great strength of fuzzy logic is that the rules are in linguistic form, allowing for the easy comprehension of the rules and understanding of how decisions are made by the system [5]. The rule base of the system was created by trial and error. The rules that define a good score are:

*IF 'holes' is good AND 'balance' is average AND 'rows' is good OR
'holes' is good AND 'balance' is good AND 'rows' is average OR
'holes' is good AND 'balance' is good AND 'rows' is good
THEN 'score' is good.*

Using the same 3 inputs and output as in the FLTP created using expert knowledge, the FLTP is trained using a genetic algorithm [6]. The genetic algorithm trains 51 aspects (chromosomes) of the system, which are stored in a gene. Each input and output have three membership functions, each membership function defined by the center of the triangle and the width of the triangle. The remaining 27 chromosomes in the gene define the rule system of the FLTP. A block diagram of this system is shown in Figure 3.

The genetic algorithm used to train the fuzzy logic system has 10 chromosomes in each population [8]. The stochastic parameters used were the probability of crossover, elitism, and the probability of mutation. Elitism helps the genetic algorithm converge onto a solution faster, because it keeps the best genes from the previous generation without altering them. Elitism was set at 0.2 so that the best 2 chromosomes were kept without mutation in the next population. The probability of crossover was set at 0.95. The probability of crossover determines how likely it is that crossover between two parents will happen. A high probability means that it is very likely that the crossover children will move to the next generation instead of the parents. A probability of crossover of 1, means parents will never move to the next generation, only the children will. A probability of 0 means the parents will always move to the next generation and there will be no crossover. A low crossover creates a global search space, but one that is not likely to converge to a solution. The higher the probability of crossover, the more focused the search space becomes. The probability of mutation was set at 0.4 and is the probability that, after crossover, a gene will undergo mutation, and become a random number in the range of the boundaries. A mutation of 1 means the genes will be mutated every time, and the search space will be very global and random. A mutation of 0 means the genes will never be mutated, and the search space will be limited to within the box created by the initial population.

Each chromosome in a population will play 3 random Tetris games, with each of these random games being the same for the chromosomes in that population. Because of the randomness of Tetris games, this creates a better estimate of the strength of a chromosome, and therefore that FLTP.

This system is the same as the system described above, other than the rules of the fuzzy logic system were set to the same rules as defined in the expert knowledge trained system. This allowed for a simplification of the gene to a gene that is 24 long, instead of 51. This reduces the complexity for the training of the fuzzy logic system by the genetic algorithm.

Results Obtained

To compare the various trained FLTPs, the same evaluation method is used across each training method. 20 sets of 100 random combination of blocks are created. If the player reaches the end of the 100 blocks, the loop starts again. In this way, each player plays the same 20 games, and the score is then an average across these games.

The FLTP created using expert knowledge is evaluated using the set of test games. The average score is evaluated to be 2873.0, and the average level achieved is 2.5. The full results of the 20 test games are shown in Table 1.

The genetic algorithm to train the FLTP is run for 2000 generations. The total time to run the 2000 generations was about 24 hours. The convergence of the genetic algorithm is shown in Figure 2. The average score is evaluated to be 11532.0, and the average level achieved is 6.3. The full results of the 20 test games are shown in Table 2.

The genetic algorithm to train the FLTP (just the membership functions) is run for 2000 generations. The total time to run the 2000 generations was about 48 hours. The average score is evaluated to be 16122.1, and the average level achieved is 5.6. The full results of the 20 test games are shown in Table 3.

Significance and Interpretation of Results

The best FLTP was the FLTP trained by the genetic algorithm, with the rules and output membership functions fixed, with an average score of 16122.05 and the highest score on the test data achieved as 136900. The second best FLTP was the FLTP completely trained by the genetic algorithm, with an average score of 11532.0 and the highest score on the test data achieved as 59678. The worst FLTP was the FLTP trained by an expert, with an average score of 2873.0 and a high score of 17611 achieved on the test data.

While it was expected that the FLTPs trained by the genetic algorithm perform better than the FLTP trained by a human expert, it is interesting that the FLTP that kept the rules of the expert trained player scores higher than the FLTP trained completely by the genetic algorithm. This is most likely due to the number of generations run. With a greater number of generations run, the FLTP trained completely by the genetic algorithm would most likely perform better than the FLTP with the rules already set.

It is interesting to observe the similarities and differences across the membership functions developed by the different training methods. The 'good' membership function for the holes input becomes much narrower in both FLTPs trained by the genetic algorithm. It is notable that there is a space not covered by membership functions in the holes input space, which may be addressed in the future by adding another membership function to this input. The membership functions for the other inputs are relatively similar across the FLTP trained by the expert and the FLTP with membership functions trained by the genetic algorithm. Further notable is that the output space of the FLTP trained completely by the genetic algorithm also has space not covered by membership functions.

It is clear, looking at the tables of the scores attained on the testing Tetris games, that the scores can vary quite greatly across the games. A human playing Tetris would have a much more even scoring level reached across any Tetris game. This shows that the order of bricks falling can have a great effect on the scores. Additional research is needed to train the FLTP with the genetic algorithm in both situations for many more generations, potentially allowing the FLTP trained only by the genetic algorithm to perform better. Techniques must be considered to increase the speed of the genetic algorithm, so that this is possible [8][9]. Further modifications would be to create more diversity in the training data so that the genetic algorithm trains for a broader range of Tetris games, and therefore performs better overall, achieving a more even range of scores on the test data.

Figures and Charts

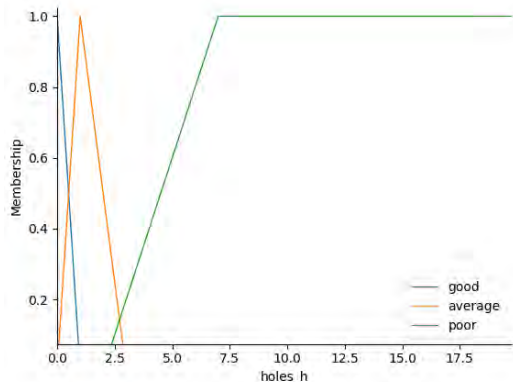


Figure 1. Input Holes.

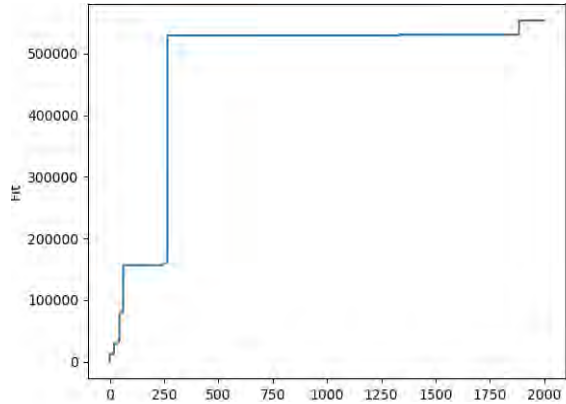


Figure 2. Convergence of the Genetic Algorithm.

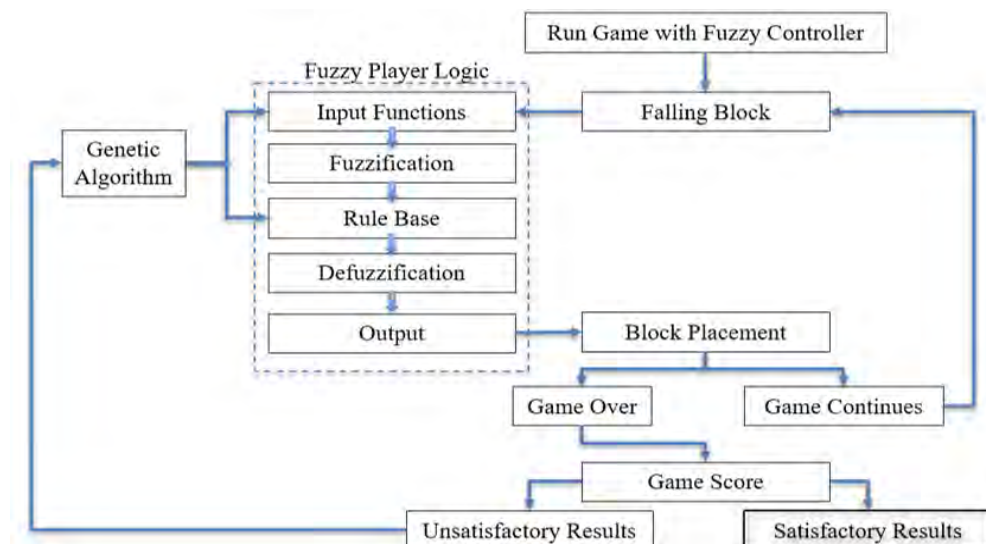


Figure 3. Block Diagram of System.

Table 1: Results FLTP Expert Training.

Run	1	2	3	4	5	6	7	8	9	10	11	12	13	14	15	16	17	18	19	20
Score (1000s)	5.2	5.3	0.6	0.7	0.6	2.1	2.7	1.5	1.0	17.6	1.2	0.5	0.5	0.6	12	0.6	2.2	0.7	0.7	0.8
Level	5	5	1	1	1	3	4	2	2	7	2	1	1	1	7	1	3	1	1	1

Table 2. Results FLTP Genetic Algorithm Training.

Run	1	2	3	4	5	6	7	8	9	10	11	12	13	14	15	16	17	18	19	20
Score (1000s)	2.1	29.2	0.4	0.9	33.6	3.1	10.8	0.7	17.9	5.7	1.6	3.7	1.1	4.3	5.9	59.7	0.6	16.4	5.9	27.2
Level	3	12	1	2	14	4	8	1	11	5	3	4	2	5	6	17	1	9	6	12

Table 3. Results FLTP Genetic Algorithm Training (Just membership functions).

Run	1	2	3	4	5	6	7	8	9	10	11	12	13	14	15	16	17	18	19	20
Score (1000s)	20.1	24.3	0.5	1.2	8.5	2.1	5.7	1.7	2.2	2.7	1.2	0.6	1.2	8.2	11.1	136.9	0.8	84.5	8.1	0.6
Level	9	9	1	2	5	3	4	3	3	3	2	1	2	7	7	24	1	18	7	1

Acknowledgments

Without the help and Guidance of my mentor, Dr. Kelly Cohen, and the support from the Ohio Space Grant Consortium, this project would have not been possible. Thank you!

References

1. Zadeh, L. A. "Fuzzylogic," in Computer, Vol. 21, No. 4, April, 1988, pp. 83-93.
2. Chabowski, Laria Carolin 2010 Tetris, github, <http://hi-im.laria.me/progs/tetrispyexefied.zip>
3. Pajitnov, A., Tetris-The game, The Tetris Company, June, 1984, <https://tetris.com/>
4. Ross, Timothy J., Fuzzy Logic with Engineering Applications. Wiley, 2017.
5. Zadeh, L. A. (1999) Fuzzy Logic = Computing with Words. In: Zadeh L. A., KacprzykJ.(eds) Computing with Words in Information/Intelligent Systems 1. Studies in Fuzziness and Soft Computing, Vol. 33. Physica, Heidelberg
6. Cordon, Oscar, et al. Genetic Fuzzy Systems: Evolutionary Tuning and Learning of Fuzzy Knowledge Bases. World Scientific, 2001.
7. Mirjalili, S., "Introduction to Genetic Algorithms: Theory and Applications", online course offered by Udemy, 2020 <https://www.udemy.com/course/geneticalgorithm/>
8. Reiko Tanese, John H. Holland, and Quentin F. Stout. 1989. Distributed genetic algorithms for function optimization. Ph.D. Dissertation. University of Michigan, USA. Order Number: AAI9001722.
9. G. R. Harik, F. G. Lobo and D. E. Goldberg, "The compact genetic algorithm," in IEEE Transactions on Evolutionary Computation, Vol. 3, No. 4, November, 1999, pp.287-297.

AR Overlay System Abstract

Student Researcher: Sara J. Roman

Advisor: Michael Gershe, M.A.

Kent State University
College of Aeronautics and Engineering

The idea of the Augmented Reality Overlay System came about during a hackathon hosted at Kent State University. My team and I first came upon the need for a guided landing system for pilots when observing airports across the country that struggle with constant fluctuating weather that interferes with landing planes. One such airport that was observed was Nantucket's that was plagued by a constant unknown of heavy fog that is known for grounding flights. We wanted to take advantage of the Augmented Reality technology that has been constantly improving over the years. The concept would allow for a projection of the runway to appear on the windshield (or pair of AR goggles for trial runs) that would help the pilots land in vision inhibiting conditions. This would not be a device used for everyday pilots but rather a safety net when landing in bad weather is required. The idea is to have beacons along the runway that will be constantly sending signals, but the design may change as research and development begins.

From the hackathon it was brought to my attention that this idea was well worth looking into further so with the help of the Ohio Space Grant and The Advanced Telerobotic Research Lab on campus I could begin the process of research and development of the AR Overlay System. Everything was in place and set to begin my venture into my first research project when the pandemic of COVID-19 swept the country. Had the situation been different I would have started working closer with my mentor Irvin Cardenas to lay out a plan and start working with The Magic Leap (AR headset) that we have available in lab. Due to the outbreak my access to vital equipment on campus can no longer be accessed. This has only pushed back plans of development; however, I can still set up the groundwork.

In the coming months I plan on doing work from home to set the stage for the AR Overlay System. Such items I know need looked into and further planned out are the communications between the ground beacons and headset. This is a vital part so the runway can be mapped out to a certain degree of precision. The regulations of airports and planes can be very restrictive of new technology, especially ones such as this, that would assist pilots in low visibility. That being said, the other item worth looking into is the legal restrictions and guidelines. Both communications and airport regulations are some of the areas to which I am least familiar, and it would benefit greatly to research them before starting any development.

If all goes well then in the coming months, I should have access to the ATR Lab again and will be able to get started on the development phase of this project. I will be in contact with my mentor throughout this whole process, however, when we have access to the lab again, I will be able to start working with The Magic Leap AR headset. I have handled it a few times but never worked with developing its graphics. This phase will take some time as I have only some experience with programming. My first goal once in the lab is to learn the language to program the layout system and understand how it can communicate with beacons in set locations. Hopefully in this phase I will be able to have a working prototype.

Using VPCA Spectral Decomposition to Analyze Optical Components Off the USVI with Sentinel – 3A/B OLCI

Student Researcher: Alex J. Rosul

Advisor: Dr. Joseph Ortiz

Kent State University
Geology

Abstract

Remote sensing is an extremely powerful tool that can be used to see things that we would otherwise not be able to visible with the naked eye. With more and more satellites being sent into space every day, and a vast arsenal of public data, it is becoming a fast-growing and important field in earth studies. In this project, Sentinel-3A/B was selected as the data source. This satellite is equipped with the Ocean and Land Color Instrument (OLCI), which provides 300 m resolution data with a swath width of 1270 km and a revisit time of two to four days. Taking data from the flyovers of the USVI and BVI, a time series was built starting when the satellite was first launched in 2016. A varimax-rotated principal component analysis (VPCA) was used to unmix the data and identify the optical constituents present in the surface waters around the islands. The method yields independent components that are orthogonal mixtures of optical constituents. Then the averaged signals were projected onto 2017 hurricane-related images to provide a visual representation of distribution and a comparison of signal intensities before and after hurricane Irma.

Introduction

In 1917 the United States Virgin Islands (USVI) were purchased from Denmark (Cosner, 1972). The economy of the islands was meager and in December of 1956, the Virgin Islands National Park was founded on St. John (Cosner, 1972). Since then, the islands driving source of income has been tourism. The economy of the territory in 2005 was 70% tourism and increased to 80% by 2010 and has undoubtedly risen since (Ennis, Brandt, Wilson Grimes, & Smith, 2016). Additionally, from a survey in 2011, almost half of the visitors surveyed claimed their reason for visiting the USVI was related to coral reefs. On top of this, the majority said they would return if the reefs remained at their current status; however, the percent of return visitors drops by almost half if coral reef quality declines (van Beukering et al., 2011). The economy of the islands is heavily dependent on the quality of its reefs and in turn the quality of their water.

One thing that can impact the health of the reefs is the growth of algae. As the development of the islands has increased, so has the nutrient inputs from the land. In some cases, this can cause an unhealthy shift in which macroalgae can outcompete corals (Ennis, Brandt, Wilson Grimes, & Smith, 2016). The increased presence of algae or other optical constituents can increase water turbidity and prevent benthic photosynthetic organisms from receiving sufficient light (Ennis, Brandt, Wilson Grimes, & Smith, 2016). In this study, we will use remote sensing techniques to monitor optical constituents in the water around the islands. This will ensure a better understanding of the zones most impacted by these optical constituents and how acute tropical storms or hurricanes can affect their distribution.

Methods

For this project I used the Kent State University varimax-rotated, principal component spectral decomposition method developed by my professor, Dr. Joseph Ortiz (Ali et al., 2012; Ortiz et al., 2013;

Ortiz and Ali, 2014; Ortiz et al, 2017; Avouris and Ortiz, 2019; Ortiz et al, 2019). The ENVI/IDL remote sensing environment, a software package made by Harrison Geospatial Solutions was used to facilitate the quick and effective manipulation of the data and process the geospatial. StatsPlus, was used to facilitate the principal component regression analysis for identification of components. IDL code written by Dr. Dulci Avouris with input from Dr. Joseph D. Ortiz was used to conduct the processing along in ENVI/IDL. First the data was re-projected to give the images the correct geographic coordinates. Next, to enhance the signal extracted from the Sentinel-3A/B OLCI images, a median filter with a size of 3x3 kernel was used to smooth the image and provide a better visual representation. Next, a region of interest (ROI) was identified, and the image was cropped down. Then the signals were simplified by taking the derivative of the spectral data. The clouds and land were masked, and the principal components were identified through principal component analysis (PCA). Finally, the data is put through a varimax-rotated to yield the final varimax-rotated principal component analysis (VPCA), The five components extracted are identified using principal component regression. The z-scores of the spectral signals are compared to the z-scores of a spectral library of optical constituents using a forward stepwise multiple linear regression. The figures display a positive or negative signal that corresponds with the coefficient value of the regression. The identification of the constituents present in the components was terminated before the regression step that exceeded a variance inflation factor (VIF) of > 2. Final figures were made with the spectral patterns with the date displayed above them for identification.

Results

A total of 14 images were processed, 12 from 2016 and 2 from 2017. The 2016 images' loadings were taken and grouped into patterns A – F based on their spectral shapes (see Figure 1 Patterns A- F). Due to sentinel-3A/B OLCI's large number of bands in the visible spectrum, it was possible to pull out five components per image. A total of six spectral patterns were recognized and then averaged between the twelve dates. It is important to note that no single spectral shape pulled out from a single day was used twice when identifying the patterns.

Next, these averaged patterns were run through the forward stepwise multiple linear regression and compared to the spectral library to identify what optical constituents are most likely present (see Table 1). Fucoxanthin, an accessory pigment to chloroplasts found in brown algae and other groups, was identified in patterns A, D, and F. Most of the signals indicated the presence of Chlorophyll-a or a degradation product of it.

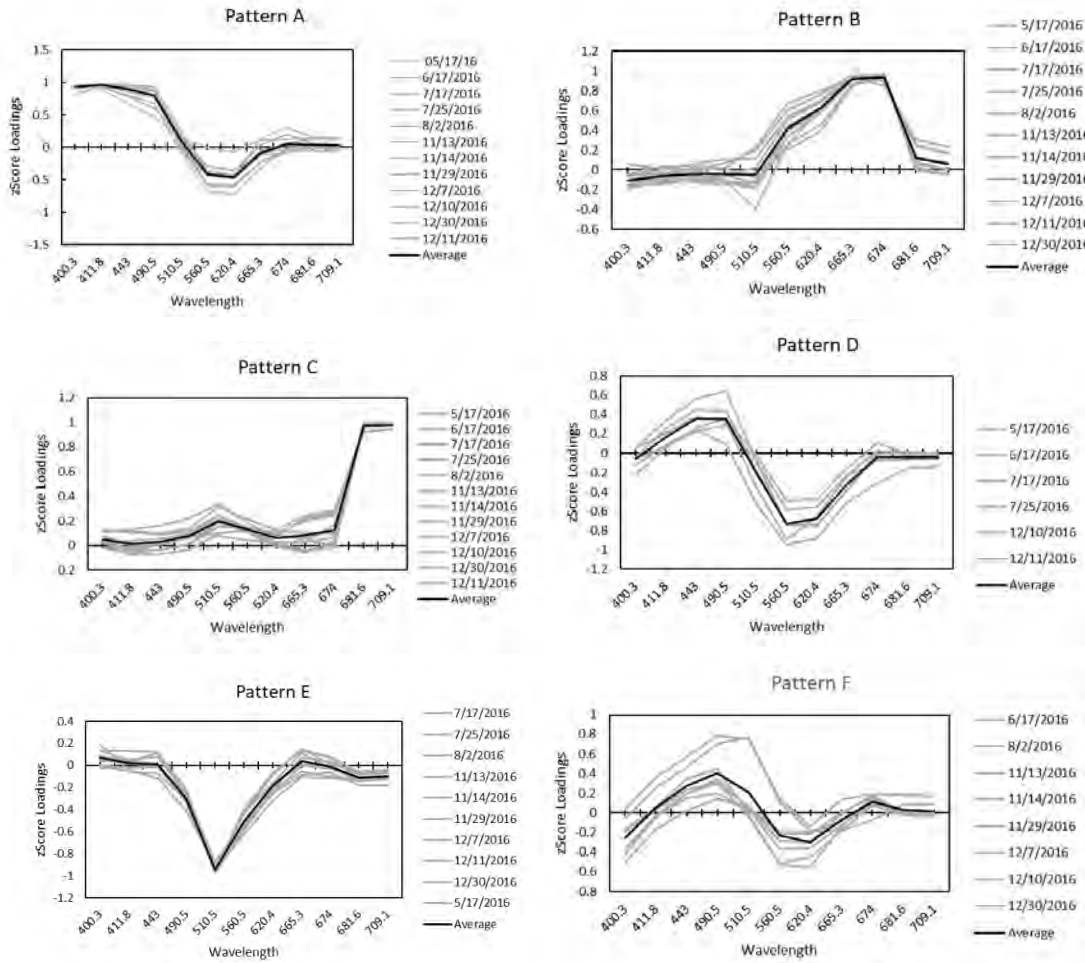


Figure 1. Patterns A - F displayed with the averaged score in black and the other shapes grouped together.

The patterns were then projected onto several images from 2016 that had the least cloud cover: 05/17/16, 07/17/16, 11/14/16, and 12/30/16. We saw that the projections did not show much variability based on the season except for a dramatic increase in signal intensity of pattern A in July. Two images from 2017 were also processed, and the averaged patterns were projected onto the ROI. These two images were before and after the 2017 hurricane Irma that struck the British Virgin Islands (BVI) on September 6th. The projected data allows for a direct comparison of the intensity of each specific signal between the two dates. We see a dramatic decrease in pattern A post-hurricane.

Table 1: Components identified after forward stepwise linear regression. Patterns A – F with coefficients identifying if the component is displayed as a positive or negative signal in the figure.

<i>Pattern A</i>	<i>Coefficients</i>	<i>Standard Error</i>	<i>Beta</i>	<i>t</i>	<i>p-value > t</i>	<i>VIF</i>	<i>TOL</i>
fucoxanthin Zdrdl	-0.4148	0.0285	-0.8479	-14.5620	6.5789E-6	1.0041	0.9959
neoxanthin Zdrdl	-0.1603	0.0332	-0.3280	-4.8218	0.0029	1.3706	0.7296
kaolinite 1.asd Zdrdl	0.1004	0.0352	0.1943	2.8564	0.0289	1.3708	0.7295
<i>Pattern B</i>	<i>Coefficients</i>	<i>Standard Error</i>	<i>Beta</i>	<i>t</i>	<i>p-value > t</i>	<i>VIF</i>	<i>TOL</i>
illite1.asd Zdrdl	-0.3447	0.0805	-0.8525	-4.2796	0.0037	1.1474	0.8716
cryptophyta Zdrdl	-0.2545	0.0770	-0.6584	-3.3053	0.0130	1.1474	0.8716
<i>Pattern C</i>	<i>Coefficients</i>	<i>Standard Error</i>	<i>Beta</i>	<i>t</i>	<i>p-value > t</i>	<i>VIF</i>	<i>TOL</i>
chlorophyll a Zdrdl	0.2755	0.0279	0.7654	9.8888	0.0002	1.3683	0.7308
chlorophyllide-b Zdrdl	0.2580	0.0304	0.7183	8.4972	0.0004	1.6318	0.6128
trans-neoxanthin Zdrdl	-0.1275	0.0304	-0.3553	-4.2008	0.0085	1.6341	0.6119
Average SargassumS3 Zdrdl (061218 BuckIs_ow24-31)	0.1043	0.0290	0.2684	3.5915	0.0157	1.2756	0.7839
<i>Pattern D</i>	<i>Coefficients</i>	<i>Standard Error</i>	<i>Beta</i>	<i>t</i>	<i>p-value > t</i>	<i>VIF</i>	<i>TOL</i>
fucoxanthin Zdrdl	-0.2029	0.0082	-0.5640	-24.8784	1.5495E-5	1.8612	0.5373
diadinoxanthin Zdrdl	-0.1307	0.0077	-0.3638	-16.9347	7.1287E-5	1.6714	0.5983
phycocyanin Zdrdl	0.1005	0.0065	0.2783	15.3368	0.0001	1.1926	0.8385
Phaeophytin-a Zdrdl	0.0801	0.0082	0.2225	9.7331	0.0006	1.8917	0.5286
chlorophyll a Zdrdl	-0.0318	0.0081	-0.0881	-3.9432	0.0169	1.8086	0.5529
<i>Pattern E</i>	<i>Coefficients</i>	<i>Standard Error</i>	<i>Beta</i>	<i>t</i>	<i>p-value > t</i>	<i>VIF</i>	<i>TOL</i>
a-PEC Zdrdl	-0.2756	0.0414	-0.9205	-6.6612	0.0002	1.0000	1.0000
<i>Pattern F</i>	<i>Coefficients</i>	<i>Standard Error</i>	<i>Beta</i>	<i>t</i>	<i>p-value > t</i>	<i>VIF</i>	<i>TOL</i>
fucoxanthin Zdrdl	-0.1927	0.0251	-0.9384	-7.6790	5.8566E-5	1.0000	1.0000

Discussion

The ability to isolate and project the averaged spectral patterns onto the Virgin Islands ROI allows for direct comparison of components day to day because they are presented on the same scale. The fact that the dates are focused around the summer and winter months may cause the average data to be biased toward conditions during that time of the year. Of course, more data makes the averages of the isolated patterns more accurate, but we are limited by images with little to no cloud cover. Sentinel-3A/B OLCI is an excellent satellite for this type of analysis because of its return cycle of two to four days. The USVI, however, due to its location within the intertropical convergence zone, experiences a lot of sporadic cloud cover. This, in turn, affected the capture of images closer in proximity to the actual touchdown of the hurricane. As this study is continued, more spectral signatures from 2017 and so on can be added to the average to increase its seasonal and interannual accuracy.

In pattern A we see kaolinite, an erosional product of hydrothermally altered rocks which include many of the islands. The component decreases in signal intensity and overall distribution post-hurricane. In Pattern B, we see both illite and cryptophyta are being identified and displayed as negative values. We see an increase in general abundance by the scale, as well as an increase in distribution around Anegada and the southern border of St. Croix. We recognize that Pattern C has an increase in the amount of chlorophyll-a around the islands as well as an increase in the deeper waters between St. Thomas and St. Croix post-hurricane. Pattern D is displaying degradation products of chlorophyll-a, and phaeophytin-a a blue accessory pigment to chlorophyll-a as a negative signal. Chlorophyll-a, diadinoxanthin and fucoxanthin as a positive signal. We see an increase in both the positive and negative signals as the scale has increased in intensity post-hurricane. In Pattern E alpha-phycoerythrocyanin (a-PEC), a pigment indicating the presence of cyanobacteria, is displayed as a negative value. After the hurricane the distribution of a-PEC increases around the coasts of all the islands and especially the southern coast of St. Croix and the coast of Anegada. Finally, in Pattern F, fucoxanthin, an accessory pigment in brown algae is displayed as negative values and shows up much more post-hurricane.

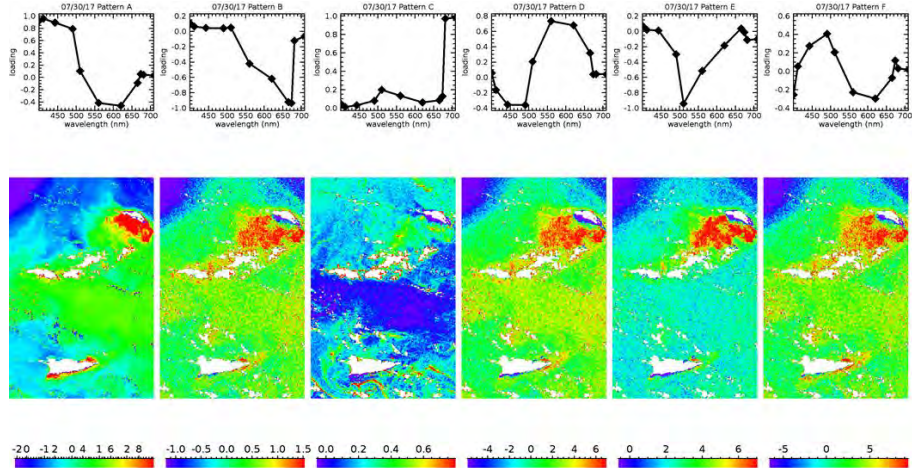


Figure 2. Pattern A – F projected onto 07/30/17 USVI and BVI region of interest prior to hurricane Irma.

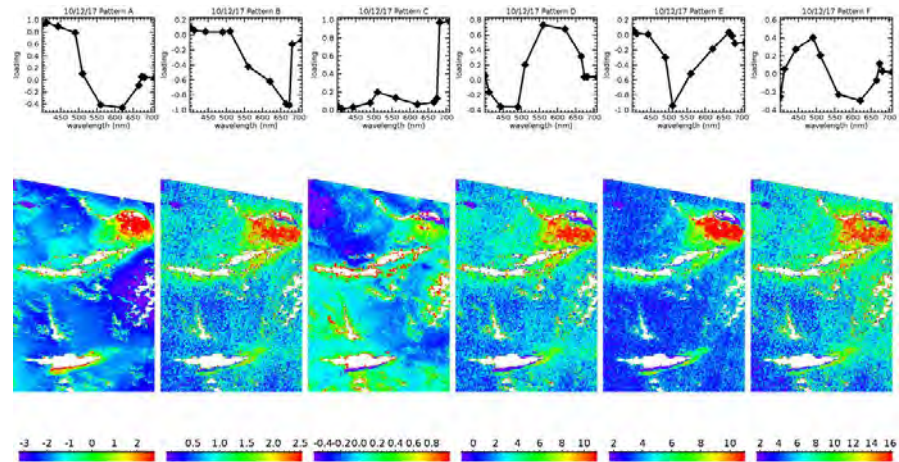


Figure 3. Pattern A – F projected onto 10/12/17 USVI and BVI region of interest post-hurricane Irma.
This image is partially cut off because the returning swath did not fully cover the region of interest.

Unfortunately for this study, the cloudless days closer to the hurricane were limited, and we were forced to use images much further apart than we would ideally choose. Also, there are differences in the signal intensities of kaolinite in Pattern A based on the month. In Figure 4, we can see how again in July 2016 with the same signal projected, the kaolinite signal intensity is high. Kaolinite is a white clay mineral that is an erosion product of hydrothermally altered silicate rocks. The sizable positive signal just southwest of Anegada that is consistently present in almost all images becomes confusing when considering the geology of those islands. Anegada of the BVI is a young limestone platform formed from the rise and fall of sea level around a great reef system (Island Resources Foundation, 2013). This means that any erosional clay products from the island would likely be carbonates. It is possible that the exemption of carbonate clays in the library could be the cause of it identifying kaolinite instead as they may have similar reflectance. Another possibility is the erosion of the hydrothermally altered rocks of the other islands and water currents consolidating it there.

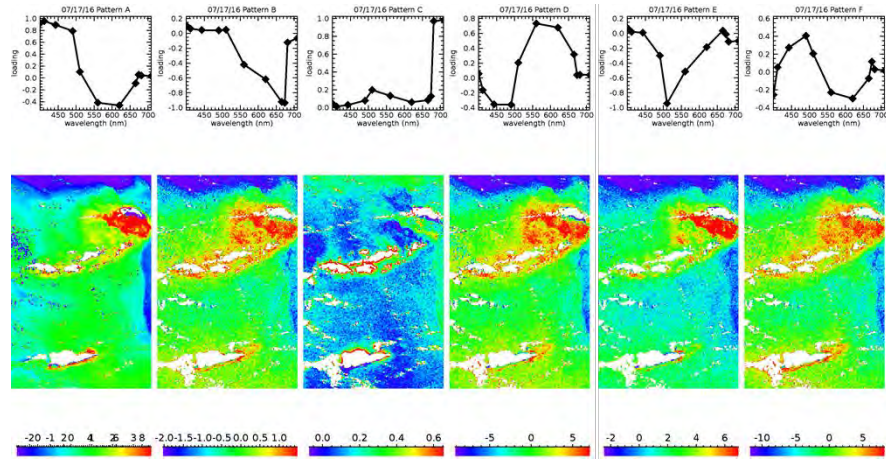


Figure 4. Patterns A – F projected onto 07/17/16 USVI and BVI region of interest.

Conclusions

With further processing of images, this method could be beneficial for the continued monitoring of the islands. The averaged patterns could become stronger and a better idea of the seasonal changes in the water column optical constituents. The large resolution size and temporal variability have made it ideal for the size of ROI and the time frame of this project. However, detailed images of distribution around the coasts were difficult to achieve at this resolution. The overall distribution of all patterns A – F post-hurricane seemed to be more disrupted and sparser likely due to the violence experienced in the surface waters. The most exciting finding was the increase in Patterns C and E, which could be due to an increase in available nutrients from the islands' watersheds.

References

1. Ali, K. A., Witter, D. L., and J. D. Ortiz, 2012, Multivariate approach to estimate color producing agents in Case 2 waters using first-derivative spectrophotometer data, Geocarto International, 10/30/2012 DOI:10.1080/10106049.2012.743601.
2. Ali, K. A., and J. D. Ortiz, Multivariate approach for chlorophyll-a and suspended matter retrievals in Case II waters using hyperspectral data, Hydrological Sciences Journal, 2014. DOI 10.1080/02626667.2014.964242
3. Cosner, O. J. (1972). Water in St. John, US Virgin Islands. US Department of the Interior Geological Survey.
4. D. M. Avouris and J. D. Ortiz, Validation of 2015 Lake Erie MODIS image spectral decomposition using visible derivative spectroscopy and field campaign data, Journal of Great Lakes Research, Volume 45, Issue 3, June 2019, Pages 466-479, 2019. <https://doi.org/10.1016/j.jglr.2019.02.005>
5. Ennis, R. S., Brandt, M. E., Wilson Grimes, K. R., & Smith, T. B. (2016). Coral reef health response to chronic and acute changes in water quality in St. Thomas, United States Virgin Islands. *Marine Pollution Bulletin*, 111 (1–2), 418–427. <https://doi.org/10.1016/j.marpolbul.2016.07.033>
6. Island Resources Foundation. 2013. An Environmental Profile of the Island of Anegada, British Virgin Islands. Island Resources Foundation. Tortola, British Virgin Islands and Washington, DC. 289 pp.
7. Ortiz, J. D., D. Avouris, S. Schiller, J. C. Luvall, J. D. Lekki, R. P. Tokars, R. C. Anderson, R. Shuchman, M. Sayers, and R. Becker, Evaluating visible derivative spectroscopy by varimax-rotated, principal component analysis of aerial hyperspectral images from the western basin of Lake Erie, Journal of Great Lakes Research, Volume 45, Issue 3, June, 2019, Pages 522-535, 2019. <https://doi.org/10.1016/j.jglr.2019.03.005>

8. Ortiz, J. D., D. Avouris, S. Schiller, J. Luvall, J. Lekki, R.P. Tokars, R.C. Anderson, R. Shuchman, M. Sayers, and R. Becker, Intercomparison of Approaches to the Empirical Line Method for Vicarious Hyperspectral Reflectance Calibration, *Front. Mar. Sci.*, vol. 4, 14 September 2017, <https://doi.org/10.3389/fmars.2017.00296>
9. Ortiz, J. D., Witter, D. L., Ali, K. A., Fela, N., Duff, M., and Mills, L., Evaluating multiple color producing agents in Case II waters from Lake Erie, *International Journal of Remote Sensing*, 34 (24), 8854-8880, 2013.van Beukering, P., Brander, L., van Zanten, B., Verbrugge, E., & Lems, K. (2011). The economic value of the coral reef ecosystems of the United States Virgin Islands, (August), 160. Retrieved from <http://www.ivm.vu.nl/en/projects/Projects/economics/Virgin-Islands/index.asp>

Effects of A PADI2 Inhibitor During Zebrafish CNS Myelination

Student Researcher: Sarah M. Shapley

Advisor: Dr. Jacqueline Morris

Baldwin Wallace University

Biology Department, program in Neuroscience

Abstract

Myelin is a lipid sheath that acts in the nervous system to propagate neuronal signaling. Demyelinating disorders, such as multiple sclerosis, disrupt this signaling process due to the leakage of ions.^[1-3] The maturation of myelin occurs in two stages. The first stage is the wrapping of the oligodendrocyte membrane around the neuronal axon, where actin is depolymerized at the leading edge.^[4-7] Secondly, compaction is the extrusion of the cytoplasm.^[1-3, 8] We hypothesize myelin basic protein (MBP), which is essential for compaction, does not interact with the membrane at this stage due to temporal regulation by the peptidyl arginine deiminase (PAD) enzyme.

Additionally, PADI2 is upregulated in myelinating oligodendrocytes and is required in oligodendrocyte differentiation and maturation.^[9,10] We hypothesize deimination of MBP prevents premature compaction, and the deimination of actin filaments promotes the filament's depolymerization. We predict a PADI2 inhibitor increases F-actin; thus, we anticipate a loss of actin depolymerization during wrapping. PADI2 was inhibited in zebrafish during myelination at 2.5 days post fertilization (dpf), 5 dpf, 7 dpf, and 10 dpf. Then, ratios of G/F-actin and mean fluorescence intensities (MFI) of myelin were analyzed to determine if the loss of PADI2 activity disrupted myelination. As expected, exposing fish to a PADI2 inhibitor did not alter oligodendrocyte cell number, nor G/F-actin ratios at 2.5 dpf. If PADI2 prevents MBP from early compaction, we hypothesized inhibiting PADI2 activity promotes premature compaction and result in a lower MFI. Overall, elucidating the regulatory role of PADI2 during myelination may assist in developing remyelination therapies for people suffering from demyelinating disorders.

Project Objectives

The central nervous system transmits its signal through neuronal axons. Axons are long, cable-like structures of the neuron that pass along an electrical signal, an action potential.^[1-3] The fatty myelin sheath assists in increasing the conductance of action potentials by reducing the resistance of the electrical potential. This myelin sheath contains the ions that flow through the cytosolic space, increasing the speed of the electrical signal. In the central nervous system, myelin is made from oligodendrocytes' phospholipid membrane by wrapping and compacting in interspersed segments around the neuronal axon.^[1-3, 8] Demyelinating disorders, such as multiple sclerosis (MS), recapitulate the importance of the myelin sheath. MS is the most common demyelinating disease. MS is characterized in MRIs by sclerotic plaques caused by chronic demyelination due to the immune system attack.^[11] Current therapies seek to reduce this immune system response as well as increasing the capacity to remyelinate.^[12]

Previous literature has found that an enzyme, peptidyl arginine deiminase type 2 (PADi2), is increased in the brain of mice before the onset of MS, suggesting PADi2 may cause demyelination.^[13] PADi2 acts on myelin basic protein (MBP) arginine residues to catalyze a deimination reaction to convert arginine to post-translationally modified citrulline. This reaction changes the overall charge of the residue and increases polarity.^[14] The study hypothesized that the reaction modifies residues to make them more susceptible to degradation by the immune system.^[13]

Interestingly, PADi2 also increases in differentiating and myelinating oligodendrocytes.^[9] Upon reviewing PADi2 expression in brain cells' RNA-seq: neurons, astrocytes, endothelial, oligodendrocytes, and microglia, it was found that oligodendrocytes had the highest PADi2 expression.^[10]

Additionally, PADi2 expression increases in oligodendrocytes as myelination occurs.^[10] It is not yet known how this enzyme may assist in myelination.

In this study, we sought to elucidate the role of PADi2 through a functionalist approach. We used an active site inhibitor at four stages of zebrafish development, 60 hours post-fertilization (hpf), 5 days post fertilization (dpf), 7 dpf, or 10 dpf, to observe changes in the differentiation of oligodendrocytes and myelination. The effects of this inhibitor were measured through G/F-actin ratios and imaging techniques. It is expected that under normal conditions, F-actin will be in high concentrations during the first and last time points, while G-actin prevails during wrapping stages. Previous literature has shown that wrapping starts at 3 dpf.^[15,16] We hypothesize that PADi2 acts on actin filaments or actin-related proteins to destabilize F-actin during wrapping. Additionally, MBP is a known substrate for PADi2 and may be temporally regulated to prevent pre-mature binding. This binding would stabilize the myelin sheath layers before wrapping is complete.^[1-3, 8] Overall, if PADi2 is responsible for mechanisms of myelination, then this enzyme may be a future target for remyelination therapies of diseases, such as in MS.

Methodology

Fish Husbandry

Adult zebrafish were kept in a 14/10 light-dark cycle at 26-30°C, fed twice daily using Zeigler's fish pellets. The evening before embryo collection, mature male and female zebrafish were paired in breeding tanks. Upon breeding the next morning, embryos were collected and bleached for five minutes in 0.06% NaClO₃ diluted in sterile fish water. Embryos were rinsed twice and separated into experimental groups.

Drug Exposure

For all assays, zebrafish were dechorionated prior to drug exposure at various time points. Zebrafish were exposed to 1 µM chloroacetamidine HCl 97% (Sigma Aldrich), known as 2-CA, or 0.02% DMSO (Sigma Aldrich) in sterile fish water for 12 hours at 60 hours post-fertilization (hpf), 5 days post fertilization (dpf), 7 dpf, or 10 dpf.

G/F-actin in vivo assay kit (Cytoskeleton, Inc #BK037)

Zebrafish were homogenized in warmed F-actin stabilization buffer at 1000 µL/ 100 mg of the tissue sample. Samples were then centrifuged after ten minutes incubation, and ATP and protease inhibitor cocktails were added. Then, samples were incubated for another ten minutes and recentrifuged at 2,000 RPM on a table-top microcentrifuge for 5 minutes at 20°C. The protein supernatant was collected for the subsequent ultracentrifugation step. 100 µL samples were then centrifuged at approximately 100,000 x

g using a Beckman-Coulter optima Max-TL temperature-controlled micro-ultracentrifuge with a TLS-55 rotor (39,000 RPM, average RCF at 99,000) at 37°C for 1 hour. After centrifugation, G-actin was collected from the supernatant while the F-actin pellet was depolymerized through the addition of 100 µL F-actin depolymerization buffer. 25 µL 5X SDS sample buffer was added to each sample and frozen at -20°C before western blot analysis.

G-actin standards (10, 20, and 50 ng) were prepared according to the kit protocol with 100 and 200 ng standards added to gels. 15 µL of each centrifuged sample was run on a stain-free 1 mm TGX FastCast acrylamide gel at 200 V for 60 minutes. Actin bands were verified by comparing them to an unstained protein ladder (Bio-Rad). The gel was transferred at 100 V for 45 minutes to a nitrocellulose membrane then blocked for 30 minutes using 5% non-fat milk in TBS-T (10 mM Tris HCl pH 8.0, 150 mM NaCl, 0.01% Tween 20). The membrane was washed with TBS-T three times for ten minutes each. The anti-actin rabbit polyclonal antibody (1:500, diluted in 0.1% milk in TBS-T) was added to the blots for 1-hour incubation at 20°C. The secondary anti-rabbit HRP conjugated antibody (1:10,000, diluted in 0.1% milk in TBS-T) was then applied to the membrane for 1 hour at 20°C, then washed with TBS-T three times for ten minutes each before adding enhanced chemiluminescent (ECL) reagents to the membrane for actin visualization using the Bio-Rad Chemi-Doc imaging system. Blots were normalized using whole protein normalization to stain-free gel images. Actin ratios were quantified using Bio-Rad's Image Lab software by creating a standard curve from gel data, then comparing the ECL developed blot for actin concentrations and normalizing to ensure equal loading across lanes.

Zebrafish Fluorescent Imaging

Zebrafish were exposed to either 1 µM 2-CA or 0.02% DMSO from 48-60 hours post-fertilization (hpf). Oligodendrocytes were counted to verify if this drug exposure affected oligodendrocyte differentiation. Tg(mbp: EGFP-CAAX)^[17] zebrafish were anesthetized with tricaine in sterile fish water and mounted between two coverslips, sealed with silicone grease. Before collecting data, fish were verified to be alive through a beating heart. The ventral and dorsal nerve cords were imaged using an Olympus BX51 fluorescent microscope with a 488 nm excitation filter to count oligodendrocytes per muscle segment. Three muscle segments were counted per fish and averaged, then compared across experimental groups.

Tg(mbp: EGFP-CAAX) zebrafish at 5 dpf were exposed to 1 µM 2-CA or 0.02% DMSO for 12 hours, anesthetized with tricaine, and mounted between two coverslips with 3% methylcellulose to prevent movement during imaging. Fish were imaged using a Zeiss Laser Scanning Microscope (LSM) 880 confocal microscope with a 488 nm excitation filter at different stages of myelination with a 20x/0.8 M27 objective lens. These images were exported and processed in ZEN Blue v3.1 by aligning and subsetting z-stacks to include green fluorescent protein positive images, then transformed into maximum intensity projections. Files were imported to ImageJ to analyze mean fluorescence intensities (MFIs) within the ventral and dorsal nerve cords. MFIs of each sample were normalized for any differences in laser intensity.^[18]

Results Obtained

If the PADI2 reaction destabilizes F-actin during wrapping, then we expect to see an increase in G-actin. Different time points were used for zebrafish to represent the various stages of myelination. At 60 hpf, it there would likely be no change in G/F-actin ratios due to the F-actin rich oligodendrocyte lamellipodial process before the initiation of wrapping (Figure 1a). By inhibiting the destabilizing agent, we expect there to be no difference and expect more F-actin to be present in the samples at this time point. To

ensure this lack of difference was indeed due to increased F-actin rather than because there were no differences across G- and F-actin, samples were further analyzed (Figure 1b). Overall, there were no differences across PADi2 inhibitor nor DMSO samples. However, both samples had increases in F-actin. This increase in F-actin is thought to be due to the lamellipodial process in early myelinating stages. It is expected that there would be more G-actin, and more differences between experimental groups, in later time points when myelin wrapping occurs.

There is evidence that PADi2 modifies histones and affects the expression of oligodendrocyte differentiation factors.^[9] At 48-60 hpf, oligodendrocytes are actively differentiating. We conducted a small study to count the number of oligodendrocytes post-drug exposure to understand if there were differentiation effects. Oligodendrocytes (Figure 2a) were imaged at 40x with a Hamamatsu c11440 camera and totaled per myotome (Figure 2b). Overall, there were no differences in the number of oligodendrocytes between the 2-CA or DMSO treated fish (Figure 2c). This finding means that the PADi2 inhibitor, 2-CA, at 1 μ M does not impact oligodendrocyte differentiation at 48-60 hpf. One discrepancy for why other studies have found differentiation effects from 2-CA is due to concentration, the timing of exposure, and animal species discrepancy between studies.^[9] Since there were no differences between oligodendrocyte numbers, then future studies can analyze maximum intensity projection images to quantify the effects of PADi2 inhibition. These metrics can be studied since oligodendrocyte quantity has not been impacted at this time point.

If PADi2 acts upon MBP to prevent early compaction, then it was hypothesized that inhibiting PADi2 activity with 2-CA would result in premature compaction and thinner myelin sheath, as measured through MFIs. However, there was no difference between these between 2-CA treated fish and the negative control at 5 dpf (Figure 3a). This result may be because compaction has already occurred, and a PADi2 inhibitor does not act on MBP post-compaction. Analysis of earlier myelination time points, such as 3 dpf, would be interesting to observe if there are any variations in MFI between experimental groups.

Acknowledgments

Thank you to Nu Rho Psi's Undergraduate Research Grant, BWU Lucille & Kenneth McCauliffe Grant & Scholarship, and the Ohio Space Grant Consortium Scholarship for directly and indirectly supporting research in this paper. Thank you to Dr. Kucenas and Dr. Fontenay from the University of Virginia for providing the Tg(mbp: EGFP-CAAX) line. The author of this paper acknowledges the use of Oberlin University's confocal microscope for imaging and Neomed's micro-ultracentrifuge for processing of zebrafish homogenates. Lastly, thank you to my mentor, Dr. Jacqueline Morris, among other Baldwin Wallace faculty, for their gracious time and support.

Figures

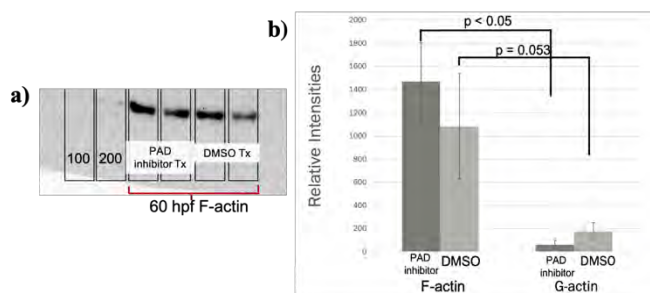


Figure 1. Results from Cytoskeleton kit for 60 hpf samples. **a)** ECL developed western blot of 60 hpf F-actin (G-actin blot not pictured) comparing treatment groups ($n = 2$). There was no statistical difference between F-actin or G/F-actin ratios between 2-CA and DMSO treated groups ($p > 0.05$). **b)** Analysis of F-actin and G-actin levels within 60 hpf western blot samples, measured in relative intensities through densitometric analysis. There is significantly more F-actin than G-actin in the 2-CA treated samples ($p < 0.05$; error bars depict standard deviation from the mean). DMSO samples are trending toward significance and are expected to have differences between F and G-actin levels. Overall, this data shows the lack of distinction between groups is not due to lack of difference between F and G-actin, but rather because their actin levels are comparable to one another.

Figure 2. Measuring PADi2 inhibitor effects on oligodendrocyte differentiation. Figure 2a&b were both imaged using a Hamamatsu c11440 camera. **a)** Sphere shapes are oligodendrocytes at 40x in a zebrafish ventral spinal cord, approximately 60 hpf **b)** Chevron patterns are muscular segments at 20x in zebrafish, used as a standardized region to count cells. Three myotomes were counted per zebrafish **c)** No differences were found between experimental groups ($n = 3$, per condition), showing that oligodendrocyte differentiation was not impacted with PADi2 was inhibited by 1 μ M 2-CA ($p > 0.05$). Error bars represent standard deviation.

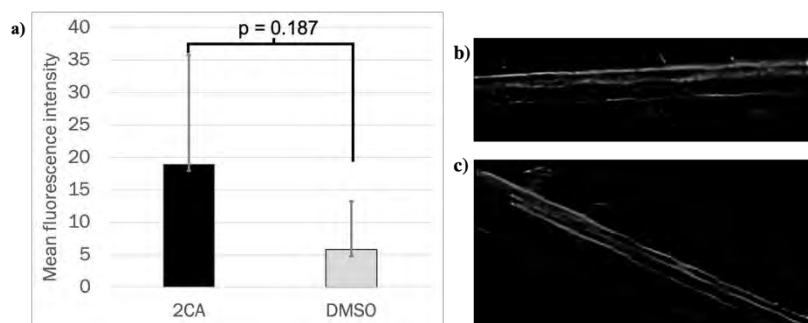
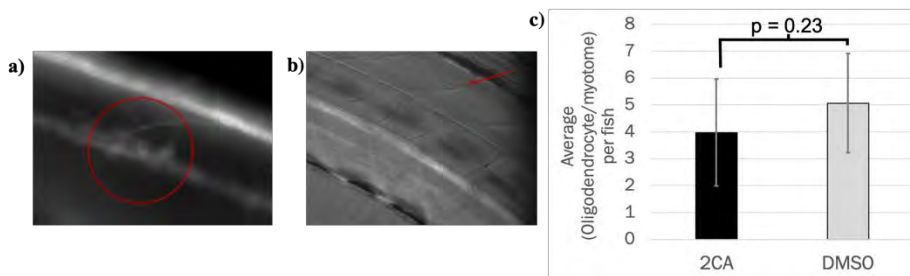


Figure 3. Measuring PADi2 inhibitor effects on myelination *in vivo*. If PADi2 is required to inhibit premature compaction, it was expected that 2-CA would result in thinner myelin, and a lower mean fluorescence intensity. **A)** at 5 dpf 1 μ M 2-CA treated zebrafish did not have differences in myelination compared to DMSO ($p = 0.187$). Representative images of 2-CA (n= 6) (**b**) and DMSO (n= 4) (**c**) treated zebrafish.



References

1. Aggarwal, S., Yurlova, L. & Simons, M. Central nervous system myelin: structure, synthesis and assembly. *Trends in Cell Biology* **21**, 585–593 (2011).
2. Deber, C. M. & Reynolds, S. J. Central nervous system myelin: structure, function, and pathology. *Clinical Biochemistry* **24**, 113–134 (1991).
3. Allen, N. J. & Lyons, D. A. Glia as architects of central nervous system formation and function. *Science* **362**, 181–185 (2018).
4. Zuchero, J. B. et al. CNS Myelin Wrapping Is Driven by Actin Disassembly. *Developmental Cell* **34**, 152–167 (2015).
5. Nawaz, S. et al. Actin Filament Turnover Drives Leading Edge Growth during Myelin Sheath Formation in the Central Nervous System. *Developmental Cell* **34**, 139–151 (2015).
6. Brown, T. L. & Macklin, W. B. The Actin Cytoskeleton in Myelinating Cells. *Neurochem Res* (2019) doi:10.1007/s11064-019-02753-0.
7. Samanta, J. & Salzer, J. L. Myelination: Actin Disassembly Leads the Way. *Developmental Cell* **34**, 129–130 (2015).
8. Fields, R. D. Myelin Formation and Remodeling. *Cell* **156**, 15–17 (2014).
9. Falcão, A. M. et al. PAD2-Mediated Citrullination Contributes to Efficient Oligodendrocyte Differentiation and Myelination. *Cell Rep* **27**, 1090–1102.e10 (2019).
10. Zhang, Y. et al. Purification and Characterization of Progenitor and Mature Human Astrocytes Reveals Transcriptional and Functional Differences with Mouse. *Neuron* **89**, 37–53 (2016).
11. Yang, L., Tan, D. & Piao, H. Myelin Basic Protein Citrullination in Multiple Sclerosis: A Potential Therapeutic Target for the Pathology. *Neurochem. Res.* **41**, 1845–1856 (2016).
12. Gruchot, J. et al. The Molecular Basis for Remyelination Failure in Multiple Sclerosis. *Cells* **8**, 825 (2019).
13. Moscarello, M. A. et al. Inhibition of peptidyl-arginine deiminases reverses protein-hypercitrullination and disease in mouse models of multiple sclerosis. *Dis Models Mech* **6**, 467 (2013).
14. Wood, D. D. et al. Myelin localization of peptidylarginine deiminases 2 and 4: comparison of PAD2 and PAD4 activities. *Lab. Invest.* **88**, 354–364 (2008).
15. Preston, M. A. & Macklin, W. B. Zebrafish as a model to investigate CNS myelination: Zebrafish Myelination. *Glia* **63**, 177–193 (2015).
16. Djannatian, M. et al. Two adhesive systems cooperatively regulate axon ensheathment and myelin growth in the CNS. *Nat Commun* **10**, 4794 (2019).
17. Almeida, R. G., Czopka, T., ffrench-Constant, C. & Lyons, D. A. Individual axons regulate the myelinating potential of single oligodendrocytes in vivo. *Development* **138**, 4443 (2011).
18. Schneider, C. A., Rasband, W. S. & Eliceiri, K. W. NIH Image to ImageJ: 25 years of image analysis. *Nat. Methods* **9**, 671–675 (2012).

The Role of Sunlight Exposure in Tasks of Inhibition in Patients with Systemic Lupus Erythematosus

Student Researcher: Hayley D. Shasteen

Advisor: Dr. Rachael Blasiman

Kent State University
Department of Psychological Sciences

Abstract

In this project, we examine the potential negative impacts that sunlight exposure has on inhibition task performance and physical and cognitive symptoms in participants with systemic lupus erythematosus (SLE). This study is a continuation of a longitudinal experiment we completed in Summer 2018. In this study, participants with SLE completed daily surveys measuring sunlight exposure, cognitive and physical symptoms, and performance on a variety of inhibition tasks, including the Stroop test, go/no go paradigm, and the Flanker test. The longitudinal design of this study allows us to further investigate fluctuations in cognitive performance and physical and cognitive symptom reporting by looking at the variations in sunlight exposure over time. In this presentation, we examine the differences between one participant's Summer 2018 and Winter 2019 data. *

*Please note that the abstract has changed from original submission. This is due to the impact of COVID-19 on the ability to access aggregate data. The following project objective and methodology will pertain to the original format of this research project, whereas result oriented sections will pertain to information presented on the poster.

Objective

The objective of this project was to identify the role of sunlight exposure in tasks of inhibition in patients with systemic lupus erythematosus (SLE), an autoimmune disease that can affect any system in the body, including the central nervous system.¹ Our previous research conducted in the Summer of 2018 suggested a negative relationship between the amount of time someone with SLE has been exposed to sunlight and their performance on tasks of inhibition, specifically the Stroop task². Additionally, our previous data supported a strong relationship between the amount of time someone with SLE has been exposed to sunlight and their reported physical symptoms and subjective cognition. In conjunction with our own research, there lies anecdotal evidence within the SLE community about the dangers of sunlight exposure as well as empirical data that shows increases of disease activity that correlate with seasonality and sunlight exposure.^{3,4} Because our previous research was conducted specifically within the summer months, we sought to run the same study during the winter months in order to compare our data. Specifically, we were interested in the relationship between scores on tasks of inhibition in relation to sunlight exposure, as well as reported physical symptoms and subjective cognition. Additionally, we included the use of healthy controls to investigate the differences.

Methodology

We recruited participants via email, seeking individuals who were diagnosed with SLE as well as age and gender matched controls, to participate in a 10-week long research study, conducted January-March. The participants were asked to complete a survey every day at the time that was most convenient to them. The survey included a modified physical symptoms scale for people with SLE and a scale of subjective cognition.^{5,6} Participants were also asked to self-report in minutes the amount of time that

they were exposed to sunlight during the day; sunlight exposure was tightly defined in that participants were asked to include the amount of time they might have been exposed to sunlight near open windows, while they were driving, and any time they were outside during daylight hours even if there was moderate cloud coverage. After completing the survey, participants were then asked to complete three tasks of inhibition via a phone application. The three tasks used in this study included the go/no go paradigm, the Flanker test, and the numerical Stroop task.

In this presentation, we utilized data from both the Summer 2018 study and the Winter 2019 study as a case-study report. One participant with SLE, a 21-year-old female, participated in both studies.

Results Obtained

Using correlation analyses, we determined that in our Summer 2018 data, there was a significant correlation between the amount of sunlight exposure and number of physical symptoms reported ($r = .421, p < .01$) (Figure 1). In this presentation, correlations between sunlight exposure and cognitive symptoms ($r = .147, p = .187$) and sunlight exposure and scores on the Stroop task ($r = -.152, p = .246$) for one participant did not reach statistical significance (Figure 2 and 3). However, in our full aggregate data set, both reach statistical significance of $p < .05$.

Using correlation analyses for our Winter 2019 data, we determined that there was a significant correlation between both sunlight exposure and physical symptoms reported ($r = .184, p < .01$) and cognitive symptoms reported ($r = .783, p < .01$) (Figure 4 and 5). However, the correlation between sunlight exposure and scores on the Stroop task failed to reach statistical significance ($r = -.006, p = .956$) in both individualized data and aggregate data (Figure 6).

Finally, we utilized one-way ANOVA tests to investigate differences between our Summer 2018 data and Winter 2019 data on an individualized level. We found that there were significant differences between the data sets in regards to physical symptoms ($F = 68.250, p < .001$), cognitive symptoms ($F = 113.336, p < .001$), and sunlight exposure ($F = 85.240, p < .001$). More physical symptoms were reported in the winter and more cognitive symptoms were reported during summer. More sunlight exposure was reported during summer months. Differences between Stroop task scores failed to reach significance ($F = .886, p = .349$). We additionally identified significant differences between several individual physical and cognitive symptoms, some of which can be found in Table 1.

Significance and Interpretation of Results

The results of our study suggest that in both winter and summer months, sunlight exposure impacts physical and cognitive symptom reporting in such a way that as sunlight exposure increases, the more physical and cognitive symptom exacerbation is reported. This identifies a clear detrimental relationship between physical and cognitive aspects of SLE and sunlight. Although our summer data suggested a negative relationship between scores on a task of inhibition and sunlight exposure, our winter data did not reach significance. This leads to several new questions; for example, it could be possible that there may be acute and long-term effects of sunlight exposure in SLE. Some aspects of the disease may only be acutely impacted by sunlight exposure, but long-term damage could impact another. We also identified significant differences between the two data sets, suggesting a seasonal effect in disease presentation. Additionally, we found significant differences between specific physical and cognitive symptoms between summer and winter, which is an interesting discovery. It's difficult to understand the complex relationship between the sun and SLE currently, which is why more research is desperately needed. Our current hypotheses include ones about circadian rhythm disruptions which could play a role in a variety of brain-based mechanisms.

Figures

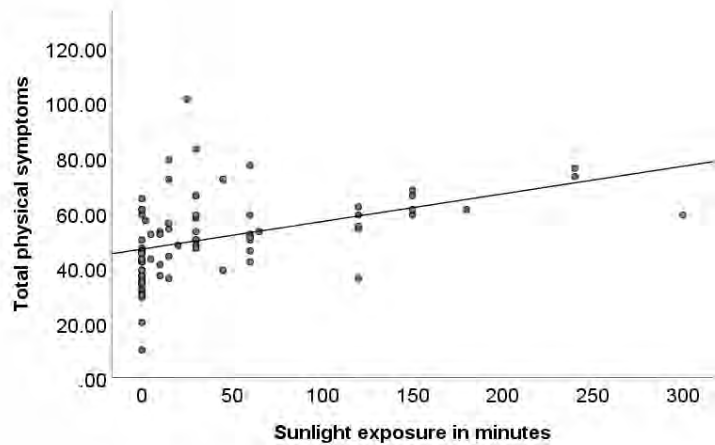


Figure 1. Relationship between total number of physical symptoms reported and the amount of time exposed to sunlight during Summer 2018 ($r = .421$, $p < .01$).

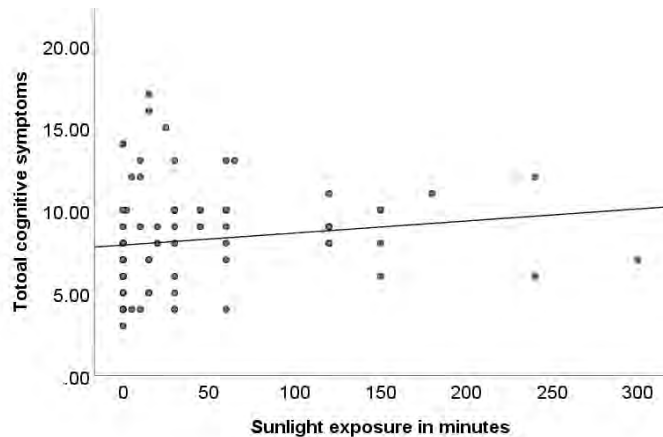


Figure 2. Relationship between total number of cognitive symptoms reported and the amount of time exposed to sunlight during Summer 2018 ($r = .147$, $p = .187$).

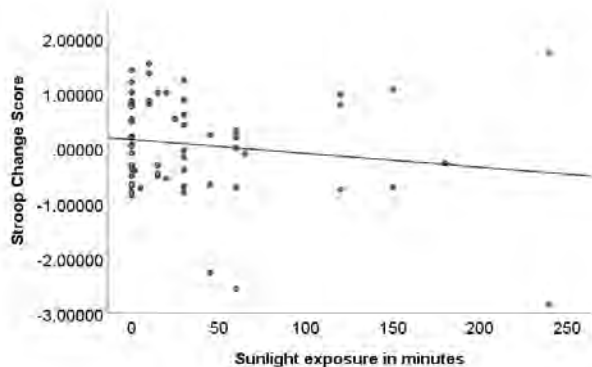


Figure 3. Relationship between Stroop task scores and the amount of time exposed to sunlight during Summer 2018 ($r = -.152$, $p = .246$).

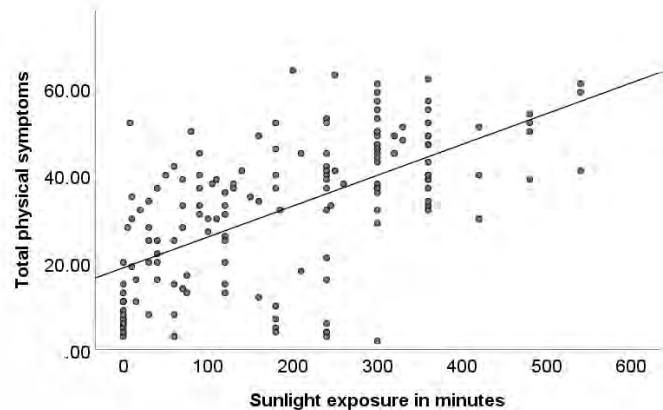


Figure 4. Relationship between total number of physical symptoms reported and the amount of time exposed to sunlight during Winter 2019 ($r = .184$, $p < .01$).

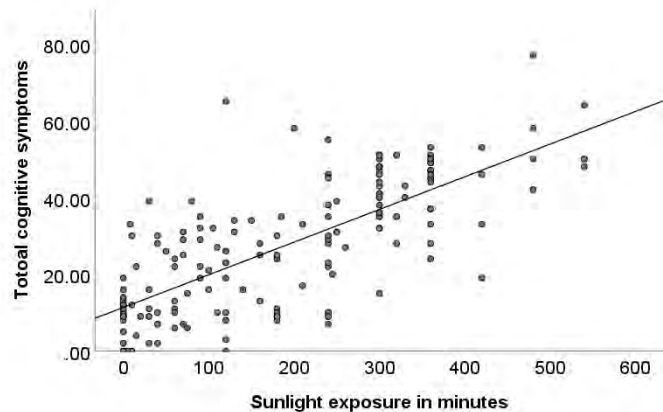


Figure 5. Relationship between total number of cognitive symptoms reported and the amount of time exposed to sunlight during Winter 2019 ($r = .783$, $p < .01$).

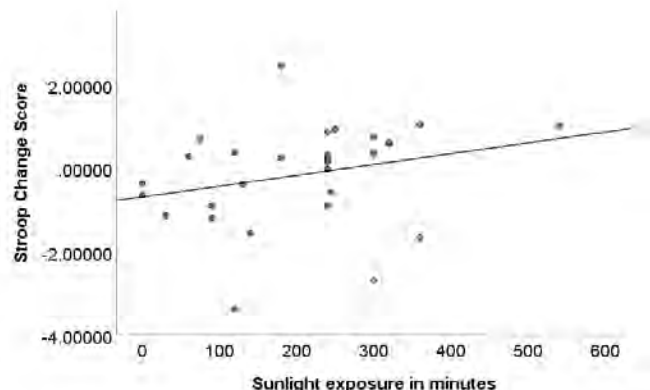


Figure 6. Relationship between Stroop task scores and the amount of time exposed to sunlight during Winter 2019 ($r = -.006$, $p = .956$)

Tables

Table 1. Differences between cognitive symptoms and physical symptoms reported during Summer 2018 and Winter 2019.

Symptom Reported	F	p
Painful joints	12.237	.001
Headache	4.587	.033
Abdominal Pain	61.663	.001
Fatigue	73.851	.001
Remembering a Word One Wishes to Say	66.697	.001
Remembering the Content of Conversations	33.673	.001
Difficulty Completing all the Steps in an Activity	6.037	.015
Difficulty Remembering One's Train of Thought When Speaking	25.876	.001

References

1. Petri, M., Genovese, M., Engle, E., & Hochberg, M. (1991). Definition, incidence, and clinical description of flare in systemic lupus erythematosus. *Arthritis & Rheumatism*, 34, 937-944.
2. Shasteen, H. D., & Blasiman, R.N. (submitted) A longitudinal investigation of cognitive function in SLE.
3. Chiche, L., Jourde, N., Ulmann, C., Mancini, J., Darque, A., Bardin, N., & Bornet, C. (2012). Seasonal variations of systemic lupus erythematosus flares in southern France. *European Journal of Internal Medicine*, 23, 250-254.
4. Krause, I., Shraga, I., Molad, Y., Guedj, D., and Weinberger, A. (1997). Seasons of the year and activity of SLE and Bechet's Disease. *Scandinavian Journal of Rheumatology*, 26, 435-439.
5. Peralta-Ramírez, M., Verdejo, A., Muñoz, M., Sabio, J., Jiménez-Alonso, J., & Pérez-García, M. (2007). Lupus Symptoms Inventory (LSI): Development and validation of a self-evaluation inventory of the subjective symptoms of systemic lupus erythematosus. *Journal of Clinical Psychology in Medical Settings*, 14, 344-350.
6. Otatti, A., & Feurestein, M. (2013). Brief Self-Report Measure of Work-Related Cognitive Limitations in Breast Cancer Survivors. *Journal of Cancer Survivorship*, 7, 262-273.

Reproducing Radial Pulse Waveforms Using a Hybrid Pulsatile System

Student Researcher: Dylan Z. Shumway

Advisor: Dr. Jeong-Hoi Koo

Miami University

Department of Mechanical and Manufacturing Engineering

Abstract

In the current age as technology continues to grow in support of the human population, the wearable technology industry has continued to expand. Most of the consumer wearable device market has been limited to functions related to activity tracking and with reliable medical functionality including only basic heartrate monitoring operations. Increasing the functionality of these devices to include the continuous monitoring of blood pressure could help predict and therefore reduce the occurrence of life-threatening cardiovascular events, such as heart attack and stroke. A major boundary to expanding the wearable market is the prohibitive nature of human testing. This project set to standardize a non-human testing model in which an existing pneumatic pulsatile system could be hybridized to allow for use with more realistic fluids on which to evaluate and develop increased functionality of wearable devices.

Project Objectives

The overarching long-term goal of this project to develop a pulse waveform simulator that can calibrate and evaluate wearable healthcare devices based on the data provided by the designed system. The specific, determined objectives of this project are to:

- Identify materials and current technologies capable of producing light-controlled pulse waveform that a sensor could detect
- Research current models for producing human pulse waveforms to further develop for future research
- Design and test a prototype capable of producing a controllable range of realistic human pulse waveforms

Methodology

The proposed hybrid pulsatile cam system used a previously verified pneumatic system produced by Yang et al. [3]. The previous study collected *in vivo* human pulsatile data from differing age groups using a produced robotic tonometry system. A consistent pressure was applied externally to a subject's forearm, and the pressure was measured and recorded. This data was then normalized and plotted in a polar plane and used to create a cam. The cam compressed a cylinder, creating the pulse that was sent through the system.

The hybrid system aims to take this working model and expand it to work with a fluid. This was to be accomplished through the implementation of a hybrid chamber, which works in a closed loop with the pressure pulses created by the hybrid system. Through applying pneumatic pulse pressure to the cylinder of liquid, water would be pushed through a check valve through a synthetic vein, and back into the cylinder creating a fluid pressure. This fluid pressure pulse could then be measured using a fluid pressure sensor.

Significant Results Obtained

Figure 1 shows the system that was developed, taking the currently available pneumatic pulsatile unit, and giving it a fluid pressure capability. On the right, is the current cylinder and cam system. Using an adjustable cylinder on the air line, the base ‘diastolic pressure’ is controlled. This is fed into a pneumatic to fluid pressure converter hybridization chamber. The pulse created travels through the synthetic vein in a loop controlled by a check valve. The internal pressure in the vein can be determined using a fluid pressure system.



Figure 1. System developed to create fluid pressure human pulse waveforms.

The pneumatic pulse pressures collected by the previously developed pneumatic system were compared to the measurements taken on the fluid component of the system. Using multiple pulsatile cams, the fluid pressure was analyzed, and the system was modified until the system followed the same trends. The results after many iterations of system design are presented in Figure 2.

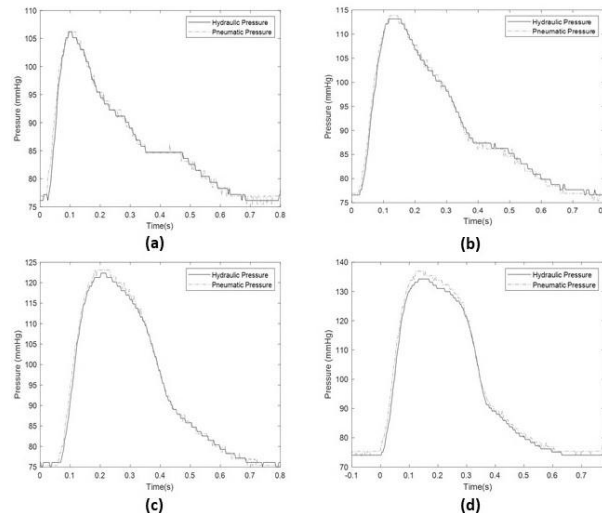


Figure 2. Experimental results comparing pneumatic and hydraulic pressures using the (a) teenage cam, (b) 35-year old cam, (c) 65-year-old cam, (d) 85-year-old cam.

References

1. Y. Jung, S. Kim, and B. Choi, “Consumer valuation of the wearables: The case of smartwatches,” *Comput. Human Behav.*, 2016.
2. T. H. Yang, J. U. Kim, Y. M. Kim, J. H. Koo, and S. Y. Woo, “A New Blood Pulsation Simulator Platform Incorporating Cardiovascular Physiology for Evaluating Radial Pulse Waveform,” *Journal of Health Care Engineering*, February 10, 2019.
3. T. H. Yang, G. Jo, J. H. Koo, S. Y. Woo, J. U. Kim, and Y. M. Kim, “A compact pulsatile simulator based on cam-follower mechanism for generating radial pulse waveforms,” *Biomed. Eng. Online*, Vol. 18, No. 1, pp. 1–18, 2019.

Life-Size Scale of Our Solar System

Student Researcher: Michael Kirby Slater

Advisor: Dr. Christopher Atchison

University of Cincinnati
Department of Middle Childhood Education

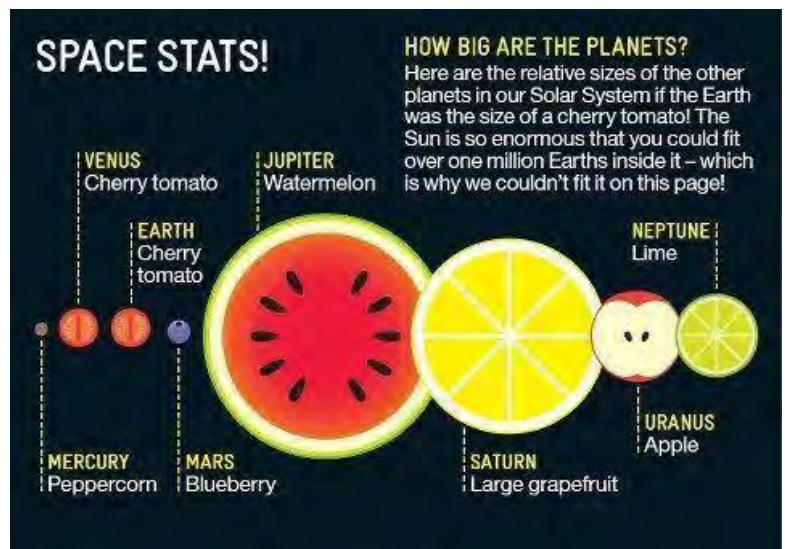
Abstract

This lesson is focused on how we can conceptually understand how large our solar system actually is. The appropriate age for this activity would be for middle grade students but could be manipulated for any age. The main idea students will take away from this lesson is that the solar system we live in is vast and the star and planets that make it up are relatively small compared to everything else around. Within this lesson, students will have the chance to not only focus on science and our solar system but will be cross disciplinary by using mathematics and having students find distances between these planets and compare them to distances on earth. The lesson will start off by actually viewing the size of our solar system and seeing how much distance there is between each of the planets. Once these distances are discovered they now need to compare these distances to distances they can imagine. Students will be given a map of the city in which they live in and will use this to help them conceptually see how large the solar system is. Groups will then be given specific objects for each of the planets to show how much larger or smaller planets are compared to one another. The goal for them is to place each of the objects in specific parts around the city to make a small-scale representation of how large the solar system is. A formula will be given to each of the groups showing how to convert the large-scale distances that are present in our solar system to our scale model each of the groups will create. Once students have found appropriate places to put each of their objects in the city they will go out and actually place these objects there. The goal of this, is to show just how large the solar system is and to think if the scale they created was increased by 100x how much larger it would look.

Lesson

This activity is focused on students understanding how large our solar system is compared to the ideas and environments around us. Students will start by finding objects that are of relative size to each of the planets and in comparison, to one another. They will then need to calculate the distance between each planet and how they can make that of relative size around us.

Once students have found a relative distance for us to see, we will then bring up a map of the town or city we currently live in. The students will then be instructed to find a place in the town which will allow for each planet to have a place and have the correct distance between one



another. They will complete this in their groups. Once completed, as a whole class, we will pick locations for each planet together on a large map.

After we find each location, as a class we will go out and place each of our planets (relative sized objects for each) within our city. Each group in class will be designated a planet and place their object in the designated area. When all planets are placed, each student will record the total distance from our starting location (the sun) to their planet. As a class we will compare these distances and see how vast our solar system is compared to what is around us.

Objectives

- To compare the vastness of our solar system to experiences relative to our students
- To practice converting units of distance and draw a conclusion from this
- To properly use coordinates on maps to find a specific location.

Standards

- 7.ESS.4 The relative patterns of motion and positions of Earth, moon and sun cause solar and lunar eclipses, tides and phases of the moon.
- 8.EE.4 Perform operations with numbers expressed in scientific notation, including problems where both decimal notation and scientific notation are used. Use scientific notation and choose units of appropriate size for measurements of very large or very small quantities, e.g., use millimeters per year for seafloor spreading. Interpret scientific notation that has been generated by technology.
- 7.RP.2 Recognize and represent proportional relationships between quantities. a. Decide whether
- 6.SS.4 Latitude and longitude can be used to identify absolute location.

Educational Theories

- Constructivism: While students work through this activity, they will need to use their prior knowledge of content to help them discover their final outcome. Students will first build up their understanding of the solar system by understanding relative size of each planet and slowly work their way up to the whole solar system itself. Students will also need to use their previous knowledge on distances to use during this to understand where each planet should go compared to one another.
- Vygotsky's Theory of Learning: While this activity is occurring, social learning will happen throughout the whole period of time. Students will be working in groups and bouncing ideas off one another to help them come up with their own schemes of how vast the solar system is to them.

Resources

Students will be needing multiple different resources during this activity. First, they will be needing 9 different objects which can be related back to each of the planets and sun. Students will also be needing the conversion formula for distances from light years to feet when they are trying to find the relative distances between planets. While students are beginning their placement of planets, they will need a large size map of the town or city the school district is in. The last resource students will need is a source of transportation while they place their planets around the map. You can use public transportation or chaperons to complete this task.

Expected Results

Since this activity wasn't performed within our classroom because of situations occurring throughout the year, there are possible results that could occur during and at the end of this activity.

Examples: After showing each group the correct way to find relative distances from light years to feet, students had the choice to pick anywhere in Mason, Ohio to locate each planet. The students shortly found out they couldn't place the sun in the middle of the map, they needed to pick a north or south end starting point because of how large the distances are from each other. Once the points were chosen for the whole class in our discussion the students were extremely excited

Assessment

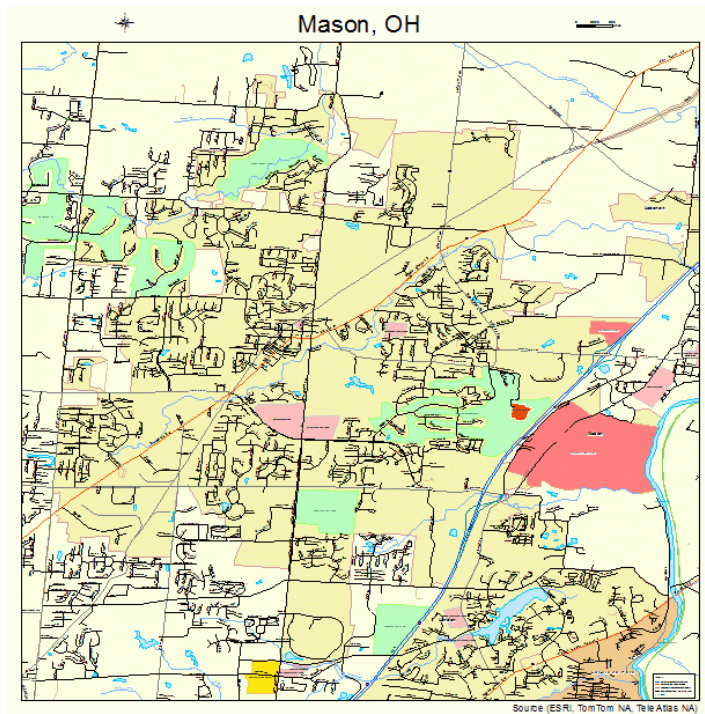
The assessment for students is to complete their groups map of the city with each planet filled into their spot. We will complete this assessment before we go out and put planets down in each location as a class. The students need to successfully justify why they placed their planets in the location they did. They also need to label the distance from the sun to each planet off to the side of their map. A map is shown as an example of where they will fill in their planets' locations.

Conclusion

This project created a hands-on, real-life example of how vast our solar system is. The students can now justify how large our solar system is and comprehend the distances between planets by using materials and distances they understand prior to the activity.

Students not only are able to see these distances but are now able to have the skills to convert distances and practice the use of maps in real-life examples.

This activity allowed students to get out of the classroom to learn new ideas and understandings that can help them in the future.



Gravitropism: Growing Plants in Space

Student Researcher: Ethan A. Smith

Advisors: Dr. Linda Young and Dr. Todd France

Ohio Northern University

Department of Biological and Health Sciences

Abstract

My project is intended for a high school biology class, but could be differentiated to fit anywhere in the K-12 curriculum. This hands-on project will demonstrate gravitropism in maize. Gravitropism is important in plants, and especially plants in space. Plant stems always grow in opposition to gravity (negative gravitropism) and plant roots always grow in the direction of gravity (positive gravitropism). Students will theorize how to successfully grow plants in space using resources from NASA, and also other known factors of stem growth, including phototropism and root cap manipulation.

Purpose

This lesson was created so students can see some of the intricacies of long-term space travel. Food is something that is needed by all living things. Plants are primary producers, meaning that they take energy directly from sunlight and convert it into matter for consumers to eat. Plants are necessary for any living environment, because without them, there would be no food for the primary, secondary, and tertiary consumers.

Learning Objectives

- To recognize that there are interactions with gravity that influence plant growth
- To theorize how to manipulate plants to make proper growth in zero gravity possible.

Ohio State Standards

Ohio Biology Standard B.C.2- Cellular Processes: *Characteristics of Life Regulated by Cellular Processes*

Theory

Gravitropism is important in plants, and especially plants in space. Plant stems always grow in opposition to gravity (negative gravitropism) and plant roots always grow in the direction of gravity (positive gravitropism). This occurs so the roots are always planted in the soil where they can obtain water and nutrients, and stems can be exposed to the atmosphere and sunlight, where they can photosynthesize.

Student Engagement

Students will be less engaged in previous lessons, learning about cellular processes and how they affect life. This lesson is intended to allow the students to get a hands-on learning experience. This way, students can use the knowledge they learn and make something tangible with it.

Resources

Each group will need two lunch trays, these will be used to hold the corn in place vertically as they germinate. These trays will be lined with paper towels and held together by rubber bands, as it is

partially submerged into water. After germination (a day), students will be able to place a few corn kernels in a petri dish, and hold them in place using plumber putty. A damp paper towel cut to fit the petri dish will be inserted to maintain moisture. The petri dish should be oriented so the roots of the corn kernels are perpendicular to the surface of the table.

Results

After even a few hours, a downward curvature of the corn roots can be seen. The next day, the roots have taken a massive downturn in growth. This supports the hypothesis that roots display positive gravitropism and grow in accordance with gravitational forces. The most tricky part of this experiment is getting good corn that will germinate. Old field corn will most likely only germinate about 20%. Fresher corn will most certainly have a better germination rate.

Assessment

Assessment can be differentiated among students. For more advanced classes, have students mark the root every millimeter before putting the corn into the petri dishes. As the root grows, have students monitor and record where the elongation zone of the root is and how it influences the curvature of the root. For other classes, have students draw the root before and after allowing it to grow for a day, to emphasize the curvature. All students will be assessed on their plan to grow plants in space, and the assessment will consist basically of the question: “Did the student come up with an original way to defy positive gravitropic effects to allow plant growth in space.”

Conclusions

This experiment allows students to have a hands-on experience with how cellular processes can influence living things. This is a fairly simple experiment that can be done in virtually any classroom and is very inexpensive. The experiment also has a very high success rate, so it is a good confidence booster for students stepping into the realm of doing labs.

Design of Heat Exchanger for Intense Cooling of Inlet Bleed Air at High Mach Numbers

Student Researcher: Erin M. Tesny

Advisor: Dr. Wei Zhang

Cleveland State University
Department of Mechanical Engineering

Abstract

Boundary-layer bleed is typically used in high-speed aircraft inlets to improve inlet performance and enhance inlet stability. At Mach numbers greater than about 3.0, the bleed air is at high temperature and low pressure, necessitating large bleed ducts that add significant weight and volume to the vehicle. A compact heat exchanger using cryogenic fuel as the working fluid is a potential method of intensely cooling the bleed air in order to reduce bleed duct size. This paper proposes a potential design of such a heat exchanger. However, the feasibility and efficiency of such a device remains unknown. A computational fluid dynamics model of the heat exchanger is set up using SolidWorks Flow Simulation. A single tube is evaluated to determine the ideal grid resolution. A parametric study is then performed using a quasi-axisymmetric bleed air model to find the optimum tube configuration. A final tube configuration is proposed to optimize heat exchanger efficiency.

Project Objectives

Bleed air from the boundary layer of high-speed aircraft inlets allows for increased performance and stability (Figure 1)^{1,2}. At high Mach numbers the bleed air is at high temperature and low pressure, necessitating large bleed-air ducts that increase both vehicle drag and weight (Figure 2). Intensely cooling the bleed air would reduce these effects by decreasing the necessary duct size. One possible method of cooling the bleed air is through a compact heat exchanger that uses a cryogenic fuel as the working fluid. Here we explore the design and feasibility of such a device that uses liquid hydrogen.

A heat exchanger was initially designed at NASA Glenn Research Center and will be the point-of-departure for this study^{2,3}. The original device was designed for a proof-of-concept (POC) test to be conducted at NASA GRC. The limitations of the test rig designed for this original study will be used here to dictate the boundary conditions of the heat exchanger performance. The original POC design utilized a radial heat exchanger, where the bleed air enters the heat exchanger through a central tube and moves radially outward past the liquid hydrogen tubing. Each hydrogen tube makes seven passes through the chamber moving inward with each pass. This configuration makes for a cross-flow heat exchanger with counter-flow passes. This small-scale test was designed to cool approximately 1% of the core flow, with an approximate flow rate of $0.038 \text{ lb}_m/\text{s}^3$.

This study will first run an analysis using computational fluid dynamics of the original design to determine the heat exchanger efficiency for the given air mass flow rate. The results will look at the average air outlet temperature as a measure of heat transfer rate. Subsequent designs will alter the angle between the hydrogen tubes and the incoming air radial air flow. By increasing the angle of the section of maximum surface area relative to the flow, the heat transfer rate is predicted to increase.

Methodology Used

The heat exchanged is designed to cool the mass flow rate of air dictated by the test rig ($0.038 \text{ lb}_m/\text{s}$) down to just above its liquefaction point of 116°R . It is assumed that 100% of the stoichiometrically

required hydrogen is available to cool the air. Fouling of the heat exchanger is not accounted for in this analysis, nor is the condensation of water vapor or carbon dioxide suspended in the air. It is assumed that for the POC test dry air will be used in the testing facility.

The original design of the heat exchanger consisted of 350 straight tubes with slot-shaped cross-sections of a high aspect ratio to increase the surface area per tube (Fig 4). The tubes are positioned in seven rows at alternating 45° angles from the core flow. The tubes are arranged in seven concentric circles of fifty tubes each. Therefore each individual row of tubes can be analyzed as a single cross-flow heat exchanger, while the device as a whole works as a counter flow heat exchanger. The simple energy balance for a heat exchanger equates the heat transfer rate required to cool the hot fluid with the rate required to heat the cold fluid⁴.

$$\dot{Q}_h = \dot{m}_h c_{p,h} (T_{h,in} - T_{h,out}) \quad (1)$$

$$\dot{Q}_c = \dot{m}_c c_{p,c} (T_{c,in} - T_{c,out}) \quad (2)$$

There is some loss of heat to the aluminum tubing that separates the two fluids. The original tube thickness is 0.02". The total heat loss to the solid can be calculated using Fourier's Law and is approximately 1.82 Btu/s (3).

$$\dot{Q}_{cond} = -kA\Delta T \quad (3)$$

At this point every quantity is known except for the exit temperature and mass flow rate of the liquid hydrogen. The final temperature of the hydrogen is not a crucial part of the analysis but the mass flow rate must be an initial condition of the simulation. The initial design analysis conducted by NASA GRC used an estimated 0.0555 lb_m/s mass flow rate for hydrogen. This will be the start point of the inputs to the CFD simulation. From the final temperature of the air in the simulation, the heat transfer rate can be found using Equation 1. This quantity can then be compared to the theoretical maximum heat transfer rate (4). In this way the different heat transfer configurations will be compared at different hydrogen mass flow rates.

$$\dot{Q}_{max} = C_{min}(T_{h,in} - T_{c,in}) \quad (4)$$

The chosen tool is SOLIDWORKS Flow Simulation because of its compatibility with the existing CAD model of the original heat exchanger. Flow Simulation, or FlowSim, has the ability to model heat conduction in solids which is critical to the heat transfer between the liquid hydrogen and air. Flow Simulation does not have the capability to model two-phase flow, so the air will not be cooled before liquefaction and the hydrogen will remain supercritical.

A quasi-axisymmetric model of the heat exchanger was used, using a 36 degree slice of the device (Fig 6). The mass flow rates of the hydrogen and air were scaled down to one tenth of the flow rate of the overall heat exchanger. The original design placed the hydrogen tubes at a 45 degree angle relative to the incoming radial air flow. This angle was modified from 0 to 80 degrees to investigate which angle resulted in the greatest heat transfer between fluids (Fig 7). A 90° configuration could not be tested because the hydrogen tubes began to overlap when placed at this angle. The average outlet temperature of the air was used as a metric of the heat transfer rate because the two are proportional (1,2). For each angle five different hydrogen flow rates were tested from 0.027-0.888 lb_m/s. A grid refinement was done with a single straight tube. The global mesh control was set, and a local mesh was seeded around the hydrogen tube itself. The same automatic mesh controls were used for the pie slice simulation runs.

Results Obtained

The average outlet temperature of the air was shown to decrease with increasing hydrogen mass flow (Fig 5). Similarly, the average outlet air temperature decreased with increasing angle relative to the flow for the same mass flow rate. This is likely due to the increase in surface area perpendicular to the incoming air flow. Because the outlet temperature is linearly related to heat transfer rate, the heat transfer rate increases with mass flow as well (Fig 8). There is a discrepancy in the data trend that shows the 45 degree configuration results in a high outlet temperature and therefore less heat transfer than the 30 degree configuration. This may be due to the limitations of the mesh size used and needs further study. The 80 degree configuration was the closest to the theoretical maximum heat transfer rate. However, although the 80 degree angle configuration resulted in the lowest outlet temperature (and therefore the greatest heat transfer rate), placing the tubes at this angle may be impractical from a mechanical design perspective. Placing the tubes at this angle may induce excessive stresses on the tubes leading to yield or buckling. Further study is needed to confirm that this configuration is a realistic design.

Significant and Interpretation

This initial study of radial heat exchanger geometry shows that a larger tube angle relative to the direction of the flow in the shell increases heat transfer between the hot and cold fluids. However, having a 80 degree angle may result in structural problems in the design of the device. Continuing work is examining other aspects of tube placement within the radial heat exchanger, including helical tube profiles. The final project will include a complex geometry that optimizes heat transfer of the heat exchanger.

Figures/Charts

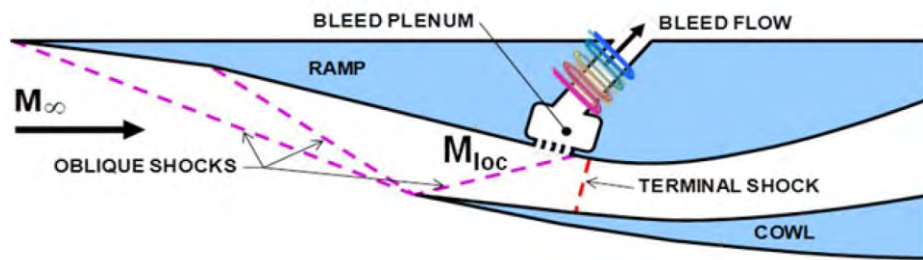


Figure 1. Mixed Compression Inlet¹



Figure 2. High Mach Number Bleed Ducts¹

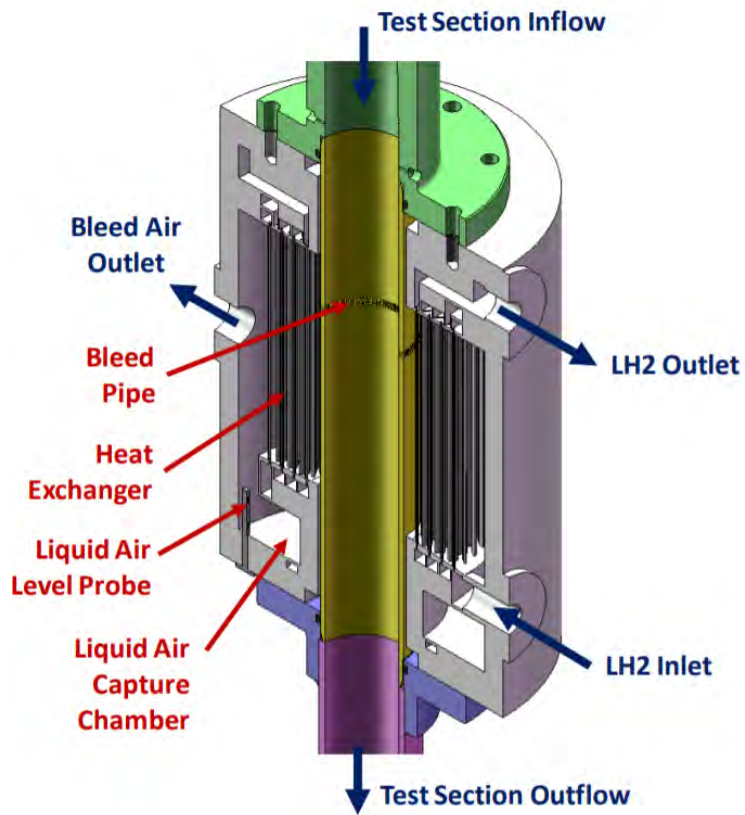


Figure 3. Side view of original Heat Exchanger²

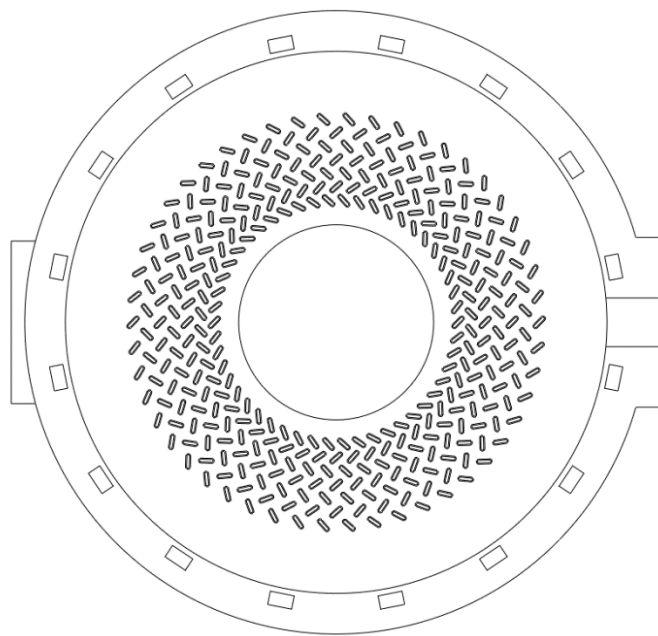


Figure 4. Top View of Original HX Design

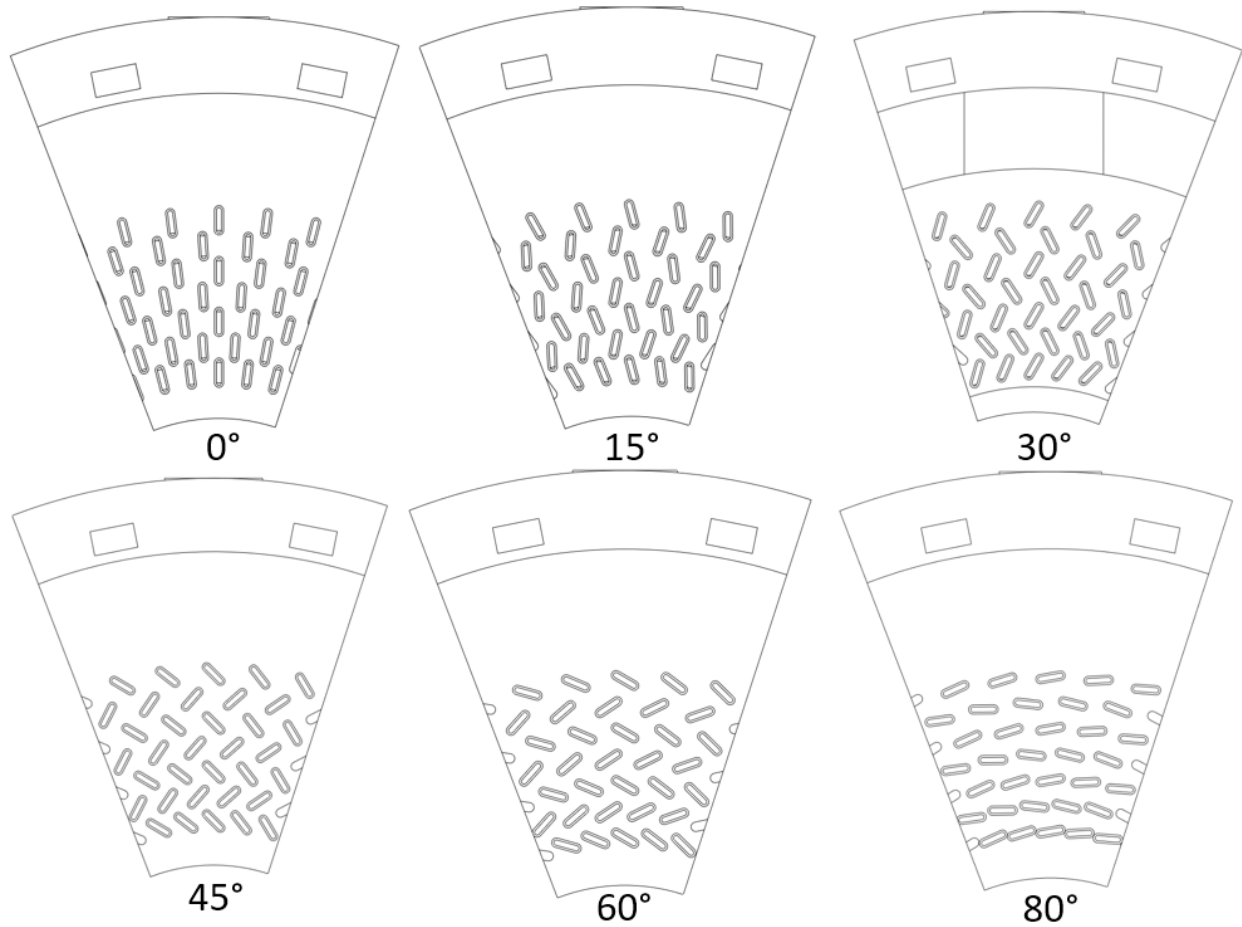


Figure 5. Top View of Heat Exchanger Slice with Different Hydrogen Tube Angles

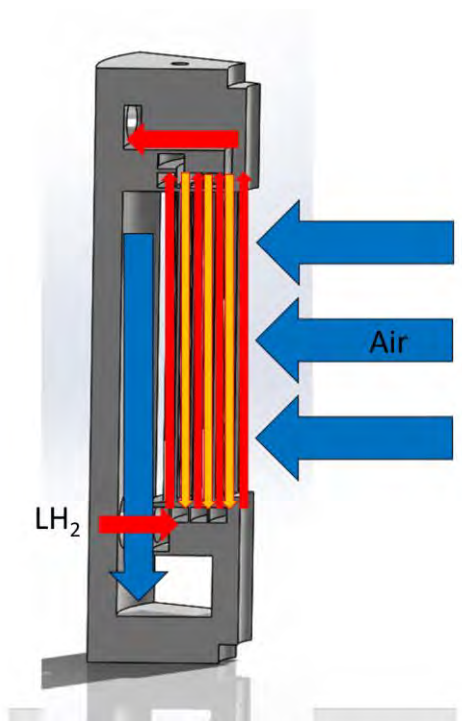


Figure 6. Side View of 36° Slice Showing Air and LH₂ Paths

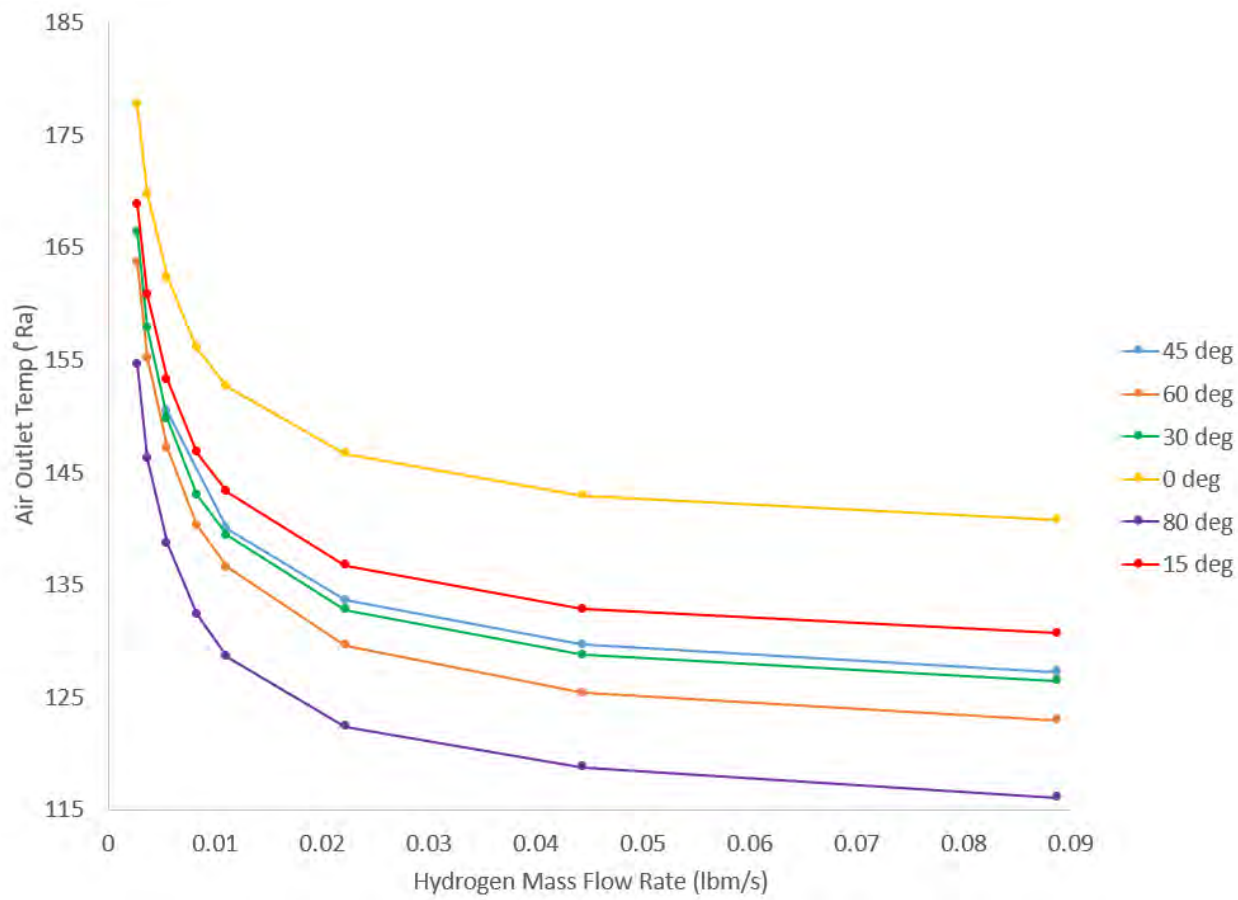


Figure 7. Plot of Hydrogen Mass Flow vs. Air Outlet Temperature

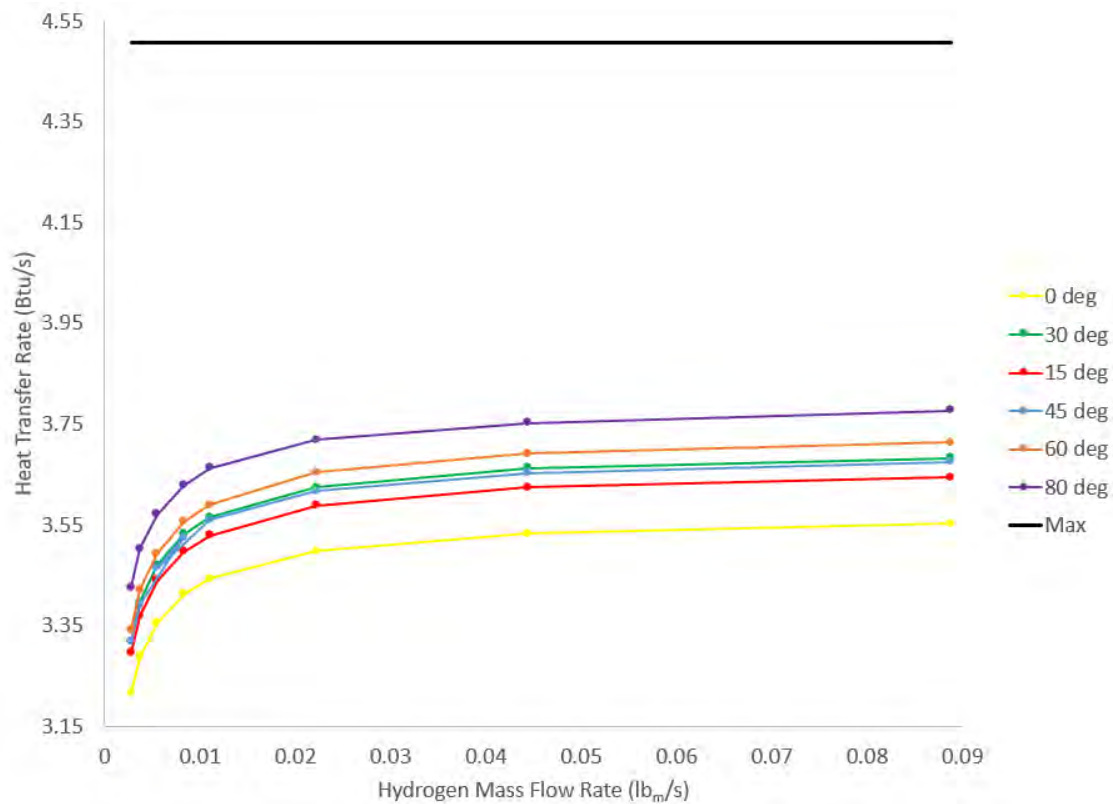


Figure 8. Plot of Hydrogen Mass Flow vs. Heat Transfer Rate

Acknowledgments

The author would like to thank the Ohio Space Grant Consortium for sponsoring this work and Dr. David Davis for his help and guidance.

References

1. Harloff, G., & Smith, G. (1995). On supersonic-inlet boundary-layer bleed flow. 33rd Aerospace Sciences Meeting and Exhibit. doi:10.2514/6.1995-38.
2. Saunders & Davis. (2013) Liquefied Bleed for Stability and Efficiency of High Speed Inlets. NASA Internal Document.
3. Saunders & Davis. (2016) Small-Scale Liquid-Bleed (SSLB) Test Requirements. NASA Internal Document.
4. Çengel, Y. A., & Ghajar, A. J. (2015). Heat and Mass Transfer: Fundamentals and Applications. New York, NY: McGraw-Hill Education.
5. Shaver, D., Carasik, L., Merzari, E., Salpeter, N., Blandford, E. (2019). Calculation of friction factors and Nusselt numbers for twisted elliptical tube heat exchangers using Nek5000. Journal of Fluids Engineering. doi:10.1115/1.4042889.

Calibration of Optical Paints for Aerodynamic Testing

Student Researcher: Grant A. Wagner

Advisor: Dr. Kevin J. Disotell

Youngstown State University

Department of Mechanical, Industrial and Manufacturing Engineering

Abstract

Pressure- and temperature sensitive paints (PSP/TSP) allow for non-intrusive aerodynamic measurements in support of NASA Aeronautics Research Mission Directorate testing of advanced air vehicles. The paints enable image-based measurements that provide full-field pressure and temperature maps across the surface of a wind-tunnel test model. Each pixel of the camera becomes a pressure/temperature sensor, greatly reducing instrumentation costs. The current work has designed, built and assembled a paint calibration apparatus to determine the relationship between measured paint emission and engineering units of pressure and temperature.

Project Objectives

The overall objective of the research was to design and construct a PSP/TSP static calibration apparatus for determining the Stern-Volmer relationship for a specific paint sample. This project was divided into two phases. Phase One occurred during the junior year of the scholarship and focused on designing the apparatus as well as selecting the necessary hardware [1]. Phase Two was completed during senior year of the scholarship and focused on assembling and testing the chamber for pressure and temperature control.

Methodology

Ultraviolet light is used to illuminate a test coupon of the paint inside the chamber (Figure 1), which is subjected to a known pressure and temperature during calibration. For PSP, the relationship between emitted intensity from the paint and the local pressure is given by the Stern-Volmer equation,

$$\frac{I_{ref}}{I} = A(T) + B(T)(\frac{P}{P_{ref}})$$

where I is the pixel intensity from a camera image, P is the local pressure, A and B are calibration coefficients which are functions of local temperature (T), and the subscript ref denotes a reference condition [2].

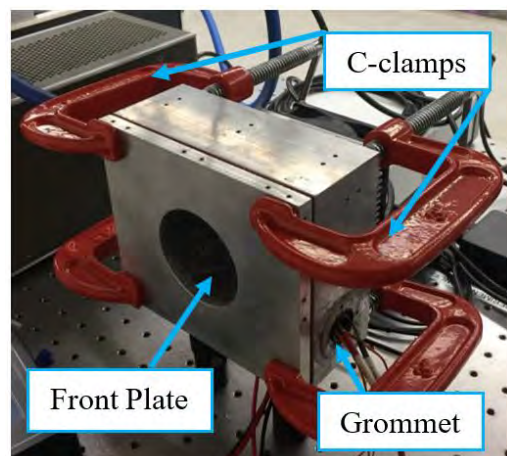


Figure 1. Constructed apparatus.

Results Obtained

Following the fabrication of the chamber and the integration of the pressure and temperature control systems, a test coupon of UniFIB PSP (Innovative Scientific Solutions, Inc.; Dayton, Ohio) was used to record the light intensity for specific pressure and temperature conditions. Figure 2 displays the resulting temperature response captured by a color camera, and Figure 3 displays the resulting pressure response.

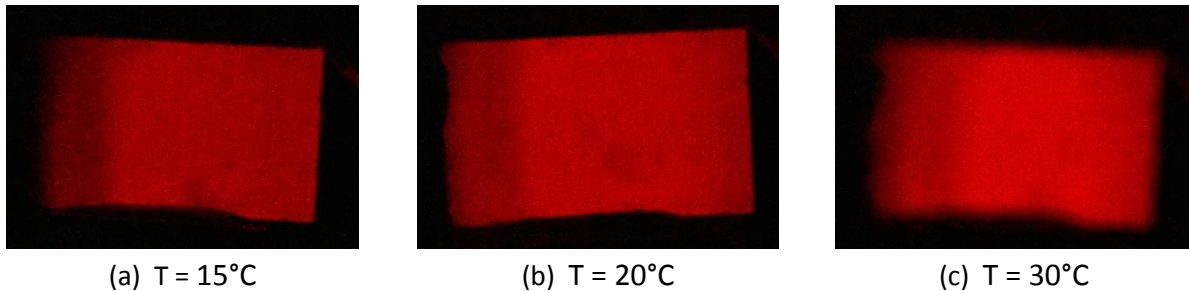


Figure 2. True-color photographs of paint response to varied temperature at constant $P_{abs} = 100$ kPa.

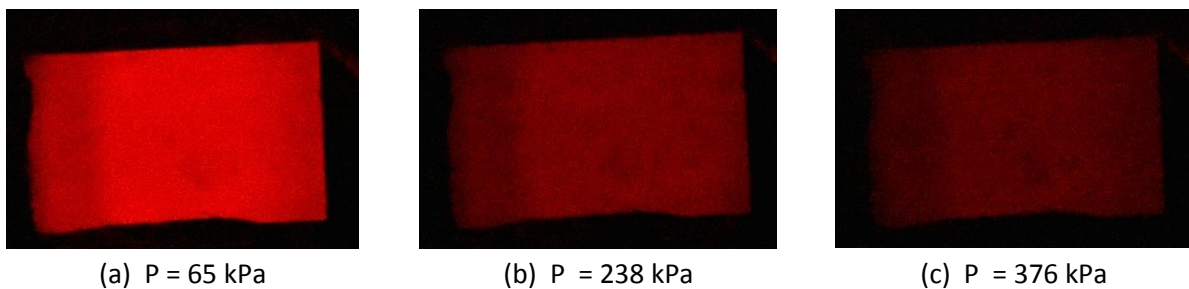


Figure 3. True-color photographs of paint response to varied pressure at constant $T = 20^\circ\text{C}$.

It has been well-established that the emitted light intensity has an inverse relationship with pressure and temperature. Therefore, as the surface pressure and/or temperature increases, the emitted light intensity decreases. These relationships are observed in the constructed calibration chamber, demonstrating pressure and temperature control from the unit. UniFIB PSP has a relatively small temperature sensitivity (0.4% per $^\circ\text{C}$ at 100 kPa) when compared to the pressure sensitivity (0.8% per kPa at 20°C) [3], which agrees with the small change in light intensity between the 15°C and 30°C images shown in Figure 2.

Future work on the apparatus should be conducted to resolve minor issues discovered while calibrating the test sample. When the chamber is pressurized near the upper limits (~ 35 psig), the grommet would deform, creating an air leak. With future work, the grommet could be resealed, or a new method such as a bulkhead fitting could be implemented to prevent leaking. Also, a new method of clamping the removable front plate should be implemented. Currently, a three-inch C-clamp in each corner of the apparatus is used to provide sealing compression.

References

1. Wagner, G.A., 2019, "Calibration of Optical Paints for Aerodynamic Testing," Ohio Space Grant Consortium Annual Research Symposium Proceedings (Cleveland, OH), April 5.
2. Quinn, M., Spinosa, E., & Roberts, D., 2017, "Miniaturization of Pressure-Sensitive Paint Measurement Systems Using Low-Cost, Miniaturized Machine Vision Cameras," *Sensors*, 17(8), 1708.
3. Innovative Scientific Solutions, Inc. "Single-Component Pressure Sensitive Paints - UniFIB." Accessed 17 March 2020: <https://inssi.com/single-component-pressure-sensitive-paints/>

**Why Software Projects Fail:
A Case Study in Implementing a GUI for a Satellite Imaging AI Training System**

Student Researcher: Sara L. Walsh

Advisor: John A. Reisner

Wright State University
Computer Science Department

Abstract

There are many methods for developing software, but a large percentage of software projects still fail. In an undergraduate software engineering course, the class was divided into 5-person teams and given real-world projects. One team was tasked with developing a browser-based Graphical User Interface (GUI) for manipulating a large set of parameters in a satellite imaging training system. This paper chronicles the team's efforts to identify various risk factors that have an impact on the success probability of a project, such as the team members' skillset, ill-defined requirements, and unrealistic timelines and schedules; some of these risk factors can be especially hard to identify, control, or mitigate. Analyzing real-life examples of development snares provides valuable insight that can be leveraged to avert future failures. This case study explores how common causes of failure can adversely affect development and provides recommendations for averting such failures in similar software projects.

Introduction

This paper is a case study on a class project. The class, "Managing the Software Development Process," was a semester-long class with a requirement of completing a real-world scientific project for a client. Each team in the class chose or was assigned a real-life software task and client. We worked in a team of five (of which I was Team Lead) and were assigned the task of making a Graphical User Interface (GUI) for an existing satellite image processing system, ASSET (AFIT Sensor and Scene Emulation Tool). Teams were required to design and build a piece of software and document the process to submit as a final project at the end of the semester.

All complex software projects will have obstacles and challenges and our project was no exception. Project success depends on being able to foresee and mitigate problems (Ewusi-Mensah, 2003, p. 189). Continued success rests on learning from past failures (Hamilton, 1999, Chapter 2, para. 1).

Background

The first assignment of the course was devoted to learning about why software projects fail. Students examined and compared published lists of software failure causes that routinely plague the industry. For example, Robert Charette (2005), the CEO of a risk-management consultancy and the author of several books on risk management, listed these as top reasons:

1. Unrealistic or unarticulated project goals
2. Inaccurate estimates of needed resources
3. Badly defined system requirements
4. Poor reporting of the project's status
5. Unmanaged risks
6. Poor communication among customers, developers, and users
7. Use of immature technology
8. Inability to handle the project's complexity

Many of these lists had recurring themes, and as a class we discussed why these issues were commonly known and yet still posing problems in software development.

Case Evaluation

Our project goal was to create a browser-based GUI that provides users with an easier way to manage and edit the many input values for the image processing system. The existing system took input values from a large tab-separated input parameter document and a starting image to generate images representative of images from real sensors. The output images are then used for industry and government-related settings for machine learning and other applications. The existing system setup required users to edit the lengthy parameter text document manually. This process required specialized knowledge of the system and each of its parameters, and the document was prone to errors in both formatting and unchecked invalid parameter values. Our task was to design a GUI that would provide an interface for editing the input values, so the user would not have to edit the input parameter document directly. This would eliminate some potential errors and provide a more user-friendly process.

We were given a set of requirements to include: the need for it to be browser and system agnostic; the need for it to be written in PyQt; to read in the input parameter document and auto-populate editable text fields with the default parameters; to write out a new parameter list that reflected the user's changes; and, the need for the GUI to be dynamically generated to allow for the possibility of the list of parameters to change.

Per class requirements, we produced a schedule within a week after the first client meeting. We scheduled one and half weeks for researching the skills and tools needed for the project. In reality, we used more than three weeks for research and, additionally, there was still continuous learning involved in all subsequent steps of progress. We set up a Gitlab repository to centralize our workflow. We regularly discussed task progress after in-class sessions, held several in-person work sessions, and used Slack to communicate on asynchronous work. The schedule called for a first prototype and demo at the end of February. It was pushed back to late March to match our progress.

From the beginning, it was clear that there were limiting issues and obvious roadblocks that would need to be addressed. One such issue was the project requirement that the GUI be written in PyQt. None of the team members had used this before. As the project progressed, we worked with the client and transitioned to Anaconda Python for the needs of the project itself. This meant a shorter learning curve for the team since some team members did have Python experience and there was a larger number of online tutorials available. When going into this project, we were not sure which skills were going to be necessary to complete the project. The project requirements projected that the use of Javascript would be optional but, after starting on the project, it became clear that it would be essential. This set of unknown unknowns made the schedule a guess at best. The timeline was limited due to this being a class-based project that was assigned several class sessions into the semester. We were limited in the amount of flexibility we could ask for. It had to be done far enough ahead of the end of the semester that we could be graded on it.

We noticed that the same common problems named on the lists of “reasons why software projects fail” were affecting our 4-month effort as well. For example:

- Inaccurate estimates of needed resources. While this is probably referencing finances or material supplies in larger projects, it applied to our project in terms of time and skills. We made some inaccurate estimates of how long it would take to acquire new skills, and which skills needed to be acquired that cost us a lot of time.
- Pushed timing. The single-semester deadline limitation is equitable to management picking an unrealistic release date. The timeline was not based on any project specifications.
- Inability to handle the project’s complexity. The many complexities – new languages, new domain – was an overwhelming amount for undergraduate students to address to make meaningful progress in such a short time span.

Our project was not finished by the time this paper was written. This was still prior to the end of the semester, but there were so many setbacks that even if we managed to finish it, there is much to be examined as to why portions of the project failed and how it got so far off schedule. It's possible that the education value of a failed software project could outweigh the value of a project that was successful on our first attempt.

By examining failures, whether total or partial, we can learn how to improve our processes. There are valuable lessons to be gathered here from the factors that contributed to project failure. Some reasons were entirely out of our control, but plenty of them were within our sphere of influence. Our short timeline was non-negotiable. Due to this being a class project there was no way that the timeline could be extended. Team members did not have expertise in the subject matter. All skills needed for the project were learned in the process of working on the project. This pushed back the milestones of our schedule. We did not know how much we did not know until we started researching. Some people caught on faster than others. Having some people catch on fast was great for the project, but left a feeling of disproportion in the team. Our class timespan coincided with the outbreak of COVID-19 and the ensuing global pandemic. Fortunately, no team members fell ill, but the cascading effects of the institutional and social changes impacted our schedule. Classes were shifted online, which caused a sharp increase in time spent on other things. Class platforms were changed or modified, requiring additional time spent on work for each class. Student housing closed, causing some team members to move with very short notice, taking away from their scheduled project work time.

Proposed Solutions

For each of these limitations and roadblocks encountered, there were various ways to address them. The best solution for a particular problem would take into account the context of the problem; things such as team size, the inflexibility of deadlines, the complexity of the project, and interconnectedness with other projects.

Our initial plan set a soft completion deadline at the end of March, allowing three weeks before our hard deadline at the end of the semester. However, going past the end of the semester was not an option. For some projects, all deadlines may be soft or flexible but with so many unknowns, it would have been wise to allow more time upfront to pin down necessary skills, or to build in the expectation of schedule adjustments. While we did work with the client to adjust the project requirements that were not possible (using PyQt in the browser), it would have benefited us to have a better idea of which requirements were prioritized. In hindsight, it would have benefited our team to gather more information on all of the requirements. This would have helped us understand the customer's priority

levels and the reasoning behind each requirement--which would have been valuable information to have when we needed to suggest adjustments. In a workplace setting, there are options to delay deployment or to hire additional team members in order to maintain the schedule. We did not have the option for either of those things. With so many unknowns upfront, we definitely should have allowed more time in our schedule for research and planning. It would benefit any plan, even a short-term one, to consider what would happen in an emergency.

Recommendations

The proposed solutions to this particular project's issues can be applied to other software projects, as well as other types of projects.

It is important to keep a flexible timeline when possible. When this is not possible, it then becomes even more important to build in "buffer" time. Contingency plans for emergencies may sound a bit extreme, but even the smallest project is vulnerable to a severe derailment from its schedule. Considering this when planning the project can help mitigate disruptions. And, it is critical to be knowledgeable about most aspects of the project before attempting to set a defined schedule.

Conclusion

In summary, there is value to be found even in failed projects, perhaps even especially in failed projects. Learning from mistakes gives us tools we can implement to attempt to avoid making the same mistakes in the future. Some of the contributing factors to project failure may be out of our control, but knowing what to plan for can make even the unknowns easier to address when they become known.

References

1. Charette, R. N. (2005, September 2). *Why Software Fails*. IEEE Spectrum.
<https://spectrum.ieee.org/computing/software/why-software-fails>
2. Ewusi-Mensah, K. (2003). *Software Development Failures*. The MIT Press.
3. Hamilton, M. (1999). *Software development : Building reliable systems*. Prentice Hall.

3D Printed Multi Materials for Aerospace Applications

Student Researcher: Paul A. Warkentien, II

Advisor: Dr. Regan Silvestri

Lorain County Community College
Chemistry Department

Abstract

Additive manufacturing/3D printing is becoming more important to industry, due to its relative ease of use and the ability to make production changes quickly. A variety of filaments are being created to fill specific needs in respective industries. Because of this, it is necessary to understand how printed materials will stand up in their environment/application. NASA is especially interested in thermal management and the evaluation of new materials is a critical part of that. The purpose of this project is to evaluate thermal properties of materials used within FDM-based 3D printing, and the effect of different processing variables on thermal diffusivity, thermal conductivity, and specific heat, along with the effect of thermal testing methods. Samples were printed both of different materials, and materials in bi-layer configurations and their thermal properties were evaluated. In this presentation, different aspects of both pre and post printing variables and their effect on thermal properties will be discussed.

Project Objectives

The purpose of this project is to evaluate the thermal properties of an additively manufactured structure and to compare the properties of different materials. Also to test the affects of using multiple materials which are additively manufactured into a single structure on that structures thermal properties. Additionally, the effects of the thermal testing on the samples structure were observed.

Methodology

Sample pucks were printed on a Hyrel 3D printer at .2mm resolution with the dimensions of 12.7mm x 2.5mm. Samples were printed in different materials in both single and multiple material versions to compare their differences. These samples were then coated in Graphite and their thermal properties were tested in a Netzsch thermal diffusivity instrument; these results were then compiled for review. After testing these samples, they were sliced in half to review their microstructure in comparison to non-thermally tested samples of the same material.

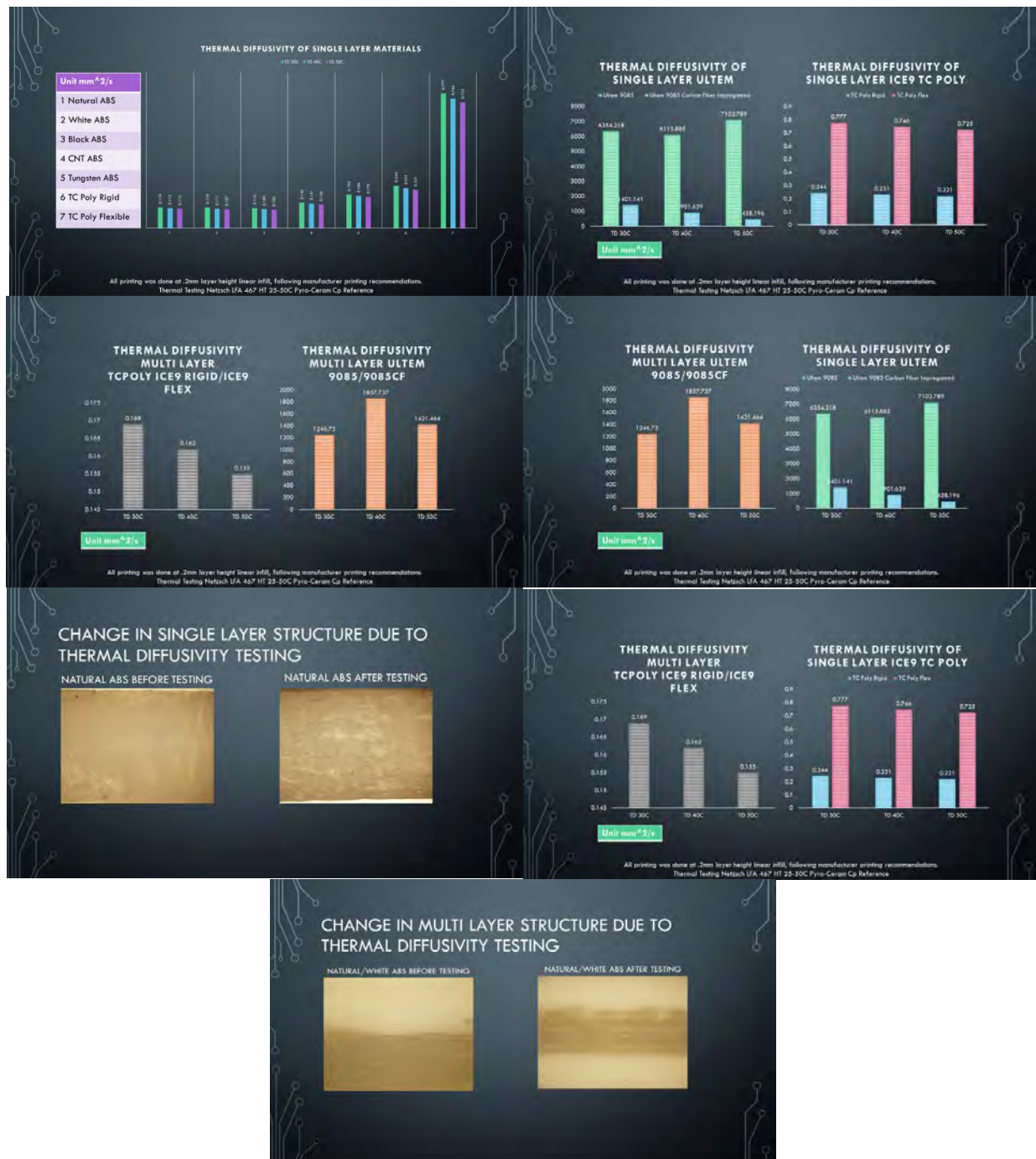
Results

The outcomes of this project show that the thermal diffusivity of a multi layer sample is biased towards the material of the two with a lower thermal diffusivity. Also that even using a “non-destructive” method of thermal testing can have a significant affect on the microstructure of a printed sample.

Significance

This project servers to help when designing a structural system where thermal management is especially important so an informed decision can be made as to what material should be used and whether multiple materials printed in a single structure can be beneficial for this purpose.

Figures/Charts



Acknowledgments

Jay Singh (OAI) -- Michael Halbig (NASA) -- Regan Silvestri (LCCC) -- Hunter Leonard – Anton Salem

Characterization of the Effects of Aging on the THP-1 Human Monocyte Cell Line

Student Researcher: Reese J. Watkins

Advisor: Dr. Kaleb Pauley

Cedarville University
Department of Science and Mathematics

Abstract

The human monocyte is a type of white blood cell functioning in innate immunity. In response to foreign pathogens, the innate immune response triggers inflammation which then draws monocytes out of the bloodstream to the infected tissue where they differentiate into macrophages. These macrophages then phagocytose, or consume, the foreign pathogen. Due to the importance of monocytes in human immunity, various monocytic cell lines have been established for *in vitro* experimentation. One common cell line, THP-1, is frequently used in immunological assays common in translational research. The THP-1 cell line was originally derived and immortalized from an acute monocytic leukemia patient in 1980. While much has been discovered over the years regarding the characteristics of this cell, there is still much that is unknown about both the THP-1 cell and monocytes in general. Currently, little is known about the effects of extended culture on this cell line. As the basis for critical research, it is necessary to exact how long these cells are stable in culture. This study sought to determine whether extended periods of continuous culture in various glucose concentrations have any impact on THP-1 phenotypes.

Project Objectives

The objective of this study was to characterize the long-term effects of continuous culture on the THP-1 cell line, while also looking at the effects of added glucose at concentrations of 5 mM and 25 mM; as a model for uncontrolled diabetes. Characterization included: analysis of TNF- α production, migration, phagocytosis, and the calculated replication rates and doubling times.

Methodology

THP-1 cells were removed from cryo-storage, thawed, and placed into a culture flask. Once the cells reached a steady viability, samples were taken and the following experiments were done according to the corresponding in-house protocols: cell count, cell viability, phagocytosis, migration, and TNF- α production detected by ELISA. These initial results were recorded under Study Week 0 data as a baseline. Remaining cells were then split into two additional flasks, making a total of three flasks. The cells in each flask were then constantly cultured in media that contained 0 mM, 5 mM, and 25 mM of glucose, respectively. All flasks were continuously cultured and split weekly where the cell count and viability were recorded; all other experiments were done every three weeks. Following Study Week 20, the 5 mM group was removed from study and a new repeat 0 mM control flask was started. Unfortunately, due to unforeseen events, only one time point was able to be taken for the 0 mM repeat.

Results

The results of this study can be seen in the figures to follow. Figure 1 shows the production of TNF- α by each of the groups following treatment with LPS. Except for Study Week 6, negative controls that were not treated with LPS consistently had negligible TNF- α production as seen in Figure 2. Interestingly, prior to Study Week 10, the levels of TNF- α had been consistently increasing. After this week, the levels began to plummet for the next 6 weeks across all groups and then began to increase once again. Additionally, glucose concentration does not appear to impact TNF- α production as values were consistent across all groups.

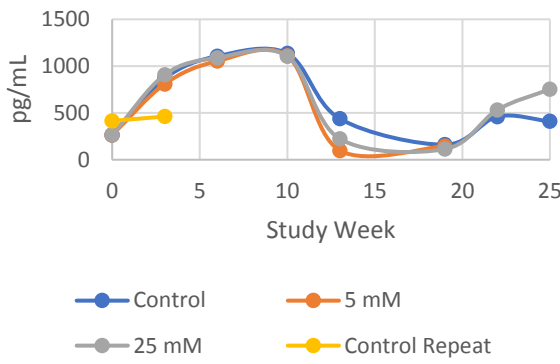


Figure 1. LPS-Treated TNF- α Production.

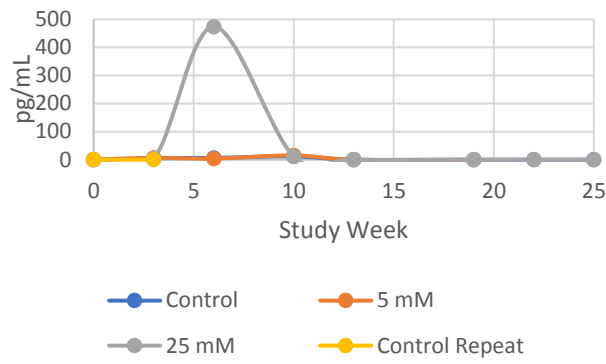


Figure 2. LPS-Untreated TNF- α Production.

Figures 3 and 4 demonstrate the number of cells migrated in the MCP1-Treated and the MCP1-Untreated control samples, respectively. The negative control values were not regular throughout the study. Once again, following Study Week 10 the values grew more consistent with fewer cells migrating in later weeks. The MCP1-Treated cells do not show any consistent trends regarding migration. However, results do appear to be the inverse of what was seen regarding TNF- α levels in Figure 1. The MCP1-Untreated control values from Figure 4 were then subtracted from the MCP1-Treated values of Figure 3 to obtain the Net Migration, represented in Figure 5. In all treatment groups, there does not appear to be a correlation between either glucose concentration and migration or age of the culture and migration.

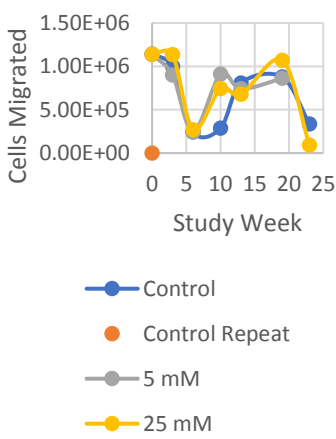


Figure 3. MCP1-Treated Migration.

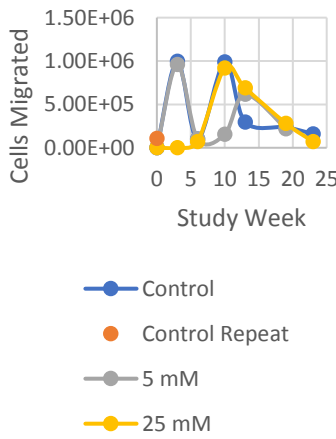


Figure 4. MCP1-Untreated Migration.

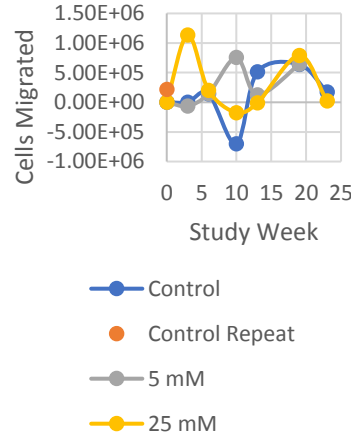


Figure 5. Net Migration.

Phagocytosis, or the ability of a macrophage to consume a pathogen, was one of the primary endpoints for this study. The fluorescent values for all PMA-Untreated controls remained constant throughout the study, as shown in Figure 6. Additionally, the PMA-Treated samples remained relatively constant but at higher values. This shows that there was no change in the cell's phagocytic activity over the course of 26 weeks. Figure 7 indicates that the standard utilized for this phagocytosis experiment, however, was not consistent. Between weeks 6 and 10, for example, the value of the standard decreased by half. As a result, when the control standard is subtracted to calculate the Net Fluorescence, the net value will simply be the opposite of the standard. This relationship is shown in Figure 8.

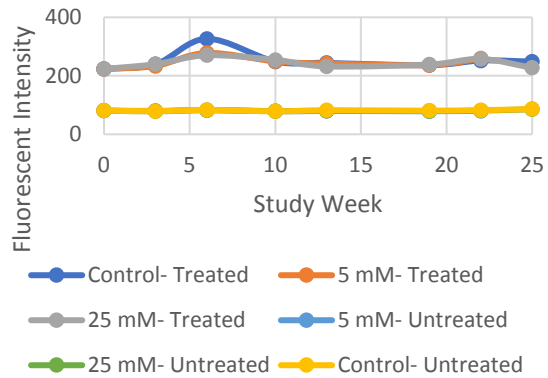


Figure 6. PMA-Treated vs PMA-Untreated.

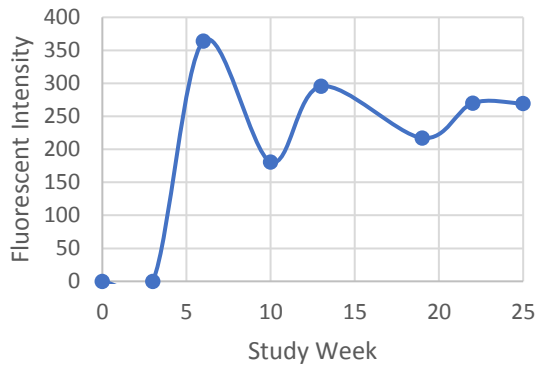


Figure 7. Fluorescent Standard.

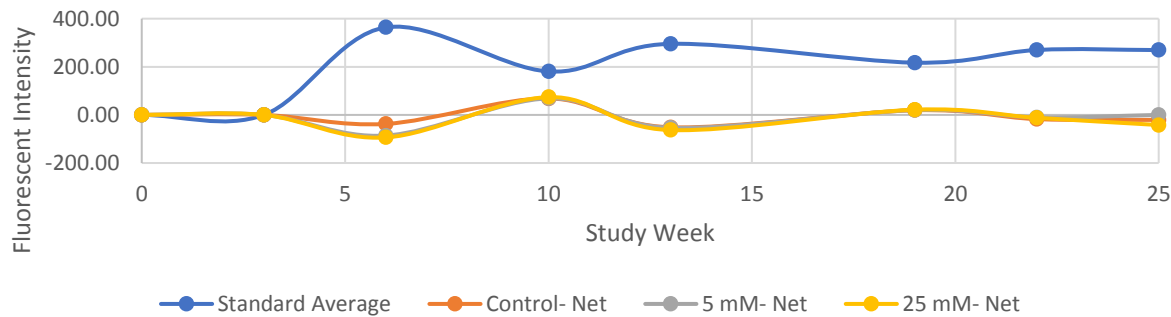


Figure 8. Net Fluorescence vs Fluorescent Standard.

Figure 9 graphs the viability of each culture at the weekly split. Data for cell count and viability was not recorded for Study Weeks 14 through 18. Overall, values were within an acceptable range for the duration of the study. Notably, there does appear to be a slower rate of recovery as the cells age, but this is not statistically supported. Figures 10 and 11 show a graphic representation of the growth rate and the inverse doubling time of the cells. This was calculated by using the weekly cell count and using the formula:

$$(\log N_t - \log N_0) / \log 2(t)$$

where N_t is the population at time t , N_0 is the starting population, and t is the time lapsed. Before Study week 10, the doubling time and the corresponding growth rate was not steady. Yet, following Study Week 10, there appears to be a short time of increased growth rates followed by a consistent decrease. This corresponds to a decrease in doubling time that is then followed by a steady increase. This, however, is not statistically significant. These results are consistent across all glucose concentration levels.

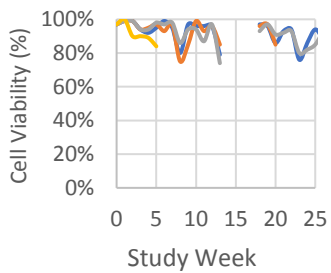


Figure 9. Cell Viability.

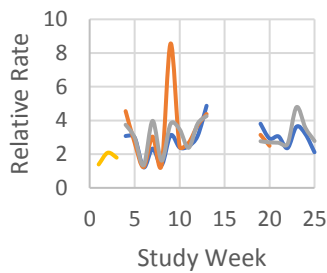


Figure 10. Cell Growth Rate.

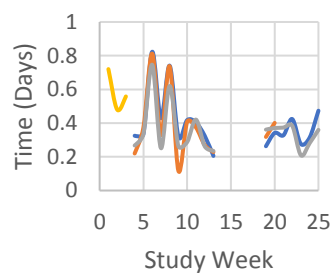


Figure 11. Cell Doubling Time.

Interpretation

Following continuous culture for a period of 26 weeks, few changes were noted in the THP-1 cell's ability to migrate, phagocytose, or produce TNF- α . Additionally, no statistically significant differences were found in the cells' replication rate. The concentration of glucose in the media also made little difference in the performance of these cells. As previously noted, however, many of these results shared an interesting shift at Study Week 10. Upon further examination, it was found that during Study Week 9 the CO₂ levels inside of the incubator were adjusted by another researcher due to difficulty growing a different cell line. This presents an interesting possibility regarding the role of CO₂ in the monocyte's overall health and its ability to perform certain tasks. Overall, the THP-1 cell line was found to be stable in continuous culture for up to 26 weeks regardless of media glucose concentration.

Acknowledgments

The author of this paper would like to thank Dr. Kaleb Pauley for her mentorship, technical guidance, and expertise for this study. Additionally, thank you to fellow researchers Katie Flint, Claire Burton, and Marie Butts for their help running various experiments.

References

1. Devaraj, S., Venugopal, S. K., Singh, U., & Jialal, I. (2005). Hyperglycemia Induces Monocytic Release of Interleukin-6 via Induction of Protein Kinase C- α and - β . *Diabetes*, 85-91.
2. Kuppan, G., Balasubramanyam, J., Monickaraj, F., Srinivasan, G., Mohan, V., & Balasubramanyam, M. (2010). Transcriptional Regulation of Cytokines and Oxidative Stress by Gallic Acid in Human THP-1 Monocytes. *Cytokine*, 229-234.

Selection of Appropriate Airfoil and Wing Parameters

Student Researcher: Ryan Watts

Advisor: Jed E. Marquart, Ph.D., P.E.

Ohio Northern University
Mechanical Engineering

Abstract

The structural design of an airplane is crafted carefully and iteratively to optimize the plane's performance for its intended mission. The purpose of this report is to describe the steps that were taken to select the airfoil and wing parameters that would be best suited for a general aviation plane. Inductive reasoning, coupled with research and past coursework, allowed for formation of initial specifications. This initial design was then tested under the simulation X-Plane 11. Adjustments were made as necessary. This trial and error approach continued until the team concluded that the NACA 23012 airfoil and a mid, unswept wing would best suit the general aviation's purpose.

Project Objectives

The objective for this project was to develop a general aviation aircraft. This meant that the aircraft would fly at relatively slower speeds, be fairly maneuverable, and have a shorter flight time. The specific requirements that the aircraft had was to seat no more than ten people, weigh a maximum of 12,500 lb, and fly at a maximum of 25,000 feet. With these goals in mind the team began developing an aircraft that would fit within all of this criteria.

Methodology Used

To begin, the team developed initial specifications based on our knowledge of the structures and their impact on the airplane's aerodynamic performance. The first determination was to start with a NACA 23012 airfoil. This airfoil was selected because of its ability to achieve a higher lift compared to an airfoil such as a NACA 2412. The team decided to use a mid wing for the aircraft as mid wings provide better aerobic maneuverability. The mid wing configuration was also originally chosen due to its ability to work well with a dihedral, which was included in the original design. The wing was kept unswept, as swept wings are better suited for high-speed flight, and our aircraft was to stay at relatively lower speeds. Additionally, the wings were chosen to be tapered due to tapered wings' ability to reduce the size of the wingtip vortices generated while flying, which creates a fair amount of drag on the aircraft.

With all of the parameters chosen, the aircraft was built and simulated. After a trial run in the simulation, the team ultimately decided to remove the dihedral on the wings, in order to increase the lift produced by the wings. With the dihedral removed, it was decided that the mid wing configuration would still work well with the aircraft. Ultimately, the majority of the initial chosen configurations for the aircraft were kept. However, the specific limitations regarding the wings configuration, such as the dimensions, were changed several times during the design in order to get the aircraft to perform as desired.

The Effectiveness of a Small Portable Solar Panel Set-up

Student Researcher: Michelle M Willoughby

Advisor: Professor Abigail Yee

Cincinnati State Community College
Electro-Mechanical Engineering Technology

Abstract

Using a remote solar panel, battery, and inverter to calculate energy absorbed and stored and the ability to transfer that energy into utility savings travel usage, such as camping or in emergencies. Employing either a magnetic or portable solar panel I will define utility savings and capabilities. To include or replace a large majority of electricity used in the home. Placement of the solar panel will be located on a car, therefore the solar panel will be able to charge whenever the weather allows for nine to ten hours of operational sunlight hours a day. Usage of two batteries to interchange when the primary battery has reached a full charging capacity will allow the user to efficiently obtain consistent benefits of the stored energy while the secondary battery continues to charge. Maintaining this cycle will contribute to the observation of the most accurate return on investment based on energy absorbed, stored and used.

Solar Energy

Solar energy is amongst several alternative energy forms that are becoming more and more popular. They are being utilized for their money-saving benefits as well as being earth-friendly. According to the article *What does it really mean to live off Grid* by Wood (2017) about 1.7 billion people around the world are living off grid. Wood (2017) references Home Power Magazine stated that about 180,000 of that number are Americans. This is based on statics from 2013 the number of people continues to grow every year. Off-grid living can be defined in multiple ways. One is to live without requiring electricity from a nearby electricity grid. However, to truly be off grid the structure must be able to fully operate without the usage of any public utility services. My objective was to make my living space off-grid, (or as much as possible). I started by measuring the wattage from my appliances in my home. Then I proceeded to research small solar panels and design a small solar setup. I will discuss each component of the solar setup, and what essential role they play. I will elaborate on the results of the solar energy I was able to capture. As well as and the energy efficiency of the project. In the final aspect of I will include the financial aspect of this project.

Measuring Wattage, and Calculating amp-hours¹

The results of measuring the wattage from each appliance used in my apartment can be found in Table 1. I used a wattmeter to measure the wattage being pulled to power each one. My apartment is powered with both gas and electric energy my focus was on the electric appliances pulling under 20 watts of power. This included every electronic device in my space other than the refrigerator and the coffee maker. I then calculated the watt-hour for each appliance. The formula for a watt-hour is found by multiplying the number of watts used by the hours the device would be on throughout the week. I then proceeded to measure the voltage using my Watt Meter. I took the calculated amp-hour from each device and divided it into the measured voltage this formula is used to find the amp-hour. The results are shown in Table 2. There must be a concrete calculation of how many amp-hours will be consumed. This allows you to accurately choose a solar panel that is capable of powering these devices. A fully charged 100-watt solar panel should produce around 30 amp-hours of power a day. The total of amp-hours I consumed a week is approximately 11.7 hours. The solar panel that most comfortable fit my

budget is a 100-watt panel. This demonstrates that my solar panel should only need one full day of sunlight or about 8 hours to be able to power all the smaller appliances in my space.

DOKIO 100 Watt 12-volt Panel

To convert the solar energy captured into power, you need to charge the solar panel then convert that power into usable energy. For this to be executed, a charging circuit and a discharging circuit were created. The schematic in *Figure 1* illustrates the charging circuit for this solar setup. Starting from the left-hand side I will expand on the brand of each component and their part in the circuit. Firstly, the solar panel, the DOKIO 100 watt 12-volt panel. It is a portable solar panel designed mainly for traveling vehicles such as RVs, campers, and caravans. The portability of the solar panel helped to capitalize on capturing the available sunlight. The DOKIO is a bendable semi-flexible thin film produced to fit irregular surfaces. I used it in both the window in my space and on top of my car.

Instapark Solar Charge Controller

Next, the solar panel is connected to the charge controller by the solar panel output adapter with a positive and negative wire. The charge controller is middle-man between the panel and the battery. It plays a very important role in the charging process. According to solarpanelsvenue.com, its key functions are protecting the battery from overcharging by limiting the charging voltage. Protecting the battery from deep and/or unwanted discharging. The charge controller automatically disconnects the loads from the battery when the battery voltage falls below a certain depth of discharge value.

Preventing the reverse current through PV modules at night. Providing information about the battery's state of charge. The charge controller used in the circuit is the Instapark INCC1205 12V / 5A Waterproof PWM Solar Charge Controller. The left-hand side of the controller is connected to the panel. The right-hand side has both a positive and negative wire and clamps that clamp to terminals of the battery.

Power Sonic 12-volt Rechargeable Battery

The battery is where the captured solar energy will be stored until it is discharged and used to power the inverter. The battery I used is the Power Sonic-1270 F1 which is a 12-volt rechargeable sealed lead-acid battery featuring 7 amp-hours. The calculated amp-hours for the week were 11.7 hours which comes out to about 1.67 amp-hours a day. Therefore, a fully charged battery would last more than four days.

In Figure 3 below you can see the second half of the solar set-up design the discharging circuit. After the solar energy charges the battery it is discharged into the inverter then inverted into usable electricity to power the appliances. Two power cables run from the positive and negative terminals of the battery to the positive and negative terminals on the inverter. The inverter I choose was the CEN-TECH 400-watt continuous power inverter. According to solarpowerworldonline.com, an inverter is the brains behind nay solar operation. Its basic function is to "invert" the direct current (DC) output into alternating current (AC). AC is the standard used by all commercial appliances, which is why many view inverters as the "gateway" between the photovoltaic (PV) system and the energy off-taker. After the energy is inverted the appliances can be plugged in and pull power.

CEN-TECH 400-watt Power Inverter

In Figure 2 below you can see the second half of the solar set-up design the discharging circuit. After the solar energy charges the battery it is discharged into the inverter then inverted into usable electricity to power the appliances. Two power cables run from the positive and negative terminals of the battery to the positive and negative terminals on the inverter. The inverter I choose was the CEN-TECH 400-watt continuous power inverter. According to solarpowerworldonline.com, an inverter is the brains behind

any solar operation. Its basic function is to “invert” the direct current (DC) output into alternating current (AC). AC is the standard used by all commercial appliances, which is why many view inverters as the “gateway” between the photovoltaic (PV) system and the energy off-taker. After the energy is inverted the appliances can be plugged in and pull power.

Panel Placement

The design of a solar set up includes how to position the panel. A solar panel has the greatest success when the placement allows it to capture the sunlight throughout the day and every season. According to the website greencoast.org the vertical tilt of the solar panel is termed as a tilt angle. The reason behind that is simple: they need maximum exposure to the sun. The sun moves throughout the day, and its position/angle also changes with the seasons. The goal is to have it exactly perpendicular to the incoming rays of the sun, as that is when they produce the most electricity. Since I used a portable solar panel that has some flexibility to it I could not replicate the exact tilt angle. Consequently, I focused on the placement, following where the sun was during the day. In the mornings I placed the solar panel in the east-facing window before sunrise. I was able to capture about 3-4 hours of direct sunlight before the sun was too high overhead. When the weather was permitting, I moved the solar panel to lay on top of my car for the afternoon into the evening hours. This allowed the panel to capture anywhere between another 2-5 hours of sunlight depending on the day. I document 38 hours of direct sunlight hours in 14 days. Reference Figure 3 below, I allowed one day in between charging the panel to see how many hours I could discharge the battery for. The goal was to be able to charge each appliance to the necessary amp-hour they required each day. Figure 5 below shows the daily power time each appliance required. The results show that the least number of hours of direct sunlight I could power the devices on was 5 hours. Therefore the 4 out of 7 days I had less than 5 hours of direct sunlight I could not power all the devices for the time I required them to be on. These numbers would, of course, vary over the course of a year. Depending on the season, this data was collected during a rainy and cloudy span in mid-March. Summer would allow for a lot more sunlight hours as well as a long span of hours. In the same sense, winter would more than likely be sunlight hours.

Finances

When it comes to the financial end, I first referenced my monthly energy bill. In order to find out exactly, what I was paying each for each kilowatt-hour (kwh) used. According to my calculations, it is right about 14 cents per kilowatt-hour. To find how many kilowatt-hours I was using a month I added up the amp-hours per day then multiplied that by 7 to get the amp-hours for the week. Reference Table 2 for the total amp-hours. I then took the amp-hours and the average voltage to find the kilowatt-hours per week. This number is 8.631 kwh. I then multiplied that number by the number of weeks in a year and divided that number by 12 to get an average of 37.401 kwh used a month on the appliances. If I multiply this by the cost per kwh of 14 cents I get \$5.24 a month with is equal to 62 dollars and 83 cents a year. In Table 3 below you can see the cost of each component of the solar set-up cost. The total cost is about \$205 which means the return on investment would take approximately 3 years and 4 months. After ten years your savings would be \$423.30 and after 20 years it would be 1,051.60. This means you would have made your investment back four times in 20 years.

Conclusion

In conclusion, the objective of making my space as off-grid as possible was a success. Using a portable solar panel, charge controller, battery and inverter. I was able to move the lightweight panel and necessary components and place them in a window on top of my car every other day for 2 weeks. At that time, I observed how the variable of the weather affected the available sunlight. I noticed the effects that sunlight hours were related to the stored energy available to be inverted. Which ended up

being the deciding factor in if there was enough power to keep the appliances on for the time that I needed. The results differed but I was able to conclude that if I got 5 hours of sunshine a day the process would be successful. Based on those calculations and variables I found that the return on cost would take a little over 3 years and the savings after 20 years would be more than \$1,000.

Figures/Charts

Table 1. Watt Hours.

Appliance	Watt	Hours	watt-hours Per Day
Candle warmer	13.3	24	319.2
Phone charger	6.0	8	48
Humidifier	12.2	12	146.4
UV plants lights	13.1	8	104.8
Water flosser	15.4	1/12	1.28
Lamp	13.2	2	26.4

Table 2. amp-hours.

Appliance	Watt-hour	Volt	amp-hour
Candle warmer	319.2	119.5	2.67
Phone charger	48	118.2	.41
Humidifier	146.4	118.7	1.23
UV plant lights	104.8	118.3	.86
Water flosser	1.28	119.5	.011
Lamp	26.4	117.7	.22
Total amp-hours			5.841

Table 3. Cost of Components

Components	Cost
Solar panel	\$114
Charge Controller	34
Battery	20
Inverter	37
Total Cost	\$205

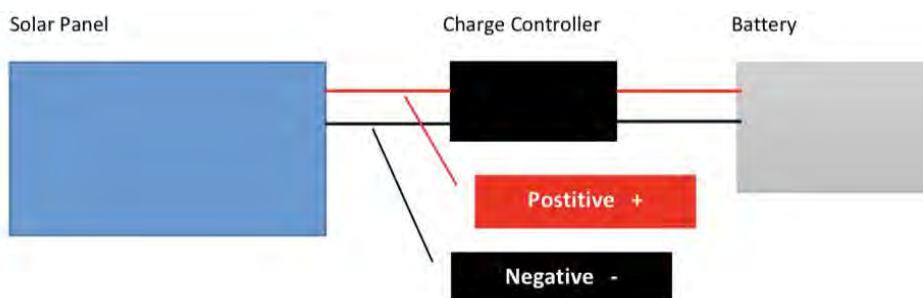


Figure 1. Charging Circuit Schematic.

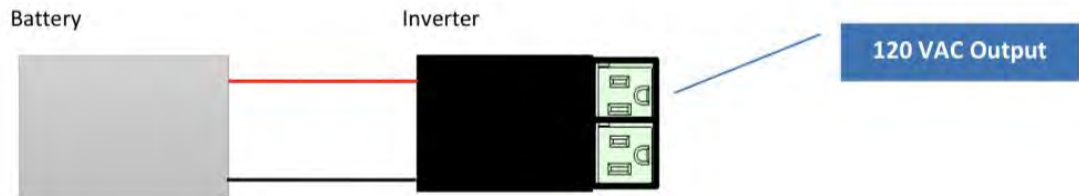


Figure 2. Discharging Circuit Schematic

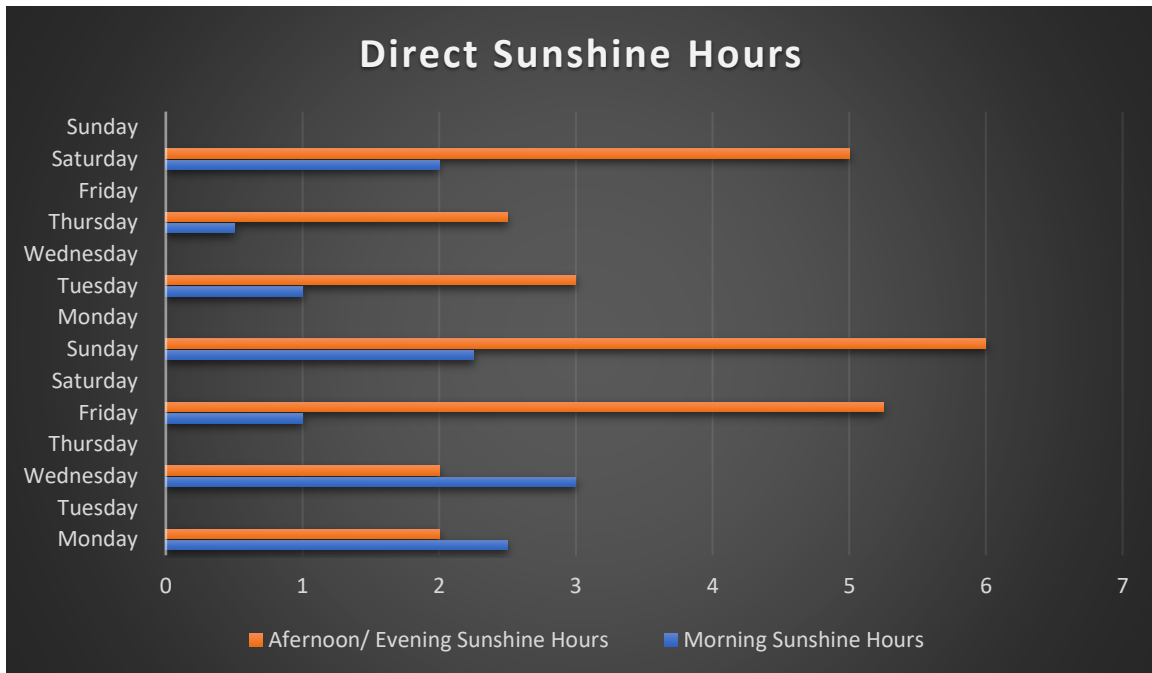


Figure 3. Second Half of the Solar Set-Up Design of the Discharging Circuit.

References

1. Green Coast | Renewable Energy and Green Living Blog. (2019). Retrieved from Green Coast website: <http://greencoast.org>
2. Home Power Magazine, infoplease.com. Accessed 2020 3AD.
3. "Solar Panels Secret Exposed." SOLAR PANEL SECRETS EXPOSED, solarpanelsvenue.com. Accessed 30 Mar. 2020.
4. "Solar Power Installation | Development | Technology News and Features." Solar Power World, 26 Oct. 2012, solarpowerworldonline.com. Accessed 30 Mar. 2020.
5. "Online Encyclopedia, Almanac, Atlas, Biographies, Dictionary, and Thesaurus." InfoPlease, 24 Jan. 2017, infoplease.com.

**Aquaporin-4 Distribution Correlates to Increase In Tau Accumulation
In Sprague Dawley Rats Fed a High Fructose Diet**

Student Researcher: Patrick G. Woller

Advisor: Dr. Jacqueline Morris

Baldwin Wallace University
Program in Neuroscience, Department of Biology and Geology

Abstract

According to the Center for Disease Control, 10% of the U.S. population has Type 2 diabetes.^[3] Type 2 diabetes is the prolonged production of insulin leading to desensitized insulin receptors not allowing glucose to enter cells. Fructose, a component of table sugar is sweeter than other sugars, thus is used as a sweetener to increase the palatability of food. In recent years, the increase of fructose in processed foods is linked to the rise in metabolic disorders and in some cases, obesity.^[8] The major blood vessels in the brain's glymphatic (waste clearance) system are covered by astrocytic end feet that form a barrier between brain tissue and the endothelial cells of the blood vessels. Aquaporin (water-channel) proteins are present in the astrocytic endfeet that surround the blood vessels and allow cerebral spinal fluid to remove waste from the brain. Inflammation and brain injury lead to a redistribution of aquaporin-4 (AQ4) channels from the endfeet to the astrocytic cell bodies.^[4] Type 2 diabetes has been shown to impair the clearance of the interstitial fluid by slowing the movement of cerebral spinal fluid.^[4] Previous disruption of the glymphatic system results in an accumulation of hyperphosphorylated tau tangles.^[9] In a streptozotocin (STZ) induced model of diabetes, AQ4 channels showed altered distribution from the blood vessels to the astrocyte cell bodies.^[5] It is expected that a diet consisting of high amounts of fructose will redistribute AQ4 away from astrocytic end-feet, thus increasing the amount of hyperphosphorylated tau tangles.

Project Objectives

The western diet consists of 60% fructose due to the added sugars in processed foods.^[6] Fructose is a common type of sugar that is found in fruits and vegetables primarily. However, the increased levels of fructose in the western diet may be a responsible for the large numbers of individuals with onset Type 2 diabetes.^[2] Fructose is metabolized primarily in the liver as opposed to glucose which is metabolized by cells throughout the body.^[2] Because of this, increased levels of fructose overwhelm the liver and non-alcoholic fatty liver has developed in some individuals which hinders the liver's ability to respond to insulin levels, which is a sign of onset Type 2 diabetes.^[2]

Streptozotocin (STZ) was used to induce Type 1 diabetes in a rat model as a positive control. STZ destroys pancreatic islet β -cells by inducing DNA strand break, thus poly (ADP-ribose) polymerase activation.^[1] Poly (ADP-ribose) polymerase activation then leads to reduction of NAD⁺, then eventually the cell death of pancreatic islet β -cells.^[1]

The aims of this study were to examine if a 60% fructose diet model using rats would alter AQ4 distribution in the brain's glymphatic system, resulting in increased hyperphosphorylated tau accumulation. Hyperphosphorylated tau accumulation correlates to the progression of cognitive decline. Diabetes has been demonstrated to decrease glymphatic cerebral spinal fluid flow, but previous studies have not determined the role of a fructose diet on AQ4 distribution in the rat brain.

Methods

Rats were obtained from the Baldwin Wallace house breeding facility and were separated into three groups at age post-natal (P)100-120. Streptozotocin (50 mg/kg intraperitoneal) was injected one week into the project, which was four weeks prior to perfusion.

A diet consisting of 60% high fructose (HF; Envigo diet TD.89247) (N=6) were fed for either 11 weeks or 14 weeks. The control rats (N=9) received regular chow CE-2 (CLEA Japan Inc.) for 11 and 14 weeks. Rats were tested for blood glucose levels at week 10 and week 12 following the high fructose diet using a Relion lancet device to determine glucose levels.

A total of 32 rats were perfused three weeks post blood glucose testing. Animals were anesthetized using intraperitoneal pentobarbital at a concentration of 150 mg/kg. A Perfusion 100 system (Leica) was then used to perfuse 4% PFA. The fixed rat brains were then sectioned (40 microns) with a Leica microtome.

Immunohistochemistry was conducted with primary antibody of aquaporin 4 (AQ4; ab9512) or phosphorylated tau (ab108387) at dilutions of 1:100 and 1:250 overnight at 4°C, respectively. Then, tissues were incubated with secondary antibodies conjugated to fluorophores anti-mouse 555 for tau (ThermoFischer A32727) and anti-rabbit 488 for AQ4 (ThermoFischer A32731) at the dilution of 1:1000 at room temperature for the duration of two hours.

Cresyl Violet staining was conducted to identify the size of the hippocampus indicating if neurodegeneration had occurred.

Non-biased stereology was conducted with the MBF Bioscience Area Fraction Fractionator for identifying and measuring accumulation of hyperphosphorylated tau tangles and the distribution of AQ4 within the hippocampus. Data were analyzed using a 2-factor analysis of variance (ANOVA), which were followed by post-hoc comparisons using Fischer's least significance difference. A P-value being less than 0.5 was described as significant.

Results Obtained

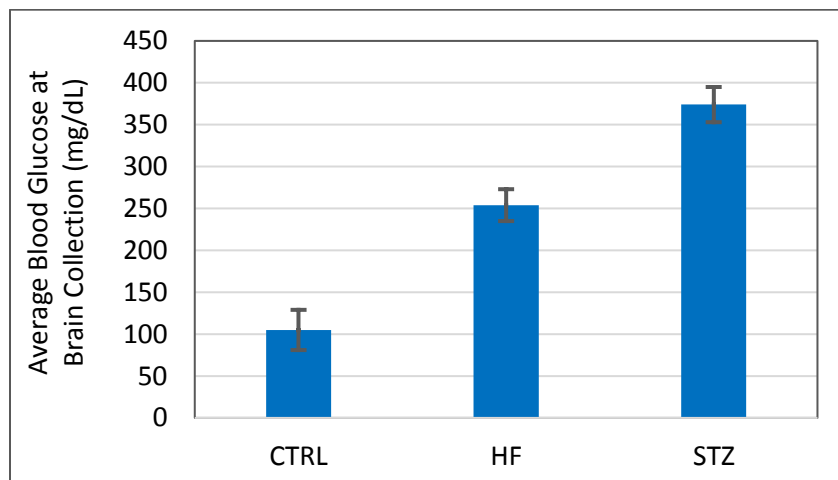


Figure 1. The blood glucose levels of CTRL rats (101 ± 35 mg/dL) were at normal blood glucose levels (90 mg/dL). In the STZ rats, blood levels (362 ± 25 mg/dL) exceeded the threshold of 270 mg/dL, which is an indicator of diabetes in rats. HF fed diet rats (251 ± 28 mg/dL) were elevated but did not reach diabetic threshold levels. There was a statistical significance in blood glucose levels between CTRL and STZ/HF fed rats ($P < 0.05$).

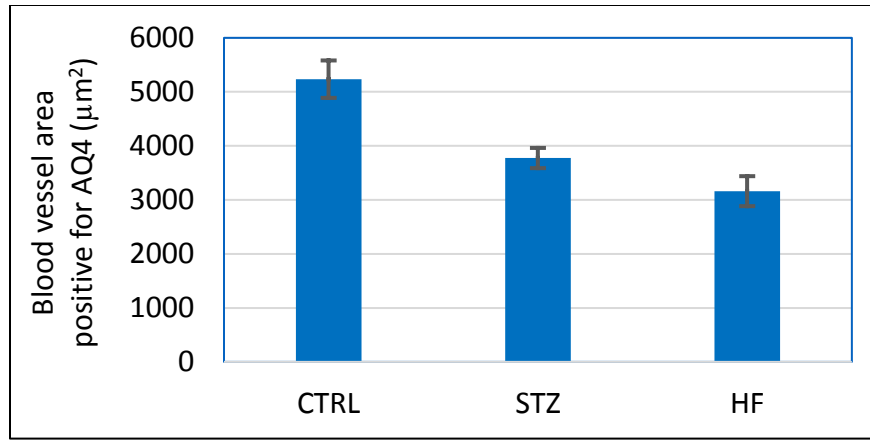


Figure 2. The hippocampus of rats fed a HF diet had lower AQ4 positive indications at astrocytic endfeet ($3161 \pm 278 \mu\text{m}^2$) than control ($5235 \pm 346 \mu\text{m}^2$). STZ induced diabetic ($3774 \pm 188 \mu\text{m}^2$) rats had similar reductions in AQ4 positive indications as HF diet animals. There was a statistical significance of AQ4 positive blood vessels between CTRL and STZ or HF fed rats ($P < 0.05$).

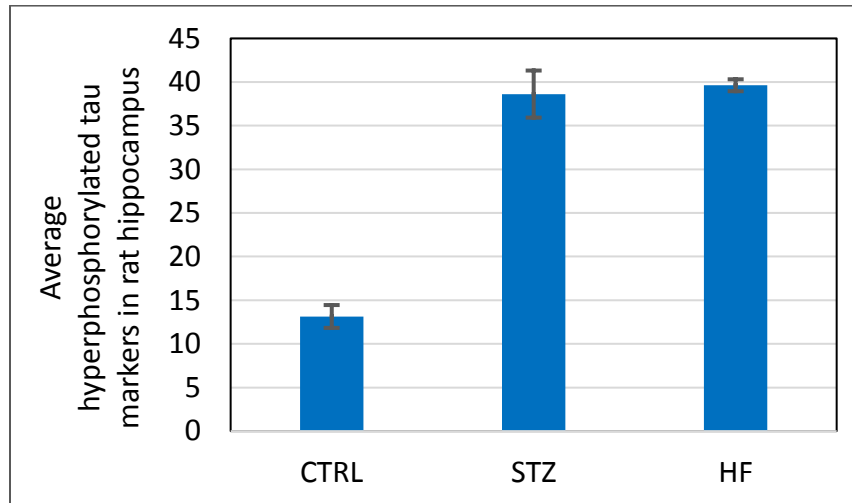


Figure 3. Rats fed 60% fructose (40 ± 0.7 tau indications) for 14 weeks had more tau positive accumulations than the control rats (13 ± 1.3 tau indications). STZ induced diabetic (39 ± 2.7 tau indications) animals had a similar increase in hyperphosphorylated tau accumulations as rats fed a high fructose diet. A statistical significance of hyperphosphorylated tau clumps markings between CTRL and STZ or HF fed rats ($P < 0.05$).

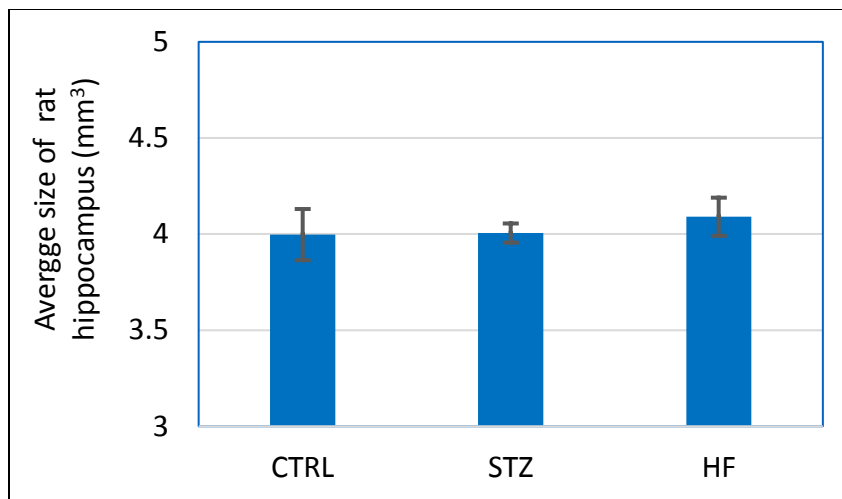


Figure 4. The hippocampus of CTRL rats ($4 \pm 0.14 \text{ mm}^3$) has similar density as the HF fed diet rats ($4.1 \pm 0.10 \text{ mm}^3$). STZ induced diabetic ($4 \pm 0.05 \text{ mm}^3$) animals showed similar hippocampus density size as HF fed diet and CTRL animals. There was not a statistical significance of hippocampus density size between CTRL and STZ or HF fed rats ($P > 0.05$).

Conclusion

Alzheimer's disease (AD) is a progressive disease that is associated with cognitive decline and neurodegeneration. One indication of AD is the development of tau tangles and a decrease in size of the hippocampus. In two diabetic models (one STZ injected and the other HF diet induced) we detected an increased accumulation of phosphorylated tau within the hippocampus compared to control ($P < 0.05$; Figure 3). However, the volume of the hippocampus was not significantly different ($P > 0.05$) (Figure 4). AQ4 distribution on the vessels was altered from the endothelial cells to the astrocytic cell bodies within the hippocampus (Figure 2). Thus, diets high in fructose may lead to alterations in aquaporin distribution that could disrupt the ability of the glymphatic system to clear waste products such as hyperphosphorylated tau.

References

1. Akbarzadeh, A., Norouzian, D., Mehrabi, M. R., Jamshidi, S. h., Farhangi, A., Verdi, A. A., Mofidian, S. M., & Rad, B. L. (2007). Induction of diabetes by Streptozotocin in rats. Indian journal of clinical biochemistry: IJCB, 22(2), 60–64. <https://doi.org/10.1007/BF02913315>.
2. Bantle D., John P. "Dietary fructose and metabolic syndrome and diabetes." *The Journal of nutrition* vol. 139,6 (2009): 1263S-1268S. doi:10.3945/jn.108.098020.
3. Centers for Disease Control and Prevention. *National Diabetes Statistics Report*. (2017).
4. Cui, B. et al. Aquaporin 4 knockdown exacerbates streptozotocin-induced diabetic retinopathy through aggravating inflammatory response. *Exp. Eye Res.* (2012). DOI 10.1016/j.exer.2012.02.013.
5. Jiang, Y. Transplantation of human fetal pancreatic progenitor cells ameliorates renal injury in streptozotocin-induced diabetic nephropathy. *J. Transl. Med.* (2017). DOI 10.1186/s12967-017-1253-1.
6. United States Department of Agriculture, Economic Research Service. USDA Sugar Supply: Tables 51-53: (2012). US Consumption of Caloric Sweeteners.
7. Xu, N. Xiao, Y. Chen, H. Huang, C. Marshall, J. Gao, Z. Cai, T. Wu, G. Hu, and M. Xiao, Deletion of aquaporin-4 in APP/PS1 mice exacerbates brain A β accumulation and memory deficits. (2015). *Mol Neu*.

8. Bray, G. Samara Joy Nielsen, Barry M Popkin, Consumption of high-fructose corn syrup in beverages may play a role in the epidemic of obesity, *The American Journal of Clinical Nutrition*, Volume 79, Issue 4, April 2004, Pages 537-543, <https://doi.org/10.1093/ajcn/79.4.537>.
9. Iliff, Jeffrey J et al. "Impairment of glymphatic pathway function promotes tau pathology after traumatic brain injury." *The Journal of neuroscience: the official journal of the Society for Neuroscience* vol. 34,49 (2014): 16180-93. doi:10.1523/JNEUROSCI.3020-14.2014.

Detection of Cocaine via Physically Functionalized Carbon Nanotubes-Sensors

Student Researcher: Reis L. Zandier

Advisor: Dr. Pedro Cortes / Dr. Eric MacDonald

Youngstown State University
Chemical Engineering

Abstract

Carbon nanotubes offer a positive outlook on the development of accurate and durable sensing technologies. Their exceptional chemical, mechanical, electrical, and optoelectronic properties allow for easy manipulation and customization of nanotube devices that target specific stimuli. Certainly, much attention for carbon nanotubes continuous to emerge from a diverse range of fields including chemistry, physics, materials science, and engineering. The development of quick and reliable methods of manufacturing carbon nanotube sensing devices will improve the platform of detection technologies available in the market.

Introduction

To date, the use of carbon nanotubes as the core detection material seems to represent a very promising nanostructure for detecting chemical agents. Indeed, one of the most promising sensing platforms of carbon nanotubes relies on the electrochemical properties of the nanostructures. In addition to the potential sensing capabilities of the aforementioned carbon nanotubes, it seems that novel supporting platforms are required where embedded circuits can be placed to assemble complex and intricate structures. The present work will investigate the incorporation of carbon nanotubes as a sensing platform into 3D printing structures for detecting hazardous solids, liquids, and gasses. This research will lead to the production of flexible sensors for the department of defense. Using CNT's for detection has been done in previous work and compares to the findings made by Elsevier Talanta in 2008. However, this research has yet to be performed to detect cocaine on 3D printed material.

Project Objectives

In the present work, carbon nanotubes were to be used on 3D printed wearable sensors to detect cocaine. Here, both epinephrine and norepinephrine solutions were tested to wrap and functionalize the CNTs to induce selectivity and sensitivity features towards cocaine. Both solutions were tested against differing concentrations of CNTs to observe which functionalization produced the best detection. The main objective of this research was to find the best combination of CNTs and solution that will most accurately detect cocaine in water.

Methodology

The type of Carbon Nanotubes used in this testing were COOH functionalized single wall CNTs. These CNTs were first mixed with D.I. water to make a solution, 1mg of CNTs for every 1mL of water. After the CNTs were prepared, two wrapping solutions were made to mix with the CNT solution which would induce selectivity and sensitivity features towards cocaine. One solution was based on norepinephrine and the other on epinephrine. Each wrapping solution had 1mg of solute per milliliter of D.I. water. In this study, two different CNT: wrapping solution ratios were investigated (1:1 and 2:1). Table 1 depicts the different sensors that were investigated.

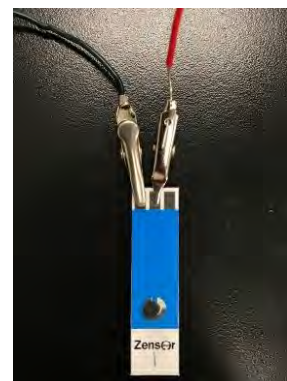


Figure 1. Prepared Electrode

Table 1. Functionalized CNTs based sensors studied in this research program.

Sensor	Concentration (CNT: E/N) E = Epinephrine N = Norepinephrine	Tested With
1A	1:1 E	Pure Water
1B	1:1 E	Cocaine in Water
2A	1:1 N	Pure Water
2B	1:1 N	Cocaine in Water
3A	2:1 E	Pure Water
3B	2:1 E	Cocaine in Water
4A	2:1 N	Pure Water
4B	2:1 N	Cocaine in Water

The preparation of the sensors included pipetting 20 microliters of the appropriate CNT: wrapping solution onto an electrode. The electrode was then cured at 60°C for one hour. The type of sensors used in the early stages of testing consisted of a 2-way carbon electrode. The electrodes were then ready for testing. The electrodes were assisted by a voltage power source, which provided about 5V and a DATAQ (Data Acquisition System), which recorded the change in resistance across the wrapped CNTs. Each sensor was ran for 3 minutes. Indeed, around one minute of the initial recording, 20 microliters of either pure D.I. water or a solution of cocaine in D.I. water (concentration = .016g in 1mL water) was added to wrapped CNTs. After the test was performed, the recorded data from the DATAQ was then transferred to excel. Here, the recorded resistance was normalized and compared across the different investigated sensors. Each sensor was studied with three replicates to avoid false positives. It is worth noting that the pure water testing was used in this work as the control.

Results Obtained

The results show that there was distinct detection among the four CNT: Epinephrine sensors tested. Figure 1 shows the three trials of the CNT:Epinephrine 1:1 ratio sensor tested with pure water as the control. Similarly, the 1:1 CNT:Epinephrine sensor was tested with cocaine in water (see Figure 2). All the trials from the water testing were averaged and then compared to the average of the cocaine in water testing. This comparison is displayed below in Figure 3. The same analysis was performed for the 2:1 (CNT:Epinephrine) sensors and displayed in Figure 4 below.

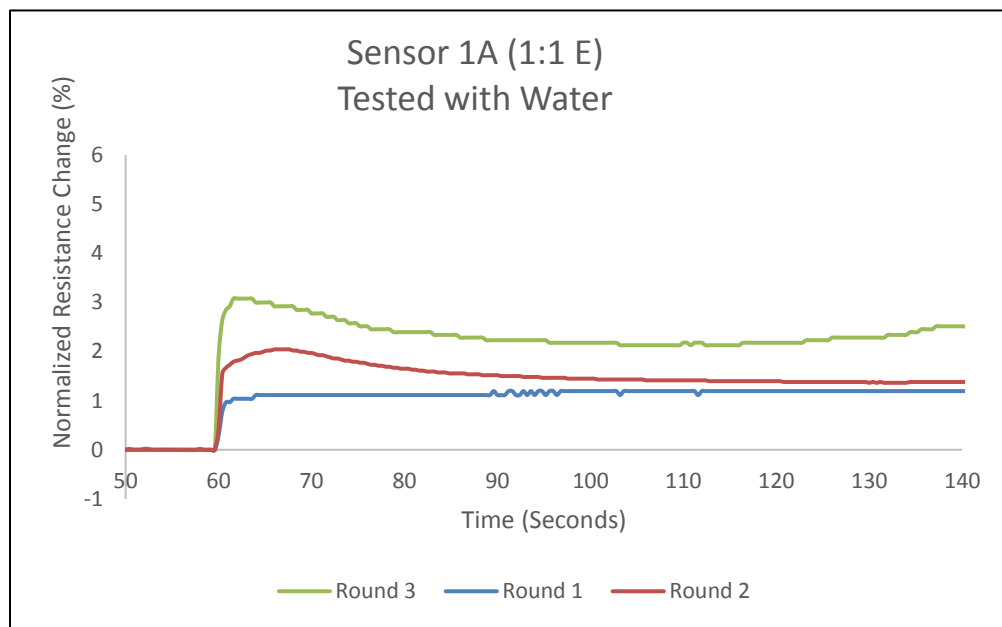


Figure 2. Normalized electrical response from the CNT:Epinephrine (1:1 ratio) sensor tested with water. (Sensor 1A)

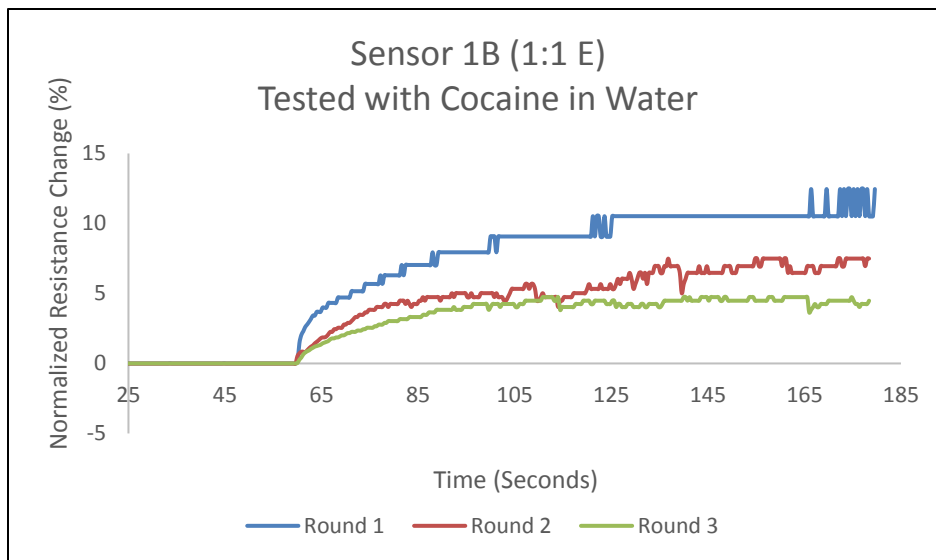


Figure 3. Normalized electrical response from the CNT:Epinephrine (1:1 ratio) sensor tested with cocaine dissolved in water. (Sensor 1A)

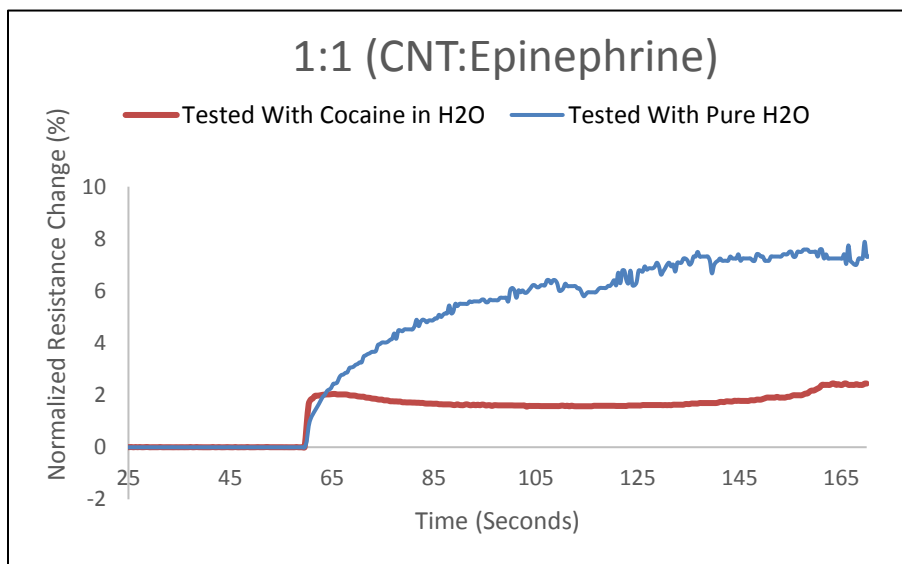


Figure 4. Comparison of the normalized electrical response from the CNT:Epinephrine (1:1 ratio) sensor against water and cocaine dissolved in water.

These results shown in Figure 3 display a clear distinction of the change of normalized resistance over time with the presence of pure water and the presence of cocaine in water. These preliminary results suggest that the use of Epinephrine on CNTs can provide a fast and inexpensive cocaine sensor.

Similar approach was followed with the CNTs:Epinephrine (2:1 ratio) sensor, and it was observed that by doubling the concentration of CNTs resulted in a lower detection selectivity (see Figure).

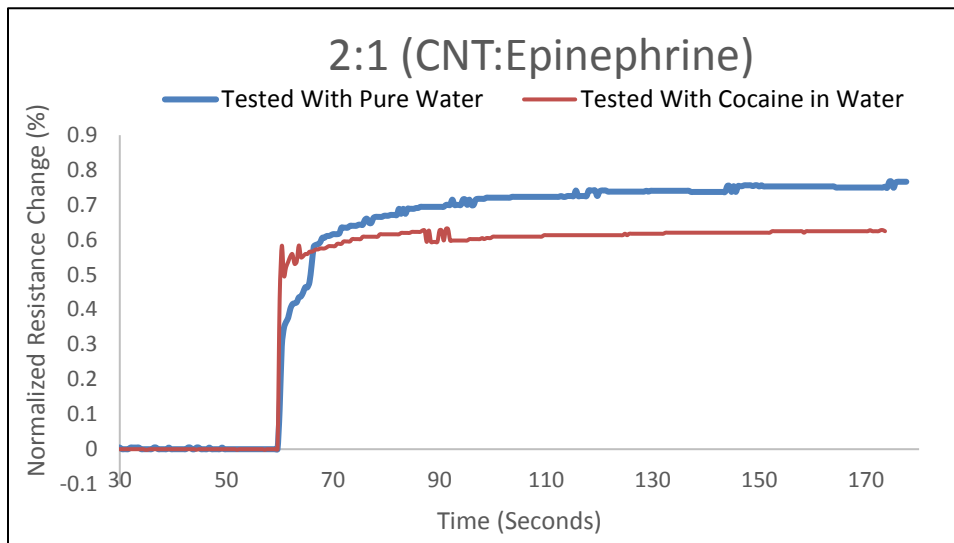


Figure 5. Comparison of the normalized electrical response from the CNT:Epinephrine (2:1 ratio) sensor against water and cocaine dissolved in water.

Figure 4 suggest that a higher concentration of Epinephrine needs to be incorporated into the CNT sensor to potentially provide a superior cocaine detection.

Additional detection tests were performed on the CNTs:Noroepinephrine sensors; however, non-conclusive results were obtained during the testing, and therefore are not presented.

Conclusions

The investigation of cocaine detection was performed on this work, and the initial results suggest that the inclusion of Epinephrine as the functional groups on CNTs seems to yield a clear detection when testing the drug dissolved in water. The results suggested that a higher functionalization-CNTs ratio needs to be incorporated to further investigate the sensitivity of the sensors. Future work on this project will focus on using 3D printed coins with electronics and LED sensing technologies as the electrode-reading platform.

References

1. www.sciencedirect.com/science/article/pii/S0039914008005523.
2. <https://www.sciencedirect.com/science/article/pii/S0956566315301640>
3. <https://www.sciencedirect.com/science/article/pii/S0003267014005844>
4. <https://pubchem.ncbi.nlm.nih.gov/compound/Cocaine>

Flavor Profile of Moonshine Homemade from Apples and Double Distilled

Student Researcher: Andrea L. Zirkle

Advisor: Dr. Regan Silvestri

Lorain County Community College
Department of Science

Abstract

Homemade moonshine prepared from fermented apples and double distilled was analyzed by gas chromatography-mass spectroscopy (GC-MS). The volatile compounds thus identified serve as a flavor profile of the spirit. As the moonshine has been fermented from apples, it was anticipated a-priori that the flavor profile would contain a wealth of pleasant aroma fruity esters. However, it was found that the flavor profile of the apple moonshine consists mainly of longer chain alcohols, butanols, pentanols and hexanols, which serve as off-flavors.

Overall, it was found that the flavor of the apple moonshine is dominated by 3-methyl-1-butanol which imparts a fusel, alcoholic, and fermented flavor often described as pungent. It is hypothesized that the fruity ester flavors were unfortunately removed during the double distillation process, which brought the spirit to 170 proof.

References

1. "Flavor Profile of Moonshine Homemade from Apples and Double Distilled", Proceeding from Society for Applied Spectroscopy 63th Annual May Conference, May 22, 2019.
2. "Flavor Profile of Moonshine Homemade from Apples and Double Distilled", The Ohio Journal of Science, Volume 120, No. 1, April 2020.